



**HAL**  
open science

# Organization within molecular layers grafted on Si surface and influence of photo-switching properties of fulgimides groups on surface.

Thang Long Nguyen Le

► **To cite this version:**

Thang Long Nguyen Le. Organization within molecular layers grafted on Si surface and influence of photo-switching properties of fulgimides groups on surface.. Material chemistry. Ecole polytechnique X, 2007. English. NNT : 2014EPXX0038 . tel-01252737

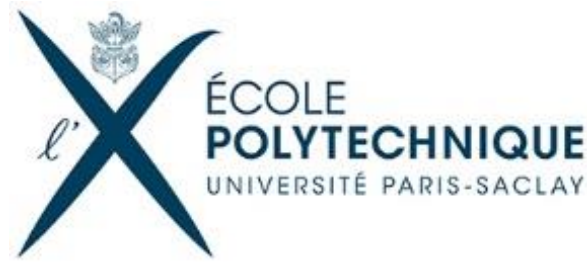
**HAL Id: tel-01252737**

**<https://pastel.hal.science/tel-01252737>**

Submitted on 8 Jan 2016

**HAL** is a multi-disciplinary open access archive for the deposit and dissemination of scientific research documents, whether they are published or not. The documents may come from teaching and research institutions in France or abroad, or from public or private research centers.

L'archive ouverte pluridisciplinaire **HAL**, est destinée au dépôt et à la diffusion de documents scientifiques de niveau recherche, publiés ou non, émanant des établissements d'enseignement et de recherche français ou étrangers, des laboratoires publics ou privés.



Thèse présentée pour obtenir le grade de

**DOCTEUR DE L'ÉCOLE POLYTECHNIQUE**

Spécialité : *Sciences des Matériaux*

Par

Thang Long NGUYEN LE

Sujet

**Organisation au sein de couches moléculaires greffées sur silicium (111), influence sur la photocommutation de groupements fulgimides.**

Soutenue le 11 juillet 2014 devant le jury composé de :

<b>M. Philippe HAPIOT</b>	<i>ENSCR</i>	<b>Président du jury</b>
<b>Mme Claire-Marie PRADIER</b>	<i>UPMC</i>	<b>Rapporteur</b>
<b>M. Yu PEI</b>	<i>Université Paris-Sud</i>	<b>Rapporteur</b>
<b>M. François OZANAM</b>	<i>Ecole Polytechnique</i>	<b>Directeur de thèse</b>
<b>Mme Catherine HENRY de VILLENEUVE</b>	<i>Ecole Polytechnique</i>	<b>Co-directrice de thèse</b>



# Acknowledgments

My deep gratitude goes first to my advisors, François Ozanam and Catherine Henry de Villeneuve, who expertly guided me through my graduate education and who shared the excitement of three years of discovery in PMC laboratory. I was very fortunate to have their support, guidance and endless help to finish this manuscript. Additionally, they were very patient and tolerant with this scientific adventure.

I am deeply indebted to Philippe Allongue for his time and effort in checking this manuscript. His unwavering enthusiasm for physics kept me constantly engaged with my research.

I am grateful to Claire-Marie Pradier and Yu Pei for reviewing the manuscript in spite of their very busy schedule. Their important suggestions enhanced this edition. My thanks are extended to Philippe Hapiot who agreed to participate in the examination committee.

I would also like to thank my friends Viacheslav Kubytskyi, Daniel Alves Dalla Corte, Di Nan, Lili Lu and Anne Moraillon for the support they have lent me over all these years. I am also deeply thankful to all the members of the laboratory for all the cheer and help.

Finally, I would like to thank my parents and my brother. Their support has been unconditional all these years.



# Table of Contents

Acknowledgments.....	a
Table of Contents .....	i
Glossary.....	iv
List of Figures.....	vi
List of Tables.....	xiv
General Introduction .....	1
References .....	5
<b>Chapter 1    <i>Mixed</i> Carboxydecyl/Decyl Monolayer on Si surface .....</b>	<b>9</b>
Introduction .....	10
1.1.        Surface preparation .....	14
1.1.1.    Silicon etching and surface hydrogenation.....	14
1.1.2.    Preparation of <i>mixed</i> $\omega$ -carboxydecyl/decyl surfaces .....	15
1.2. <i>Mixed</i> monolayers prepared from ethyl undecylenate/decene mixtures .....	17
1.2.1.    AFM characterization.....	17
1.2.2.    FTIR measurements.....	19
1.3. <i>Mixed</i> monolayers prepared from undecylenic acid/decene mixtures .....	27
1.3.1.    Surface characterization prior to and after <i>surface wiping</i> .....	27
1.3.2.    Surfaces after the <i>complete wiping</i> procedure .....	34
1.3.3.    Linkage of molecular-label onto the acid end-groups .....	48
1.4.        Discussion.....	54
Conclusions .....	62
References .....	63
<b>Chapter 2    Surface adsorption of undecylenic acid on H-Si surface .....</b>	<b>64</b>
Introduction .....	65
2.1.        Experimental procedures and results .....	69
2.1.1. <i>In situ</i> FTIR measurements.....	69
2.1.2.    AFM Imaging .....	73
2.2.        Discussion.....	75

Conclusions .....	79
References .....	80
<b>Chapter 3    Photoswitching properties of fulgimides in solution .....</b>	<b>81</b>
Introduction .....	82
3.1.        Experimental illumination set-up and procedures.....	84
3.2.        Photoswitching of amino-fulgimide in solution.....	85
3.2.1.    UV-Vis absorption spectra of C- and E/Z-forms.....	86
3.2.2.    Composition at PSSs .....	88
3.2.3.    Kinetics of photoswitching.....	90
3.3.        Discussion .....	93
3.3.1.    Photoswitching mechanism .....	93
3.3.2.    Kinetics of reactions .....	95
3.3.3.    Photo-isomerization cross-section .....	96
3.3.4.    Comparison between UV and Vis isomerization cross-sections .....	97
Conclusions .....	99
References .....	100
<b>Chapter 4    Fulgimide monolayer on Si surface .....</b>	<b>101</b>
Introduction .....	102
4.1.        Surface preparation .....	103
4.2.        Surface characterization.....	104
4.2.1.    Qualitative FTIR analysis .....	104
4.2.2.    Quantitative analysis.....	109
4.3.        Discussion .....	111
Conclusions .....	115
References .....	116
<b>Chapter 5    Photoswitching properties of fulgimides at Si surface .....</b>	<b>117</b>
Introduction .....	118
5.1.        Experimental illumination set-up and procedures.....	120
5.2.        FTIR measurements .....	124
5.2.1.    Qualitative analysis.....	124
5.2.2.    Quantitative analysis.....	127
5.2.3.    Kinetics of fulgimide photoswitching .....	131
5.3.        Discussion .....	139
5.3.1.    Photoswitching mechanism .....	139

5.3.2. The concentration of photo- <i>isomerizable</i> species on <i>dense</i> and <i>diluted</i> surfaces.....	140
5.3.3. Local electric field at fulgimide surfaces.....	141
5.3.4. Kinetic parameters.....	143
Conclusions .....	146
References .....	147
<b>General Conclusion .....</b>	<b>148</b>
<b>Appendix I Amplitude Modulation – Atomic Force Microscopy .....</b>	<b>151</b>
<b>Appendix II FTIR Spectroscopy in ATR geomtry .....</b>	<b>156</b>
<b>Appendix III Kinetics of photo-isomerization reaction .....</b>	<b>171</b>
<b>Appendix IV NMR analysis of fulgimides in solution.....</b>	<b>174</b>

# Glossary

Abs	Integrated absorbance
ATR	Attenuated total reflection
CMC	Critical micelle concentration
DCM	Dichloromethane
EDC	N-(3-Dimethylaminopropyl)-N'-ethylcarbodiimide
$\phi$	Photon flux
FTIR	Fourier transform infrared spectroscopy
FulgiC	C-form fulgimides
FulgiEZ	E/Z-form fulgimides
FWMH	Full width at half maximum
HPLC	High-performance liquid chromatography
H-Si	Hydrogenated silicon surface
$k_i$	Rate constant
LED	Light-emitting diode
MES	4-Morpholineethanesulfonic acid
ML	Monolayer
NC-AFM	Non-Contact – Force Atomic Microscopy
NH <sub>4</sub> F	Ammonium fluoride
NHS	N-Hydrosuccinimide
NMR	Nuclear magnetic resonance
NPE	Nitrophenethyl
NPEA	Nitrophenethyl alcohol
PC	Photochromic
PSS	Photostationary state
RMS	Root mean squared
SAM	Self-Assembled Monolayer
THF	Tetrahydrofuran
UPW	Ultra-pure water

UV	Ultraviolet
Vis	Visible
$\delta$	Deformation mode
$\eta_{\text{isomerized}}$	Number of photo-isomerized species
$\nu_a$	Asymmetric stretch
$\nu_s$	Symmetric stretch
$\sigma$	Photo-isomerization cross-section
$\sigma_{\text{normalized}}$	<i>Intensity normalized</i> photo-isomerization cross-section
$\tau$	Time constant

# List of Figures

Figure 1.1. Reaction scheme for the preparation of <i>mixed</i> carboxydecyl/decyl monolayer by hydrosilylation onto hydrogenated Si surfaces: (a) <i>Two-step</i> route by grafting from ethyl undecylenate/decene mixtures and subsequent hydrolysis, (b) <i>one-step</i> route by <i>direct</i> grafting from undecylenic acid/decene mixtures. ....	11
Figure 1.2. (A) Absorbance ratio of the ester carbonyl stretch to the total methylene asymmetric stretch as a function of the mole fraction of ethyl undecylenate in decene, <sup>17</sup> suggesting a proportionality between the ester content in the grafting solution and the surface concentration of grafted ester chains (B) Surface concentration, as determined by quantitative infrared spectroscopy, of carboxydecyl and decyl chains in grafted monolayers by the <i>one-step</i> route as a function of the acid fraction in solution. <sup>16</sup> .....	12
Figure 1.3. The distribution of COOH terminated chains in <i>mixed</i> carboxyalkyl/alkyl monolayers. (A) Homogenously distributed acid chains and (B) segregated acid chains. ....	12
Figure 1.4. Large-field AFM images (10 $\mu$ m $\times$ 10 $\mu$ m) – topography (left) and phase (right) – of a <i>pure</i> ester surface prior to and after hydrolysis. Topography and phase images of <i>pure</i> Si <sup>ester</sup> prior to (A, B) and after hydrolysis (C, D). Topography and phase images after hydrolysis of a <i>mixed</i> Si <sup>ester10</sup> (E, F).....	18
Figure 1.5. Topography (left) and phase (right) AFM images of a <i>pure</i> Si-acid <sup>ester</sup> surface (A, B) and a <i>mixed</i> Si-acid <sup>ester-10</sup> surface (C, D).....	19
Figure 1.6. FTIR spectra of a <i>pure</i> Si-ester monolayer prior to (a) and after hydrolysis (b). In both cases, the reference is the as-prepared hydrogenated surface prior to the grafting of the carboxylic esters. ....	20
Figure 1.7. Narrow FTIR spectra showing the $\nu$ C=O peak (A) and the $\nu$ CH bands (B) of different MLs prepared from ethyl undecylenate/decene mixtures with 100%, 30% and 10% ester content.....	22
Figure 1.8. Narrow FTIR spectra showing the $\nu$ C=O peak (A) and the $\nu$ CH bands (B) of different MLs after hydrolysis of the ester groups. ....	22
Figure 1.9. Experimental spectra and spectral deconvolution of the $\nu$ C=O bands of a <i>mixed</i> Si-ester <sup>30</sup> surface prior to (A) and after hydrolysis (B). The experimental spectra are plotted in grey (A) and dark blue (B). The red plots correspond to the resulting fitting curves. The two components used to fit the spectrum in (B) are assigned to acid (blue) and residual ester (purple) groups. ....	23
Figure 1.10. Integrated absorbance per reflection of the ester-related $\nu$ C=O bands prior to (Abs <sup>0</sup> <sub>ester</sub> , ●) and after hydrolysis (Abs <sup>hyd</sup> <sub>ester</sub> , Δ) and of the acid-related $\nu$ C=O bands (Abs <sup>hyd</sup> <sub>acid</sub> , ▲) as a function of the ester fraction in the grafting solution. ....	24
Figure 1.11. Surface composition of <i>mixed</i> MLs prepared from ethyl undecylenate/decene mixtures. Blue dots (●) stand for the nominal surface concentration of ester groups prior to hydrolysis, empty blue triangles (Δ) correspond to residual ester groups after hydrolysis and red triangles (▲) stand for surface concentration of acid groups after hydrolysis. Black squares (■) stand for the total concentration of alkyl chains (carboxyl + decyl). ....	26

Figure 1.12. Evolution of the frequency of the ester- (A) or acid- (B) related peaks as a function of the surface concentration of ester or acid end-groups in the MLs prior to or after hydrolysis, respectively.....	27
Figure 1.13. AFM images ( $2\mu\text{m} \times 2\mu\text{m}$ ) of a <i>pure</i> Si-acid surface after usual rinsing in hot acetic acid (A) and a <i>mixed</i> Si-acid <sup>20</sup> surface after successive rinsing in hot acetic acid and in dichloromethane, and finally cleaned by an additional <i>wiping</i> procedure (B).....	28
Figure 1.14. Optical (A, B) and large field AFM images (C, D, E, F) of a <i>mixed</i> Si-acid <sup>10</sup> surface, prior to <i>surface wiping</i> (A, C, E, F) and after (B, D) the first <i>wiping</i> procedure. Top view (E) and 3D (F) AFM images at greater magnification highlighting the spherical dome shape of few molecular structures and the presence of molecular aggregates on areas in between the molecular structures.....	29
Figure 1.15. Topography AFM images at different magnification of a <i>mixed</i> Si-acid <sup>10</sup> surface after the first <i>wiping</i> procedure. (A) Large-field image ( $10\mu\text{m} \times 10\mu\text{m}$ ) and (B and C) images at greater magnification showing the footprint of a molecular structure partially destroyed. Outside the disk-like area where excess matter is still present, the surface exhibits a staircase structure. Images (B) and (C) are zooms corresponding to the blue and red dashed areas in images (A) and (B), respectively.....	31
Figure 1.16. Topography AFM images of a <i>mixed</i> Si-acid <sup>10</sup> surface after the <i>complete wiping</i> procedure.....	31
Figure 1.17. (A) FTIR spectra (p-polarization) of a <i>mixed</i> Si-acid <sup>10</sup> surface prior to <i>surface wiping</i> (red) and after (black) the <i>complete wiping</i> procedure. (B) Spectrum of <i>mixed</i> Si-acid <sup>10</sup> surface prior to <i>surface wiping</i> referred to that after <i>wiping</i> procedure showing the absorption bands <i>specifically</i> related to the molecular entities composing the molecular structures, having disappeared after the <i>complete wiping</i> procedure.....	33
Figure 1.18. Topography (A) and phase (B) images of a <i>mixed</i> Si-acid <sup>10</sup> surface after <i>complete wiping</i> procedure. The surface is the same as the one shown in Fig. 1.15. The phase and topography images were recorded simultaneously thus warranting that the images refer to the same location at the surface.....	35
Figure 1.19. High-magnification topography and phase AFM images ( $200\text{nm} \times 200\text{nm}$ ) of a <i>mixed</i> Si-acid <sup>10</sup> surface: images of an area located outside domains (A, E) and inside a domain (B, F). Height profiles (C) and (D) of blue lines on (A) and (B), respectively, showing the distinct roughness on the terraces. (G) The histograms of the phase amplitudes for (E) and (F).....	36
Figure 1.20. AFM phase images of <i>pure</i> Si-acid, Si-decyl and <i>mixed</i> Si-acid <sup>V</sup> surfaces (V corresponds to acid fraction in acid/decene mixtures). The scanned area is $10\mu\text{m} \times 10\mu\text{m}$ except for image (C) for which the scanned area is $5\mu\text{m} \times 5\mu\text{m}$ .....	38
Figure 1.21. Distribution of the diameter of <i>micro</i> -domains on four different <i>mixed</i> acid surfaces.....	39
Figure 1.22. Surface coverage of <i>micro</i> -domains as a function of the acid content in solution.....	40
Figure 1.23. Phase AFM images at high magnification ( $200\text{nm} \times 200\text{nm}$ ) of <i>mixed</i> acid surfaces : (A) Si-acid <sup>20</sup> , (B) Si-acid <sup>10</sup> , (C) Si-acid <sup>1</sup> , (C) Si-acid <sup>0.1</sup> .....	41
Figure 1.24. AFM images of a <i>mixed</i> Si-acid <sup>0.01</sup> surface. (A) Topography image of the surface prior to <i>surface wiping</i> , (B) Cross-section along one single terrace of image (A) showing the size of the bright molecular aggregates. Topography (C, D) and phase images (E, F) of the same surface after the <i>complete wiping</i> procedure.....	42

Figure 1.25. FTIR spectrum of a <i>pure</i> Si-acid surface (p-polarization).....	43
Figure 1.26. Narrow FTIR spectra in the $\nu\text{C}=\text{O}$ range (A) and in the $\nu\text{CH}$ range (B) of <i>pure</i> Si-acid and <i>mixed</i> Si-acid <sup>V</sup> MLs. Each surface with its acid fraction in solution V is labelled on each corresponding spectrum.....	45
Figure 1.27. Experimental data and fitting curves for the $\nu\text{C}=\text{O}$ band of a <i>mixed</i> Si-acid <sup>20</sup> surface. Fitting curves obtained using one single (A) or two components (B).....	46
Figure 1.28. Sums of integrated absorbance in p- and s- polarization of the peaks centered at $\sim 1690$ ( $\text{Abs}^{\text{p+s}}_{1690}$ , $\diamond$ ) and $\sim 1715$ ( $\text{Abs}^{\text{p+s}}_{1715}$ , $\circ$ ) $\text{cm}^{-1}$ as determined from the fits and the sum of the two previous quantities ( $\text{Abs}^{\text{p+s}}_{1690+1715}$ , $\blacksquare$ ) as a function of the acid fraction in the grafting solution.....	47
Figure 1.29. Position (A, C) and linewidth (B, D) of the two $\nu\text{C}=\text{O}$ components at $\sim 1690$ (upper plots - A, B) and $\sim 1715$ $\text{cm}^{-1}$ (bottom plots - C, D) as a function of the acid fraction in the grafting solution.....	48
Figure 1.30. Reaction scheme for the covalent coupling of nitrophenethyl alcohol (NPEA) onto <i>mixed</i> carboxydecyl/decyl MLs.....	49
Figure 1.31. FTIR spectra of a Si-acid surface prior to (red) and after nitrophenethyl coupling (blue). The spectra are referred to that of the initial hydrogenated silicon surface.....	50
Figure 1.32. FTIR spectra of <i>pure</i> and <i>mixed</i> nitrophenethyl-terminated surfaces. The references are the acid-terminated surfaces prior to esterification.....	51
Figure 1.33. Narrow FTIR spectra showing the ester-related $\nu\text{C}=\text{O}$ peak after coupling on a <i>pure</i> Si-acid ML and a <i>mixed</i> Si-acid <sup>1</sup> ML.....	52
Figure 1.34. Surface concentration of nitrophenyl as a function of the acid fraction in the grafting solution.....	53
Figure 1.35. (A) Composition of the monolayers prepared by the <i>two-step</i> route as a function of the acid fraction in solution. Acid concentration is determined from the integrated absorbance of the acid-related peak ( $\blacktriangle$ ) (B) Composition of the monolayers prepared by the <i>one-step</i> route as a function of the acid fraction in the grafting solution. Acid concentration is determined from the total integrated absorbance of two peaks at 1690 and 1715 $\text{cm}^{-1}$ ( $\bullet$ ). Nitrophenyl concentration ( $\blacklozenge$ ) in monolayer after coupling with nitrophenethyl alcohol cross-check the acid quantification method. (A and B) Total chain concentrations of all monolayers ( $\blacktriangle$ , $\blacksquare$ ) were determined from the concentration of methylene groups.....	55
Figure 1.36. The maximum contribution of <i>micro</i> -domains (red) to the acid content of the monolayers as a function of the total acid concentration in MLs. The red bars remain much below the dashed line, figuring a hypothetical 100% contribution, which shows that the micro-domain contribution remains negligible.....	56
Figure 1.37. Peak position (A and C) and linewidth (B and D) of $\nu\text{C}=\text{O}$ peak as a function of the acid concentration in MLs prepared by the <i>two-step</i> (up) and <i>one-step</i> routes (down). The colored zone indicates the surface acid concentration range for which domains have been observed.....	57
Figure 1.38. Schematic represents a <i>mixed</i> alkyl/carboxyalkyl layers. The $\text{C}=\text{O}$ mode creates an angle of $\theta$ to the surface.....	59
Figure 1.39. The average degree of the dynamic dipole of $\nu\text{C}=\text{O}$ to surface, $\theta$ , determined from the number vibrators which have dynamic dipole parallel ( $N_{//}$ ) and perpendicular ( $N_{\perp}$ )	

to the surface, versus acid content in ML prepared by the (A) <i>two-step</i> and (B) <i>one-step</i> routes.....	59
Figure 2.1. Schematic illustration of self-assembly process of amphiphilic molecules as a function of their concentration in aqueous solution. (A) Self organization at concentration below and above the critical micelle concentration (CMC). (B) Examples of supra-molecular arrangements at large amphiphilic concentration. ....	66
Figure 2.2. Schema of individual amphiphilics, their possible reverse micelle or reverse bilayer self-assembled structures in a non-polar solvent. The polar head of the amphiphilics and their hydrophobic tail are colored respectively in orange and green. ....	66
Figure 2.3. Experimental set-up for the <i>in situ</i> FTIR analysis in ATR geometry. ....	69
Figure 2.4. FTIR spectra (s-polarization) in the 1150-1850 $\text{cm}^{-1}$ range (A) and in the 2750-3050 $\text{cm}^{-1}$ range (B) of undecylenic acid/decene mixtures containing acid content from 0.06 to 4% (from bottom to top). For all the spectra the reference is pure decene solution.....	70
Figure 2.5. Integrated absorbance (per reflection) of the acid-related $\nu\text{C=O}$ band as a function of the acid content in solution, in p- (left) and s- (right) polarization. Blue and red data correspond to FTIR measurements of undecylenic acid / decene solution at H-Si/solution interface. These measurements are compared to measurements of undecanoic acid/decane solution at Si-decyl/solution interface, used for the calibration of $\nu\text{C=O}$ band (see Appendix II). For the calibration experiment, the surface of the silicon prism was passivated with a decyl ML to prevent physisorption of decanoic acid. ....	71
Figure 2.6. (A) Integrated absorbance of <i>physisorbed</i> acid chains as a function of acid content in solution. (B) Surface concentration of acid chains physisorbed onto the H-Si surface exhibiting an adsorption isotherm shape. ....	72
Figure 2.7. AFM images of the surface topography of H-Si(111) surfaces exposed in the neat solution of decene (A) or in undecylenic acid/decene mixtures containing different acid fraction : (B) 0.02%, (C) 0.1% and (D) 1%. All images are plotted with the same Z-range ( $\Delta Z = 3$ nm). (E and F) Height profiles showing the peak-to-peak roughness on a single terrace of H-Si <sup>decene</sup> (from A) and H-Si <sup>acid-1</sup> surfaces (from D), respectively. (G) Surface roughness ( $R_{\text{RMS}}$ ) calculated on different images over 1 $\mu\text{m} \times 1 \mu\text{m}$ areas (black ■) or 500 nm x 500 nm areas (red ■), as a function of the acid content in solution. ....	74
Figure 2.8. AFM images of the H-Si surfaces after exposure in solution containing 0.02% (A), 0.1% (B) and 1% (C) acid fraction (same surfaces as those above discussed). For each image, the cross sections show the height of the aggregates. Notice the increasing density when the acid content increases in solution. ....	75
Figure 2.9. Suggested molecular organization on the Si surfaces <i>prior to grafting</i> (top) and <i>after grafting and cleaning procedures</i> (bottom) as a function of the undecylenic acid content in the grafting solution. The regions (A) and (B) refer to concentration range for which domains were observed on surface ( <i>nano</i> -domains in zone A and <i>nano</i> and <i>micro</i> -domains in zone B). Green sticks represent the decene molecules. Undecylenic acid molecules are represented by orange sticks (alkyl chains) and red balls (acid tail groups).....	76
Figure 2.10. Concentration of acid chains on Si surfaces as function of the acid content in undecylenic acid/decene mixtures. The black dots (●) correspond to surface	

concentration of <i>physisorbed</i> undecylenic acids on H-Si surfaces, the red squares (■) correspond to acid chains concentration in the MLs prepared by the <i>one-step</i> route and after the <i>complete wiping</i> procedure. ....	77
Figure 3.1. Photochromism of indolyfulgimide under Vis/UV irradiation. ....	82
Figure 3.2. Absorption spectra of the pure C-form (black line), of the pure E-form (black dashed) and of a mixture between the E- and the Z-form (black dotted). Figure is taken from ref <sup>23</sup> .....	83
Figure 3.3. Experimental set-up for <i>in situ</i> Vis or UV illumination in the UV-Vis spectrophotometer. Vis ( $\lambda = 525$ nm, viewing half angle of $\pm 8^\circ$ ) and UV ( $\lambda = 365$ nm, viewing half angle of $\pm 10^\circ$ ) LEDs were used as light source. ....	84
Figure 3.4. Absorption spectra in the UV/Vis spectral range of the “pure E/Z” solution or Fulgi-E/Z solution (blue dashed line), of the “pure C” solution (red dotted line) and of the Fulgi-C solution (red line).....	87
Figure 3.5. Evolution of UV/Vis absorption spectra of “pure C” (A) and “pure E/Z” (B) solutions during the first Vis or UV illumination cycle. Up-down and down-up arrows point out, respectively, a diminution or a raise of the bands intensity. Red and green spectra (A) correspond respectively to the spectra of the “pure C” solution prior to illumination and at PSS <sub>Vis</sub> . Blue and purple spectra on (B) correspond to the spectra of the “pure E/Z” solution prior to illumination and at PSS <sub>UV</sub> , respectively.....	88
Figure 3.6. Fraction of C- (red) and E/Z-forms (blue) at PSS after successive UV/Vis illumination cycles starting from <i>pure</i> Fulgi-C (A) or <i>pure</i> Fulgi-E/Z (B) solutions. ....	89
Figure 3.7. Evolution of the concentration of C- (▲) and E/Z-forms (●) in acetonitrile during the first two illumination cycles. (A) As-prepared Fulgi-C solution was illuminated with Vis then UV. (B) As-prepared Fulgi-E/Z solution was exposed to UV then Vis light. Dots and triangles are experimental data. The purple and green plots are the fitting curves for UV and Vis illumination cycle, respectively.....	91
Figure 3.8. Time constants $\tau^{\text{Vis}}$ (■), $\tau_1^{\text{UV}}$ (●) and $\tau_2^{\text{UV}}$ (○) of different illumination cycles starting from Fulgi-C (A) and Fulgi-E/Z (B) solutions. A break on Y-axis from 100 to 200 s. ....	92
Figure 3.9. Rate constants as a function of the photon flux determined from the Vis- (A) or UV-transients (B). ....	93
Figure 3.10. Photochromism of 2-aminoethylindolyfulgimide under Vis (→) or UV (←) illumination. The various $k_i$ 's stand for rate constants associated with different reaction paths.....	94
Figure 3.11. Absorption spectra in the UV/Vis spectral range of an as-prepared Fulgi-C solution prior to any illumination (red line) and after 10 min under UV illumination (purple dashed line). ....	94
Figure 3.12. Photo-isomerization cross section $\sigma^{\text{Vis}}$ (green square) and $\sigma_1^{\text{UV}}$ , $\sigma_2^{\text{UV}}$ and $\sigma_0^{\text{UV}}$ (purple circle) over successive cycles of as-prepared Fulgi-C (A) and Fulgi-EZ (B) solutions. ....	98
Figure 4.1. Multi-step protocol for the covalent coupling of amino indolyfulgimides onto acid terminated monolayer. (1) Conversion of the carboxylic acid tail groups into semi-stable succinimidyl esters ( <i>surface activation</i> ). (2) Covalent coupling of C-isomers (path A) or E-isomers (path B) through aminolysis. ....	102

Figure 4.2. FTIR spectra at the different steps of the surface preparation of a <i>dense</i> Si-fulgiEZ surface. (a) <i>pure</i> acid surface prepared by the two-step route, (b) the same surface after activation, (c) the same surface after the coupling of amino substituted fulgimide (E/Z-form). For all the spectra, the reference is the H-Si surface prior to grafting. ....	105
Figure 4.3. Narrow FTIR spectra of <i>dense</i> Si-fulgiC (a) and Si-fulgiEZ (b) surfaces. ....	106
Figure 4.4. Chemical structures of C- and E-form indolylfulgimides coupled through amide bonds to monolayers. Atoms in the fulgimide core were numbered for FTIR identification. ....	106
Figure 4.5. FTIR spectra of different fulgimide-terminated monolayers. (a) <i>dense</i> Si-fulgiEZ, (b) <i>diluted</i> Si-fulgiEZ <sup>30</sup> , (c) <i>dense</i> Si-fulgiC and (d) <i>diluted</i> Si-fulgiC <sup>10</sup> surfaces. For all spectra the reference is the H-Si surface prior to grafting. ....	108
Figure 4.6. AFM topography images at different magnification of as-prepared Si-FulgiEZ monolayer. ....	110
Figure 4.7. In-plane model of densely packed fulgimide ML on top of densely packed alkyl ML grafted on Si(111) surface. (a) The (1×1) structure of the Si(111) surface is plotted as grey circles, the black circles represent the ideal (2×1) structure corresponding to maximal packing of the carboxyl chains, the blue circles represent fulgimide arranged according to a (2×3) structure corresponding to a surface fulgimide density of $1.3 \times 10^{14} \text{ cm}^{-2}$ close to the maximal density determined experimentally. (b, c) C- and E-forms arranged according to a (2×3) structure. Notice that this structure allows for accommodating the fulgimide groups without lateral steric hindrance but corresponds to close-packing of fulgimide groups close to the maximum. ....	112
Figure 4.8. Nature and fraction of end-groups present on <i>dense</i> and <i>diluted</i> fulgimide-terminated surfaces. ....	113
Figure 4.9. Top (a) and side (b) views of the structure of C, E and Z isomers linked on top of carboxyl chains grafted on Si surface, through aminoethyl linker. ....	114
Figure 5.1. First experimental set-up used for <i>in situ</i> Vis/UV illumination of Si-Fulgi surface inside ATR chamber of the FTIR spectrophotometer. ....	120
Figure 5.2. Second experimental set-up used for <i>in situ</i> Vis/UV illuminations in the ATR-chamber of the FTIR spectrophotometer. ....	121
Figure 5.3. Third set-up designed for <i>in situ</i> Vis/UV illumination inside the ATR-chamber of the FTIR spectrophotometer. ....	122
Figure 5.4. Scheme of the different optical elements set on the beam path. The filters allow for reducing the photon flux, the cylindrical lens converts the divergent beam into parallel and homogeneous beam, the polarizer allows for selecting one of the component of the electromagnetic field (s- or p-polarization). ....	122
Figure 5.5. Photochromism of indolylfulgimide under Vis/UV irradiation. ....	124
Figure 5.6. FTIR absorbance spectra of <i>dense</i> Si-fulgiEZ and <i>dense</i> Si-fulgiC showing the main carbonyl $\nu_{\text{C=O}}$ bands stand respectively at 1689.9 and 1698.3 $\text{cm}^{-1}$ . ....	125
Figure 5.7. Evolution of FTIR absorbance spectra of a <i>dense</i> Si-fulgiEZ surface ( $1.7 \times 10^{14}$ E/Z-forms $\text{cm}^{-2}$ ) under UV (A) and then Vis (B) illuminations. ....	126
Figure 5.8. Position of the main $\nu_{\text{C=O}}$ peak at $\text{PSS}_{\text{UV}}$ and $\text{PSS}_{\text{Vis}}$ after successive UV/Vis illumination cycles of as-prepared <i>dense</i> Si-fulgiEZ (A) and <i>dense</i> Si-fulgiC (B) surfaces. The red and blue dotted lines correspond to its position found in the initial spectra of two surfaces prior to any illumination. ....	127

- Figure 5.9. Experimental spectrum of of an as-prepared *dense* Si-fulgiEZ surface after UV illumination (black plot) and its spectral deconvolution using a linear combination of the spectrum of a *pure* FulgiC- (red plot) and a *pure* FulgiE/Z (blue plot) surface. The resulting fitting curve is plotted in orange..... 128
- Figure 5.10. Isomeric composition of an as-prepared *dense* Si-fulgiC surface at the PSSs after successive Vis/UV illumination. (A) Surface concentration of open forms E/Z (●) and closed forms C- (■). The black triangles (▲) are the sum of C and EZ concentration. (B) Isomeric fraction as a function of the illumination cycles. Red bars correspond to the fraction of C isomers and blue bars to that of EZ isomers. Dashed red bars indicate the fraction of *non photoactive* C-isomers (see text) Odd numbers on X-axis refer to PSSs reached after Vis illuminations and even number to PSSs reached after UV illuminations. “0” gives the ML composition prior to any illumination. The surface was illuminated with the first experimental set-up ( $\phi_{UV} = 0.32 \times 10^{16} \text{ cm}^{-2} \text{ s}^{-1}$  and  $\phi_{Vis} = 3.17 \times 10^{16} \text{ cm}^{-2} \text{ s}^{-1}$ ). ..... 130
- Figure 5.11. Isomeric composition of an as-prepared *dense* Si-fulgiEZ monolayer at the PSSs after successive UV/Vis illumination cycles. (A) Surface concentration of E/Z- (●) and C- (■) forms. The black triangles (▲) represent the sum of C and E/Z forms. (B) Isomeric fraction as a function of the number of illumination cycles. The red bars refer to the ratio of C forms and the blue bars to that of EZ forms. Dashed red bars represent the fraction of C forms that become non-photoactive during illuminations. On the X axis odd numbers refer to PSS reached under UV illumination and even numbers to those reached under Vis illumination. “0” gives the composition of the ML prior to any illumination..... 131
- Figure 5.12. Differential FTIR spectra highlighting changes in C- and E/Z-isomers during first UV (A) and subsequent second Vis illumination (B). Arrows indicate the evolution of E/Z- (blue) and C-form (red) concentrations. The reference is that of the initially *dense* Si-fulgiEZ surface. The green and purple arrow corresponds to the time axe of illumination. .... 132
- Figure 5.13. (A) Differential spectrum (black) of the *dense* Si-fulgiEZ surface at 180s of its first UV cycle and the fitting curve (orange) corresponding to 0.21 of the differential spectrum of its first PSS<sub>UV</sub>. (B) Evolution of *isomerized* coefficient of the first UV cycle on an as-prepared *dense* Si-fulgiEZ surface and its fitting curve (red line)..... 133
- Figure 5.14. Time dependence of the surface concentration of *isomerized* fulgimide during the first UV illumination cycle of the *dense* Si-fulgiEZ surface. The slope B gives the *initial* isomerization rate and A the concentration of *photo-active* fulgimides. .... 134
- Figure 5.15. Photochromism of 2-aminoethylindolylfulgimide under Vis (→) or UV (→) irradiation. The various  $k_i$ 's stand for rate constants associated with the specific reactions. .... 140
- Figure 5.16. Isomeric composition of an as-prepared *diluted* Si-fulgiC surface at the PSSs after successive illumination cycles. (A) Surface concentration of E/Z- (●) and C- (■) forms. The black triangles (▲) represent the sum of E,Z and C forms. (B) Isomeric fraction of fulgimides (E/Z- (blue) and C- (red) forms) in the monolayer as a function of the illumination cycles. Odd numbers refer to the PSSs reached after Vis illumination and even to PSSs reached after UV. “0” gives the composition of surface prior to any illumination..... 141

Figure 5.17. Scheme of an incidence light beam at an angle $\theta$ with respect to normal surface, reflected onto an absorbing surface.....	142
Figure I.1. Schematic description of the operation principle of AFM. The feedback loop monitors the cantilever deflection and keeps it constant by adjusting the vertical position of the cantilever. ....	152
Figure I.2. Interaction forces as a function of tip-sample distance.....	153
Figure I.3. Dynamic Atomic Force Microscopy. ....	154
Figure II.1. ATR-IR system for <i>ex situ</i> (a) and <i>in situ</i> (b) measurements and the schematic of the evanescent field at the surface.....	157
Figure II.2. Examples of the one-peak and two-peak fitting process of the $\nu\text{C}=\text{O}$ band of 60 mM undecanoic acid in decane.....	159
Figure II.3. Examples of the one-peak and two-peak fitting process of the $\nu\text{C}=\text{O}$ band of a <i>mixed</i> Si-acid <sup>20</sup> surface.....	160
Figure II.4. Examples of the two-peak fitting process of the $\nu\text{C}=\text{O}$ band of a <i>mixed</i> Si-acid <sup>ester-30</sup> surface. ....	160
Figure II.5. The Assembly of Calibration System.....	161
Figure II.6. The integrated absorbance in s-polarization as a function of the undecanoic acid concentrations in decane solution. Points correspond to the experimental values and lines correspond to the linear regression fits. ....	162
Figure II.7. Examples of the one peak fitting process of the $\nu\text{C}=\text{O}$ band of a <i>mixed</i> Si-ester <sup>30</sup> surface. ....	163
Figure II.8. The integrated absorbance of the $\nu\text{C}=\text{O}$ bands in s polarization as a function of the ethyl undecanoate concentrations in decane solution. Points correspond to the experimental values and lines correspond to the linear regression fits. ....	164
Figure II.9. Experimental spectra of a <i>mixed</i> Si-acid <sup>20</sup> monolayer (black) and spectral deconvolution of $\nu\text{CH}$ bands (the resulting envelop and the different components are plotted respectively in red and different colors).....	165
Figure II.10. The integrated absorbance in s polarization of $\nu_s\text{CH}_2$ bands as a function of the decane concentrations in THF solution. Points correspond to the experimental values and lines correspond to the linear regression fits. ....	167
Figure II.11. Examples of the one peak fitting process of two $\nu_s\text{NO}_2$ and $\nu_a\text{NO}_2$ bands of a <i>mixed</i> Si-acid <sup>10</sup> surface after esterification (Si-nitro <sup>acid-10</sup> ). ....	168
Figure II.12. The integrated absorbance in s-polarization of $\nu_s\text{NO}_2$ and $\nu_a\text{NO}_2$ bands as a function of the nitrophenethyl alcohol concentration in DCM solution. Points correspond to the experimental values and lines correspond to the linear regression fits. ....	169
Figure III.1. Photochromism of fulgimide precursors under Vis ( $\rightarrow$ ) or UV ( $\rightarrow$ ) illumination. The various $k_i$ 's stand for rate constants associated with the specific reactions.....	171
Figure IV.1. NMR spectrum of EZ-isomer showing a ratio E:Z = 0.75:0.25. ....	175
Figure IV.2. NMR spectrum of C-isomer. ....	176

# List of Tables

Table 1.1. Positions and band assignments of the band observed on FTIR spectra of a <i>pure</i> Si-ester monolayer prior to and after hydrolysis.....	21
Table 1.2. Integrated absorbance per reflection of the ester- and acid-related $\nu\text{C}=\text{O}$ peaks and hydrolysis yield determined. The hydrolysis yield was calculated as the difference of the integrated absorbance of the ester-related peak prior to ( $\text{Abs}_{\text{ester}}^0$ ) and after hydrolysis ( $\text{Abs}_{\text{ester}}^{\text{hyd}}$ ) normalized to the nominal integrated absorbance prior to hydrolysis ( $\text{Abs}_{\text{ester}}^0$ ).....	25
Table 1.3. Surface concentration of acid and methylene groups on a <i>mixed</i> Si-acid <sup>10</sup> surface prior to <i>surface wiping</i> and after the <i>complete wiping</i> procedure.....	33
Table 1.4. Assignment and position of the IR bands observed on the spectrum in Fig. 1.25.....	44
Table 1.5. Assignments and positions of the nitrophenyl-related bands.....	50
Table 1.6. Integrated absorbance of the acid-related ( $1715\text{ cm}^{-1}$ ) and ester-related ( $1740\text{ cm}^{-1}$ ) $\nu\text{C}=\text{O}$ peaks prior to and after esterification, and esterification yield.....	52
Table 3.1. Characteristics of the experimental illumination set-up used for the study of fulgimide in solution.....	85
Table 3.2. C/E/Z isomeric ratios in solution “pure E/Z” and “pure C” as determined from NMR analysis.....	86
Table 3.3. C/E/Z isomeric fractions in solution at PSSUV and PSSVis as determined from different techniques: UV-Vis spectroscopy or HPLC.....	89
Table 3.4. Fitting parameters of the transients obtained during the first Vis illumination for an as-prepared FulgiC solution. The transients were fitted to an exponential function.....	91
Table 3.5. Fitting parameters of the transients obtained during the second UV illumination for an as-prepared FulgiC solution. The transients were fitted to a bi-exponential function.....	92
Table 4.1. Peak positions and assignments at the different steps of the surface modification. (*) Fulgimide bands were assigned in agreement with the experimental and predicted data from Koller <i>et al.</i> <sup>2</sup> . Numbered atoms refer to the labels shown in Fig. 4.4.....	107
Table 4.2. Surface concentrations of carboxyl (-COOH), hydroxysuccinimide (-NHS) and indolylfulgimide groups and the activation and coupling yield for four different surfaces.....	110
Table 5.1. Characteristics of the incident beam in the first experimental set-up.....	121
Table 5.2. Characteristics of Vis beam light in the third experimental set-up.....	123
Table 5.3. Characteristics of the UV beam light in the third experimental set-up.....	123
Table 5.4. Kinetic parameters of the first UV illumination cycle of as-prepared dense Si-fulgiEZ surface. $\phi_{\text{UV}} = 3.2 \times 10^{15}\text{ s}^{-1}\text{ cm}^{-2}$ .....	135
Table 5.5. Kinetic of fulgimide photo-isomerization for an as-prepared <i>dense</i> Si-fulgiEZ monolayer during UV illumination cycle. $\phi_{\text{UV}} = 3.2 \times 10^{15}\text{ s}^{-1}\text{ cm}^{-2}$ .....	136
Table 5.6. Kinetic of fulgimide photo-isomerization for an as-prepared <i>dense</i> Si-fulgiEZ monolayer during Vis illumination cycle. $\phi_{\text{Vis}} = 3.2 \times 10^{16}\text{ s}^{-1}\text{ cm}^{-2}$ .....	136

Table 5.7. Kinetic of fulgimide photo-isomerization for an as-prepared <i>dense</i> Si-fulgiC monolayer during Vis illumination cycle. $\phi_{\text{Vis}} = 3.2 \times 10^{16} \text{ s}^{-1} \text{ cm}^{-2}$ .....	136
Table 5.8. Kinetic of fulgimide photo-isomerization for an as-prepared <i>dense</i> Si-fulgiC monolayer during UV illumination cycle. $\phi_{\text{UV}} = 3.2 \times 10^{15} \text{ s}^{-1} \text{ cm}^{-2}$ .....	136
Table 5.9. Kinetic of fulgimide photo-isomerization during Vis illumination cycles for different experiments.....	137
Table 5.10. Kinetic of fulgimide photo-isomerization during UV illumination cycles for different experiments.....	138
Table 5.11. Dielectric coefficients of silicon surface at 525 and 365 nm (data obtained from the ref <sup>19</sup> ).....	142
Table 5.12. Surface intensity coefficient for illumination at 525 and 365 nm.....	143
Table 5.13. Kinetic parameters of Vis illumination cycle for different experiments.....	144
Table 5.14. Kinetic parameters of UV illumination cycle for different experiments.....	144
Table II.1. Example of fitting parameters used for the spectral deconvolution of the $\nu\text{C}=\text{O}$ bands in the spectra of 60mM undecanoic acid in decane in Fig. II.2b.....	160
Table II.2. Example of fitting parameters used for the spectral deconvolution of $\nu\text{C}=\text{O}$ bands in the spectra of a <i>mixed</i> Si-acid <sup>20</sup> monolayer in Fig. II.3b.....	161
Table II.3. Example of fitting parameters used for the spectral deconvolution of $\nu\text{C}=\text{O}$ bands in the spectra of a <i>mixed</i> Si-acid <sup>ester-30</sup> monolayer in Fig. II.4.....	161
Table II.4 : Example of fitting parameters used for the spectral deconvolution of $\nu\text{C}=\text{O}$ bands in the spectra of a <i>mixed</i> Si-ester <sup>30</sup> monolayer.....	163
Table II.5 : Example of fitting parameters used for the spectral deconvolution of the spectra of a <i>mixed</i> Si-acid <sup>20</sup> monolayer in $\nu\text{CH}$ region.....	166
Table II.6. Example of fitting parameters used for the spectral deconvolution of $\nu_{\text{s}}\text{NO}_2$ and $\nu_{\text{a}}\text{NO}_2$ bands in the spectra of a <i>mixed</i> Si-nitro <sup>acid-10</sup> monolayer.....	168



# General Introduction

The design of functional surfaces is a very active research field because of the important fallouts for a wide field of applications. Within this context, the functionalization of solid surfaces through the anchoring of molecular entities exhibiting specific functionality has received great attention and is currently a widely developed strategy.

Such monolayers can be formed through chemisorption or physisorption. While chemisorption tends to form a robust chemical bond, physisorption is based on a weak Van der Waals interaction. The most studied systems are monolayers of alkanethiolates on gold by spontaneous adsorption from either the liquid or the vapor phase.<sup>1-8</sup> Monolayers can assemble and form closely packed and ordered layers through formation of fairly stable sulfur-metal bonds ( $\sim 100 \text{ kJ mol}^{-1}$ ). Thiol groups also adsorb on others metal such as silver, copper, palladium, platinum, mercury, and alloys of these metals. Another widely studied system are alkylsilane monolayers on oxide surfaces, such as  $\text{SiO}_2/\text{Si}$ .<sup>9-11</sup> The organosilane monolayers on  $\text{SiO}_2$  were widely used in silicon technology for optical devices or biosensors. The alkyl silane monolayers can be formed by the covalent Si-O-Si binding of silanol group to the surface.<sup>12</sup> It was reported that the monolayers are stable in air up to about  $150^\circ\text{C}$ <sup>13,14</sup> and also in different organic solvent or hot water or detergent solutions<sup>15,16</sup>. However, the system has several disadvantages due to the present of oxide layer, such as limited electrochemical performance,<sup>17</sup> poor electronic properties or insufficient electric insulating strength.<sup>18</sup>

In 1993, Chidsey et al. reported for the first time a densely packed alkyl monolayer covalently bound directly to the silicon surface.<sup>19</sup> It was an important step forward in the important area of the fabrication of new semiconductor-based sensors and devices, providing new capabilities in optical, electronic, biological and mechanical properties.<sup>20</sup> Among different methods for direct bounding monolayers on silicon surface, thermal and photochemical hydrosilylation of alkenes is quite attractive because of the mild reaction conditions, low cost and high quality of monolayer.<sup>21</sup> The monolayers can be closely packed and stable under different environments, including boiling water, organic solvents, acids and bases, and air and over long period of time.<sup>22-25</sup> Examples of monolayers on silicon containing functional groups assembled via thermal or photochemical hydrosilylation include esters,<sup>26-28</sup> carboxylic acids,<sup>28-32</sup> alcohols,<sup>28,33</sup> amines,<sup>34,35</sup> aldehydes,<sup>36,37</sup> NHS<sup>38</sup> and acyl fluoride<sup>39</sup>.

Among all functional groups, carboxylic acids have received special consideration because they can be used for the binding of complex organic or biological molecule by a simple chemical route, such as the NHS/EDC-activated amidation. The coupling with primary amine (amidation reaction) forms a stable amide linkage.<sup>40</sup> It was reported that the carboxyalkyl monolayers can be prepared in two steps by grafting ester-alkene chains and subsequent hydrolysis<sup>41</sup> or by *direct* grafting acid-alkene chains.<sup>30</sup> It leads to an easy and direct preparation method of acid-functionalized monolayers.<sup>42</sup>

Mixed monolayers (i.e., monolayers in which the functional chains are dispersed among non-functional ones) can be useful for different purposes e.g., critically controlling the interfaces properties or creating free space to avoid crowding for bulky molecules coupled on functional tail groups<sup>43,44</sup>. Boukherroub<sup>45</sup> and Faucheux<sup>32</sup> reported that a *mixed* acid monolayer can be assembled on silicon in the presence of an alkyl chain, i.e. decyl, to dilute the functional group concentration in a mixed monolayer. Mixed monolayers are usually obtained by reacting the surface with a mixture of functional and non-functional precursors. However, the ratio of functional groups in the monolayer does not always map that in the grafting solution. The distribution of functional end-groups in such *mixed* monolayers on silicon has also been scarcely investigated. It has been suggested that the homogeneity in the distribution of acid groups in these layers varies as a function of the preparation route.<sup>46</sup> Several other studies conclude that functional end-groups are randomly distributed when the mixed monolayer are prepared in the two-step route.<sup>26,27,47,48</sup> However, all these conclusions rely on indirect evidences and additional assumptions.

In the specific context of functional molecular layers, the anchoring of stimuli-responsive molecules is currently receiving great attention because of their potential for the design of “smart” surfaces whose properties might be piloted by external stimuli such as light, electric field, chemical agents (e.g., pH or redox species). Organic photochromes are bi-stable molecular systems that undergo isomerization under illumination or in some cases under electrical polarization. The isomerization is generally accompanied of changes of properties (optical absorption, conductivity, charge, refractive index...). The immobilization of such systems on solid surfaces opened interesting perspective for the development of various optically triggered-based devices.

Among the different families of organic photochromes (spiropyran and spiroaxazine, azobenzene, naphthopyran, diarylethene...), indolyfulgide compounds and their derivatives

indolyl fulgimides exhibit interesting properties that make them good candidates for applications like optical memories or optical switches.<sup>49</sup> In solution, reversible photo commutation is reported. The isomers are thermally stable and exhibit great photostability under repeated illumination cycles. In addition ultra-fast reaction dynamics are reported.<sup>27,28,50</sup> However, the anchoring of complex molecular entities on a solid surface while keeping their functionality remains very often a challenge. Up to now, most of the studies dealing with the photo-switching properties of organic photochromes immobilized on surfaces concerned Self Assembled Monolayers on metals (SAMs on Au or Pt)<sup>1,2</sup> and much more scarcely and more recently on semiconductor surfaces.<sup>3-5</sup> The read-out of the photo-commutation, which is not trivial because of the low concentration of photochromes, is performed indirectly through macroscopic measurements of wetting properties (contact angle)<sup>51-53</sup>, or variations of UV-Vis optical properties (refractive index<sup>53,54</sup>, reflectance<sup>55</sup>, fluorescence<sup>56</sup>, absorbance<sup>57</sup>), conductance measurements<sup>58</sup>. Spectroscopic measurements (SERS or SPR)<sup>54,59,60</sup> are also used as well as electrochemical measurements<sup>54,61</sup>, or more locally using Scanning probe Microscopy (STM<sup>58,62-64</sup>, CAFM<sup>65</sup>). Over all, these works report photoswitching properties that differ from those in solution. The origin of this different behavior is generally assigned to the specific environment of the photochromes. Steric effects, interactions between photoswitchable groups and/or with the surface as well as electronic effects related to the vicinity of the metallic surface are pointed out to explain the changes in the photo reactivity on the surfaces.

The present work has been devoted to the study of the photoswitching properties of indolylfulgimide monolayers anchored on silicon surfaces. The study mainly addresses the issue of the influence of i) the molecular organization (density, distribution, conformation of the photoswitchable groups) and ii) properties of the electromagnetic fields (intensity and/or polarization) on the photo-commutation properties.

Indolyl fulgimide groups have been immobilized by covalent linkage on top of carboxylic acid monolayers grafted on hydrogenated silicon surfaces by hydrosilylation methods.<sup>32</sup> Particular emphasis was put on the preparation of acid-terminated molecular layers with controlled density and distribution of acid anchoring sites in order to vary in controlled manner the density of fulgimide groups on the surface.

## Aim and outline of thesis

The first scope of this thesis was to undertake comprehensive investigation of the properties of *mixed* carboxydecyl/decyl monolayers. One of the main concerns was to better understand the factors governing their formation and their composition in order to be able to tailor functionalized surfaces with tunable density and distribution of anchoring sites. The capability of achieving *mixed* surfaces with homogenous distribution of acid tail groups has subsequently been used to immobilize indolylfulgimide groups and investigate their photo-switching properties on silicon surfaces.

The thesis is divided into five chapters following the present general introduction.

Chapter 1 describes the preparation and characterization of *mixed* carboxyalkyl/alkyl surfaces by either a *one-step* or a *two-step* route. The homogeneity of mixed surfaces at molecular level has been investigated using a detailed spectroscopic FTIR study combined with high-resolution AFM imaging.

Chapter 2 studies the specific adsorption of undecylenic acid chains on hydrogenated silicon surfaces for obtaining a better understanding of the mechanism responsible for the large-scale inhomogeneity of the surfaces after the *one-step* grafting.

Chapter 3 reviews the photochromism of indolylfulgimide precursors in solution. The kinetics of fulgimide photoswitching were studied by *in situ* UV/Vis spectrophotometry and kinetic models have been revisited.

Chapter 4 describes the preparations and characterization of fulgimide-terminated monolayers with different densities of photoswitchable groups.

In Chapter 5, the photoswitching properties of the fulgimide-terminated surfaces were investigated using FTIR spectroscopy under Vis-UV irradiation. A specific illumination set up was designed for that purpose. It allows for *in situ* illumination inside the IR spectrophotometer and therefore the monitoring of the photoisomerization as a function of the illumination duration. The obtained results allowed for identifying the key experimental requirements to be fulfilled in order to perform a detailed study of the influence of the electromagnetic field on the photoswitching.

# References

- (1) Dubois, L. H.; Nuzzo, R. G. *Annual Review of Physical Chemistry* **1992**, *43*, 437.
- (2) Finklea, H. O.; Hanshew, D. D. *J Electroanal Chem* **1993**, *347*, 327.
- (3) Camillone, N.; Chidsey, C. E. D.; Liu, G. Y.; Scoles, G. *Journal of Chemical Physics* **1993**, *98*, 3503.
- (4) Bertilsson, L.; Liedberg, B. *Langmuir* **1993**, *9*, 141.
- (5) Mar, W.; Klein, M. L. *Langmuir* **1994**, *10*, 188.
- (6) Sun, F.; Grainger, D. W.; Castner, D. G.; Leachscampavia, D. K. *Macromolecules* **1994**, *27*, 3053.
- (7) Sondaghuethorst, J. A. M.; Schonberger, C.; Fokkink, L. G. J. *J Phys Chem-Us* **1994**, *98*, 6826.
- (8) Love, J. C.; Estroff, L. A.; Kriebel, J. K.; Nuzzo, R. G.; Whitesides, G. M. *Chemical Reviews* **2005**, *105*, 1103.
- (9) Wasserman, S. R.; Tao, Y. T.; Whitesides, G. M. *Langmuir* **1989**, *5*, 1074.
- (10) Onclin, S.; Ravoo, B. J.; Reinhoudt, D. N. *Angewandte Chemie-International Edition* **2005**, *44*, 6282.
- (11) Ulman, A. *Chemical Reviews* **1996**, *96*, 1533.
- (12) Silberzan, P.; Leger, L.; Ausserre, D.; Benattar, J. J. *Langmuir* **1991**, *7*, 1647.
- (13) Wang, R. W.; Baran, G.; Wunder, S. L. *Langmuir* **2000**, *16*, 6298.
- (14) Calistri Yeh, M.; Kramer, E. J.; Sharma, R.; Zhao, W.; Rafailovich, M. H.; Sokolov, J.; Brock, J. D. *Langmuir* **1996**, *12*, 2747.
- (15) Tillman, N.; Ulman, A.; Schildkraut, J. S.; Penner, T. L. *J. Am. Chem. Soc.* **1988**, *110*, 6136.
- (16) Tillman, N.; Ulman, A.; Penner, T. L. *Langmuir* **1989**, *5*, 101.
- (17) Dalchiele, E. A.; Aurora, A.; Bernardini, G.; Cattaruzza, F.; Flamini, A.; Pallavicini, P.; Zanoni, R.; Decker, F. *J Electroanal Chem* **2005**, *579*, 133.
- (18) Faber, E. J.; de Smet, L.; Olthuis, W.; Zuilhof, H.; Sudholter, E. J. R.; Bergveld, P.; van den Berg, A. *Chemphyschem* **2005**, *6*, 2153.
- (19) Linford, M. R.; Chidsey, C. E. D. *J. Am. Chem. Soc.* **1993**, *115*, 12631.
- (20) Boukherroub, R. *Curr Opin Solid St M* **2005**, *9*, 66.
- (21) Ciampi, S.; Harper, J. B.; Gooding, J. J. *Chemical Society Reviews* **2010**, *39*, 2158.
- (22) Linford, M. R.; Fenter, P.; Eisenberger, P. M.; Chidsey, C. E. D. *J. Am. Chem. Soc.* **1995**, *117*, 3145.
- (23) Royea, W. J.; Juang, A.; Lewis, N. S. *Appl Phys Lett* **2000**, *77*, 1988.
- (24) Gorostiza, P.; de Villeneuve, C. H.; Sun, Q. Y.; Sanz, F.; Wallart, X.; Boukherroub, R.; Allongue, P. *J Phys Chem B* **2006**, *110*, 5576.
- (25) Faucheux, A.; Yang, F.; Allongue, P.; De Villeneuve, C. H.; Ozanam, F.; Chazalviel, J. N. *Appl Phys Lett* **2006**, *88*.
- (26) Liu, Y. J.; Navasero, N. M.; Yu, H. Z. *Langmuir* **2004**, *20*, 4039.
- (27) Polster, D.; Graaf, H.; Baumgartel, T.; von Borczyskowski, C.; Benedikt, U.; Auer, A. A. *Langmuir* **2010**, *26*, 8301.
- (28) Asanuma, H.; Bishop, E. M.; Yu, H. Z. *Electrochim Acta* **2007**, *52*, 2913.
- (29) Sieval, A. B.; Demirel, A. L.; Nissink, J. W. M.; Linford, M. R.; van der Maas, J. H.; de Jeu, W. H.; Zuilhof, H.; Sudholter, E. J. R. *Langmuir* **1998**, *14*, 1759.

- (30) Voicu, R.; Boukherroub, R.; Bartzoka, V.; Ward, T.; Wojtyk, J. T. C.; Wayner, D. D. M. *Langmuir* **2004**, *20*, 11713.
- (31) Perring, M.; Dutta, S.; Arafat, S.; Mitchell, M.; Kenis, P. J. A.; Bowden, N. B. *Langmuir* **2005**, *21*, 10537.
- (32) Faucheux, A.; Gouget-Laemmel, A. C.; de Villeneuve, C. H.; Boukherroub, R.; Ozanam, F.; Allongue, P.; Chazalviel, J. N. *Langmuir* **2006**, *22*, 153.
- (33) Fabre, B.; Lopinski, G. P.; Wayner, D. D. M. *J Phys Chem B* **2003**, *107*, 14326.
- (34) Sieval, A. B.; Linke, R.; Heij, G.; Meijer, G.; Zuilhof, H.; Sudholter, E. J. R. *Langmuir* **2001**, *17*, 7554.
- (35) Zhang, X. C.; Teplyakov, A. V. *Langmuir* **2008**, *24*, 810.
- (36) Rosso, M.; Giesbers, M.; Schroen, K.; Zuilhof, H. *Langmuir* **2010**, *26*, 866.
- (37) Juang, A.; Scherman, O. A.; Grubbs, R. H.; Lewis, N. S. *Langmuir* **2001**, *17*, 1321.
- (38) Yang, M.; Teeuwen, R. L. M.; Giesbers, M.; Baggerman, J.; Arafat, A.; de Wolf, F. A.; van Hest, J. C. M.; Zuilhof, H. *Langmuir* **2008**, *24*, 7931.
- (39) Scheres, L.; ter Maat, J.; Giesbers, M.; Zuilhof, H. *Small* **2010**, *6*, 642.
- (40) Moraillon, A.; Gouget-Laemmel, A. C.; Ozanam, F.; Chazalviel, J. N. *Journal of Physical Chemistry C* **2008**, *112*, 7158.
- (41) Boukherroub, R.; Wayner, D. D. M. *J. Am. Chem. Soc.* **1999**, *121*, 11513.
- (42) Chazalviel, J. N.; Allongue, P.; Gouget-Laemmel, A. C.; de Villeneuve, C. H.; Moraillon, A.; Ozanam, F. *Science of Advanced Materials* **2011**, *3*, 332.
- (43) Fabre, B.; Hauquier, F. *J Phys Chem B* **2006**, *110*, 6848.
- (44) Dutta, S.; Perring, M.; Barrett, S.; Mitchell, M.; Kenis, P. J. A.; Bowden, N. B. *Langmuir* **2006**, *22*, 2146.
- (45) Boukherroub, R.; Morin, S.; Bensebaa, F.; Wayner, D. D. M. *Langmuir* **1999**, *15*, 3831.
- (46) Aureau, D.; Ozanam, F.; Allongue, P.; Chazalviel, J. N. *Langmuir* **2008**, *24*, 9440.
- (47) Polster, D.; Graaf, H. *Applied Surface Science* **2013**, *265*, 88.
- (48) Wei, F.; Zhao, X. S. *Thin Solid Films* **2002**, *408*, 286.
- (49) Minkin, V. I. *Chemical Reviews* **2004**, *104*, 2751.
- (50) Chen, X.; Islamova, N. I.; Garcia, S. P.; DiGirolamo, J. A.; Lees, W. J. *Journal of Organic Chemistry* **2009**, *74*, 6777.
- (51) Pei, X.; Fernandes, A.; Mathy, B.; Laloyaux, X.; Nysten, B.; Riant, O.; Jonas, A. M. *Langmuir* **2011**, *27*, 9403.
- (52) Dietrich, P.; Michalik, F.; Schmidt, R.; Gahl, C.; Mao, G.; Breusing, M.; Raschke, M. B.; Priewisch, B.; Elsaesser, T.; Mendelsohn, R.; Weinelt, M.; Rueck-Braun, K. *Applied Physics a-Materials Science & Processing* **2008**, *93*, 285.
- (53) Wen, Y. Q.; Yi, W. H.; Meng, L. J.; Feng, M.; Jiang, G. Y.; Yuan, W. F.; Zhang, Y. Q.; Gao, H. J.; Jiang, L.; Song, Y. L. *J Phys Chem B* **2005**, *109*, 14465.
- (54) Jung, U.; Filinova, O.; Kuhn, S.; Zargarani, D.; Bornholdt, C.; Herges, R.; Magnussen, O. *Langmuir* **2010**, *26*, 13913.
- (55) Chen, Y.; Xiao, J. P.; Yao, B. L.; Fan, M. G. *Optical Materials* **2006**, *28*, 1068.
- (56) Rath, S.; Hellig, M.; Port, H.; Wrachtrup, J. *Nano Letters* **2007**, *7*, 3845.
- (57) Kohno, Y.; Tamura, Y.; Matsushima, R. *Journal of Photochemistry and Photobiology a-Chemistry* **2009**, *201*, 98.
- (58) Katsonis, N.; Kudernac, T.; Walko, M.; van der Molen, S. J.; van Wees, B. J.; Feringa, B. L. *Advanced Materials* **2006**, *18*, 1397.

(59) Jung, U.; Mueller, M.; Fujimoto, N.; Ikeda, K.; Uosaki, K.; Cornelissen, U.; Tucek, F.; Bornholdt, C.; Zargarani, D.; Herges, R.; Magnussen, O. *Journal of Colloid and Interface Science* **2010**, *341*, 366.

(60) Zheng, Y. B.; Payton, J. L.; Chung, C.-H.; Liu, R.; Cheunkar, S.; Pathem, B. K.; Yang, Y.; Jensen, L.; Weiss, P. S. *Nano Letters* **2011**, *11*, 3447.

(61) Browne, W. R.; Feringa, B. L. In *Annual Review of Physical Chemistry* 2009; Vol. 60, p 407.

(62) Snegir, S. V.; Marchenko, A. A.; Yu, P.; Maurel, F.; Kapitanchuk, O. L.; Mazerat, S.; Lepeltier, M.; Leautic, A.; Lacaze, E. *Journal of Physical Chemistry Letters* **2011**, *2*, 2433.

(63) Comstock, M. J.; Levy, N.; Kirakosian, A.; Cho, J.; Lauterwasser, F.; Harvey, J. H.; Strubbe, D. A.; Frechet, J. M. J.; Trauner, D.; Louie, S. G.; Crommie, M. F. *Physical Review Letters* **2007**, *99*.

(64) Weiss, P. S. *Accounts of Chemical Research* **2008**, *41*, 1772.

(65) Uchida, K.; Yamanoi, Y.; Yonezawa, T.; Nishihara, H. *Journal of the American Chemical Society* **2011**, *133*, 9239.



# Chapter 1

## *Mixed Carboxydecyl/Decyl Monolayer on Si surface*

---

### Table of Contents

---

Introduction .....	10
1.1. Surface preparation .....	14
1.1.1. Silicon etching and surface hydrogenation .....	14
1.1.2. Preparation of <i>mixed</i> $\omega$ -carboxydecyl/decyl surfaces .....	15
1.1.2.1. The <i>two-step</i> route.....	15
1.1.2.2. The <i>one-step</i> route.....	15
1.2. <i>Mixed</i> monolayers prepared from ethyl undecylenate/decene mixtures .....	17
1.2.1. AFM characterization .....	17
1.2.2. FTIR measurements.....	19
1.2.2.1. Qualitative analysis.....	19
1.2.2.2. Quantitative analysis.....	22
1.3. <i>Mixed</i> monolayers prepared from undecylenic acid/decene mixtures .....	27
1.3.1. Surface characterization prior to and after <i>surface wiping</i> .....	27
1.3.1.1. AFM characterization of <i>pure</i> and acid-rich <i>mixed</i> surfaces .....	28
1.3.1.2. Surface characterization of acid-poor <i>mixed</i> surfaces.....	28
1.3.1.3. Composition of the dome-like molecular structures : FTIR analysis .....	32
1.3.2. Surfaces after the <i>complete wiping</i> procedure .....	34
1.3.2.1. AFM characterization .....	34
1.3.2.1.1. Phase-contrast imaging of a mixed Si-acid <sup>10</sup> surface.....	34
1.3.2.1.2. Density and size of the domains on mixed surfaces .....	37
1.3.2.1.3. Characterization of extremely diluted acid MLs.....	41
1.3.2.2. FTIR measurements .....	42
1.3.2.2.1. Surface composition: Qualitative analysis .....	42
1.3.2.2.2. Quantitative analysis of the $\nu$ C=O band .....	45
1.3.3. Linkage of molecular-label onto the acid end-groups .....	48
1.3.3.1. Coupling protocol .....	49
1.3.3.2. FTIR measurements .....	49
1.3.3.2.1. Qualitative analysis.....	49
1.3.3.2.2. Quantitative analysis.....	51
1.4. Discussion.....	54
Conclusions .....	62
References .....	63

---

# Introduction

The anchoring of molecular or supramolecular entities or nano-objects onto solid surfaces is a widely developed strategy for the design of functional surfaces in numerous application fields (nano-electronics, biological or chemical sensors...). If in some cases entities tethered with a specially designed linker can be directly attached on the surfaces, this is not always the case. Thus, alternative approaches have been developed that very often rely on the coupling onto surfaces functionalized with organic monolayers. Functionalized monolayers prepared by self-assembly of thiols onto metal surfaces (Au, Ag, Cu...) or silane onto silicon oxide or glass have been used for long time as primary anchoring layers for the immobilization of biomolecules, NPs,...<sup>1-10</sup> Among different types of surface termination, monolayers bearing carboxylic acid (-COOH) or amino (-NH<sub>2</sub>) groups has received peculiar attention because these groups allow for coupling reactions in mild conditions suited, in particular, to the immobilization of biomolecules.

During the last two decades, the grafting of organic groups onto *oxide-free* silicon surfaces has attracted great attention because it allows for the formation of very stable silicon/organic layer interfaces. Among different grafting methods, the anchoring of alkyl monolayers (MLs) onto hydrogenated surfaces by hydrosilylation of alkene derivatives has received peculiar interest. This method allows for the grafting of  $\omega$ -functionalized carboxyl monolayers directly anchored onto silicon through covalent Si-C linkages.<sup>11,12</sup> Compared to other systems, such SAMs on Gold or Silicon oxide or glass, the Si/organic ML surfaces thus obtained exhibit greater chemical stability because of the rather high energy of the Si-C (~4.5 eV) linkages and their weak polarity.

Silicon surfaces functionalized by carboxyl-terminated monolayer can be obtained either by the direct grafting of long-chain carboxylic acids (*one-step* route) or by the grafting of carboxylic esters and their subsequent hydrolysis (*two-step* route).<sup>13</sup> The *two-step* route was originally implemented because the reaction of the carboxyl acid groups with the hydrogenated surface of porous silicon had been reported.<sup>12,14</sup> However since then, several works have shown that monolayers with carboxyl tail groups could be prepared directly from neat solution of undecylenic acid and using photochemical activation without significant reaction of the acid groups with the surface.<sup>15,16</sup>

The preparation of mixed monolayers, in *one-step* or *two-step*, by reaction in mixtures of  $\omega$ -functionalized and simple alkyl chains has been realized in order to vary the density of the functional groups in the monolayer (Fig. 1.1). First, alkyl chains can make the functional group more accessible by releasing steric hindrance constraints. Second, they can give to the grafted molecular layer an enhanced stability because they pack more densely than the chains with bulky functional groups. It was shown that these monolayers can be obtained with variable concentration and free of residues.<sup>16,17</sup> It was reported that the concentration of  $\omega$ -functionalized groups in the monolayer prepared by the *two-step* route is proportional to that in the grafting solution (Fig. 1.2A). However, the second step is usually not complete. The *one-step* route was developed later to overcome that problem. However, the studies raised several issues: an over-concentration of acids was evidenced in the monolayer (Fig. 1.2B),<sup>16</sup> difficulties to get reproducible and reliable concentration of carboxyl groups were faced for large dilution (typically < 20%) and the distribution of the carboxyl groups on the surface remained an opened issue, although some results suggested a non-homogeneous distribution and the existence of acid-rich domains.<sup>18</sup>

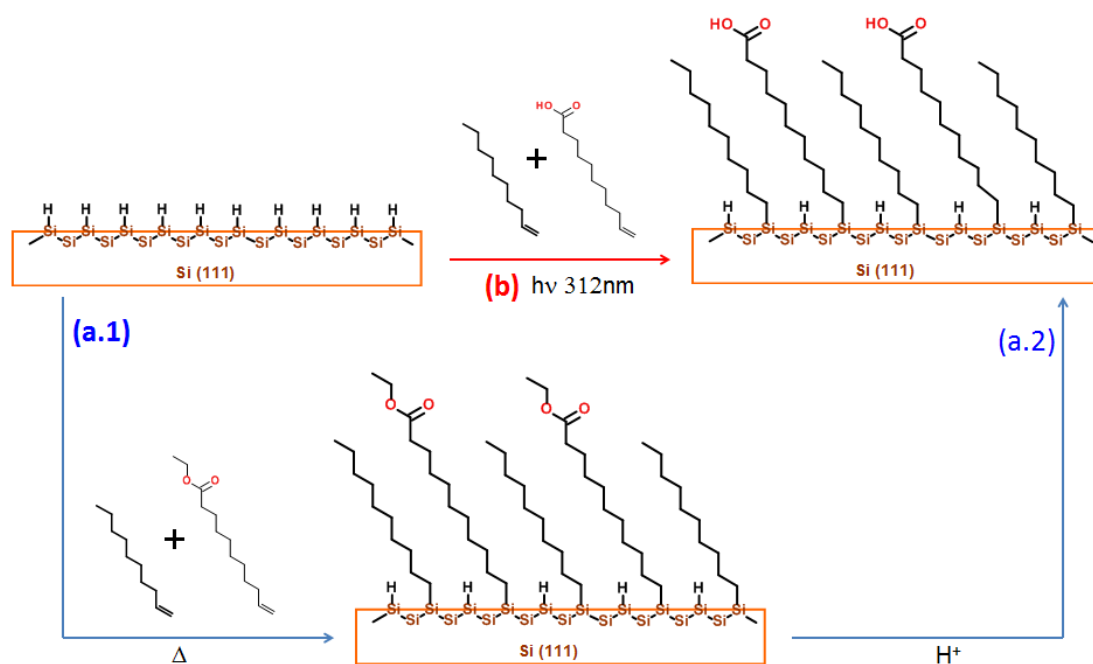


**Figure 1.1.** Reaction scheme for the preparation of *mixed carboxydecyl/decyl monolayer* by hydrosilylation onto hydrogenated Si surfaces: (a) *Two-step* route by grafting from ethyl undecylenate/decene mixtures and subsequent hydrolysis, (b) *one-step* route by *direct* grafting from undecylenic acid/decene mixtures.

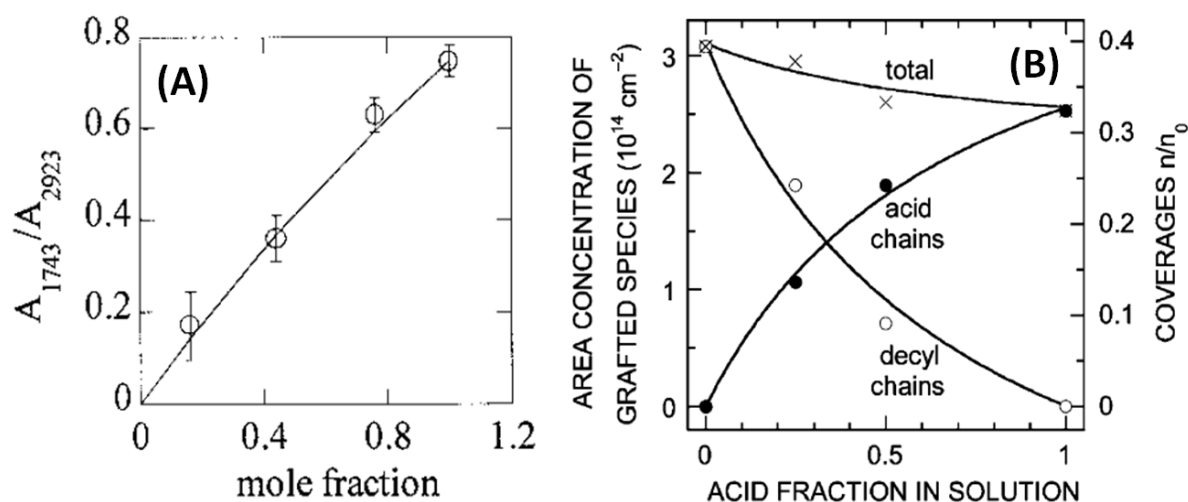


Figure 1.2. (A) Absorbance ratio of the ester carbonyl stretch to the total methylene asymmetric stretch as a function of the mole fraction of ethyl undecylenate in decene,<sup>17</sup> suggesting a proportionality between the ester content in the grafting solution and the surface concentration of grafted ester chains (B) Surface concentration, as determined by quantitative infrared spectroscopy, of carboxydecyl and decyl chains in grafted monolayers by the *one-step* route as a function of the acid fraction in solution.<sup>16</sup>

Specifically, it suggested that the *mixed* monolayer obtained by the *one-step* route could be chemically inhomogeneous at the molecular level, with possibly existence of phase separation between decyl and acid chains.<sup>18</sup> From surface titration of the COO<sup>-</sup>/COOH groups in the MLs by quantitative FTIR measurements in solutions of various pH, they have shown the evolution of COO<sup>-</sup> concentration in mixed monolayers as a function of pH they observed experimentally, could be accounted for was corresponding to by a computed model assuming that segregation of the acid chains (Fig. 1.3B).

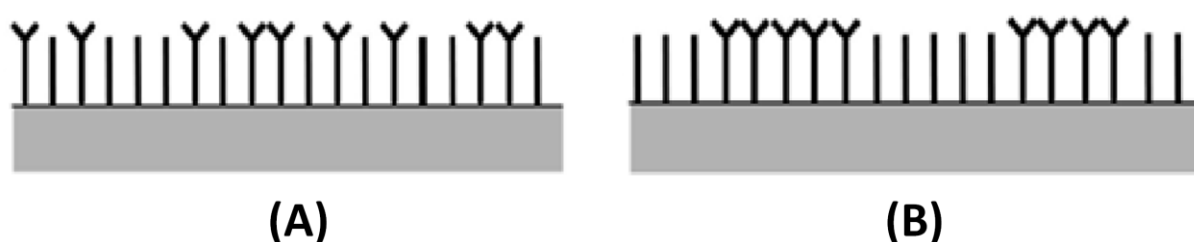


Figure 1.3. The distribution of COOH terminated chains in *mixed* carboxyalkyl/alkyl monolayers. (A) Homogeneously distributed acid chains and (B) segregated acid chains.

Within this work, we have undertaken further comprehensive investigations of the properties of *mixed* monolayers prepared by the *one-step* or *two-step* routes. One of the main concerns was to better understand the factors governing their formation and their final

composition in order to be able to tailor functionalized surfaces with tunable density and distribution of anchoring sites. For this purpose, we have investigated *mixed* alkyl monolayers – made of alkyl chains methyl or carboxyl tail-groups – grafted onto oxygen free Si (111) surfaces. Analysis by FTIR spectroscopy combining with high-resolution NC-AFM observation will be presented.

## 1.1. Surface preparation

The preparation of *mixed* carboxydecyl/decyl monolayers was performed *via* hydrosilylation reaction onto hydrogenated silicon surfaces (H-Si) using  $\omega$ -carboxydecyl alkenes and decene as reactants.<sup>13</sup> The two preparation methods schemed in Fig. 1.1 were studied, i.e.,

- a) the grafting of long chain ester and their subsequent hydrolysis on the surface (*two-step* route),
- b) the *direct* grafting of long chain acid (*one-step* route).

### 1.1.1. Silicon etching and surface hydrogenation

Silicon samples were cut in n-type Si(111) wafers with 0.2° miscut along the  $[\bar{1}\bar{1}2]$  direction. This peculiar choice was made because it allows for the preparation of nearly ideal surfaces exhibiting flat and regular (111) terraces of ~100 nm width. For FTIR measurements, double-side polished and float zone (FZ-) purified wafers were used. The Si samples (15mm × 15mm) were shaped as prisms with two opposite edges beveled at 45° in order to perform FTIR analysis in the ATR mode. For AFM characterizations, same sample for FTIR measurements can be used for imaging. In addition, Czochralski grown (CZ), 1-10 Ω cm and one-side polished wafers were also used when only AFM characterizations were carried out.

At air contact, silicon surfaces are naturally covered by a thin oxide layer (~1 nm) that can be removed by treatment in a fluoride solution. After exposure in fluoride solution, oxide-free and entirely hydrogen-passivated surfaces are obtained.<sup>19</sup> These hydrogenated surfaces are enough stable to be handled in air with negligible re-oxidation.

In this work, H-terminated silicon surfaces were prepared by chemical etching in oxygen-free 40% NH<sub>4</sub>F solutions. Such conditions are known to favor an anisotropic etching of silicon leading to the formation of extended (111) terraces flat at the atomic scales.<sup>20</sup>

Prior to etching, the samples were carefully cleaned, first by wiping with ethanol and acetone to remove silicon dust and then by two successive exposures in 3:1 concentrated H<sub>2</sub>SO<sub>4</sub>:H<sub>2</sub>O<sub>2</sub> solution (Piranha solution) for 15 min at 100°C to remove traces of organic contaminants. After cleaning, the samples were thoroughly and carefully rinsed with ultra-pure water (UPW, Millipore<sup>®</sup>, 18 MΩ cm) and then immersed for 15 min in 40% NH<sub>4</sub>F

containing ~10 mM  $(\text{NH}_4)_2\text{SO}_3$  as an oxygen scavenger. The hydrogenated surfaces were then rapidly taken out of the etching solution, quickly rinsed under flowing UPW. The hydrogenated samples were then stored in a glass reactor under argon flowing during 30-60 min until its transfer into the grafting solution.

### 1.1.2. Preparation of *mixed $\omega$ -carboxydecyl/decyl surfaces*

#### 1.1.2.1. The *two-step route*

Mixtures of ethyl 1-undecylenate  $\text{CH}_2=\text{CH}-(\text{CH}_2)_8-\text{COC}_2\text{H}_5$  (97% Sigma Aldrich) and 1-decene  $\text{CH}_2=\text{CH}-(\text{CH}_2)_7-\text{CH}_3$  (97% Sigma-Aldrich) were used as grafting solutions.

##### *First step: thermal grafting of ester chains*

Both ester and decene reagents were freshly purified by elution on fluorisil<sup>®</sup> column using pentane as eluent. They were then poured into a Schlenk reactor and outgassed by argon bubbling at ambient for 10 min then heated at 100°C for (at least) 30 min while maintaining argon flowing. The freshly prepared H-Si surface was then introduced into the grafting solution after cooling down to room temperature keeping Ar flowing. Argon was kept bubbling for 30 min still before the Schlenk tube was hermetically closed. The grafting reaction was then thermally activated by heating at 180°C for ~20 h. After grafting, the ester-terminated surfaces were twice rinsed successively in boiling tetrahydrofuran (THF) and dichloromethane (DCM) for 10 min each.

##### *Second step: hydrolysis of ester end-groups*

Conversion of the carbonyl ester groups on the surface into carboxylic acid were done by hydrolysis in de-oxygenated 5.6 M HCl. The HCl solution was outgassed with argon bubbling prior to the introduction of the sample. The reaction was let to proceed for 3h at 60°C. The surface was then rinsed copiously under flowing UPW.

#### 1.1.2.2. The *one-step route*

Mixtures of 1-undecylenic acid  $\text{CH}_2=\text{CH}-(\text{CH}_2)_8-\text{COOH}$  (99% Acros Organics) and 1-decene  $\text{CH}_2=\text{CH}-(\text{CH}_2)_7-\text{CH}_3$  (97% Sigma-Aldrich) were used as the grafting solution.

### Monolayer grafting

The same protocol (as that described above for the ester grafting) was used except for the grafting reaction itself that was activated by UV irradiation for 3h in a home-made photoreactor (312 nm, 6 mW cm<sup>-2</sup>).

### Cleaning procedures

Different cleaning procedures were used depending on the composition of the grafting solution. For *pure* decyl layer, the surfaces were twice rinsed successively in boiling THF and then in boiling DCM. For *pure* acid layer, the surfaces were twice rinsed in hot acetic acid at 70°C during 30 min, according to the procedure developed by Faucheux *et al.*<sup>16</sup>

For acid-rich *mixed* monolayers (acid content in solution  $\geq 20\%$ ), the surfaces were twice rinsed in hot acetic acid (70°C, 30 min) and subsequently twice rinsed in boiling DCM (40°C, 15 min). The above successive rinsing procedures allow for removing mostly the excess of undecylenic acid and decene precursors, respectively.

For acid-poor *mixed* monolayers (acid content in solution  $\leq 10\%$ ), it turned out that the rinsing procedure mentioned above was not sufficient to remove the excess of physisorbed precursors. We investigated various rinsing conditions (sequential exposures to different organic solvents or solvent mixtures, under stirring, heating, sonication, in aqueous solutions at different pH with or without surfactants added...) but none of them proved to be efficient to remove the excess of matter. The sole issue we found out was to "mechanically" remove the excess matter by wiping the surface with a cotton swab moistened with organic solvents. One *wiping* procedure is defined as surface is wiped with a cotton swab moistened with EtOH then with another one moistened with DCM and subsequently rinsed in hot acetic acid for 5 min and in boiling dichloromethane for 5 min, successively. A *complete wiping* procedure repeats 3 times the *wiping* procedure. One *complete wiping* procedure is usually enough to remove all the excess of matter.

For all surfaces, AFM imaging sometimes can reveal the present of small and few nm-size impurities even they were well rinsed and wiped with procedures mentioned above. In this case, an additional *wiping* procedure is largely enough to rend the surface completely clean.

## 1.2. *Mixed* monolayers prepared from ethyl undecylenate/decene mixtures

This section presents the AFM and FTIR characterizations of *mixed* carboxydecyl/decyl monolayers prepared by the *two-step* route, i.e., by using ethyl undecylenate/decene mixtures as grafting solution and the subsequent hydrolysis of the ester groups on the surface. In the following, **Si-ester** and **Si-acid<sup>ester</sup>** will refer to the as-prepared *pure* ester-terminated monolayer and to the *pure* acid-terminated monolayer after hydrolysis, respectively. *Mixed* monolayers will be labelled with the fraction of ester in the grafting solution, e.g., *mixed* **Si-ester<sup>10</sup>** and **Si-acid<sup>ester-10</sup>** surfaces will refer to ML prepared in 10% ester/ 90% decene mixture prior to and after hydrolysis, respectively.

### 1.2.1. AFM characterization

Figures 1.4 and 1.5 display topography and phase images of a pure Si-ester surface prior to and after hydrolysis. After grafting, the AFM images show a surface topography reminiscent of H-Si surface, consisting in flat terraces separated by atomic steps (3.1 Å high), whatever the composition of the grafting solution (ester/decene ratio). Over extended areas, the surfaces are free of contaminants and at greater resolution the images show that the terraces are smooth and homogeneous indicating the grafting of a dense ML. The phase images recorded simultaneously with the topography are featureless which indicates chemical homogeneity at these magnifications. After hydrolysis, no significant change was detected observed.

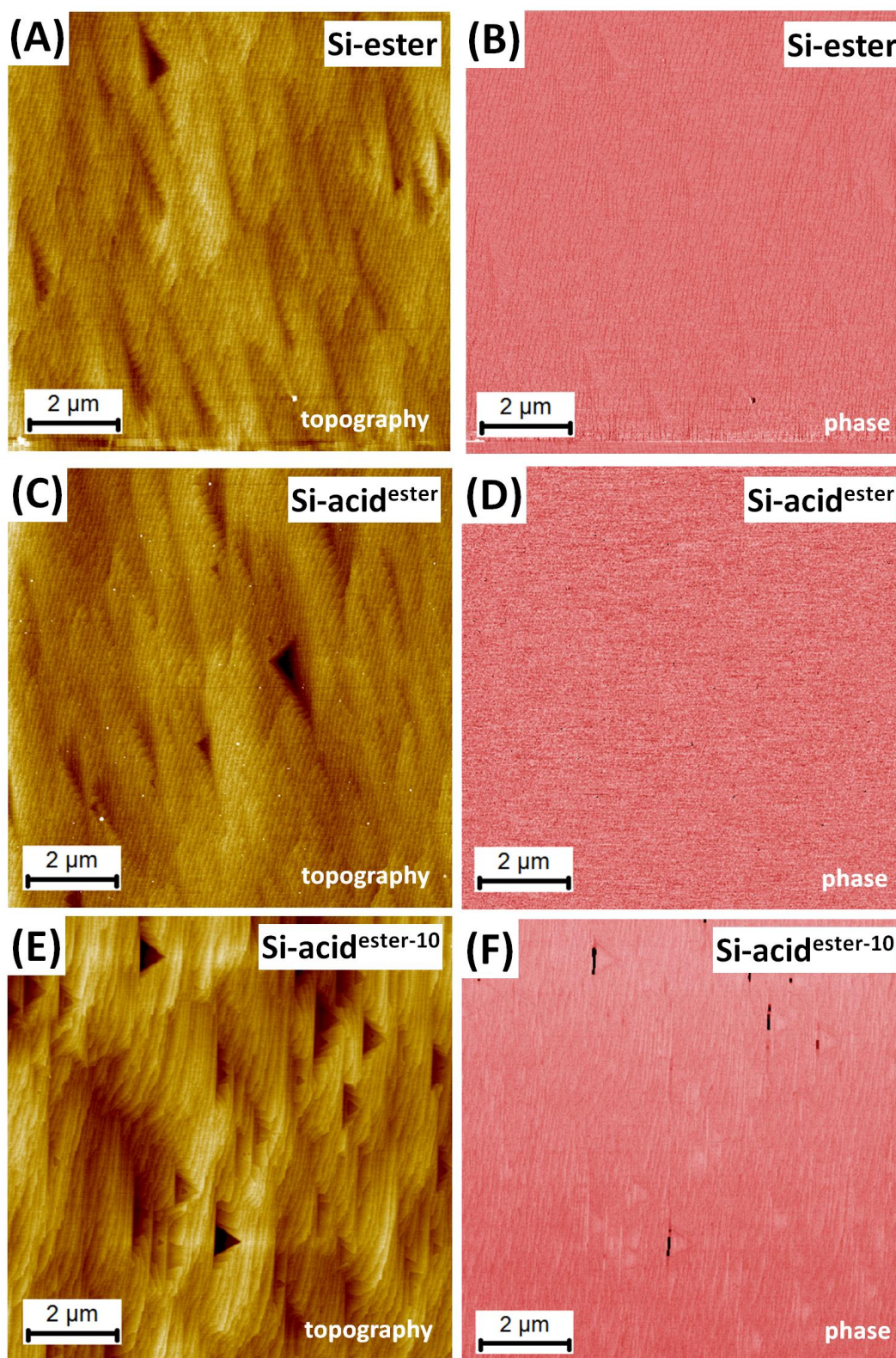


Figure 1.4. Large-field AFM images ( $10\mu\text{m} \times 10\mu\text{m}$ ) – topography (left) and phase (right) – of a *pure* ester surface prior to and after hydrolysis. Topography and phase images of *pure*  $\text{Si}^{\text{ester}}$  prior to (A, B) and after hydrolysis (C, D). Topography and phase images after hydrolysis of a *mixed*  $\text{Si}^{\text{ester}10}$  (E, F).

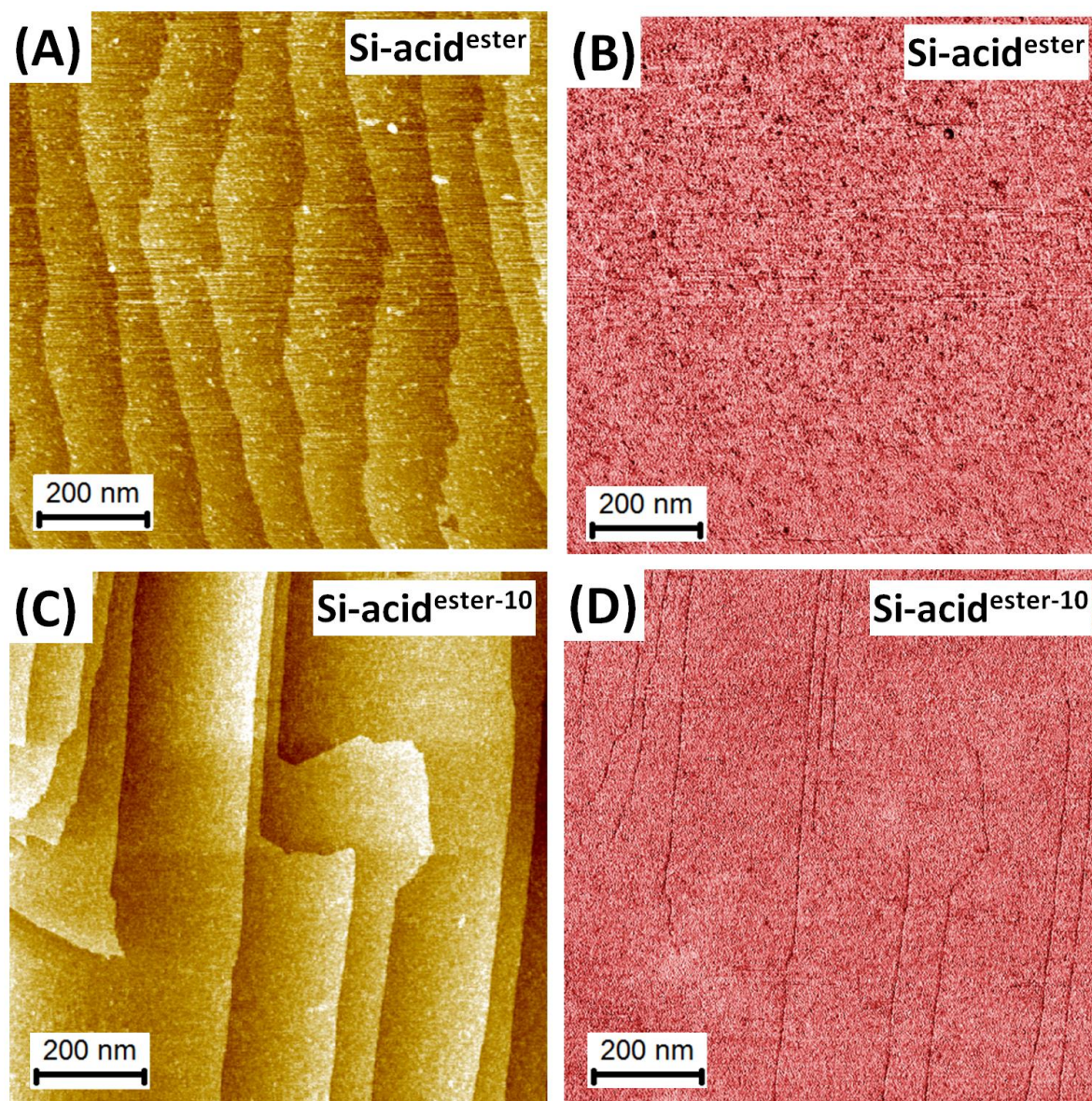


Figure 1.5. Topography (left) and phase (right) AFM images of a *pure* Si-acid<sup>ester</sup> surface (A, B) and a *mixed* Si-acid<sup>ester-10</sup> surface (C, D).

## 1.2.2. FTIR measurements

### 1.2.2.1. Qualitative analysis

The FTIR spectra of a *pure* Si-ester surface prior to and after hydrolysis are shown in Fig. 1.6. For both spectra, the reference is the hydrogenated silicon surface (H-Si) prior to the grafting of the carboxylic ester. Therefore, the positive bands observed on the spectrum (a) correspond to the chemical species present on the surface after the grafting (a) and those on spectrum (b) to those corresponding to the species present after hydrolysis. The present of the

negative sharp peak at  $2083\text{ cm}^{-1}$  ( $\nu\text{Si-H}$  stretching mode) indicates the substitution of Si-H by Si-C bonds when going from hydrogenated to grafted surface, in agreement with the hydrosilylation reaction scheme (Fig. 1.1). The observed characteristic peaks indicate the presence of the carboxylic ester on the surface (Fig. 1.6a). The peak at  $1739\text{ cm}^{-1}$  is assigned to the  $\nu\text{C=O}$  stretching mode of ester groups and the three observable bands in  $2800\text{-}3000\text{ cm}^{-1}$  range is assigned to the symmetric (at  $2852\text{ cm}^{-1}$ ) and antisymmetric (at  $2923\text{ cm}^{-1}$ ) stretching modes of the methylene units of the alkyl chains ( $\nu_s\text{CH}_2$  and  $\nu_a\text{CH}_2$ ), and the  $\nu\text{CH}_3$  band at  $2980\text{ cm}^{-1}$  of the methyl groups from the ethoxy moieties of the ester groups. A peak at  $1177\text{ cm}^{-1}$ , assigned to the  $\nu\text{C-OC}$  stretching vibration of the ester groups, is also observed. After hydrolysis, the bands assigned to ester groups ( $\nu\text{C=O}$  at  $1739\text{ cm}^{-1}$ ,  $\nu\text{C-OC}$  at  $1177\text{ cm}^{-1}$  and  $\nu\text{CH}_3$  at  $2980\text{ cm}^{-1}$ ) have vanished and the appearance of a new  $\nu\text{C=O}$  peak at the position expected for carboxylic acid groups at  $1715\text{ cm}^{-1}$  (Fig. 1.6b). The peak position and assignment of the different bands observed on the spectra are summarized in Table 1.1.

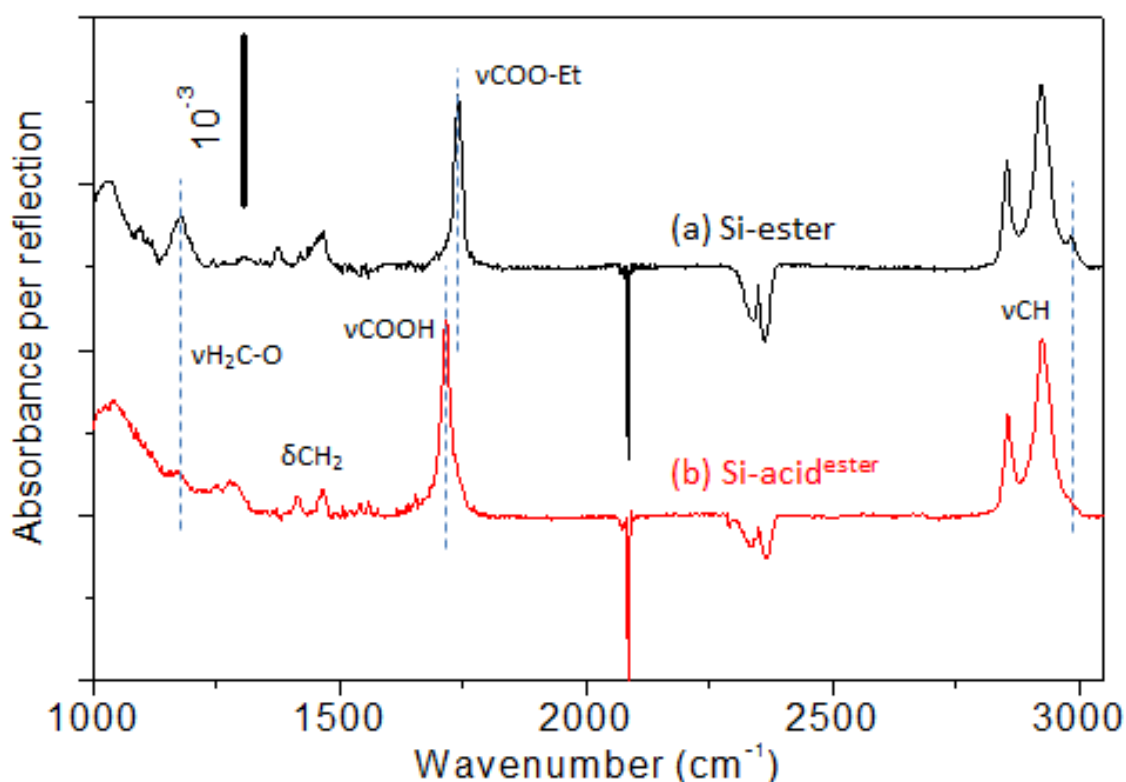
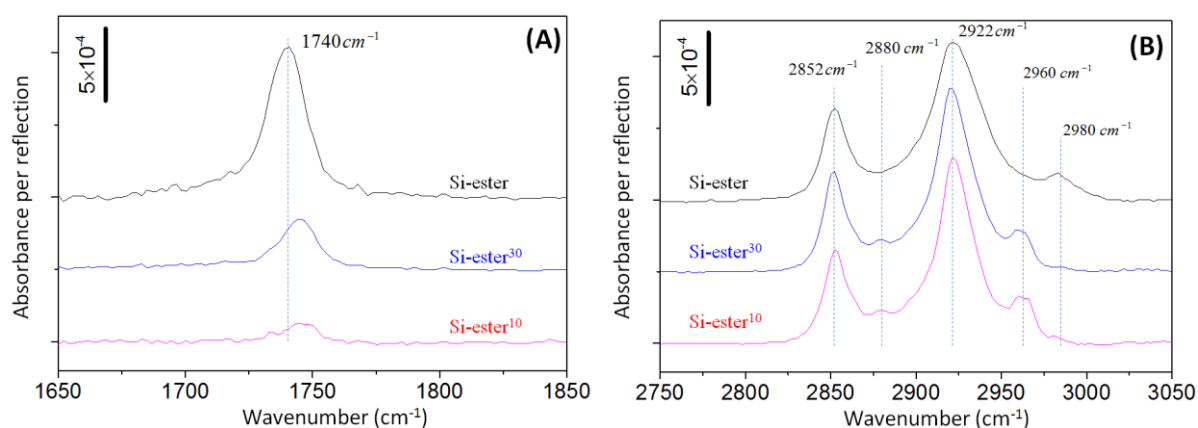


Figure 1.6. FTIR spectra of a *pure* Si-ester monolayer prior to (a) and after hydrolysis (b). In both cases, the reference is the as-prepared hydrogenated surface prior to the grafting of the carboxylic esters.

Band assignment	Si-ester ( $\text{cm}^{-1}$ )	Si-acid <sup>ester</sup> ( $\text{cm}^{-1}$ )
$\nu_a\text{CH}_3$	2980	
$\nu_a\text{CH}_2$	2923	2923
$\nu_s\text{CH}_2$	2852	2852
$\nu\text{SiH}$	2083	2083
$\nu\text{C=O}$	1740	1713
$\delta\text{CH}_2$	1463	1463
$\nu\text{H}_2\text{C-O}$	1177	

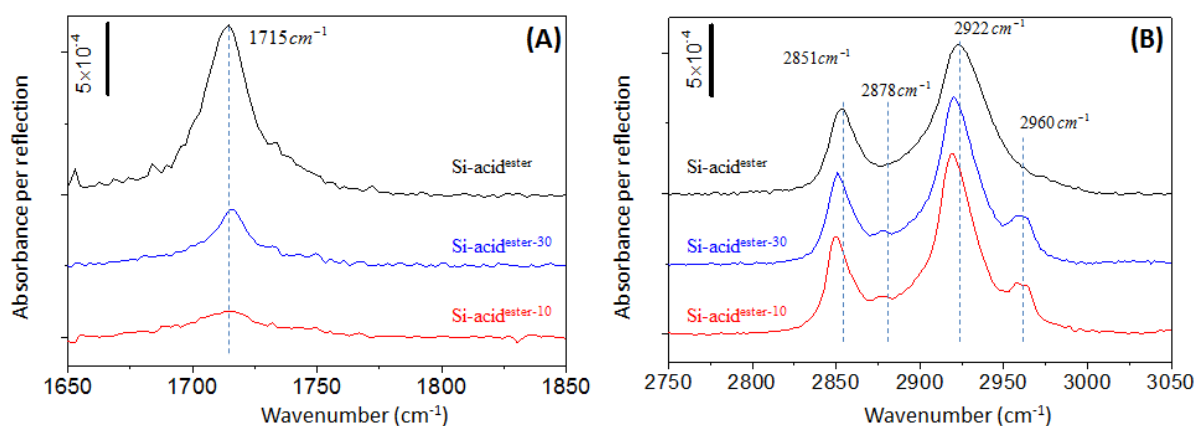
**Table 1.1. Positions and band assignments of the band observed on FTIR spectra of a *pure* Si-ester monolayer prior to and after hydrolysis.**

Figure 1.7 displays narrow FTIR spectra (p polarization) of the region of the carbonyl  $\nu\text{C=O}$  and methylene  $\nu\text{CH}_2$  stretching bands of a *pure* Si-ester ML and *mixed* MLs prepared in solution with various ester content. As expected, the intensity of the  $\nu\text{C=O}$  bands is decreasing upon dilution of ester in solution. Besides, one can also observe a blue shift of the position of the  $\nu\text{C=O}$  peaks upon diminution of its intensity. In the  $\nu\text{CH}$  range (Fig. 1.7B), the intensity of the  $\nu\text{CH}_2$  bands at  $\sim 2850$  and  $\sim 2923 \text{ cm}^{-1}$  remains qualitatively almost unchanged. Two additional bands are however detected in the case of the mixed MLs that are assigned to stretching modes of the methyl end-groups of the decyl chains ( $\nu_s\text{CH}_3$  at  $\sim 2870 \text{ cm}^{-1}$  and  $\nu_a\text{CH}_3$  at  $\sim 2960 \text{ cm}^{-1}$ ). The diminution of the ester-related peak and the simultaneous appearance of the peak assigned to the methyl groups ( $\nu\text{CH}_3$ ) pertain to the formation of *mixed* monolayers with various fraction of carboxylic ester.



**Figure 1.7.** Narrow FTIR spectra showing the  $\nu\text{C}=\text{O}$  peak (A) and the  $\nu\text{CH}$  bands (B) of different MLs prepared from ethyl undecylenate/decene mixtures with 100%, 30% and 10% ester content.

Figure 1.8 shows the spectra of the same surfaces after hydrolysis. One notices a shift of the carbonyl peak toward lower wavenumber at  $\sim 1715\text{ cm}^{-1}$  and the disappearance of the ethoxy-related band  $\nu\text{CH}_3$  at  $2980\text{ cm}^{-1}$ . This evolution indicates that most of the ester groups have been hydrolyzed into carboxylic acid. Detailed spectral analysis of the carbonyl bands will be discussed in the next section.



**Figure 1.8.** Narrow FTIR spectra showing the  $\nu\text{C}=\text{O}$  peak (A) and the  $\nu\text{CH}$  bands (B) of different MLs after hydrolysis of the ester groups.

### 1.2.2.2. Quantitative analysis

Detailed quantitative analysis of the absorption bands related to the carboxylic ester and acid groups have been done in order to determine the fraction of carboxylic chains in the monolayers. The integrated absorbance (in p and s-polarization) inferred from this analysis have been used to determine the absolute surface concentration of carboxylic chains on the

surfaces. The surface concentration of ester and acid end-groups was determined from the integrated absorbance of the ester-related and acid-related  $\nu\text{C}=\text{O}$  bands using quantitative analysis methods (see Appendix II for further details).

### Spectral deconvolution/ fitting procedure

Figure 1.9 shows one example of experimental spectra and the fitting of the  $\nu\text{C}=\text{O}$  bands in the case of a *mixed* Si-ester<sup>30</sup> ML. The  $\nu\text{C}=\text{O}$  peak corresponding to the as-prepared ester-terminated ML is shown on Fig. 1.9A, those of the surface after hydrolysis on Fig. 1.9B. The ester-related  $\nu\text{C}=\text{O}$  band has been fitted with one profile centered at  $\sim 1740\text{ cm}^{-1}$  and one linear baseline (Fig. 1.9A). After hydrolysis, the  $\nu\text{C}=\text{O}$  bands must be fitted with two components centered at  $\sim 1715$  and  $\sim 1740\text{ cm}^{-1}$  and one linear baseline (Fig. 1.9B). While the peak at  $\sim 1715\text{ cm}^{-1}$  is related to acid groups, the peak at  $\sim 1740\text{ cm}^{-1}$  is straightforwardly assigned to the residual ester groups.

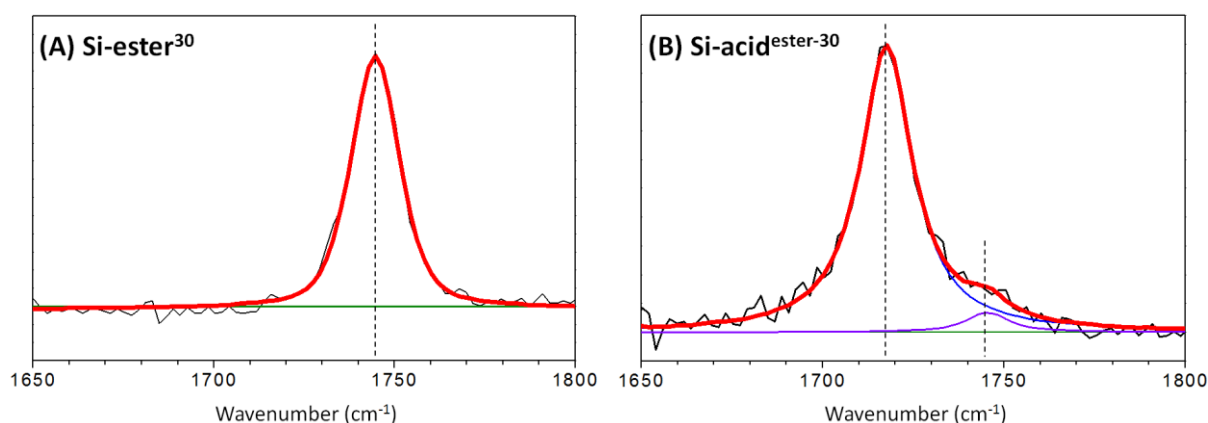


**Figure 1.9.** Experimental spectra and spectral deconvolution of the  $\nu\text{C}=\text{O}$  bands of a *mixed* Si-ester<sup>30</sup> surface prior to (A) and after hydrolysis (B). The experimental spectra are plotted in grey (A) and dark blue (B). The red plots correspond to the resulting fitting curves. The two components used to fit the spectrum in (B) are assigned to acid (blue) and residual ester (purple) groups.

### Integrated absorbance of the $\nu\text{C}=\text{O}$ peaks

Figure 1.10 displays the variations of integrated absorbance of the ester- and acid-related  $\nu\text{C}=\text{O}$  peaks as a function of the ester fraction in the grafting solution, for the three different surfaces discussed above. The integrated absorbance of the ester-related peak ( $\text{Abs}_{\text{ester}}^0$ ) of the monolayers prior to hydrolysis are plotted as blue circles (●). Red (▲) correspond to the integrated absorbance of the acid-related peak ( $\text{Abs}_{\text{acid}}^{\text{hyd}}$ ) and empty blue triangles (△) to that of the residual ester-related peak ( $\text{Abs}_{\text{ester}}^{\text{hyd}}$ ) after hydrolysis. The

integrated absorbance of all three peaks scales linearly with the ester content in the grafting solution.

The comparison of the integrated absorbance of the ester-related peak prior to (●) and after hydrolysis (▲) was used to determine the hydrolysis yield. The results are given in Table 1.2. The hydrolysis reaction is almost quantitative for the *pure* Si-ester and *mixed* Si-ester<sup>30</sup> surfaces, with a hydrolysis yield of ~90%. The hydrolysis yield diminishes when the ester fraction in solution decreases. If, in the case of the *mixed* Si-ester<sup>30</sup> surface, it remains close to that observed on the *pure* Si-ester surface (~90%), it falls at 80% in the case of the *mixed* Si-ester<sup>10</sup> surface.

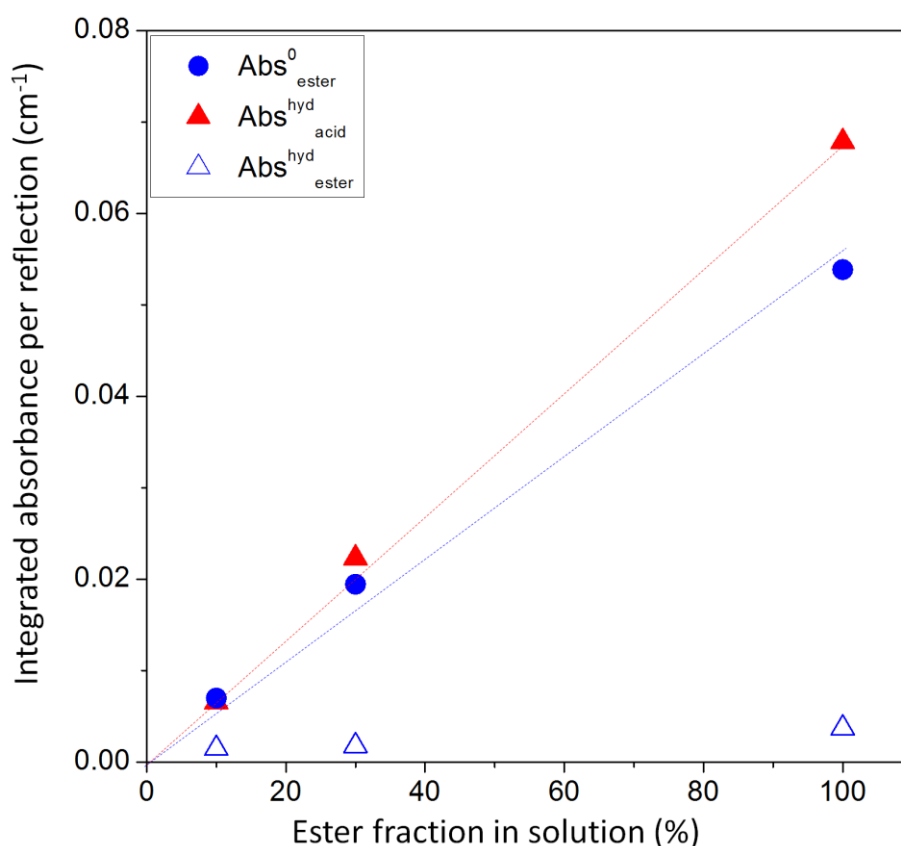


**Figure 1.10.** Integrated absorbance per reflection of the ester-related  $\nu C=O$  bands prior to ( $Abs_{ester}^0$ , ●) and after hydrolysis ( $Abs_{ester}^{hyd}$ , ▲) and of the acid-related  $\nu C=O$  bands ( $Abs_{acid}^{hyd}$ , ▲) as a function of the ester fraction in the grafting solution.

Ester fraction in solution (%)	Integrated absorbance (cm <sup>-1</sup> )			Hydrolysis yield (%) $\frac{Abs^0_{ester} - Abs^{hyd}_{ester}}{Abs^0_{ester}}$
	Prior to hydrolysis	After Hydrolysis		
	$Abs^0_{ester}$ ester-related peak	$Abs^{hyd}_{acid}$ acid-related peak	$Abs^{hyd}_{ester}$ ester-related peak	
100	0.0539	0.0678	0.0037	93
30	0.0190	0.0223	0.0018	91
10	0.0070	0.0065	0.0015	79

**Table 1.2.** Integrated absorbance per reflection of the ester- and acid-related  $\nu$ C=O peaks and hydrolysis yield determined. The hydrolysis yield was calculated as the difference of the integrated absorbance of the ester-related peak prior to ( $Abs^0_{ester}$ ) and after hydrolysis ( $Abs^{hyd}_{ester}$ ) normalized to the nominal integrated absorbance prior to hydrolysis ( $Abs^0_{ester}$ ).

#### Surface concentration of acid and decyl chains in the monolayers

Figure 1.11 shows the composition of monolayers prepared from ethyl undecylenate/decene mixtures prior to and after hydrolysis. The ester concentration (●, Δ) was derived from the integrated absorbance of the ester-related  $\nu$ C=O peak at  $\sim 1740$  cm<sup>-1</sup> (in p and s polarization). Similarly, the acid concentration in monolayers after hydrolysis (▲) was derived from the integrated absorbance of the acid-related  $\nu$ C=O band at  $\sim 1715$  cm<sup>-1</sup>. The total concentration of alkyl chains (ester + decyl) (■) was derived from the integrated absorbance of the  $\nu_s$ CH<sub>2</sub> band at  $2852$  cm<sup>-1</sup> taking into account of the different number of methylene units in the ester chains (11 CH<sub>2</sub>) and in the decyl chains (9 CH<sub>2</sub>). The total concentration of alkyl chains was determined prior to and after hydrolysis. A good agreement was found from the two determinations.

The ester concentration in the monolayers increases linearly upon increasing of the ester fraction in solution. The same holds true, after hydrolysis, for the acid concentration (proportional to the integrated absorbance of the  $1715$  cm<sup>-1</sup> peak). The acid concentration in monolayers after hydrolysis (▲) is slightly smaller than that of initial ester groups (●). The difference is in agreement with the hydrolysis yields ( $\sim 80 - 90$  %) given in the Table 1.2. This indicates the absence of any loss during hydrolysis and is a good check of the consistency of

the calibration procedure. Finally, the total concentration of total alkyl chains in MLs is nearly unchanged whatever the composition of the grafting solution prior to and after hydrolysis which indicates the absence of any loss during hydrolysis.

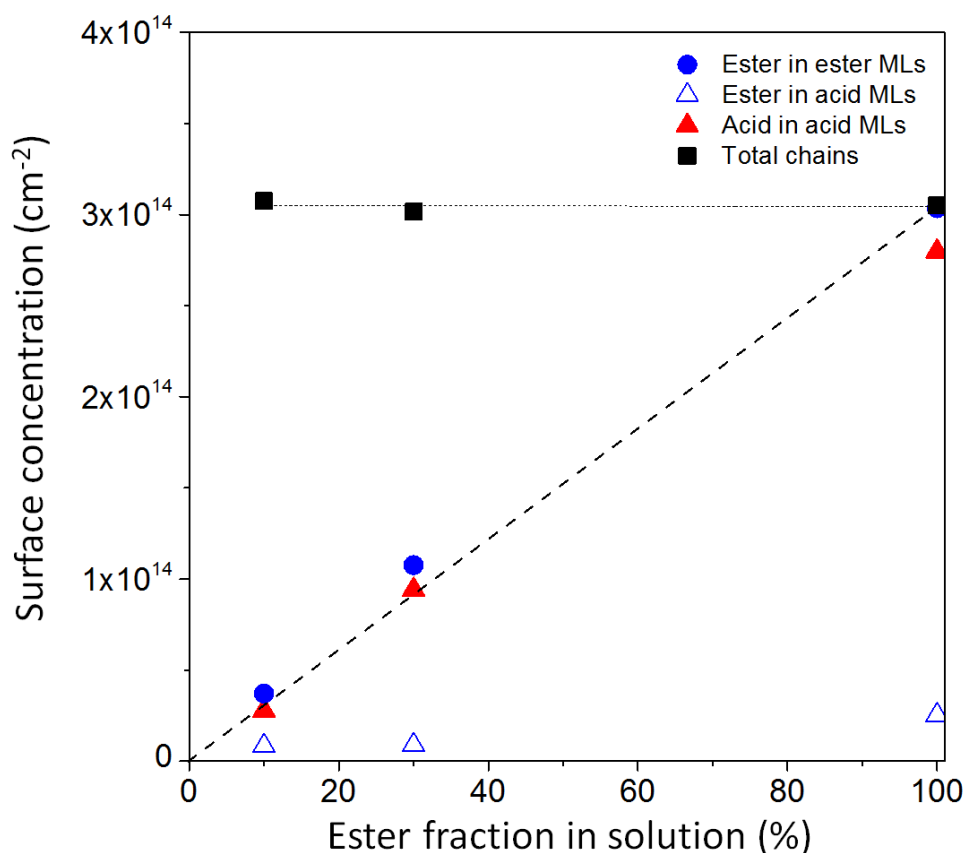


**Figure 1.11.** Surface composition of *mixed* MLs prepared from ethyl undecylenate/decene mixtures. Blue dots (●) stand for the nominal surface concentration of ester groups prior to hydrolysis, empty blue triangles (△) correspond to residual ester groups after hydrolysis and red triangles (▲) stand for surface concentration of acid groups after hydrolysis. Black squares (■) stand for the total concentration of alkyl chains (carboxyl + decyl).

**Position of the  $\nu\text{C}=\text{O}$  peak as a function of the concentration of carboxylic chains in monolayer**

The position of the *ester-related*  $\nu\text{C}=\text{O}$  bands and that of the *acid-related*  $\nu\text{C}=\text{O}$  bands (after hydrolysis) is plotted as a function of the concentration of carboxyl chains in the monolayers in Fig. 1.12. Obviously, the frequency of the ester-related peak shifts linearly to lower wavenumber when the ester concentration in the monolayers increases. After hydrolysis, a shift of the acid-related peak is also observed. In this case, its frequency increases when going from Si-acid<sup>ester-10</sup> to Si-acid<sup>ester-30</sup> ML but then decreases when going from the Si-acid<sup>ester-30</sup> to the Si-acid<sup>ester</sup> ML.

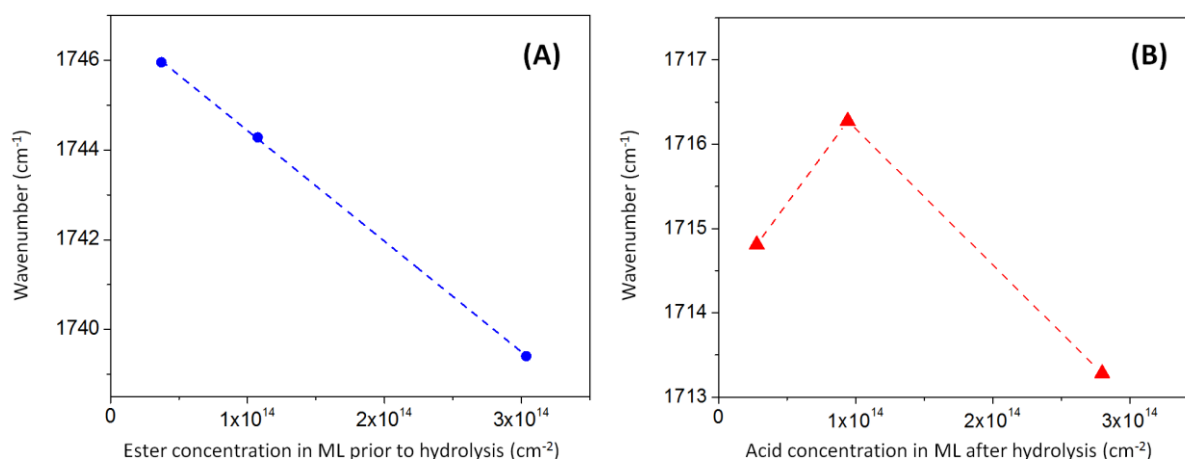


**Figure 1.12.** Evolution of the frequency of the **ester-** (A) or **acid-** (B) related peaks as a function of the surface concentration of **ester** or **acid** end-groups in the MLs **prior to** or **after** hydrolysis, respectively.

### 1.3. *Mixed* monolayers prepared from undecylenic acid/decene mixtures

This section focuses on the characterizations of *mixed* monolayers prepared by the direct grafting of acid chains using mixtures of undecylenic acid and decene as grafting solution (*one-step* route). *Pure* decyl and acid monolayers are labelled **Si-decyl** and **Si-acid**, respectively. *Mixed* monolayers are labelled as **Si-acid<sup>V</sup>** where V corresponds to the acid volume fraction in the grafting solution. For example, a *mixed* **Si-acid<sup>10</sup>** monolayer refers to that prepared in 10% undecylenic acid/ 90% decene mixture.

#### 1.3.1. Surface characterization prior to and after *surface wiping*

The surfaces functionalized with *mixed* monolayers were prepared using the protocols described in Section 1.1.2.2. Contrary to MLs prepared in acid-rich mixtures, in the case of MLs prepared in undecylenic acid/decene mixtures containing acid fraction lower than or equal to 10 %, we faced difficulties to clean the surface after grafting. Despite of using successive rinsing in solvents which able to solubilize both precursors, the surfaces still looked like generally less mirror-like/shiny and a fuzzy film was observed when looking carefully at the surface by eyes. The *wiping* procedures (see Section 1.1.2.2) proved to be necessary to remove the film. This change of surface appearance motivated a careful microscopy and FTIR analysis of the surface prior to and after *surface wiping*.

### 1.3.1.1. AFM characterization of *pure* and acid-rich *mixed* surfaces

Figure 1.13A shows AFM image of a *pure* Si-acid surface after rinsing in hot acetic. The *pure* Si-acid surface exhibits a featureless topography with a staircase structure which was generally observed on H-Si (111) surfaces (flat and smooth terraces separated by 3.1 Å high steps).<sup>20</sup> In the case of acid-rich *mixed* surfaces (prepared in solution containing acid fraction larger than or equal to 20%), similar surface state was obtained generally after successive rinsing in hot acetic acid and then in dichloromethane. If in some cases, low amounts of impurities was still observed on AFM images after this rinsing, it turned out that they could be removed by an additional *wiping* procedure. An AFM image of a *mixed* Si-acid<sup>20</sup> surface is shown in Fig. 1.13B exhibiting a clean surface without significant amount of residues.

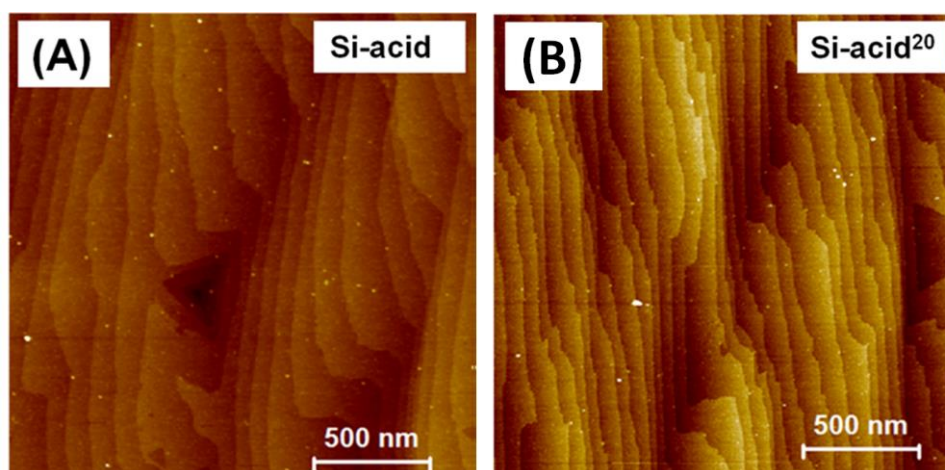


**Figure 1.13.** AFM images ( $2\mu\text{m} \times 2\mu\text{m}$ ) of a *pure* Si-acid surface after usual rinsing in hot acetic acid (A) and a *mixed* Si-acid<sup>20</sup> surface after successive rinsing in hot acetic acid and in dichloromethane, and finally cleaned by an additional *wiping* procedure (B).

### 1.3.1.2. Surface characterization of acid-poor *mixed* surfaces

This section focuses on mixed MLs prepared in solution containing acid fraction lower than or equal to 10% for which a very different surface state was evidenced after a classical rinsing procedure used for the acid-rich *mixed* surfaces. The surfaces look like less mirror-like and large amount of residual matter was evidenced on the surfaces. To remove this excess of matter, an additional cleaning procedure had to be implemented for these surfaces (*wiping* procedure, see Section 1.1.2.2). Fig. 1.14 shows, as an example, optical and AFM images of a *mixed* Si-acid<sup>10</sup> surface prior to *surface wiping* and after the first *wiping* procedure.

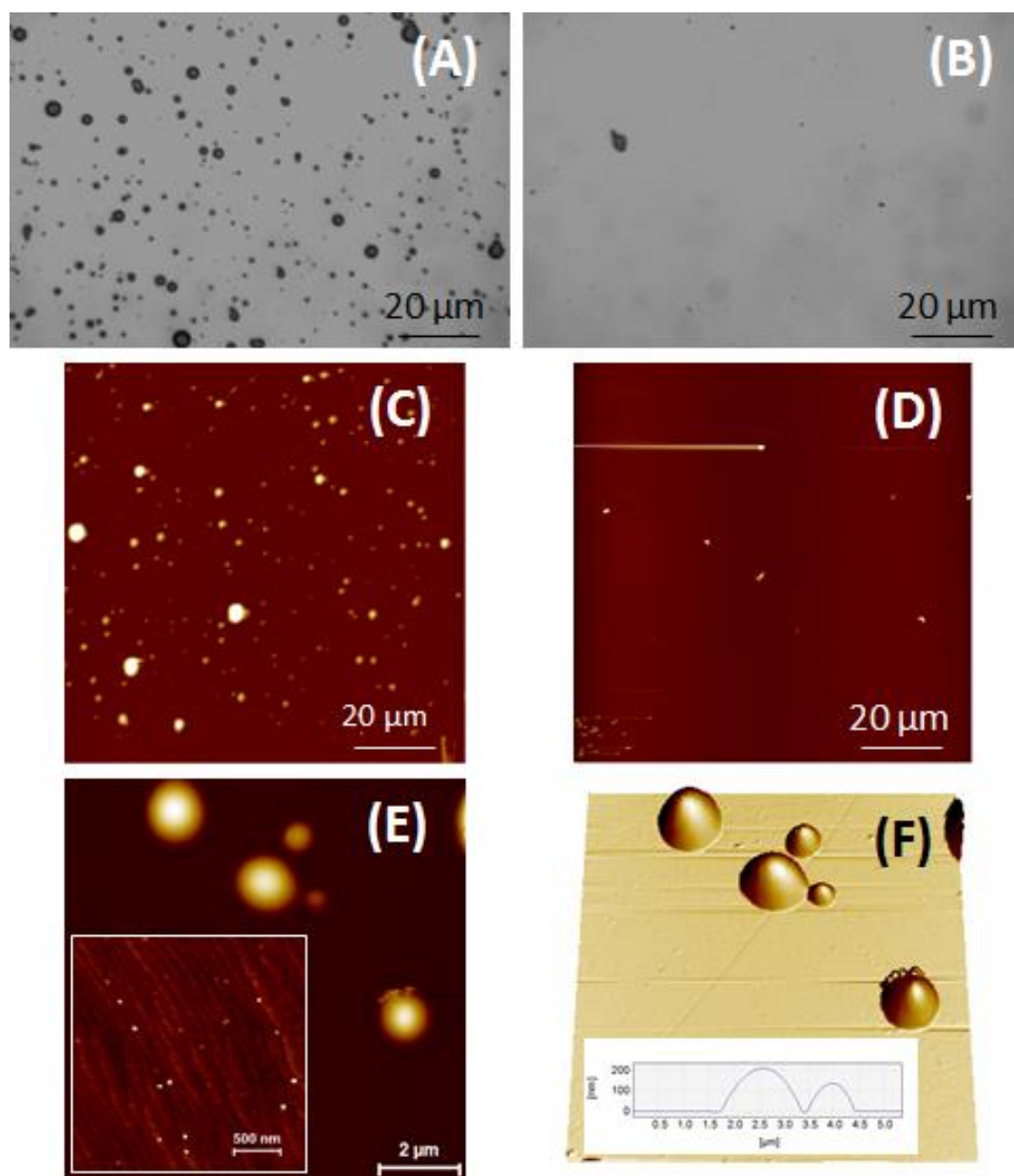


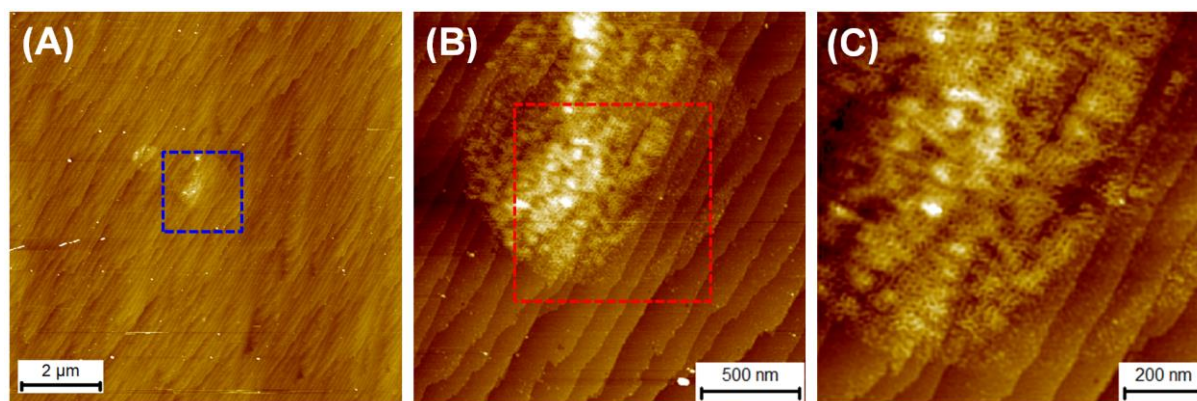
**Figure 1.14.** Optical (A, B) and large field AFM images (C, D, E, F) of a *mixed* Si-acid<sup>10</sup> surface, prior to *surface wiping* (A, C, E, F) and after (B, D) the first *wiping* procedure. Top view (E) and 3D (F) AFM images at greater magnification highlighting the spherical dome shape of few molecular structures and the presence of molecular aggregates on areas in between the molecular structures.

Prior to *surface wiping*, peculiar bright features with diameters reaching up to several μm, and distributed over the whole surface are observed on both optical (Fig. 1.14A) and large-field AFM images (Fig. 1.14C, E, F). We will see hereafter that the features observed on these images are molecular structures composed of alkenes precursors. After the first *wiping* procedure, both techniques indicate the removal of these molecular structures and let see

homogeneous and almost featureless images (Fig. 1.14B, D). At greater magnification, the AFM images show that the structures have characteristic spherical dome shapes (Fig. 1.14E, F). On areas in between the molecular structures, the image shows surface topography more or less comparable to that of the *pure* or acid-rich *mixed* surfaces (insert on Fig. 1.14E). Herein, the staircase structure is observed as well as low density (coverage < 1%) of nm-size molecular aggregates (diameters ~15 nm, height ~2 nm).

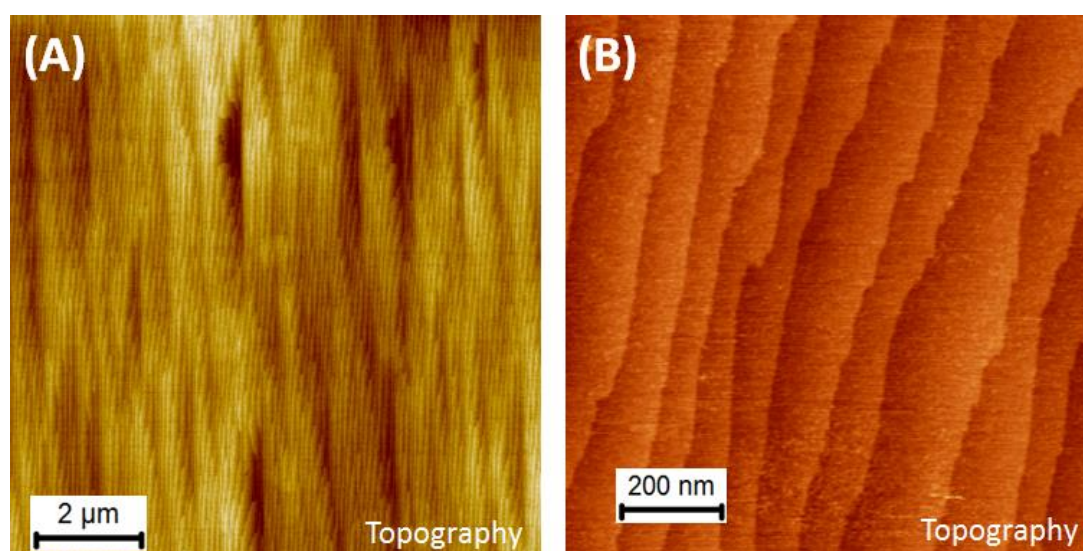
Assuming that the dome-like molecular structures are composed of alkene reactants present in the grafting solution (undecylenic acid or decene), the average surface concentration of residual molecules was estimated by considering the total volume of all the structures ( $\sum V_i = \sim 6.7 \times 10^8 \text{ nm}^3$ , determined on surfaces of  $10 \mu\text{m} \times 10 \mu\text{m}$ ), divided by the volume of one molecule ( $V_m \sim 0.2 \text{ nm}^3$ , determined using Alchemy® model for both reactants). This rough estimation gives a concentration of residual molecules of  $\sim 3.4 \times 10^{15} \text{ cm}^{-2}$ . This is one order of magnitude larger than the usual concentration of alkyl chain in a grafted monolayer. Such molecular structures have been observed systematically on *mixed* surfaces prepared in undecylenic acid/decene mixtures containing acid range from 0.1% to 10%.

Figure 1.15 displays AFM images at greater resolution of the same *mixed* Si-acid<sup>10</sup> surface after the first *wiping* procedure. No 3D structure is observed but residual matter can be however distinguished on localized area (Fig. 1.15B, C). The particular disk-like shape and the size of this area where residual matter are present strongly suggest that this is the footprint of one large molecular structures observed on the surface prior to the *surface wiping*.



**Figure 1.15.** Topography AFM images at different magnification of a *mixed Si-acid*<sup>10</sup> surface after the first *wiping* procedure. (A) Large-field image ( $10\mu\text{m} \times 10\mu\text{m}$ ) and (B and C) images at greater magnification showing the footprint of a molecular structure partially destroyed. Outside the disk-like area where excess matter is still present, the surface exhibits a staircase structure. Images (B) and (C) are zooms corresponding to the blue and red dashed areas in images (A) and (B), respectively.

After the *complete wiping* procedure, no trace of molecular structure and aggregate can be distinguished anymore on the topography image (Fig. 1.16A). The surface looks homogeneous over extended areas. At greater magnification, the topography is almost featureless only showing the staircase structure (Fig. 1.16B). Similar surface state was obtained independently of the composition of the solution after the *complete wiping* procedure.



**Figure 1.16.** Topography AFM images of a *mixed Si-acid*<sup>10</sup> surface after the *complete wiping* procedure.

### 1.3.1.3. Composition of the dome-like molecular structures : FTIR analysis

Figure 1.17 displays spectra of a *mixed* Si-acid<sup>10</sup> monolayer prior to *surface wiping* (red) and after (black) the *complete wiping* procedure. Prior to *surface wiping* (Fig. 1.17A), the spectrum is dominated by characteristic bands assigned to carboxylic acid groups ( $\nu\text{C}=\text{O}$  at  $1715\text{ cm}^{-1}$ ) and the methylene ( $\nu\text{CH}_2$ ) bands ( $2800\text{--}3000\text{ cm}^{-1}$  range). After the *complete wiping* procedure, a huge decrease of the intensity of the  $\nu\text{C}=\text{O}$  and  $\nu\text{CH}_2$  bands is observed and a spectrum characteristic of a *mixed* carboxydecyl/decyl monolayer is recovered. To better analyze the composition of molecular structures, we plotted the absorbance of the sample prior to *surface wiping* referred to that after the *complete wiping* procedure (differential spectrum, Fig. 1.17B). This spectrum resembles closely to that of undecylenic acid. No significant contribution of decene is observed, since the  $\text{CH}_3$  contribution is absent. The amount of removed  $\nu\text{C}=\text{O}$  and  $\nu_s\text{CH}_2$  bands has been determined by considering their integrated absorbance in the differential spectrum (Fig. 1.17B). The concentrations of acid and methylene groups were determined using the quantitative analysis methods described in Appendix II. The results are summarized in Table 1.3.

The concentration of acid and methylene groups having disappeared after the complete removal of the dome-like molecular structures are  $1.89 \times 10^{15}\text{ cm}^{-2}$  and  $2.04 \times 10^{16}\text{ cm}^{-2}$ , respectively. If one assumes that the structures are constituted only of undecylenic acid, then one would expect a methylene/acid ratio of 8 (8  $\text{CH}_2$  and 1 acid group per chain). Actually the ratio is  $\sim 10.8$  which is larger than expected. It is noteworthy that no peak related to the terminal  $\text{C}=\text{C}$  bonds ( $\nu\text{C}=\text{C}$  at  $1640\text{ cm}^{-1}$ ) of the two alkene precursors are observed on the spectra. This means that the structures are not constituted by only undecylenic acid or/and decene. Polymerization of vesicles made of undecylenic acid, leading to the formation of very robust supramolecular assemblies, and activated by heating or UV irradiation have already been reported.<sup>21</sup> So, the absence of  $\nu\text{C}=\text{C}$  peak on the spectra strongly suggests that polymerization could have occurred during the grafting under UV irradiation. Our results indicate therefore that the large supramolecular assemblies are formed in the undecylenic acid / decene mixture during the grafting. Polymerization process is very likely responsible for their great resistance with respect to the different rinsing procedures we tried.

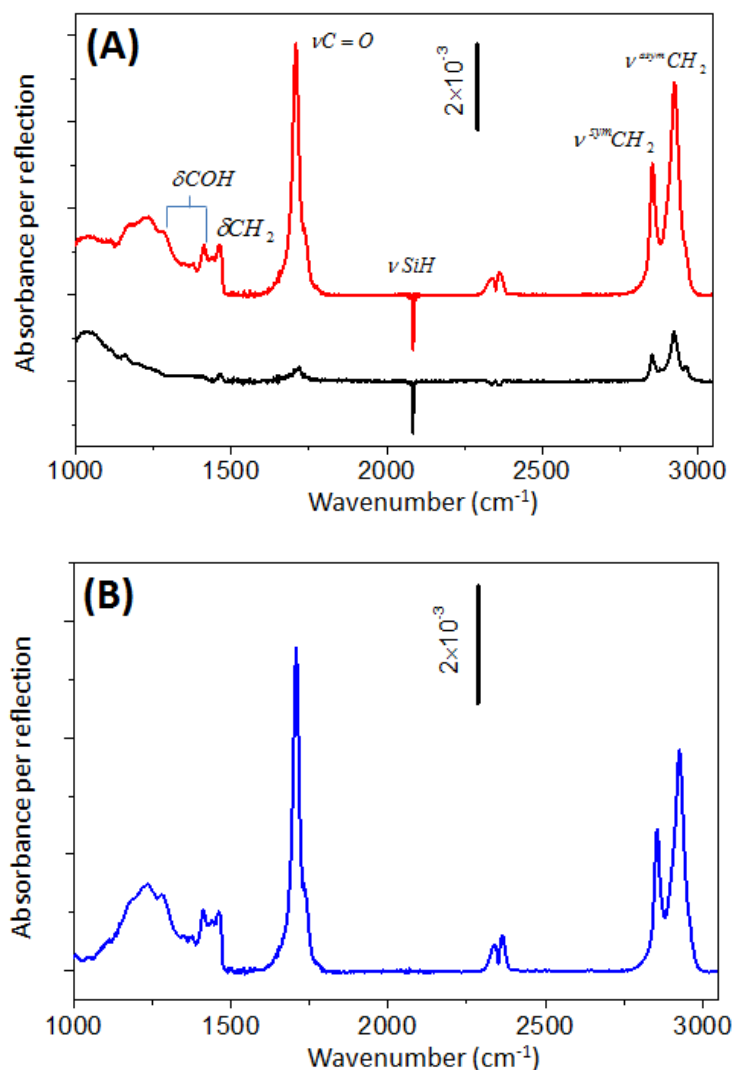


Figure 1.17. (A) FTIR spectra (p-polarization) of a *mixed* Si-acid<sup>10</sup> surface prior to *surface wiping* (red) and after (black) the *complete wiping* procedure. (B) Spectrum of *mixed* Si-acid<sup>10</sup> surface prior to *surface wiping* referred to that after *wiping* procedure showing the absorption bands *specifically* related to the molecular entities composing the molecular structures, having disappeared after the *complete wiping* procedure.

	Acid groups cm <sup>-2</sup>	Methylene groups cm <sup>-2</sup>	Methylene/Acid ratio
<b>Prior to</b> <i>surface wiping</i>	<b>2.00×10<sup>15</sup></b>	<b>2.3×10<sup>16</sup></b>	<b>11.5</b>
<b>After</b> <i>wiping</i> procedures	1.07×10 <sup>14</sup>	2.57×10 <sup>15</sup>	24.0
<b>Removed</b> matters	<b>1.89×10<sup>15</sup></b>	<b>2.04×10<sup>16</sup></b>	<b>10.8</b>

Table 1.3. Surface concentration of acid and methylene groups on a *mixed* Si-acid<sup>10</sup> surface prior to *surface wiping* and after the *complete wiping* procedure.

### 1.3.2. Surfaces after the *complete wiping* procedure

The results discussed hereinafter deal with clean *mixed* surfaces only, i.e., after the *complete wiping* procedure. The *mixed* Si-acid<sup>V</sup> monolayers have been grafted from undecylenic acid/decene mixtures. Two *pure* Si-acid and Si-decyl monolayers are also used for comparison.

#### 1.3.2.1. AFM characterization

After the *complete wiping* procedure, the *mixed* acid surfaces generally exhibit homogeneous topography without significant amount of contaminants, independently of the acid content in the solution. A typical example of the surface topography has been given in Fig. 1.16. We recall that the topography images show featureless surfaces except the staircase structure reminiscent of the as-prepared H-Si(111) surfaces. In the following, particular emphasis is made on the characterization of the surfaces using phase contrast imaging.

##### 1.3.2.1.1. *Phase-contrast imaging of a mixed Si-acid<sup>10</sup> surface*

The topography and phase images of a *mixed* Si-acid<sup>10</sup> surface are shown in Fig. 1.18. As already discussed, the topography image only displays the staircase structure of the surface (Fig. 1.18A). On the phase image, a disk-like area exhibiting a darker contrast is observed (Fig. 1.18B). At this magnification, the area corresponding to the dark domain look seemingly not correlated to any change in topography which suggests, at the first glance, that the phase contrast arises from the existence of different physicochemical properties on some localized areas. It should be outlined that the phase image was recorded simultaneously with the topography one, meaning that both images give a mapping of the same surface area.

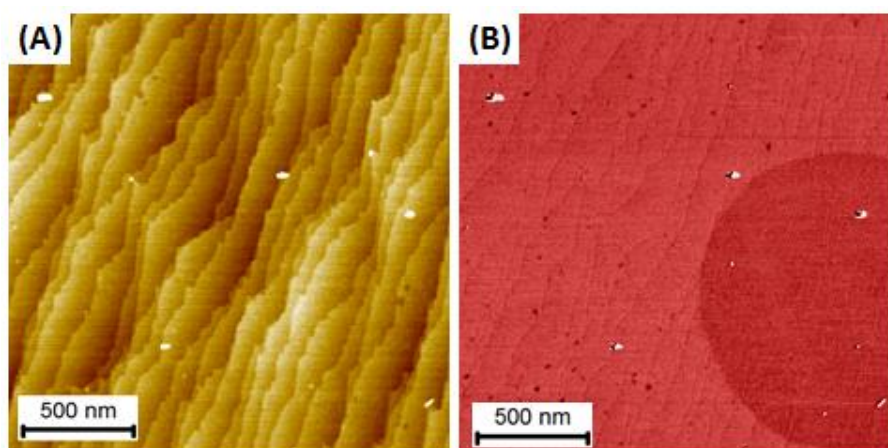


**Figure 1.18.** Topography (A) and phase (B) images of a *mixed Si-acid*<sup>10</sup> surface after *complete wiping* procedure. The surface is the same as the one shown in Fig. 1.15. The phase and topography images were recorded simultaneously thus warranting that the images refer to the same location at the surface.

Figure 1.19 presents greater resolution AFM images captured on areas located outside and inside a domain. Topography and phase images showing areas extended over three terraces are displayed for either location. Outside the domain (Fig. 1.19A), the terraces look smooth with peak-to-valley roughness lower than 1 Å, as measured from the height profile taken on a single terrace (Fig. 1.19C). Inside the domain (Fig. 1.19B), the terraces look rougher with peak-to-valley roughness reaching ~3 Å (Fig. 1.19D). The RMS on a single terrace outside the domain is 0.36 Å (a value close to that measured on pure Si-decyl or Si-acid surfaces) and is almost twice larger (0.70 Å) than that inside the domain. As images were recorded with the same tip, the observed variations are significant and not linked to any effect related to tip resolution.

Figure 1.19E and F show the corresponding phase images captured simultaneously with the topography. Contrary to what is observed at lower magnification the phase signal inside the domain looks inhomogeneous and the difference inside and outside domain areas is small. However, detailed analysis of the images reveals different phase contrast distribution and larger phase amplitude variations on domain areas. Outside the domain (Fig. 1.19E), the darker areas look much more localized forming small circular spots (diameters ~ 10 nm) whereas inside the domain (Fig. 1.19F), dark and bright areas look much more inter-diffuse. The larger variations of phase amplitude inside the domain are clearly evidenced on the phase histograms (FWMH= 1.66 ° against 1° for the image captured outside the domain area) (Fig. 1.19G). No clear correlation between phase contrast and topography could be evidenced.

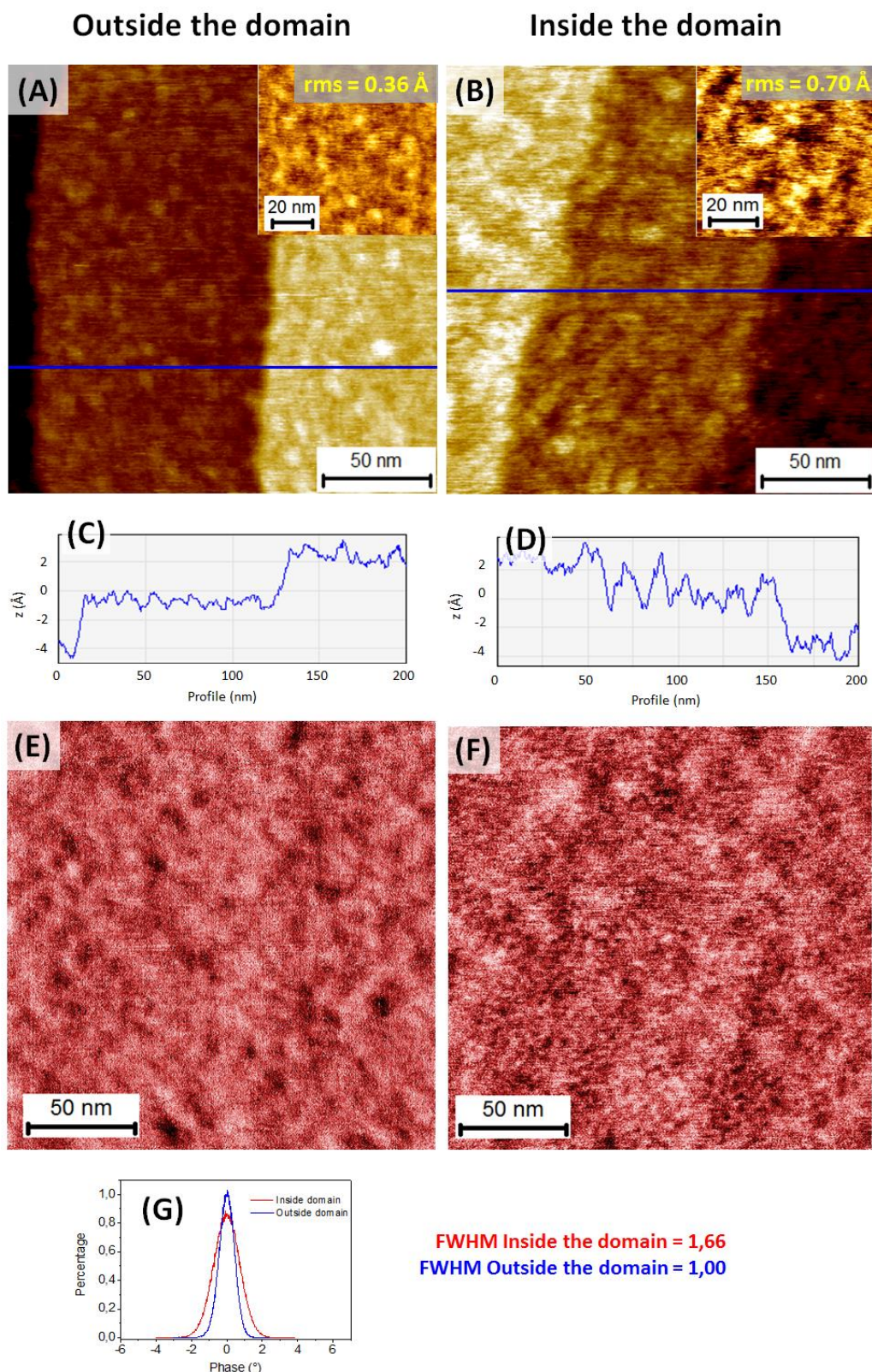
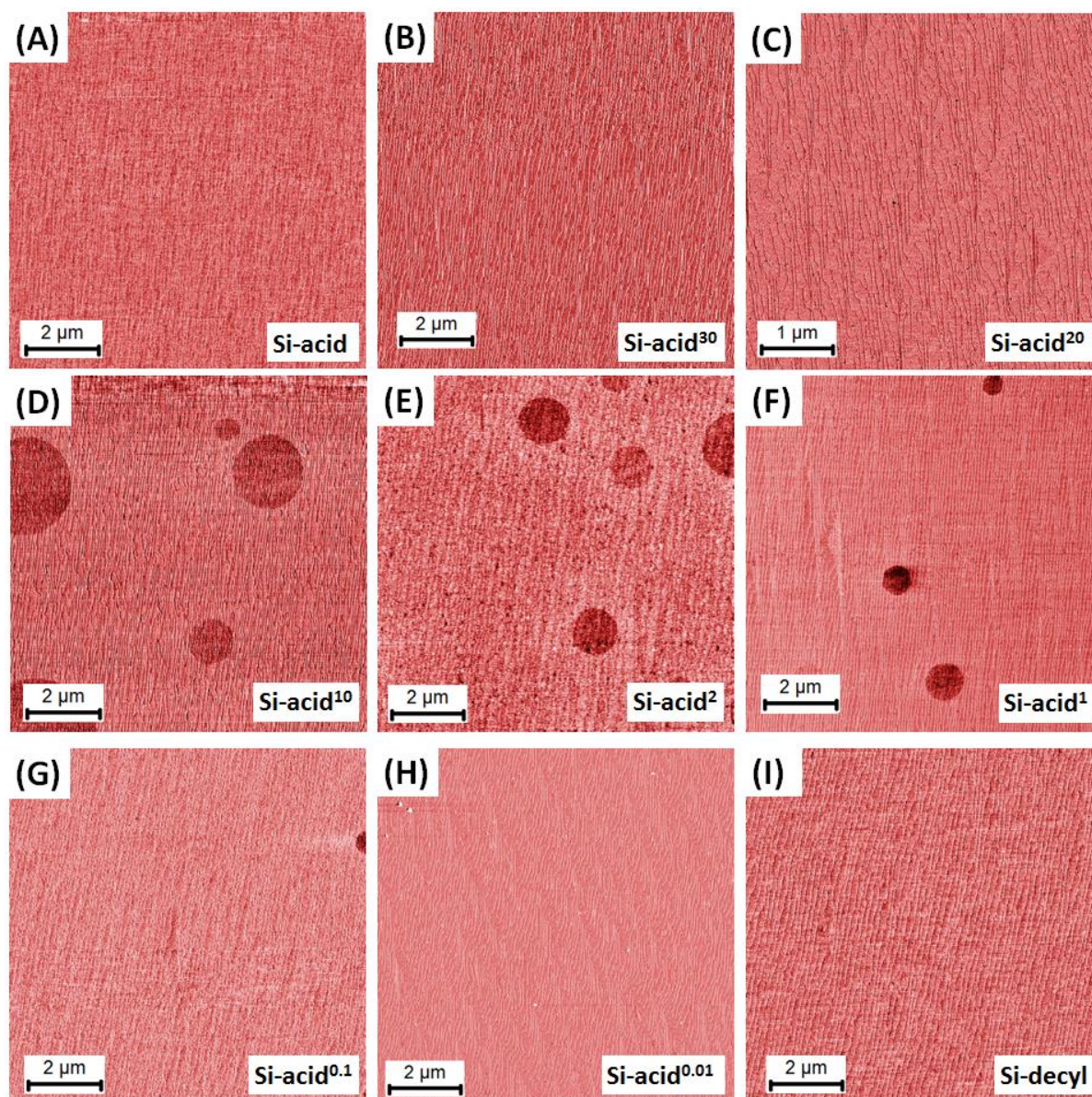


**Figure 1.19.** High-magnification topography and phase AFM images ( $200\text{nm} \times 200\text{nm}$ ) of a *mixed* Si-acid<sup>10</sup> surface: images of an area located outside domains (A, E) and inside a domain (B, F). Height profiles (C) and (D) of blue lines on (A) and (B), respectively, showing the distinct roughness on the terraces. (G) The histograms of the phase amplitudes for (E) and (F).

Such domains have been observed only on acid-poor surfaces prepared in solution containing acid fraction lower than or equal to 10%. Their density and size have been investigated as a function of the acid content in solution. The results are presented in the next section.

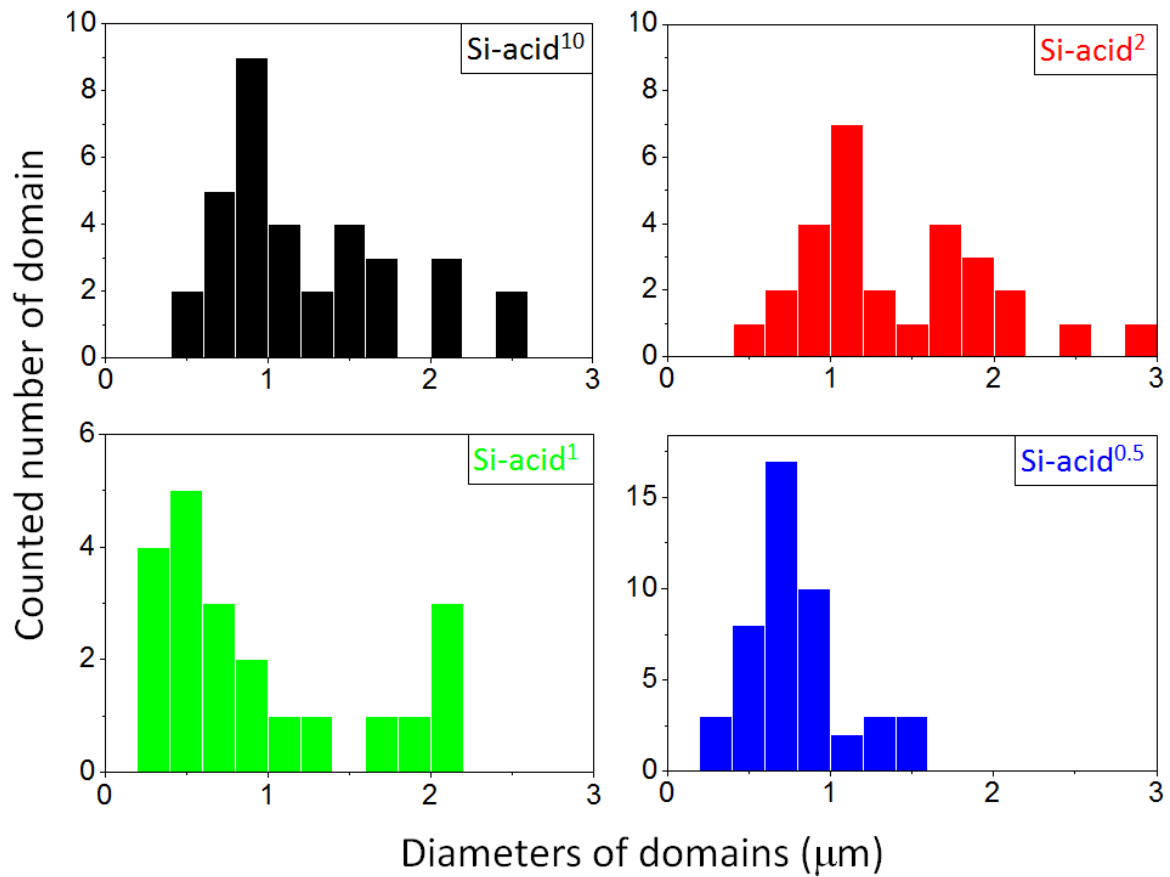
#### ***1.3.2.1.2. Density and size of the domains on mixed surfaces***

Figure 1.20 compares large-field phase images of *pure* Si-acid, Si-decyl and *mixed* Si-acid<sup>V</sup> surfaces. For all sample, the corresponding topography images (not shown) show featureless surface similar to the one displayed in the Fig. 1.16. For acid-rich *mixed* surfaces, no domain was observed (Fig. 1.20A, B, C). The phase images are homogeneous and featureless at this magnification. For *mixed* surfaces prepared in solution containing acid fraction (V) range from 0.1 to 10% (Fig. 1.20D, E, F, G), circular domains with size varies from a few hundreds nm up to a few  $\mu\text{m}$  are observed. For surface prepared in extremely low acid fraction (V = 0.01% - Fig. 1.20H), such domains are not evidenced at this magnification as also observed on a *pure* Si-decyl surface (Fig. 1.20I). These circular dark domains will be hereinafter called as *micro*-domains.



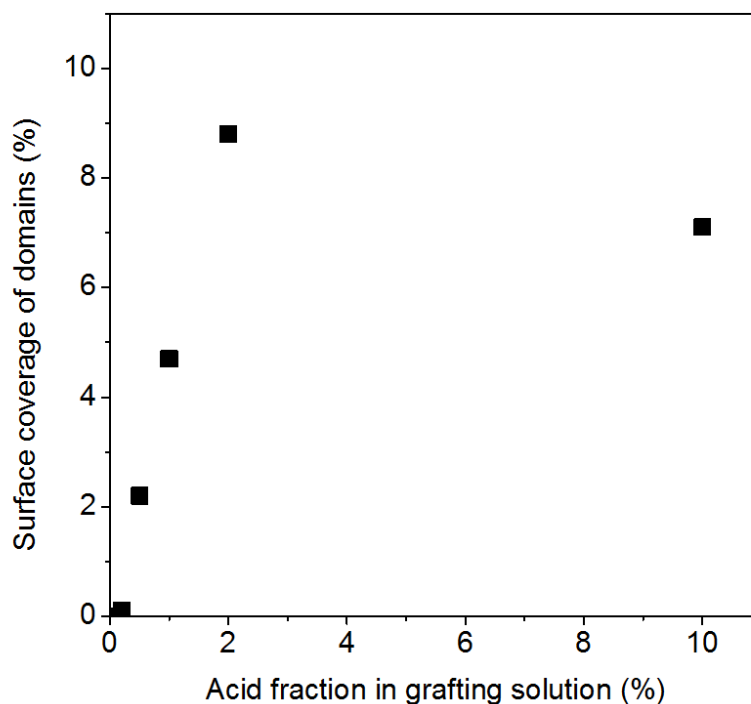
**Figure 1.20.** AFM phase images of *pure* Si-acid, Si-decyl and *mixed* Si-acid<sup>V</sup> surfaces (V corresponds to acid fraction in acid/decene mixtures). The scanned area is 10 $\mu\text{m}$   $\times$  10 $\mu\text{m}$  except for image (C) for which the scanned area is 5 $\mu\text{m}$   $\times$  5 $\mu\text{m}$ .

The diameter and surface coverage of the *micro*-domains have been measured through analysis of the AFM images. It has been done by imaging different locations on the samples, randomly chosen, in order to try to collect statistical data. Figure 1.21 shows the diameter distribution of *micro*-domains for four different mixed surfaces (Si-acid<sup>10</sup>, Si-acid<sup>2</sup>, Si-acid<sup>1</sup>, Si-acid<sup>0.5</sup>). In agreement with the qualitative overview given by the AFM phase images shown in Fig. 1.20, the histograms clearly show that the size of the *micro*-domain tends to decrease upon dilution of acid in solution (in spite of few statistics).



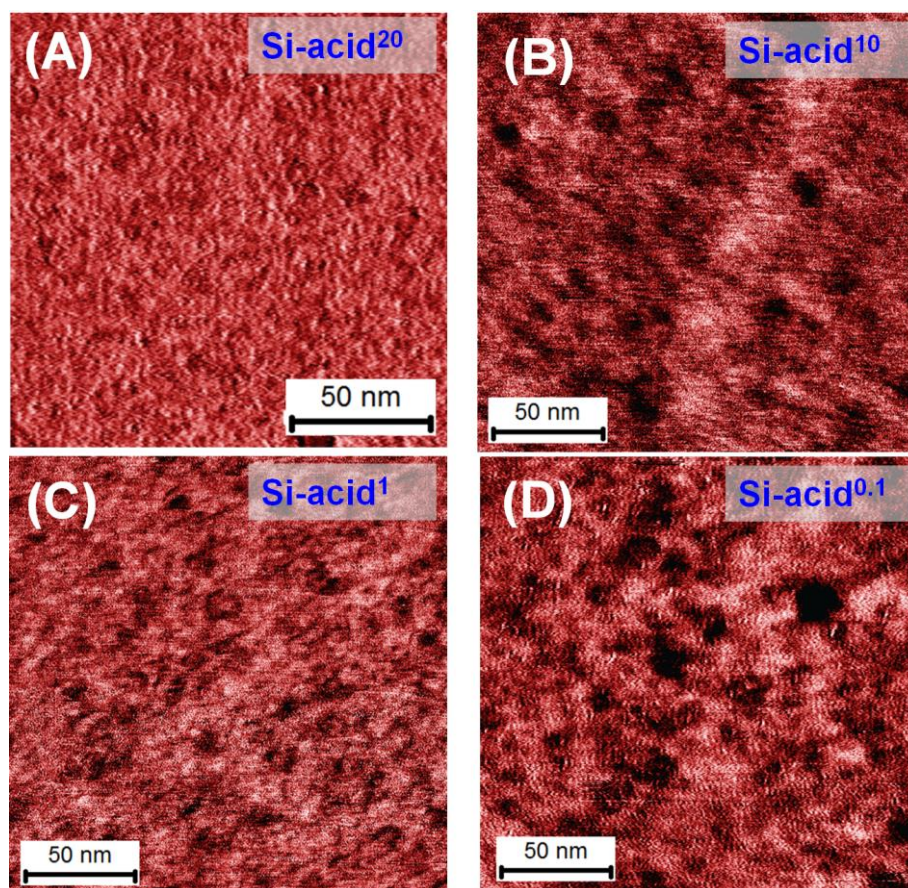
**Figure 1.21.** Distribution of the diameter of *micro*-domains on four different *mixed* acid surfaces.

Figure 1.22 displays that the surface coverage of *micro*-domains increases abruptly for an acid fraction in solution larger than 0.1%. Above 2%, the surface coverage of *micro*-domains seems to saturate for both *mixed* Si-acid<sup>2</sup> and Si-acid<sup>10</sup>. Above 10%, we recall that the *micro*-domains are not observed anymore.



**Figure 1.22.** Surface coverage of *micro*-domains as a function of the acid content in solution.

Figure 1.23 compares phase images at high magnification ( $200\text{nm} \times 200\text{nm}$ ) on the areas located outside the *micro*-domain (if present) for *mixed* surfaces prepared in solutions containing acid fraction ranging from 0.1% to 20%. Compared to the *mixed* Si-acid<sup>20</sup> (acid-rich) surface for which the image displays homogeneous distribution of phase contrast (Fig. 1.23A), nano-size dark spots (*nano*-domains) are observed within a brighter background on three other *mixed* surfaces (Fig. 1.23B, C, D). Although, it is extremely difficult to quantify the surface coverage of these nano-domains, we tentatively estimated it and found a surface coverage from 20 to 50%.



**Figure 1.23.** Phase AFM images at high magnification ( $200\text{nm} \times 200\text{nm}$ ) of *mixed acid surfaces* : (A)  $\text{Si-acid}^{20}$ , (B)  $\text{Si-acid}^{10}$ , (C)  $\text{Si-acid}^1$ , (C)  $\text{Si-acid}^{0.1}$ .

### 1.3.2.1.3. Characterization of extremely diluted acid MLs

This section focuses on the characterization of *extremely diluted acid surfaces* prepared in solution containing 0.01% acid. For such surfaces, large-field AFM phase images show homogeneous surfaces without any evidence of *micro-domain* (see Fig. 1.20H).

Figure 1.24 displays AFM images of a *mixed*  $\text{Si-acid}^{0.01}$  surface prior to *surface wiping* and after the *complete wiping* procedure. Prior to *surface wiping*, topography image shows the presence of molecular aggregates (bright spots  $\sim 1$  nm in height and  $\sim 10$  nm in diameter) homogeneously distributed over the whole surface (Fig. 1.24A). After the *complete wiping* procedure, these molecular aggregates have been completely removed and the images show smooth and flat terraces free of residue (Fig. 1.24C). On the phase image recorded simultaneously with the topography (Fig. 1.24D), nm-size domains (*nano-domains*) corresponding to localized dark areas with diameter  $\sim 8$ -10 nm are observed. Their size and distribution are similar to those of the molecular aggregates observed on the surface prior to

*surface wiping* (Fig. 1.24A). On high-resolution images (Fig. 1.24D and E), it can be seen that the *nano*-domains are not correlated to topographic features. Finally, the surface coverage of *nano*-domains is measured  $\sim 7\%$ . It is noteworthy that, in Fig. 1.24D, topographic features with lateral size much lower than the diameter of the *nano*-domains can be observed. This means that the size of the *nano*-domains as-measured on the image is not significantly enlarged because of tip convolution effects.

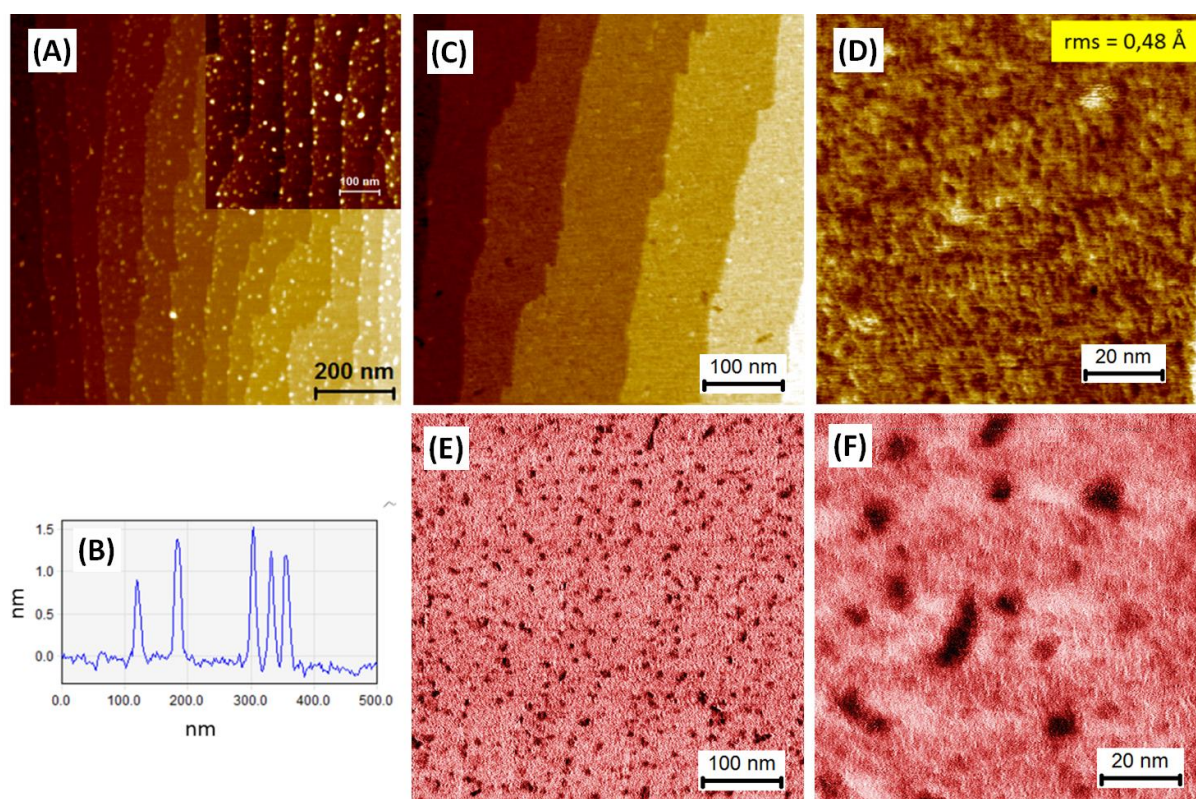


**Figure 1.24.** AFM images of a *mixed* Si-acid<sup>0.01</sup> surface. (A) Topography image of the surface prior to *surface wiping*, (B) Cross-section along one single terrace of image (A) showing the size of the bright molecular aggregates. Topography (C, D) and phase images (E, F) of the same surface after the *complete wiping* procedure.

### 1.3.2.2. FTIR measurements

#### 1.3.2.2.1. Surface composition: Qualitative analysis

The anchoring of the acid chains on the surface was confirmed by FTIR analysis of *pure* Si-acid monolayer (Fig. 1.25). The reference is the hydrogenated silicon surface prior to monolayer grafting. The peak at  $1715\text{ cm}^{-1}$  is assigned to  $\nu\text{C=O}$  stretching mode of carbonyl involved in carboxylic acid groups and the bands at  $2852$  and  $2922\text{ cm}^{-1}$  to symmetric and

antisymmetric stretching modes  $\nu\text{CH}_2$  of the methylene units composing the alkyl chains. Two main bands correspond to symmetric and antisymmetric stretching modes of the methylene units composing the alkyl chains are observed at  $2852$  ( $\nu_s\text{CH}_2$ ) and  $2922$   $\text{cm}^{-1}$  ( $\nu_a\text{CH}_2$ ). These bands are correlated to smaller ones at  $1463$  and  $1414$   $\text{cm}^{-1}$  assigned respectively to  $\delta\text{CH}_2$  bending mode and  $\nu\text{C-OH}$  stretching mode. In addition, the observation of a sharp negative peak at  $2083$   $\text{cm}^{-1}$  assigned to  $\nu\text{Si-H}$  stretching mode, indicates the disappearance of Si-H bonds when going from hydrogenated to grafted surfaces, in agreement with the reaction scheme of hydrosilylation (Fig. 1.1). No other additional peaks are observed which indicates a well-controlled surface composition with only carboxylic acid chains on the surface (the negative doublet at  $\sim 2300$   $\text{cm}^{-1}$  is related to variations of  $\text{CO}_2$  concentration in the spectrometer during the IR measurements). The peak positions and assignments are summarized in Table 1.4.

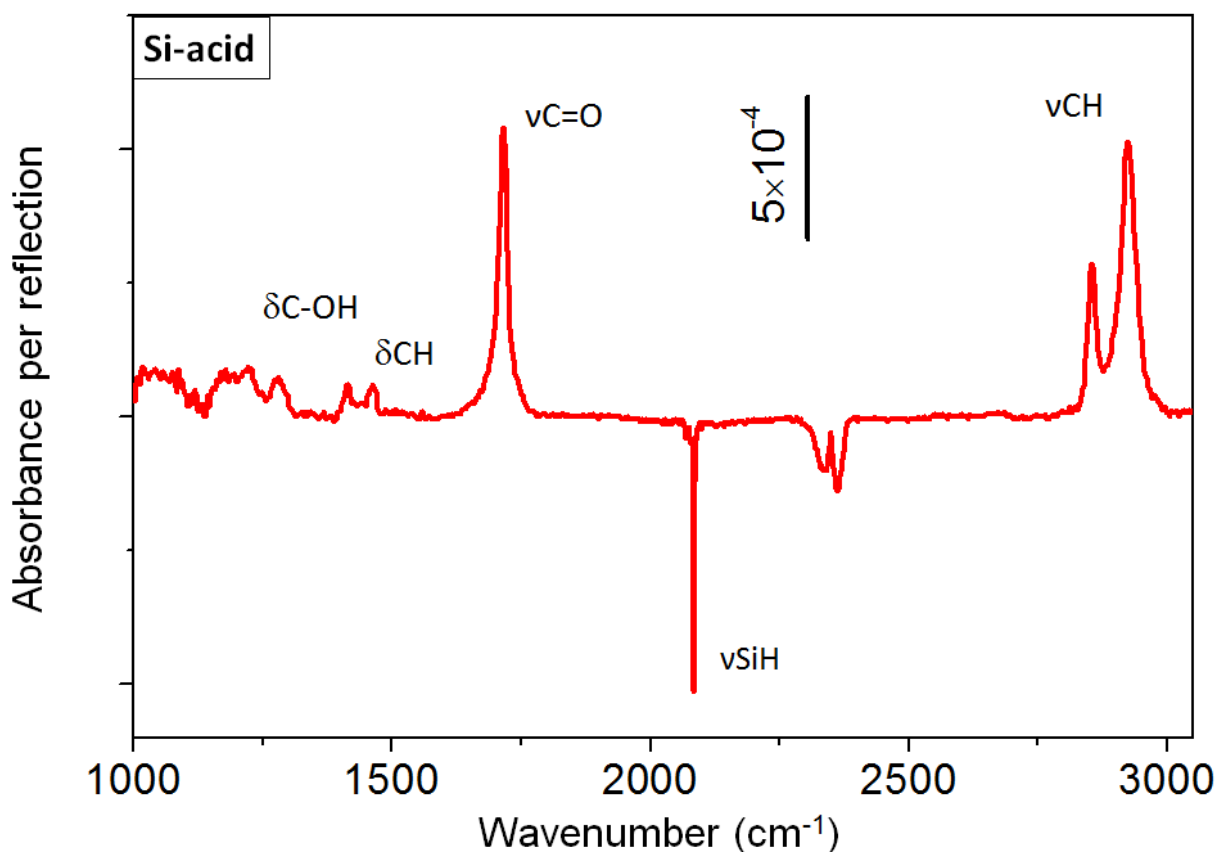
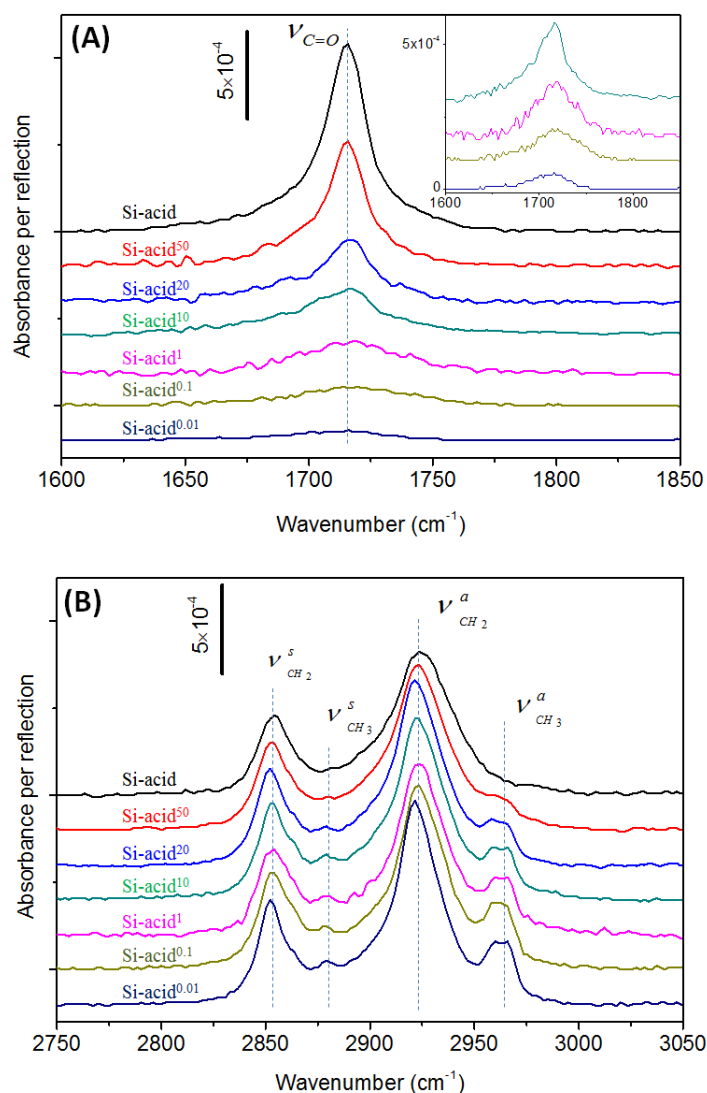


Figure 1.25. FTIR spectrum of a *pure* Si-acid surface (p-polarization).

Band assignments	Peak position (cm <sup>-1</sup> )
$\nu_a\text{CH}_2$	2922
$\nu_s\text{CH}_2$	2852
$\nu\text{SiH}$	2083
$\nu\text{C=O}$	1715
$\delta\text{CH}_2$	1463
$\nu\text{C-OH}$	1414

**Table 1.4. Assignment and position of the IR bands observed on the spectrum in Fig. 1.25.**

Figure 1.26 displays the narrow spectra of a *pure* Si-acid and *mixed* Si-acid<sup>V</sup> surfaces (acid fraction in solution  $V = 0.01 - 50\%$ ). The general appearance of these spectra is very similar of that of *pure* **Si-acid** surfaces. Figure 1.26A shows the evolution of the  $\nu\text{C=O}$  carbonyl band related to acid groups and Fig. 1.26B shows the evolution of the  $\nu\text{CH}_2$  and  $\nu\text{CH}_3$  bands related to the alkyl chains as a function of the acid content in solution. The spectra have been vertically shifted for clarity. The insert in Fig. 1.26A displays the spectra of the acid-poor *mixed* surfaces ( $V = 0.01 - 10\%$ ), at higher magnification. The main changes observed on the spectra are the decrease of the  $\nu\text{C=O}$  band intensity and the appearance of additional bands at  $2873\text{ cm}^{-1}$  and  $2963\text{ cm}^{-1}$  assigned to the symmetric and antisymmetric stretching vibrations of the methyl end-groups of the decyl chains ( $\nu_s\text{CH}_3$  and  $\nu_a\text{CH}_3$ ) upon decreasing of the acid content in solution. At first glance, no significant evolution of the  $\nu\text{CH}_2$  bands (at  $2852$  and  $2922\text{ cm}^{-1}$ ) is observed, which indicates that the global amount of total alkyl chains (acid + decyl chains) does not sizeably change. Acid and decyl chains have a very close number of methylene groups (10  $\text{CH}_2$  per the carboxydecyl chains and 9  $\text{CH}_2$  per the decyl chain) so that only 10% variation is expected if acid chains are replaced by decyl chains (or *vice versa*) in the monolayer.



**Figure 1.26.** Narrow FTIR spectra in the  $\nu\text{C}=\text{O}$  range (A) and in the  $\nu\text{CH}$  range (B) of *pure* Si-acid and *mixed* Si-acid<sup>V</sup> MLs. Each surface with its acid fraction in solution V is labelled on each corresponding spectrum.

#### 1.3.2.2.2. Quantitative analysis of the $\nu\text{C}=\text{O}$ band

Similar to the surface prepared by the *two-step* route, detailed quantitative analysis has been carried out in order to determine the surface concentration of decyl and acid chains in the grafted monolayers (see Section 1.2.2.2.). The same quantitative analysis method was used (see Appendix II). The detail of the quantitative analysis of the carbonyl peak is presented hereafter. The integrated absorbance obtained from this analysis has been used for the determination of the surface concentration of grafted acid chains as function of the acid content in solution. The composition of the monolayers will be discussed later (see Section 1.3).

Spectral deconvolution / fitting procedure

In a first approach, the  $\nu\text{C=O}$  bands has been fitted with only one peak and one linear baseline. In many cases for *mixed* surface, it turned out that the model curve could not satisfactorily fit to the data. An example of curve fitting on a *mixed* Si-acid<sup>20</sup> surface is shown in Fig. 1.27A. A shoulder on the left-hand side of main peak is obviously needed. Adding a second component improves very much the fit of the  $\nu\text{C=O}$  band (see Appendix II).

All the  $\nu\text{C=O}$  bands of mixed surfaces were then fitted to a model consisting of two components, e.g. shown in Fig. 1.27B. One component is at  $\sim 1715\text{ cm}^{-1}$  and other is at  $\sim 1690\text{ cm}^{-1}$ . A linear baseline was added to the model. In cases where the fit yields unphysically large value for the linewidth of the  $1690\text{ cm}^{-1}$  component, this value was arbitrarily set to  $24\text{ cm}^{-1}$ , i.e., a value close to that found for the solution (see Appendix II).

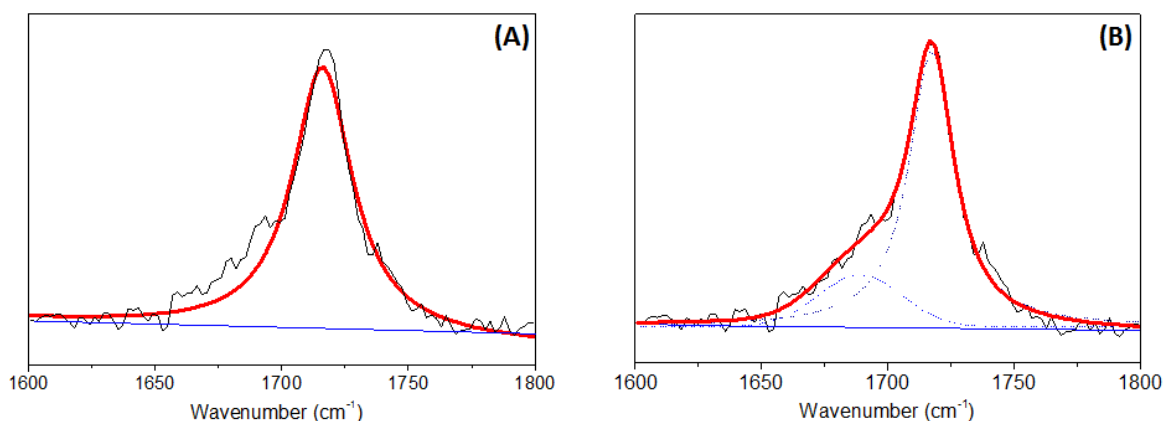


**Figure 1.27.** Experimental data and fitting curves for the  $\nu\text{C=O}$  band of a *mixed* Si-acid<sup>20</sup> surface. Fitting curves obtained using one single (A) or two components (B).

Integrated intensity of the  $\nu\text{C=O}$  band

Figure 1.28 displays the integrated absorbance of the two peaks centered at  $\sim 1690$  and  $\sim 1715\text{ cm}^{-1}$  as well as their sum as a function of the acid fraction in the grafting solution. For either peak the integrated absorbance plotted on the figure is the sum of the integrated absorbance of the peak in s- and p-polarization ( $\text{Abs}^{\text{p}} + \text{Abs}^{\text{s}}$ ). The solid and dashed lines are guide to eye. For all the surfaces, the integrated absorbance of the peak at  $\sim 1715\text{ cm}^{-1}$  ( $\text{Abs}^{\text{p+s}}_{1715}$ ,  $\circ$ ) represents the major contributions to the total integrated absorbance ( $\text{Abs}^{\text{p+s}}_{1690+1715}$ ,  $\blacksquare$ ). Its intensity globally increases upon increasing of the acid content in solution. Three regimes are distinguished: for acid fraction from 0.01 to 1%, the integrated absorbance increases abruptly from zero to  $0.025\text{ cm}^{-1}$ ; for acid fraction in between 1 and 20 %, it remains almost constant  $\sim 0.025\text{ cm}^{-1}$ ; and finally for acid fraction above 30 %, it

increases again from 0.025 to 0.06  $\text{cm}^{-1}$ . In comparison, the intensity of the peak centered at  $\sim 1690 \text{ cm}^{-1}$  ( $\text{Abs}^{\text{p+s}}_{1690}$ ,  $\diamond$ ) is much lower and remains almost constant whatever the acid fraction in solution. Its weight with respect to the total integrated absorbance remains low ( $< 10 \%$ ) except in the case of ML prepared in the *extremely diluted* mixture (0.01% acid), its contribution is  $\sim 15\%$ .

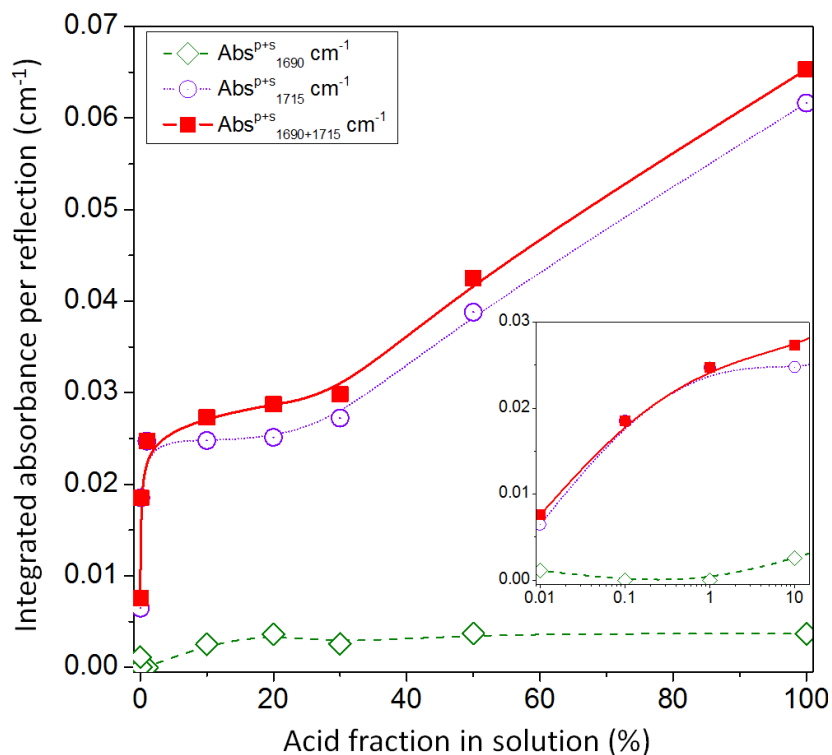


**Figure 1.28.** Sums of integrated absorbance in p- and s- polarization of the peaks centered at  $\sim 1690$  ( $\text{Abs}^{\text{p+s}}_{1690}$ ,  $\diamond$ ) and  $\sim 1715$  ( $\text{Abs}^{\text{p+s}}_{1715}$ ,  $\circ$ )  $\text{cm}^{-1}$  as determined from the fits and the sum of the two previous quantities ( $\text{Abs}^{\text{p+s}}_{1690+1715}$ ,  $\blacksquare$ ) as a function of the acid fraction in the grafting solution.

#### Position and linewidth of the two $\nu\text{C}=\text{O}$ components

In Fig. 1.29, the position and linewidth of the two  $\nu\text{C}=\text{O}$  peaks are plotted as a function of the acid fraction in the grafting solution. For acid fraction range from 0.01% to 10%, the peak at  $\sim 1690 \text{ cm}^{-1}$  is so small that its position and line width need to be fixed at  $1690 \text{ cm}^{-1}$  and  $24 \text{ cm}^{-1}$ , respectively (Fig. 1.29A and B). Above 10%, the peak shifts to higher wavenumber while its linewidth remains almost constant  $\sim 24 \text{ cm}^{-1}$ . In parallel, the frequency of the peak at  $\sim 1715 \text{ cm}^{-1}$  shifts to lower wavenumber upon increasing of the acid fraction in solution (Fig. 1.29C). The peak is rather broad (30-60  $\text{cm}^{-1}$  width) for acid fraction lower than

10 % while its linewidth is smaller and remains almost constant at  $\sim 20 \text{ cm}^{-1}$  for acid fraction larger than 10 % (Fig. 1.29D).

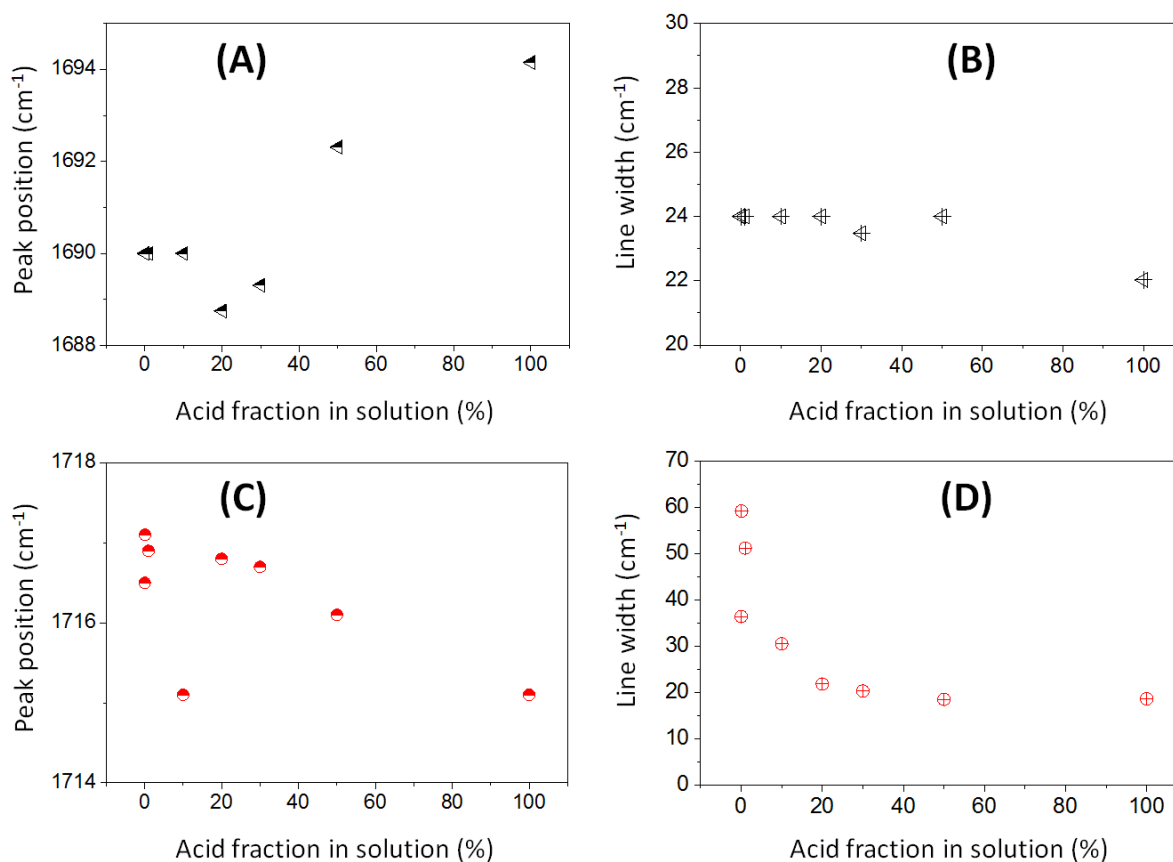


**Figure 1.29.** Position (A, C) and linewidth (B, D) of the two  $\nu\text{C}=\text{O}$  components at  $\sim 1690$  (upper plots - A, B) and  $\sim 1715 \text{ cm}^{-1}$  (bottom plots - C, D) as a function of the acid fraction in the grafting solution.

### 1.3.3. Linkage of molecular-label onto the acid end-groups

The coupling of molecular labels to acid surface sites was investigated to cross-check the surface concentration of the acid groups. For this purpose, nitrophenethyl (NPE) groups were covalently attached on acid end-groups of the *mixed* MLs by esterification reaction (Fig. 1.30). Nitrophenyl have been chosen because the nitro groups give rise to strong and characteristic IR absorption bands, making them good markers for a cross correlation of the concentration of the carboxylic group using FTIR analysis. In the following, *pure* and *mixed* nitro-terminated surfaces are labelled as  $\text{Si-NPE}^{\text{acid}}$  and  $\text{Si-NPE}^{\text{acid-V}}$  where V refers to the acid fraction in the grafting solution, e.g., a *mixed*  $\text{Si-NPE}^{\text{acid-10}}$  monolayer has been obtained

by coupling onto a *mixed* Si-acid<sup>10</sup> surface. Surface cleanliness was controlled systematically by AFM imaging for all monolayers at its final state (not shown).

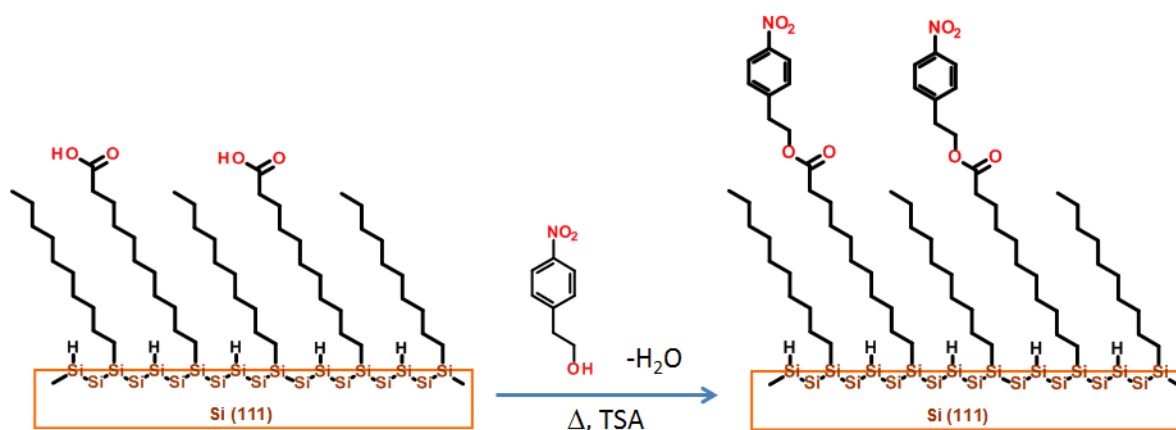


**Figure 1.30.** Reaction scheme for the covalent coupling of nitrophenethyl alcohol (NPEA) onto *mixed* carboxydecyl/decyl MLs.

### 1.3.3.1. Coupling protocol

Nitrophenethyl (NPE) was coupled onto surface by the esterification between nitrophenethyl alcohol (NPEA) and acid end-groups. *p*-Toluene Sulfonic Acid (TSA) was used as a catalyst. The solution (100 mM NPEA + 10 mM TSA in mesitylene) was heated at 110°C and outgassed by argon bubbling for 30 min prior to introducing the acid terminated surfaces. The esterification reaction was let to proceed at 110°C under continuous argon flowing for 2h. The samples were then twice rinsed in acetonitrile at 60°C for 10 min each time.

### 1.3.3.2. FTIR measurements

#### 1.3.3.2.1. Qualitative analysis

Figure 1.31 shows FTIR absorbance spectra of a *pure* Si-acid surface prior to (red) and after reaction with NPEA (blue). After esterification, the spectrum shows the disappearance of the *acid-related*  $\nu\text{C}=\text{O}$  peak (at  $\sim 1715\text{ cm}^{-1}$ ) and the appearance of new bands assigned to nitrophenyl groups and a new  $\nu\text{C}=\text{O}$  peak standing at position characteristic of carbonyl involved in ester linkage ( $\sim 1740\text{ cm}^{-1}$ ). The small shoulder observed at the left-hand side of the  $\nu\text{C}=\text{O}$  band indicates the presence of residual acid groups. Additionally, the  $\nu\text{CH}$  bands remain unchanged indicating that the alkyl layer was not damaged during the

coupling reaction. The three bands observed at 1348, 1527 and 1610  $\text{cm}^{-1}$  are assigned to the nitrophenyl groups. The two bands centered at 1348 and 1527  $\text{cm}^{-1}$  are related respectively to the symmetric and antisymmetric stretching modes of  $\text{NO}_2$  group ( $\nu_s\text{NO}_2$  and  $\nu_a\text{NO}_2$ ). These two peaks have narrow line width and stay far away from  $\text{H}_2\text{O}$  absorption range (1600 - 1800  $\text{cm}^{-1}$ ), which makes them attractive for FTIR analysis. Finally, the band at 1610  $\text{cm}^{-1}$  is assigned to quadrat stretching mode of the phenyl ring enhanced by the presence of the nitro substituent (Fig. 1.31, blue). The evolution of the IR spectra clearly indicates the success of the coupling reaction, in agreement with the reaction scheme in Fig. 1.30. The position and assignment of nitrophenyl-related bands are summarized in Table 1.5.

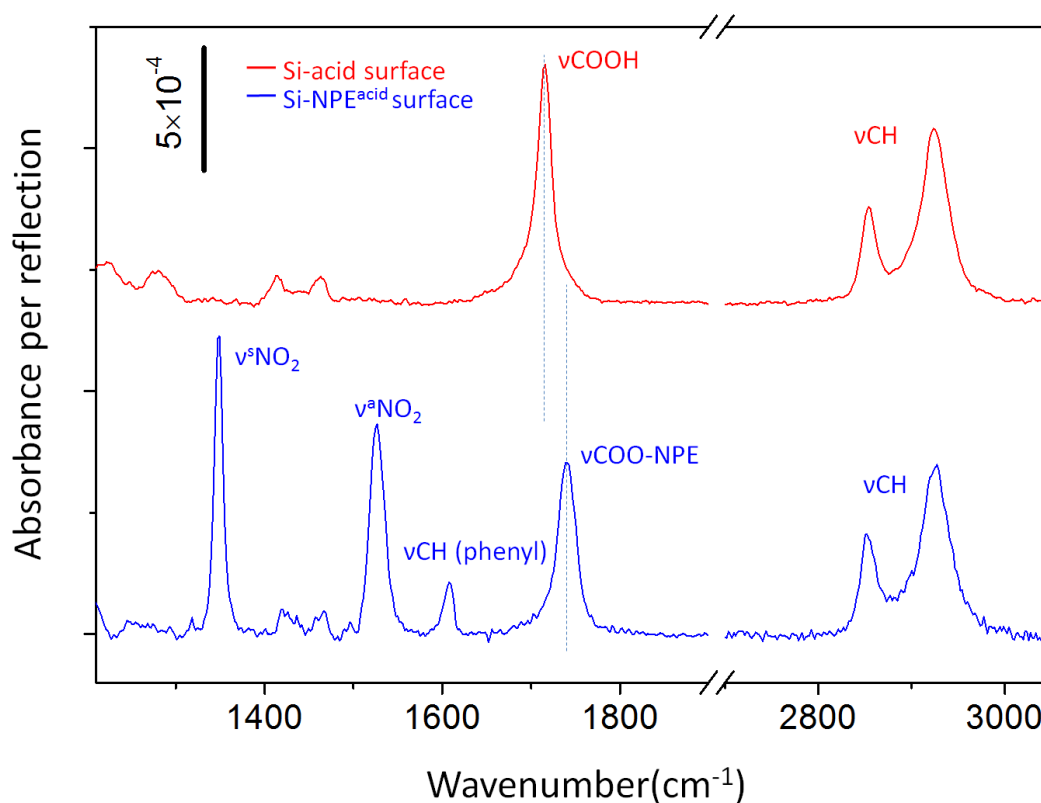


Figure 1.31. FTIR spectra of a Si-acid surface prior to (red) and after nitrophenethyl coupling (blue). The spectra are referred to that of the initial hydrogenated silicon surface.

Band assignment	Peak position ( $\text{cm}^{-1}$ )
$\nu_s\text{NO}_2$	1348
$\nu_a\text{NO}_2$	1527
$\nu\text{Ar-H}$	1610

Table 1.5. Assignments and positions of the nitrophenyl-related bands.

Figure 1.32 displays narrow FTIR spectra after the coupling of nitrophenyl groups on *pure* and *mixed* Si-acid surfaces. For either spectrum the reference is the surface prior to coupling reaction. Thus, only the changes due to esterification can be detected on the spectra. The figure focuses on the 1250 – 1650  $\text{cm}^{-1}$  range where the characteristic bands of nitro groups are observed. The shape of the each band looks very similar for the different surfaces. Only a diminution of their intensity is observed upon decreasing of the acid content in solution. Quantitative analysis of the two nitrophenyl bands (at 1348 and 1527  $\text{cm}^{-1}$ ) is presented in the next section.

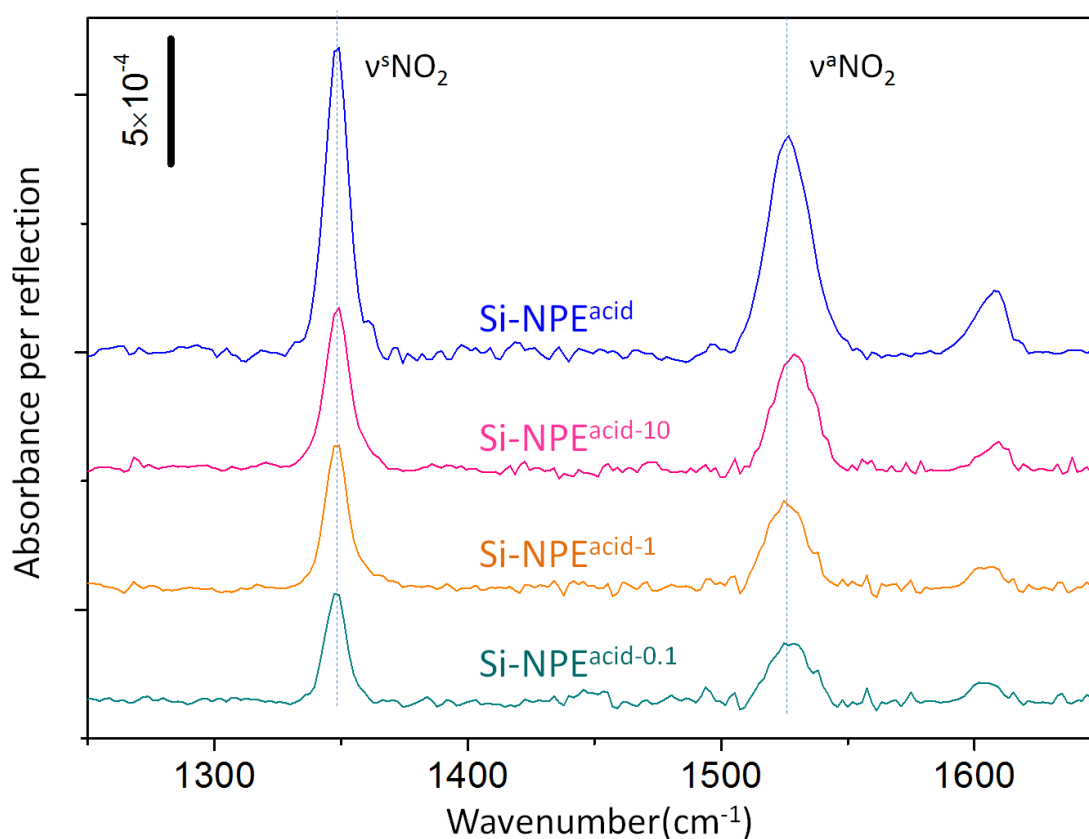


Figure 1.32. FTIR spectra of *pure* and *mixed* nitrophenethyl-terminated surfaces. The references are the acid-terminated surfaces prior to esterification.

#### 1.3.3.2.2. Quantitative analysis

##### Determination of coupling yield

The esterification yield has been calculated from the integrated intensity of the acid-related  $\nu\text{C}=\text{O}$  bands (at 1715  $\text{cm}^{-1}$ ) prior to and after nitrophenethyl coupling. The  $\nu\text{C}=\text{O}$  band was fitted with 2 components (Voigt functions): one at  $\sim 1715 \text{ cm}^{-1}$  accounting for residual acid and one at  $\sim 1740 \text{ cm}^{-1}$  accounting for the ester linkage arising from the nitrophenethyl

linkage, and a linear baseline. The esterification yield was determined as the ratio of the integrated intensity of the residual acid-related peak ( $1715\text{ cm}^{-1}$ ) after esterification  $\text{Abs}_{\text{acid}}^{\text{NPE}}$  normalized to its nominal integrated intensity  $\text{Abs}_{\text{acid}}^0$  (prior to esterification). The integrated absorbance of the different peaks and the esterification yield is given for a *pure*  $\text{Si-NPE}^{\text{acid}}$  and a *mixed*  $\text{Si-NPE}^{\text{acid-1}}$  surface in Fig. 1.33.

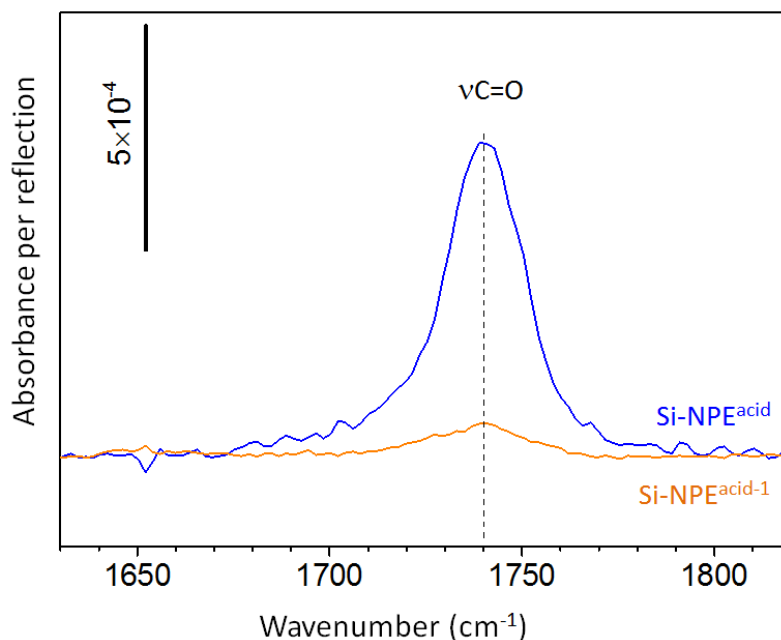


Figure 1.33. Narrow FTIR spectra showing the ester-related  $\nu\text{C}=\text{O}$  peak after coupling on a *pure* Si-acid ML and a *mixed* Si-acid<sup>1</sup> ML.

Surfaces	Prior to esterification	After esterification		Esterification yield $\text{Abs}_{\text{acid}}^{\text{NPE}} / \text{Abs}_{\text{acid}}^0$
	$\text{Abs}_{\text{acid}}^0$	$\text{Abs}_{\text{acid}}^{\text{NPE}}$	$\text{Abs}_{\text{ester}}^{\text{NPE}}$	
<i>pure</i> Si-acid	0.0616	0.0048	0.0533	92%
<i>mixed</i> Si-acid <sup>1</sup>	0.0247	0.0010	0.0204	96%

Table 1.6. Integrated absorbance of the acid-related ( $1715\text{ cm}^{-1}$ ) and ester-related ( $1740\text{ cm}^{-1}$ )  $\nu\text{C}=\text{O}$  peaks prior to and after esterification, and esterification yield.

#### Surface concentration of Nitrophenyl groups

The surface concentration of NPE groups was determined from the integrated intensity of  $\text{NO}_2$ -related bands at  $1348\text{ cm}^{-1}$  and  $1525\text{ cm}^{-1}$ . The infrared cross-sections of these two vibrational modes have been calibrated from FTIR measurements in solutions (see Appendix

II). The two bands at  $1348$  and  $1525\text{ cm}^{-1}$  were fitted with a single component (Voigt function) and a linear base line. Their integrated intensity measured on the different acid surface was then converted into nitrophenyl concentration using the quantification method and the calibration data detailed in Appendix II.

In Fig. 1.34, the surface concentration of nitrophenyl groups on different *mixed* surfaces is plotted as a function of the acid content in the grafting solution. The surface concentration is  $\sim 2.2 \times 10^{14}\text{ cm}^{-2}$  on *pure* Si-acid surface. In the case of the *mixed* surfaces the NPE surface concentration is - as expected - lower ( $\sim 0.7 \cdot 10^{14}\text{ NPE/ cm}^{-2}$ ) but was found to few evolve though the acid fraction in the solution used for the preparation of the MLs varies over a wide range.

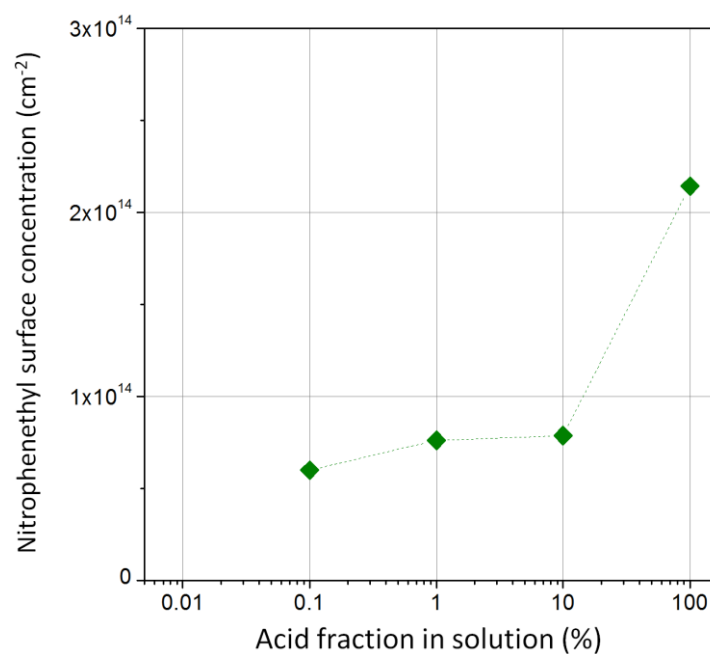


**Figure 1.34. Surface concentration of nitrophenyl as a function of the acid fraction in the grafting solution.**

## 1.4. Discussion

The characteristics of the  $\nu\text{C}=\text{O}$  band (intensity, position, linewidth) provide not only information about the surface concentration of acid groups but also information about the molecular environment of the acid groups. As shown in Fig. 1.35A, the surfaces prepared by the *two-step* route exhibit a simple behavior. The molecular density is about constant, i.e., independent on the acid content of the monolayer, and close to  $3 \times 10^{14} \text{ cm}^{-2}$ . The grafted acid surface concentration exhibits a linear variation as a function of the acid content in the grafting solution. As described in Section 1.3.2.2.2, the  $\nu\text{C}=\text{O}$  band of all *one-step* MLs presents two contributions. While the peak at  $\sim 1715 \text{ cm}^{-1}$  is unambiguously assigned to the stretching  $\nu\text{C}=\text{O}$ , the origin of the peak at  $\sim 1690 \text{ cm}^{-1}$  is not clear. As shown in Fig. 1.35B, we quantify the acid concentration in MLs by using the total integrated absorbance of the 1690 and 1715  $\text{cm}^{-1}$  peaks (Fig. 1.35B, ●). The contribution of the 1690  $\text{cm}^{-1}$  peak is merely negligible to the total integrated absorbance of the band. We compare the values obtained by this calibration method to the surface concentration of nitrophenethyl groups coupled on acid end-groups (independently determined from the absorption of the nitro groups, as previously explained). The surface concentration of nitrophenyl (◆) in the monolayer after coupling is close to but systematically lower than that of acid groups determined by the usual methods. This slight discrepancy is mostly accounted for by the coupling yield which is  $\sim 90\%$ .

As shown in Fig. 1.35B, the acid concentration in the monolayer decreases upon decreasing of the acid content in solution. However, the variation is far from being directly proportional. In agreement with Faucheux et al.,<sup>16</sup> the proportion of acid chain is slightly larger than that in the precursor mixture in the case of mixtures with an acid content larger than 30%. The surprising observation is the existence of a large range of solution compositions ( $1\% < \text{acid fraction} < 30\%$ ) which yield a surface concentration in grafted acid chains nearly constant and close to  $10^{14} \text{ cm}^{-2}$ . For very low acid content ( $< 0.1\%$ ), the surface concentration in grafted acid chains is finally decreasing.

Over the whole investigated range of composition of the grafting mixtures, the total chain density (decyl + carboxydecyl) present at surfaces prepared by the *one-step* route remains unchanged and closes to  $2.5 \times 10^{14} \text{ cm}^{-2}$ . This value is somewhat lower than that found at surface prepared by the *two-step* route ( $\sim 3 \times 10^{14} \text{ cm}^{-2}$ ). These distinct values are due to the differences in the grafting methods. The thermal activation of the grafting used in the *two-step*

route creates denser layers than the photochemical activation of the grafting used in the *one-step* route. Even if one takes into account that the yield of the hydrolysis step in the *two-step* route is  $\sim 90\%$ , the surface concentration in grafted acid chains is  $\sim 10\%$  larger in pure acid layers prepared by the *two-step* route than in similar layers prepared by the *one-step* route.

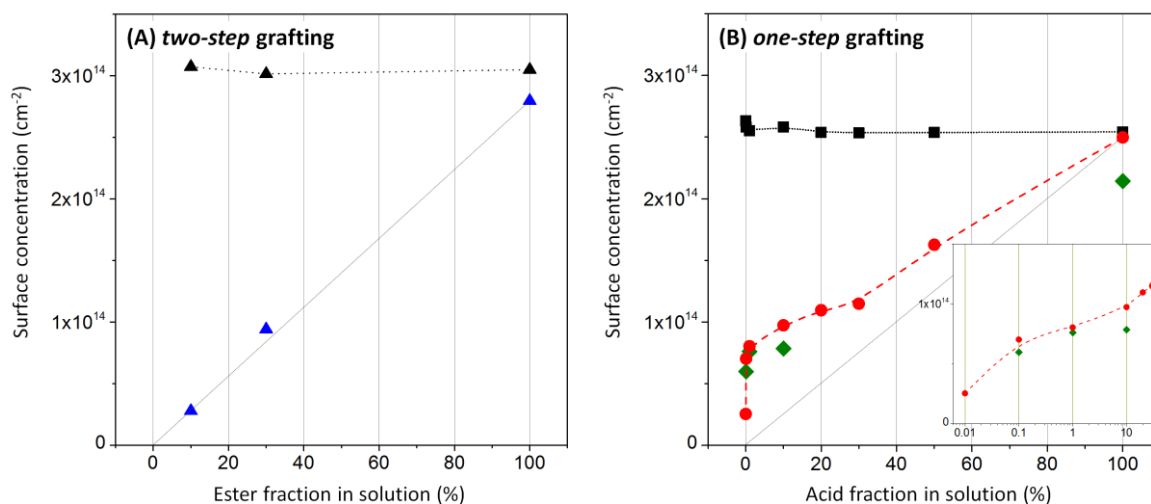


**Figure 1.35.** (A) Composition of the monolayers prepared by the *two-step* route as a function of the acid fraction in solution. Acid concentration is determined from the integrated absorbance of the acid-related peak ( $\blacktriangle$ ) (B) Composition of the monolayers prepared by the *one-step* route as a function of the acid fraction in the grafting solution. Acid concentration is determined from the total integrated absorbance of two peaks at  $1690$  and  $1715\text{ cm}^{-1}$  ( $\bullet$ ). Nitrophenyl concentration ( $\blacklozenge$ ) in monolayer after coupling with nitrophenethyl alcohol cross-check the acid quantification method. (A and B) Total chain concentrations of all monolayers ( $\blacktriangle$ ,  $\blacksquare$ ) were determined from the concentration of methylene groups.

The total surface concentration in acid groups within the grafted monolayers has therefore been determined using IR spectroscopy. Let us now discuss the repartition of these acid groups in the monolayers on the basis of the AFM results. On monolayers prepared by the *one-step* route in mixtures containing an acid fraction lower than 20%, the AFM topography images are featureless whereas phase images exhibit dark *micro-* and *nano-*domains. If *micro-*domains are assumed to solely consist of grafted acid molecules packed with the same density as for a pure acid surface, the corresponding acid content can be compared to the total surface acid concentration determined from the infrared analysis. Such comparison is shown in Fig. 1.36. Clearly, the *micro-*domain contribution is by far too low to account for the amount of acid chains grafted on the surface and most of the acid chains are located outside the *micro-*domains. It is plausible to consider that the acid chains are actually

located in the *nano*-domains. These *nano*-domains are clearly evidenced at low acid surface concentration (see Fig. 1.24). In this case the coverage associated to *nano*-domains (7%) considers with the acid surface concentration determined by the infrared analysis. At larger acid surface concentrations, AFM phase images are much more irregular. In these conditions, the estimation of a surface coverage of the *nano*-domains is quite uncertain, since the obtained values rather sensitively depend upon arbitrary choices made for the image analysis (contrast, offset, threshold...). It can only be said that the acid surface coverage derived from the infrared analysis (~30%) is in the range of the values obtained from the analysis of AFM images.

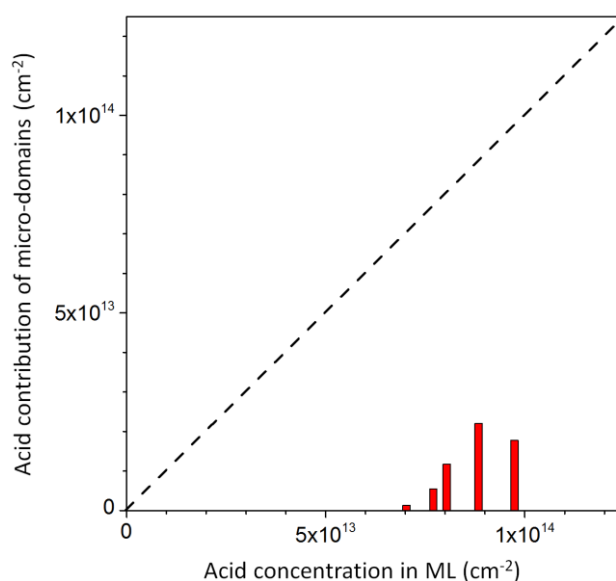


**Figure 1.36.** The maximum contribution of *micro*-domains (red) to the acid content of the monolayers as a function of the total acid concentration in MLs. The red bars remain much below the dashed line, figuring a hypothetical 100% contribution, which shows that the *micro*-domain contribution remains negligible.

Let us now try to refine the analysis of the characteristics of the  $\nu\text{C}=\text{O}$  bands as a function of the surface concentration of the vibrating species. The peak position and linewidth of acid-related peak of *mixed* acid monolayers prepared by the *two-step* route are plotted as a function of the grafted acid chain concentration (Fig. 1.37A and B). For better comparison, results of C. Douarche<sup>22</sup> have been added to the plot (dark yellow). In Fig. 1.37C, except for one isolated point, the peak position is seen to shift linearly to lower frequency when the acid concentration is increasing. As discussed in the following, this behavior can be accounted for by lateral dipolar interaction between vibrators. The linewidth of the peak remains close to 20  $\text{cm}^{-1}$  (Fig. 1.37B). Figure 1.37C and D shows the position and linewidth of the  $\nu\text{C}=\text{O}$  band as

a function of the grafted acid chain concentration in ML prepared by the *one-step* route. In both cases, two regions can clearly be distinguished: for acid concentration lower than  $\sim 1 \times 10^{14}$  acid.cm<sup>-2</sup>, the peak position essentially remains close to  $\sim 1716.5$  cm<sup>-1</sup> and the linewidth is quite broad, in the 30 to 60 cm<sup>-1</sup> range. For acid concentration larger than  $\sim 1 \times 10^{14}$  acid.cm<sup>-2</sup>, the frequency of the  $\nu$ C=O mode linearly decreases when the acid concentration in the monolayer increases and the linewidth remains nearly unchanged at  $\sim 20$  cm<sup>-1</sup>. This behavior is clearly distinct from that found for the monolayers produced by the *two-step* route. Especially, a clear difference appears between monolayers with high acid concentration and those with low acid concentrations. The latter case coincides with the range where domains have been observed by AFM. Let us first discuss the evolution of the  $\nu$ C=O frequency as a function of the acid surface concentration.

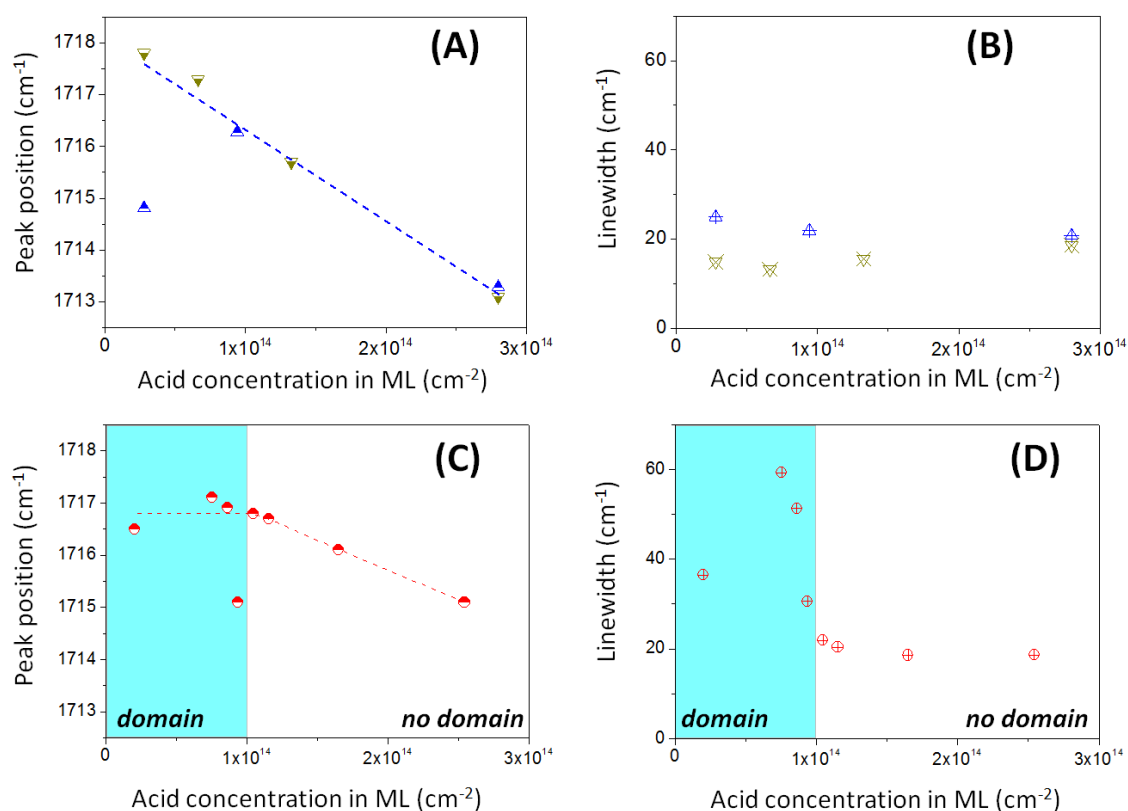


**Figure 1.37.** Peak position (A and C) and linewidth (B and D) of  $\nu$ C=O peak as a function of the acid concentration in MLs prepared by the *two-step* (up) and *one-step* routes (down). The colored zone indicates the surface acid concentration range for which domains have been observed.

As already mentioned, lateral interactions between vibrating dipoles are known to account for a frequency shift depending on surface concentration of identical vibrators. This

effect has widely been studied for CO adsorbed on metals<sup>22-25</sup> or insulators<sup>26</sup> through isotopic <sup>12</sup>C/<sup>13</sup>C dilution experiments. This effect has also been carefully modelled.<sup>27,28</sup> In these case studies (corresponding to “on-top” adsorption of CO molecules), the vibrating dipoles are perpendicular to the surface and the vibration frequency increases when the surface vibrator concentration increases. However, as explained in another context for oxide vibrations, in the case of vibrating dipoles parallel to the surface, the vibration frequency decreases when the surface vibrator concentration increases<sup>29</sup>, which is the tendency observed in our results (Fig. 1.37A and C). These frequency shifts can be estimated by summing the interaction of one vibrating dipole with all the other similar vibrating dipoles over the surface. For identical, parallel dipoles inclined by an angle  $\theta$  on the surface plane this summation yields a frequency shift

$$\Delta\nu = \frac{1}{16\pi^2\nu} \frac{e^{*2}}{\mu} \frac{(2 - 3 \cos^2 \theta) \sum_{other\ dipoles} 1/R_i^3}{4\pi\epsilon_0 + \frac{\alpha_e}{2} (2 - 3 \cos^2 \theta) \sum_{other\ dipoles} 1/R_i^3} \quad \text{Equation 1.1}$$

In this expression,  $\nu$  is the frequency of the isolated vibrator,  $e^*$  its effective charge,  $\mu$  its reduced mass,  $\alpha_e$  the electronic polarizability of the surface molecules, and  $R_i$  the distances between the considered dipole and the other dipoles. It can be seen that the sign of the shift changes for a  $\theta$  value close to  $35.3^\circ$ . In order to verify, at least qualitatively, those dipolar interactions might account for the frequency shifts of Fig. 1.37A and C, it is of prime importance to determine the orientation of the  $\nu\text{C=O}$  vibrating dipole with respect to the surface plane in the present case.

As a matter of fact, because of the distinct forms of the continuity conditions when an electromagnetic radiation is s- or p- polarized, the quantification method used to determine the acid content in monolayers allows for obtaining the effective number of vibrators which have a dynamic dipole parallel ( $N_{//}$ ) or perpendicular ( $N_{\perp}$ ) to the surface (see Appendix II). These numbers actually refer to the equivalent number of vibrators associated with the component of the vibrating dipole parallel and perpendicular to the surface, respectively. Therefore, the average orientation of this dipole with respect to the surface plane is simply determined from those two numbers. More precisely, if  $\theta$  is the angle between the vibrating dipole and the surface plane (Fig. 1.38),  $\theta$  is simply obtained as:

$$\theta = \arctan \left( \sqrt{\frac{N_{\perp}}{N_{//}}} \right)$$

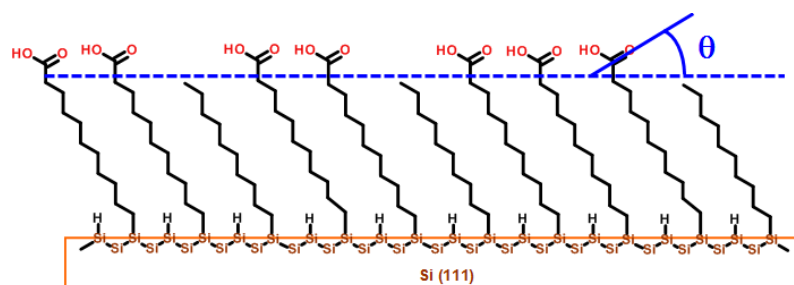


**Figure 1.38.** Schematic represents a *mixed* alkyl/carboxyalkyl layers. The C=O mode creates an angle of  $\theta$  to the surface.

The dependence of  $\theta$  is plotted as a function of the acid content in the ML prepared by both the *one-step* and *two-step* routes (Fig. 1.39). In general,  $\theta$  is always  $< 30^\circ$  meaning that the dynamic dipole of the  $\nu\text{C}=\text{O}$  mode is almost parallel to the surface plane and that the vibrating frequency decreases when the surface concentration in vibrators (accounted for by the extent of the sum in Eq. 1.1) increases. Therefore, the  $\theta$  values plotted in Fig. 1.39 are consistent with a qualitative explanation of the evolution of the  $\nu\text{C}=\text{O}$  frequency as a function of the acid surface concentration in terms of dipolar interactions, at least in the case of the monolayers obtained by the *two-step* route or by the *one-step* route in the high-concentration regime.

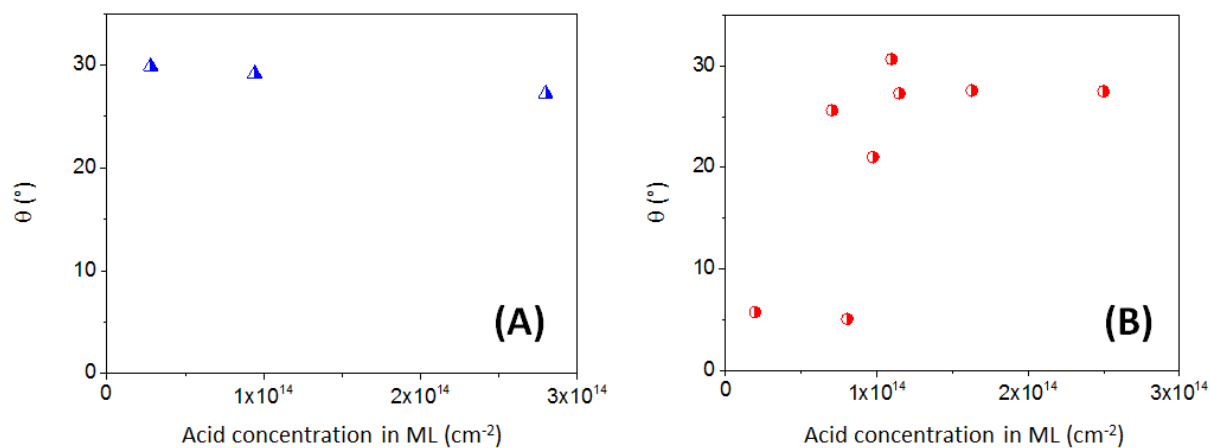


**Figure 1.39.** The average degree of the dynamic dipole of  $\nu\text{C}=\text{O}$  to surface,  $\theta$ , determined from the number vibrators which have dynamic dipole parallel ( $N_{\parallel}$ ) and perpendicular ( $N_{\perp}$ ) to the surface, versus acid content in ML prepared by the (A) *two-step* and (B) *one-step* routes.

A closer look on the derivation of  $N_{\parallel}$  and  $N_{\perp}$  reveals that a fluctuation of the experimental values of the interpreted absorbance in s- and p- polarization by an amount less than 10% can result in a change in  $\theta$  values from  $\sim 27^\circ$  to  $\sim 5^\circ$ . For surface prepared by the *one-step* route, in the low concentration range where infrared signals are rather weak, such a

fluctuation might be present, resulting, e.g., from an improper baseline adjustment in the fit procedure. Such an uncertainty does not appreciably change the surface concentration determination (associated to the sum  $N_{//} + N_{\perp}$ ), but much more sensitively affect the  $\theta$  value (derived from the ratio  $N_{\perp} / N_{//}$ ). The two very low  $\theta$  values found in the low-concentration range in Fig. 1.39B can therefore be considered as poorly reliable. Unfortunately, it also means that a quantitative account for the evolution of the  $\nu\text{C=O}$  frequency as a function of the surface acid concentration is likely out of reach, in view of the uncertainty on the determination of  $\theta$  in the low-concentration range.

Qualitatively, if the two abnormally low values of  $\theta$  in the Fig. 1.39B are ignored, the evolution of the  $\nu\text{C=O}$  frequency as a function of the acid surface concentration might be considered as constant in the low-concentration range, and weakly, linearly decreasing in the high concentration range. If one assumes that dipolar interactions govern the change in the  $\nu\text{C=O}$  frequency, such a behavior is consistent the presence of acid *nano*-domains in these *mixed* alkyl/carboxyalkyl layers. Schematically, the weak change at high acid concentration is associated with the contribution of dipolar interactions between vibrators located in different domains. When the concentration becomes low enough for considering the domains isolated from each other at the scale of dipolar interactions, only the dipolar interactions within one domain dominates and the  $\nu\text{C=O}$  frequency does not evolve anymore. The observation the two regimes (constant  $\nu\text{C=O}$  at low concentration and concentration-dependent  $\nu\text{C=O}$  at high concentration) requires that the size of the domains is actually in the few nm range,<sup>29,30</sup> in agreement with the *nano*-domains revealed by AFM. In this picture, it remains however unclear why the  $\nu\text{C=O}$  frequency of a pure acid layer obtained by the *two-step* route is significantly lower than that of a pure acid layer obtained by the *one-step* route. In both cases, the minute differences in the experimental values of  $\theta$  and of the surface concentration appear unable to account for the observed difference. Once again, we are touching here the limits of the quantitative interpretation.

The last observation concerns the huge broadening of the  $\nu\text{C=O}$  absorption band from 30 to 60  $\text{cm}^{-1}$  in the range of low acid surface concentration for surface prepared by the *one-step* route (Fig. 1.37B). A distribution of dipolar interaction seems unable to account for such a large effect. A possible explanation can tentatively be sought for in terms of inhomogeneous distributions of short-range interactions (e.g., hydrogen bonding or steric effects). Such a possibility requires that a large part of the  $\nu\text{C=O}$  vibrators experiences a situation where such inhomogeneities are present, like e.g., at the boundary of phase segregated domains. In view

of the small size of the *nano*-domains (less than 10 nm in diameter), a large fraction of the molecules located in the domain are actually close to the domain border (in a 8 nm diameter domain, ~45% of the molecules are located within less than 1 nm from the border). As previously mentioned these borders are obvious sources of inhomogeneities in the molecule environment, which could be the origin of the observed spectral broadening.

## Conclusions

In summary, *mixed* acid surfaces were successfully prepared by the *one-step* or *two-step* routes. These surfaces were then characterized by NC-AFM and FTIR measurements. FTIR is able to quantitatively assess the composition of the monolayers. *Mixed* alkyl/carboxyalkyl monolayers prepared by the *two-step* route exhibit a FTIR signature consistent with a homogeneous distribution of acid chains in the monolayer. On the opposite, *mixed* surfaces prepared by the *one-step* route from diluted acid ( $\leq 10\%$  *in vol.*) appear inhomogeneous. AFM phase images reveal the existence of *micro-* and *nano-*domains on these surfaces, and FTIR spectra exhibit a broadening of the  $\nu\text{C=O}$  band associated to the inhomogeneity of the acid chain environment. Quantitative comparison of AFM and FTIR results demonstrate that most of the acid chains are located in the *nano-*domains which might also explain the  $\nu\text{C=O}$  broadening. Therefore, the segregation of the acid chains in the *nano-*domains appears to satisfactorily account for most of the experimental results. However, the origin of this segregation remains to be identified. Moreover, a striking fact is the huge acid enrichment of the monolayers in the range when they are obtained from the grafting solution of low acid content, which persists at rather high acid dilution in the grafting solution. Preferential acid adsorption has been suggested in order to account for these observations. This aspect will be investigated in the next chapter.

## References

- (1) Finklea, H. O.; Hanshew, D. D. *J Electroanal Chem* **1993**, 347, 327.
- (2) Camillone, N.; Chidsey, C. E. D.; Liu, G. Y.; Scoles, G. *Journal of Chemical Physics* **1993**, 98, 3503.
- (3) Bertilsson, L.; Liedberg, B. *Langmuir* **1993**, 9, 141.
- (4) Mar, W.; Klein, M. L. *Langmuir* **1994**, 10, 188.
- (5) Sun, F.; Grainger, D. W.; Castner, D. G.; Leachscampavia, D. K. *Macromolecules* **1994**, 27, 3053.
- (6) Sondaghuethorst, J. A. M.; Schonberger, C.; Fokkink, L. G. J. *J Phys Chem-Us* **1994**, 98, 6826.
- (7) Dubois, L. H.; Nuzzo, R. G. *Annual Review of Physical Chemistry* **1992**, 43, 437.
- (8) Ulman, A. *Chemical Reviews* **1996**, 96, 1533.
- (9) Whitesides, G. M.; Laibinis, P. E. *Langmuir* **1990**, 6, 87.
- (10) Love, J. C.; Estroff, L. A.; Kriebel, J. K.; Nuzzo, R. G.; Whitesides, G. M. *Chemical Reviews* **2005**, 105, 1103.
- (11) Linford, M. R.; Chidsey, C. E. D. *J. Am. Chem. Soc.* **1993**, 115, 12631.
- (12) Linford, M. R.; Fenter, P.; Eisenberger, P. M.; Chidsey, C. E. D. *J. Am. Chem. Soc.* **1995**, 117, 3145.
- (13) Boukherroub, R. *Curr Opin Solid St M* **2005**, 9, 66.
- (14) Asanuma, H.; Lopinski, G. P.; Yu, H. Z. *Langmuir* **2005**, 21, 5013.
- (15) Voicu, R.; Boukherroub, R.; Bartzoka, V.; Ward, T.; Wojtyk, J. T. C.; Wayner, D. D. M. *Langmuir* **2004**, 20, 11713.
- (16) Faucheux, A.; Gouget-Laemmel, A. C.; de Villeneuve, C. H.; Boukherroub, R.; Ozanam, F.; Allongue, P.; Chazalviel, J. N. *Langmuir* **2006**, 22, 153.
- (17) Boukherroub, R.; Wayner, D. D. M. *J. Am. Chem. Soc.* **1999**, 121, 11513.
- (18) Aureau, D.; Ozanam, F.; Allongue, P.; Chazalviel, J. N. *Langmuir* **2008**, 24, 9440.
- (19) Higashi, G. S.; Chabal, Y. J.; Trucks, G. W.; Raghavachari, K. *Appl Phys Lett* **1990**, 56, 656.
- (20) Allongue, P.; de Villeneuve, C. H.; Morin, S.; Boukherroub, R.; Wayner, D. D. M. *Electrochim Acta* **2000**, 45, 4591.
- (21) Jae-Ho Lee, D. D., Srinivasa R; Raghavan *Langmuir* **2009**, 25, 1566.
- (22) Crossley, A.; King, D. A. *Surf Sci* **1977**, 68, 528.
- (23) Hollins, P.; Pritchard, J. *Surf Sci* **1979**, 89, 486.
- (24) Ortega, A.; Hoffman, F. M.; Bradshaw, A. M. *Surf Sci* **1982**, 119, 79.
- (25) Linke, R.; Curulla, D.; Hopstaken, M. J. P.; Niemantsverdriet, J. W. *Journal of Chemical Physics* **2001**, 115, 8209.
- (26) Noda, C.; Ewing, G. E. *Surf Sci* **1990**, 240, 181.
- (27) Mahan, G. D.; Lucas, A. A. *Journal of Chemical Physics* **1978**, 68, 1344.
- (28) Scheffler, M. *Surf Sci* **1979**, 81, 562.
- (29) Ozanam, F.; Chazalviel, J. N. *J Electroanal Chem* **1989**, 269, 251.
- (30) Crossley, A.; King, D. A. *Surf Sci* **1980**, 95, 131.

# Chapter 2

## Surface adsorption of undecylenic acid on H-Si surface

---

### Table of Contents

---

Introduction .....	65
2.1. Experimental procedures and results .....	69
2.1.1. <i>In situ</i> FTIR measurements.....	69
2.1.2. AFM Imaging .....	73
2.2. Discussion.....	75
Conclusions .....	79
References .....	80

---

## Introduction

In the previous chapter, the composition of mixed acid/decyl monolayers has been quantitatively investigated from FTIR analysis. If the fraction of carboxylic chains in the monolayers prepared by the *two-step* route (i.e. *via* ester grafting then subsequent hydrolysis) was found to be directly proportional to the carboxylic ester content in the grafting solution, very different results were obtained in the case of mixed monolayers prepared in *one-step* (i.e., *via* direct acid grafting). In the latter case, a non-linear dependence and an over concentration of grafted acid chains were evidenced on the surface, with respect to the acid content in solution. For *mixed* surfaces prepared in undecylenic acid/decene mixtures containing an acid fraction range from 0.1% to 1%, a particularly large acid excess was observed and the acid fraction is weakly dependent of the solution composition. For acid fractions from 20% to 30%, the surface concentration of grafted acid chain is significantly larger than the acid fraction in solution. Such an acid-enrichment in monolayer prepared by the *one-step* route had already pointed out by Faucheux *et al.*<sup>1</sup>

The surface enrichment calls for preferential grafting of the acid chains. Long chain carboxylic acids are amphiphilic molecules composed of two moieties exhibiting antagonist properties: a nonpolar hydrophobic tail (the long alkyl chain) and a hydrophilic head-group (the carboxyl group). This particular structure gives rise to peculiar physicochemical properties in solution that might be at the origin of the preferential grafting of the acid chains. In aqueous solution, because the hydrophobic alkyl chain/water contacts are energetically unfavorable,<sup>2-4</sup> long chain acids tend to self-organize with their polar carboxyl groups facing the solution, either at the interfaces or forming supramolecular structures in the medium (Fig. 2.1).

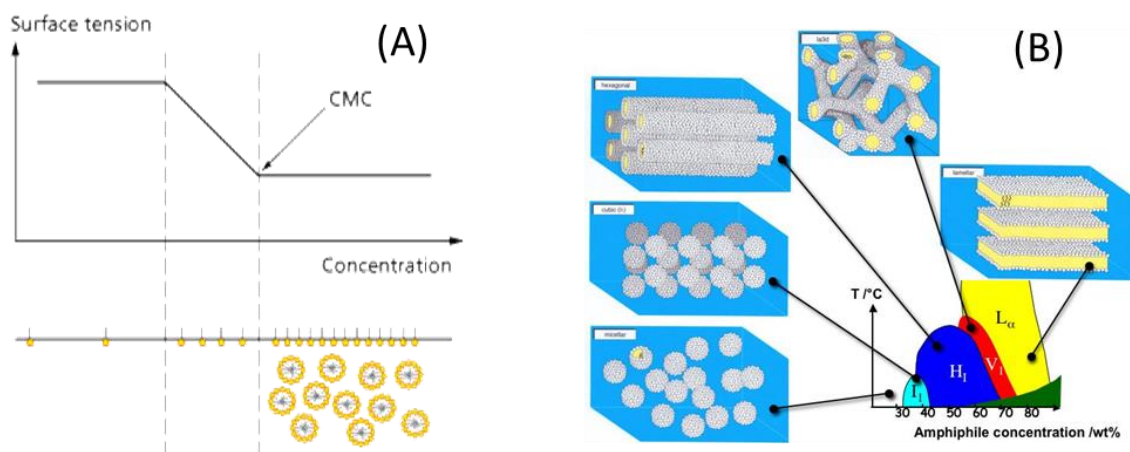


**Figure 2.1.** Schematic illustration of self-assembly process of amphiphilic molecules as a function of their concentration in aqueous solution. (A) Self organization at concentration below and above the critical micelle concentration (CMC). (B) Examples of supra-molecular arrangements at large amphiphilic concentration.

By analogy to what is going on in aqueous solutions, self-organization of long chain acids in non-polar solvent may be also anticipated, the driving force being in that case the low affinity of the polar carboxyl groups with the surrounding non-polar medium, i.e., decene in the present case. Therefore, the formation of reverse structures like reverse micelles, reverse lamellar phases, etc... are expected (Fig. 2.2).

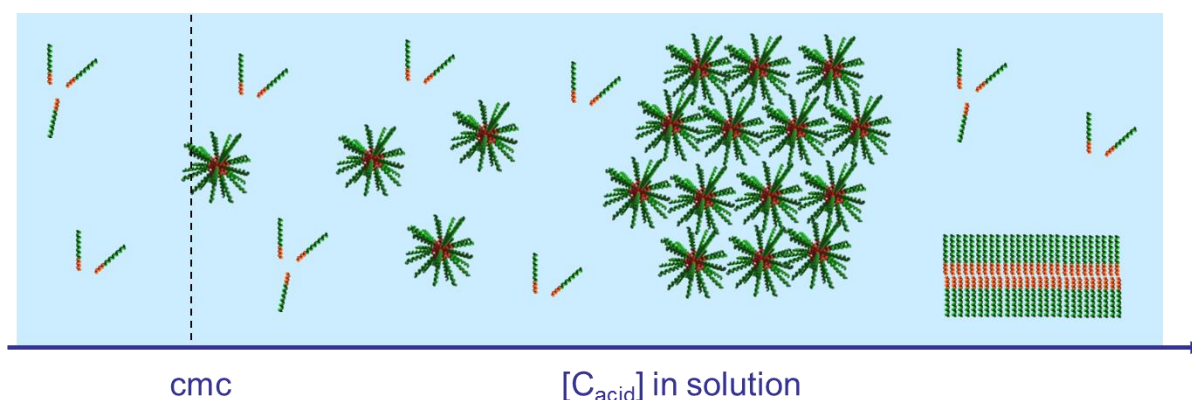


**Figure 2.2.** Schema of individual amphiphilics, their possible reverse micelle or reverse bilayer self-assembled structures in a non-polar solvent. The polar head of the amphiphilics and their hydrophobic tail are colored respectively in orange and green.

The properties of nonionic amphiphiles - *in general* -, and long chain acids - *more particularly* - in nonpolar media have been scarcely investigated and remain rarely documented. However some examples can be found in literature. Most often the studies report

on self-organization of amphiphiles in oil-rich / water mixtures. Additional amount of water (or other kinds of polar solvent) in the “oil” medium or intrinsic hydration water is considered as an essential component for the formation/stabilization and the size control of the reverse micelles. Recent works report the formations of nonionic reverse micelles of mono- or diglycerol fatty acid esters ( $\text{CH}_3\text{-(CH}_2\text{)}_{10}\text{-COOGly}$ ), even in absence of water or polar solvent added. From SAXS measurements, Shrestha and al. have evidenced the formation of spheroid micelles (radius of  $\sim 1.1$  nm) in aromatic or alkane solvents.<sup>5,6</sup> Besides these experimental works, one can find also a few theoretical works dealing with calculations of reverse micelle structure or for the prediction of the critical micelle concentration (CMC), the concentration above which formation of reverse micelles are expected.<sup>7-9</sup> All above mentioned works deal with aggregation of nonionic amphiphiles having hydrophobic tails comparable to undecylenic acid ( $\sim 10$   $\text{CH}_2$  units or more) but longer hydrophilic polar heads made of one or several oxyethylene ( $-\text{O-CH}_2\text{-CH}_2-$ ) or glycerol ( $-\text{O-CH}_2\text{-CHOH-CH}_2\text{O-}$ ) units, exhibiting stronger hydrophilic character than the carboxyl groups.

We have not found any reported data dealing with aggregation of long chain acids and the formation of supramolecular structures like reverse micelles in nonpolar medium. Only very old studies report on the formation of acid dimers and trimers. Such studies do not discard the possibility that higher aggregation number could exist.<sup>10</sup> Because amphiphile aggregation processes are known to be strongly dependent on the system (nature of the surfactant, of the solvent,  $T^\circ \dots$ ), is not a priori obvious that undecylenic acid might aggregate and form supra-molecular structures in decene.

Within the previous chapter, several results are however showing that self-assembly of undecylenic acid does exist in decene, in solution with acid fraction below  $\sim 20\%$ . The most obvious one is the doubtless observation of the large-size dome-like structures on the surfaces prepared in diluted solution (acid fraction  $\leq 10\%$ ). Their very peculiar spheroid shape and their composition (majority of carboxylic acid chains) strongly call for self-assembly process of undecylenic acid molecules. AFM images captured at intermediate rinsing step (Fig. 1.15) show to footprints corresponding to assemblies of nm-size aggregates that suggest that the large supra-molecular structures are actually made of assembly of these nm-size aggregates. The existence of individual nm-size structures has been also evidenced independently of the large structures in the case of the *extremely diluted* acid surface. Their density and size were found to be correlated to those of the *nano*-domains observed after the complete cleaning of the surface (Fig. 1.24). By comparison with self-organization processes in aqueous solution,

one can therefore anticipate that segregation/self-assembly of the acid chains at the H-Si/solution interface may also take place.

In this chapter, we have undertaken experimental studies aiming at getting further experimental insights into the phenomena leading to acid enrichment in the mixed MLs prepared by direct grafting of carboxylic acid chains. For this purpose, freshly prepared H-Si(111) surfaces were exposed in undecylenic acid/decene mixtures in ambient conditions, without UV illumination, in order to investigate whether specific adsorption of the undecylenic acid chains take place at the onset of the grafting. The interaction of undecylenic acid with the H-Si surfaces has been investigated by AFM and *in situ* FTIR analysis.

## 2.1. Experimental procedures and results

### 2.1.1. *In situ* FTIR measurements

The preparation of H-Si(111) surfaces has been already described in Section 1.1.1. The surface/solution interface was investigated by *in situ* FTIR measurements in ATR geometry (see Appendix II) using a Teflon fluid cell (Fig. 2.3).

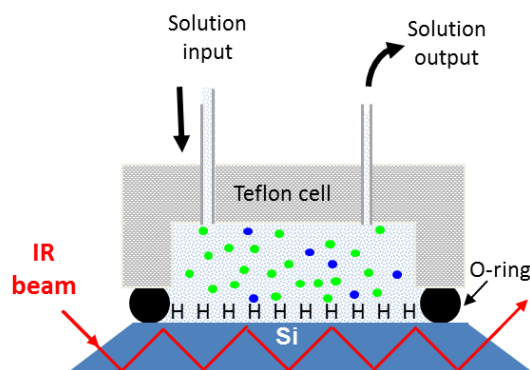


**Figure 2.3.** Experimental set-up for the *in situ* FTIR analysis in ATR geometry.

Freshly etched H-Si(111) silicon prism was mounted on the Teflon cell depicted in Fig. 2.3, in which one side of sample was exposed to undecylenic acid/decene mixtures. Experiments were performed with undecylenic acid/decene mixtures containing acid fraction range from 0.02 to 4% ( $1 < [\text{acid}] < 200 \text{ mM}$ ). Spectra in p- and s- polarization were recorded successively in each solution starting from the less concentration. In ATR geometry the IR beam is propagating inside the Si prism and is reflected at the Si/air and Si/solution interfaces because of the difference of refractive index ( $n_{\text{Si}} = 3.4$ ,  $n_{\text{air}} = 1$ ,  $n_{\text{acid/decene}} \sim 1.4$ ). Each reflection gives rise to an evanescent wave propagating in the external medium (air or solution) that can be absorbed by the medium. At wavenumber corresponding to acid-related carbonyl absorption ( $\nu_{\text{C=O}}$  at  $\sim 1715 \text{ cm}^{-1}$ ), the IR evanescent wave probes the solution over a distance of  $\delta = 445 \text{ nm}$  from the surface, which means that only undecylenic acid molecules contained in a finite layer of solution nearby the Si surface are probed by the IR evanescent wave.

Figure 2.4 displays the FTIR spectra of solutions with different acid content. The reference is the spectrum of the neat decene solution (0% undecylenic acid). The main IR bands observed on the spectra are the carbonyl band at  $1715 \text{ cm}^{-1}$  assigned to the  $\nu_{\text{C=O}}$  stretching mode of acid head-groups (Fig. 2.4A). The weak-intensity peak at  $1640 \text{ cm}^{-1}$  is

assigned to the stretching mode of the terminal C=C bonds of decyl and carboxyl chains. As expected, the intensity of the acid-related band  $\nu\text{C}=\text{O}$  increases with increasing undecylenic acid fraction in solution. The  $\nu\text{CH}_2$ ,  $\nu\text{CH}_3$  bands in the range  $2800\text{--}3000\text{ cm}^{-1}$  are assigned to the methylene units of the alkyl chains and the methyl end-groups of the decyl chains (Fig. 2.4B). As both undecylenic acid and decene have the same number of methylene units per chain, the intensity of the  $\nu\text{CH}_2$  bands remains unchanged. Only the disappearance of  $\text{CH}_3$  is observed at high enough acid concentration.

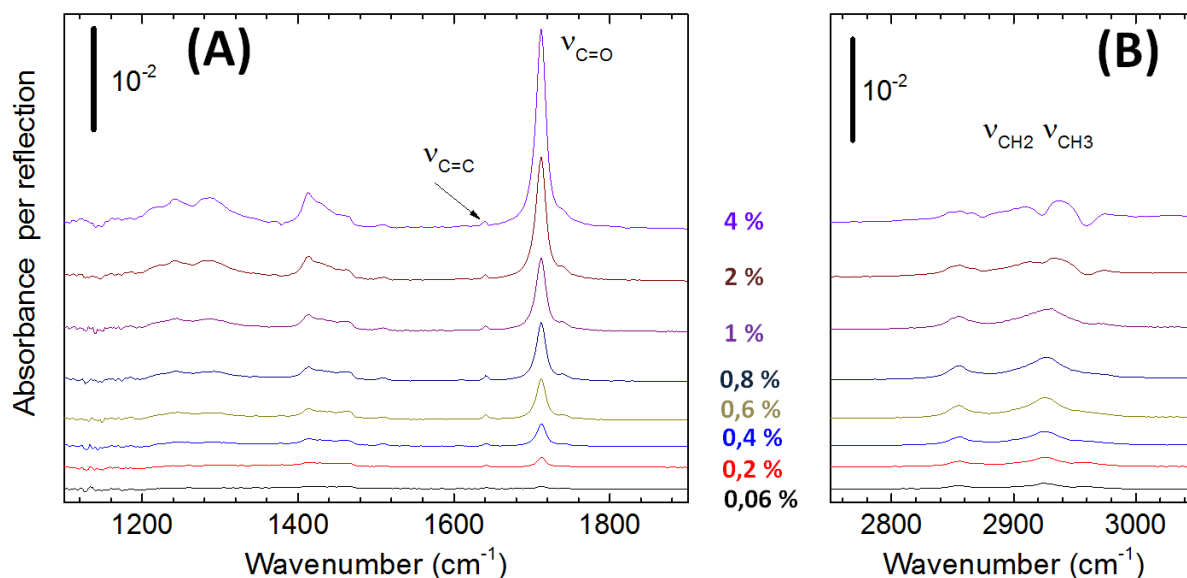


**Figure 2.4. FTIR spectra (s-polarization) in the  $1150\text{--}1850\text{ cm}^{-1}$  range (A) and in the  $2750\text{--}3050\text{ cm}^{-1}$  range (B) of undecylenic acid/decene mixtures containing acid content from 0.06 to 4% (from bottom to top). For all the spectra the reference is pure decene solution.**

The integrated absorbance in p- (blue ●) and s- (red ■) polarization of the  $\nu\text{C}=\text{O}$  peak is plotted as a function of the acid content in the solution in Fig. 2.5. The data are compared to those obtained from the calibration measurements (○ and □). As expected, the absorbance increases with the acid content, for both polarizations. However, contrary to the calibration measurements, for which the absorbance was found to be directly proportional to the acid concentration in solution, a different behavior is observed in the case of the undecylenic acid/decene // H-Si system. In this case two regimes are observed: a non-linear regime at low acid fractions ( $\leq 1\%$ ), and a linear regime above 1% acid content with a slope that is very close to that corresponding to the calibration measurements. Therefore, the behavior in the undecylenic acid/decene mixture may be interpreted as follows: physisorption of undecylenic acid chains occurs at the surface and the intensity of the  $\nu\text{CO}$  band is dominated by this

phenomenon at low acid fractions in solution. However, as soon as the previous phenomenon saturates and the concentration of acid chains in solution becomes large enough, only the molecules far from the surface contributes to the  $\nu_{\text{C=O}}$  bands and their corresponding contribution is proportional to the acid fraction in solution as in the calibration experiment (See Appendix II).

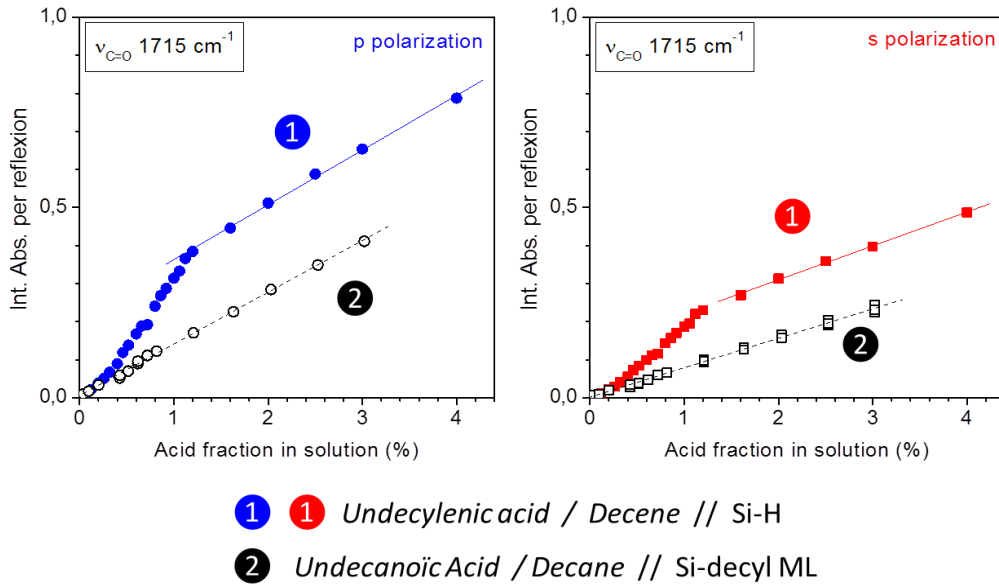


**Figure 2.5.** Integrated absorbance (per reflection) of the acid-related  $\nu_{\text{C=O}}$  band as a function of the acid content in solution, in p- (left) and s- (right) polarization. **Blue** and **red** data correspond to FTIR measurements of undecylenic acid / decene solution at H-Si/solution interface. These measurements are compared to measurements of undecanoic acid/decane solution at Si-decyl/solution interface, used for the calibration of  $\nu_{\text{C=O}}$  band (see Appendix II). For the calibration experiment, the surface of the silicon prism was passivated with a decyl ML to prevent physisorption of decanoic acid.

In order to determine the amount of *physisorbed* acids, we considered that the integrated absorbance plotted in Fig. 2.5 ( $Abs_{exp}^p$ ,  $Abs_{exp}^s$ ) splits into two contributions: the absorbance of acid chains in solution ( $Abs_{sol}^p$ ,  $Abs_{sol}^s$ ), and that of acid chains *physisorbed* on the surface ( $Abs_{surf}^p$ ,  $Abs_{surf}^s$ ):

$$Abs_{exp}^p = Abs_{sol}^p + Abs_{surf}^p \quad \text{Equation 2.2}$$

$$Abs_{exp}^s = Abs_{sol}^s + Abs_{surf}^s \quad \text{Equation 2.3}$$

The fitting of experimental data in the linear regime (acid fraction  $> 1\%$ ) gives the following equations:

$$Abs^p = 0.2188 + 0.142 F_{acid} \quad \text{Equation 2.4}$$

$$Abs^s = 0.1317 + 0.089 F_{acid} \quad \text{Equation 2.5}$$

with the absorbance  $Abs^p_{(F_{acid}=0)} = 0.2188$  and  $Abs^s_{(F_{acid}=0)} = 0.1317$  giving the absorbance of the *physisorbed* acid layer at saturation.

For each solution composition, the absorbance related to acid *physisorbed* on the surface  $Abs^p_{surf}$ ,  $Abs^s_{surf}$  were calculated using Eq. 2.6 and Eq. 2.7:

$$Abs^p_{surf} = Abs^p_{exp} - Abs^p_{sol} = Abs^p - 0.142 F_{acid} \quad \text{Equation 2.6}$$

$$Abs^s_{surf} = Abs^s_{exp} - Abs^s_{sol} = Abs^s - 0.089 F_{acid} \quad \text{Equation 2.7}$$

The integrated absorbance ( $Abs^{p,s}_{surf}$ ) related to *physisorbed* acid chains is plotted as a function of the acid fraction in solution in the Fig. 2.6A. The plots exhibit an isotherm shape. The absorbance increases with increasing acid fraction in solution from 0.02% to 1%. Above 1%, it reaches a saturation value.

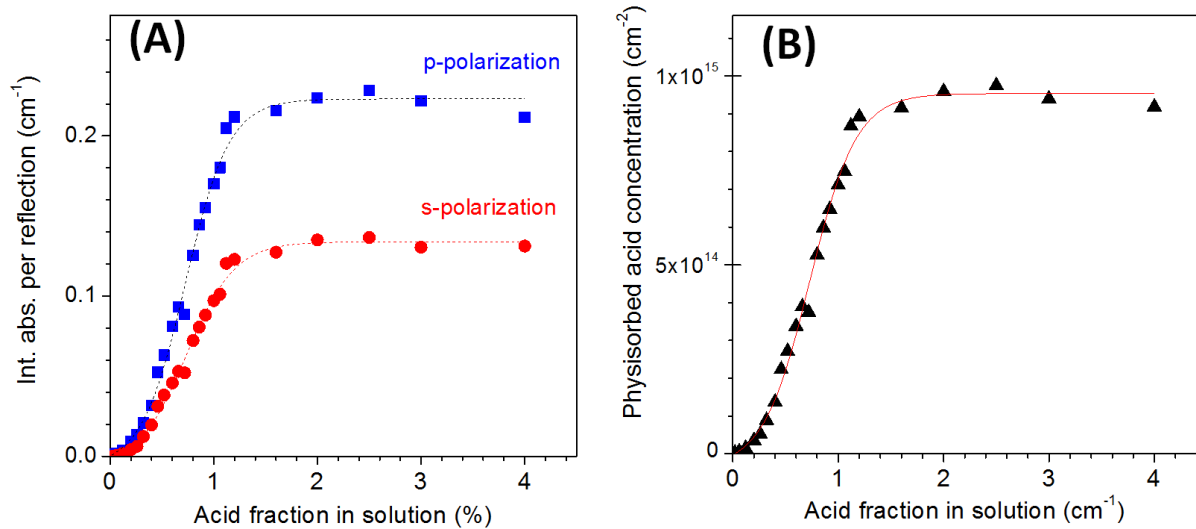


**Figure 2.6. (A) Integrated absorbance of *physisorbed* acid chains as a function of acid content in solution. (B) Surface concentration of acid chains physisorbed onto the H-Si surface exhibiting an adsorption isotherm shape.**

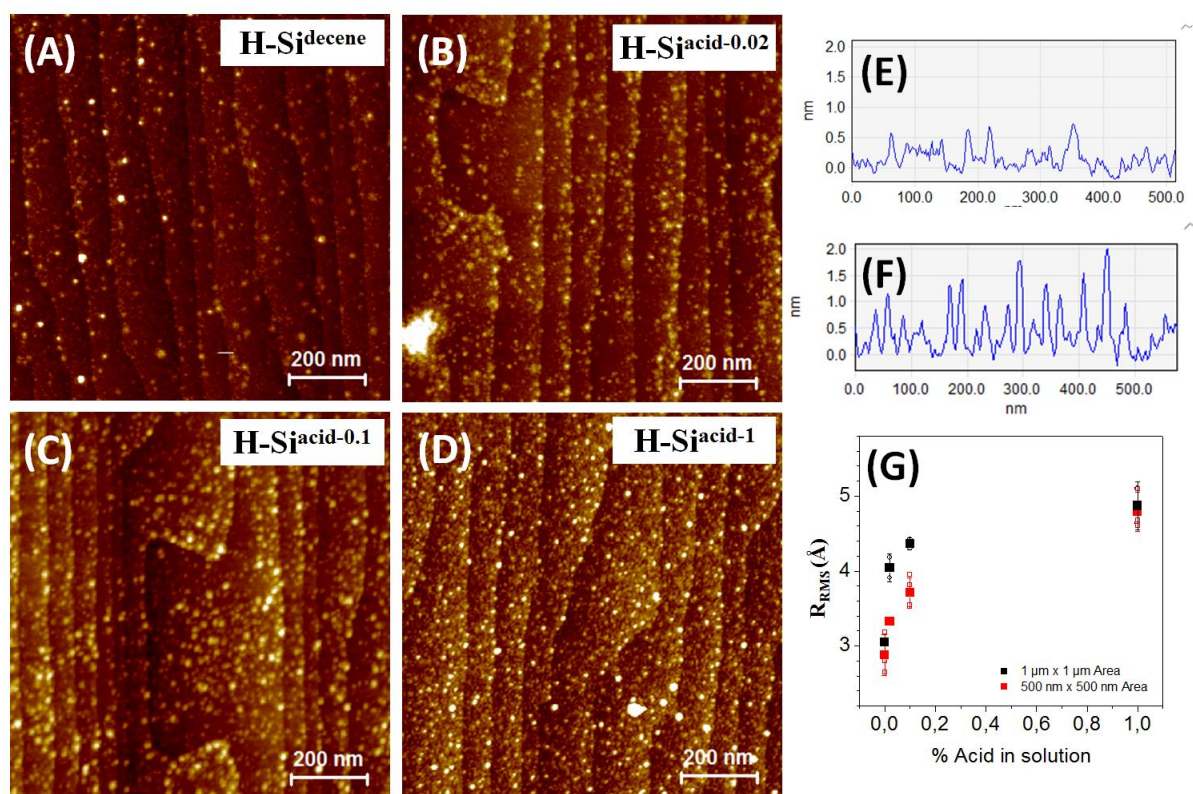
The integrated absorbance related to the *physisorbed* acids were transformed into a surface concentration using equations given in ref.<sup>11</sup>. We use the slope of the linear regression in Eq. 2.5 as a calibration coefficient allowing for relating the integrated absorbance in Fig. 2.6A to the concentration of acid chains physisorbed on surface. It should be stressed that using the calibration coefficient as-determined from the calibration measurements in

undecanoic acid / decane solution (see Appendix II) and taking into account the difference of experimental conditions (incident angle of IR beam, and dielectric properties of the solution) yields to concentration values very close to those obtained from the slope in Fig. 2.5 (~ 5% deviation). The calibrated adsorption isotherm is plotted in Fig. 2.6B. (black ▲) showing that the concentration of physisorbed acids increases upon increasing of the acid fraction in solution and saturates for acid fraction above 1%. At saturation, the acid concentration is  $\sim 9.5 \times 10^{14} \text{ cm}^{-2}$ , which is  $\sim 3$  times larger than that of grafted acid chains in a *pure* Si-acid monolayer. Therefore, the present results strongly suggest the formation of a multilayer.

### 2.1.2. AFM Imaging

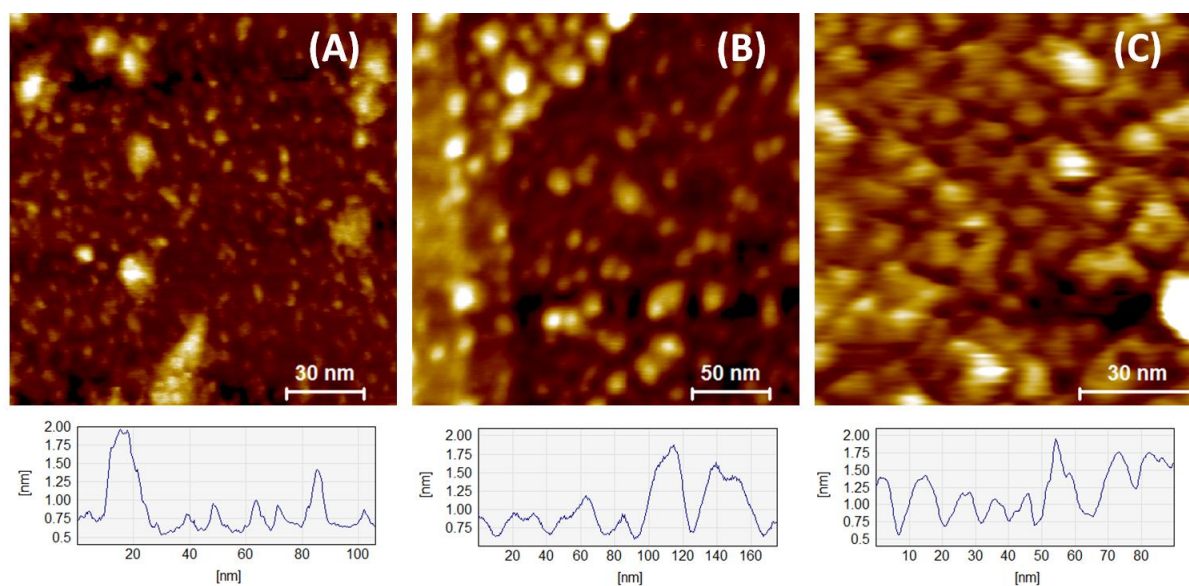
To try to get informations about the structure/arrangement of undecylenic acid molecules on the surface, H-Si(111) surfaces were exposed in undecylenic acid/decene mixtures and were characterized by AFM (*ex situ*). For these experiments freshly prepared H-Si surfaces were exposed in solutions containing acid fractions range from 0.02 to 1% (concentration range below and up to the saturation). One H-Si surface was exposed to pure decene as control experiment. All the surfaces were exposed 20mn in the solution and then rinsed briefly in dichloromethane for 5 min. Surfaces exposed in acid/decene mixtures will be named **H-Si<sup>acid-V</sup>**, with V corresponding to the acid fraction in the solution. The surface exposed to neat decene solution will be named **H-Si<sup>decene</sup>**.

Figure 2.7 display AFM images of the H-Si surfaces after exposure the different solutions. All images are represented with the same Z scale ( $\Delta Z = 3 \text{ nm}$ ). After exposure in neat decene (Fig. 2.7A), nm-size bright spots randomly distributed on surface are observed. Their small height ( $\leq 5 \text{ \AA}$ , see the cross section in Fig. 2.7E) suggests that they could be decyl chains lying on the surface. In the case of the surface exposed in acid/decene mixtures (using similar rinsing), one observes a much larger density of nm-size aggregates on the surface (Fig. 2.7B, C, D) and their average height 1 – 1.5 nm is also much greater (see the cross section in Fig. 2.7F). Moreover, their density increases with the acid content in solution. A quantitative grain analysis of the above images proved to be rather difficult because the shallow height of the surface features. An alternative way to account for the above trends, is plotting the surface roughness ( $R_{\text{RMS}}$ ) measured on the different surfaces as function of the acid content in solution (Fig. 2.7G). The increase of the  $R_{\text{RMS}}$  is in fact consistent with an increasing density of aggregates on the surfaces



**Figure 2.7.** AFM images of the surface topography of H-Si(111) surfaces exposed in the neat solution of decene (A) or in undecylenic acid/decene mixtures containing different acid fraction : (B) 0.02%, (C) 0.1% and (D) 1%. All images are plotted with the same Z-range ( $\Delta Z = 3$  nm). (E and F) Height profiles showing the peak-to-peak roughness on a single terrace of H-Si<sup>decene</sup> (from A) and H-Si<sup>acid-1</sup> surfaces (from D), respectively. (G) Surface roughness ( $R_{RMS}$ ) calculated on different images over  $1 \mu\text{m} \times 1 \mu\text{m}$  areas (black ■) or  $500 \text{ nm} \times 500 \text{ nm}$  areas (red ■), as a function of the acid content in solution.

Figure 2.8 displays AFM images at greater magnification of the three surfaces exposed to acid/decene mixtures. The evolution of the density of aggregates is correlated to the acid content in solution. Isolated spots of  $\sim 10$  nm lateral size and  $\sim 1$ - $1.5$  nm height can be measured on H-Si<sup>acid-0.02</sup> and H-Si<sup>acid-0.1</sup> surfaces (Fig. 2.8A and B). For H-Si<sup>acid-1</sup> surface (Fig. 2.8C), bright-spots form a quasi-continuous layer.



**Figure 2.8.** AFM images of the H-Si surfaces after exposure in solution containing 0.02% (A), 0.1% (B) and 1% (C) acid fraction (same surfaces as those above discussed). For each image, the cross sections show the height of the aggregates. Notice the increasing density when the acid content increases in solution.

## 2.2. Discussion

The above data clearly evidenced spontaneous segregation of undecylenic acid chains at the H-Si/solution interface. The adsorption phenomenon is detected for acid fraction in solution as low as 0.02% (1mM) and a surface saturation is observed for acid content above 1% (50 mM). At saturation, the surface concentration of *physisorbed* acid chains (undecylenic acid) is  $\sim 9 \cdot 10^{14} \text{ cm}^{-2}$ , which corresponds to one *equivalent* bilayer of close-packed acid carboxylic chains if we refer to the concentration of densely packed Langmuir Blodgett MLs or fatty acid SAMs onto gold surface.<sup>12,13</sup> Actually, within the concentration range investigated, the AFM images do not show the formation of a homogeneous layer but the formation of *nano*-aggregates.

The molecular organization on the Si surfaces *prior to grafting* (top) and *after grafting and cleaning* (bottom), as a function of undecylenic acid content in the grafting solution, is schematized in Fig. 2.9.

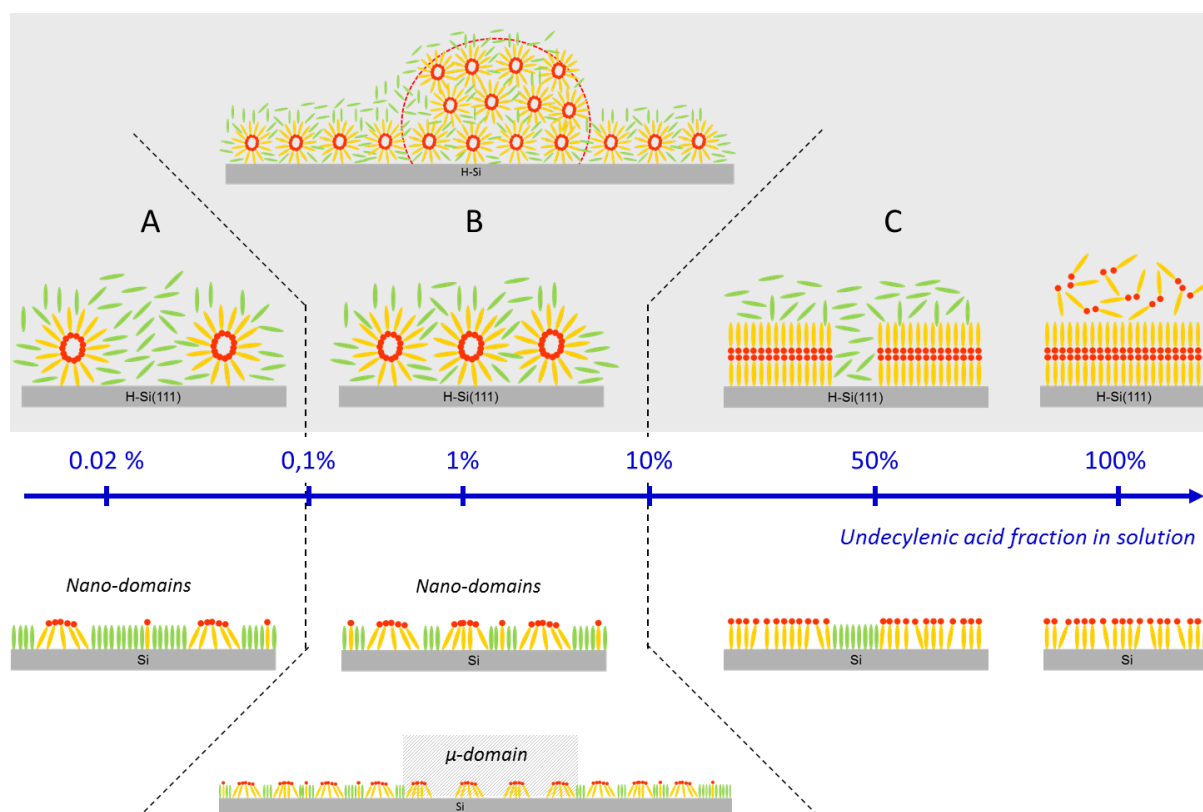


**Figure 2.9.** Suggested molecular organization on the Si surfaces *prior to grafting* (top) and *after grafting and cleaning procedures* (bottom) as a function of the undecylenic acid content in the grafting solution. The regions (A) and (B) refer to concentration range for which domains were observed on surface (*nano*-domains in zone A and *nano* and *micro*-domains in zone B). Green sticks represent the decene molecules. Undecylenic acid molecules are represented by orange sticks (alkyl chains) and red balls (acid tail groups).

In very diluted undecylenic acid solutions (zone A), reverse micelle are formed in solution and they spontaneously adsorb on the H-Si surfaces, *via* interactions of the outer alkyl chains with the hydrophobic H-Si surface. This leads to individual nm-size aggregates as was evidenced on AFM images after simple exposure of H-Si surfaces into undecylenic acid/decene mixtures (Fig. 2.7B). Upon grafting, these aggregates probably lead to the *nano*-domains observed in Fig. 1.24 since individual domains can be identified at sufficiently low acid chain concentration.

Increasing the acid fraction in solution (zone B) leads to an increase of the density of *nano*-aggregates *physisorbed* on the surface (Fig. 2.7C, D). Since *micro*-domains are occasionally observed we suggest that they are the footprints of larger supra-molecular structures (assembly of *nano*-aggregates of acid chains) observed prior to *surface wiping*. As

a result, the *micro*- domains would correspond to acid-rich areas depleted in decyl chains, by comparison to the surrounding molecular carpet.

Describing in details how the adsorbed reverse micelles and/or supramolecular structures observed in Fig. 2.9 (prior to grafting) leads to the *nano*- and *micro*-domains observed in phase images (after grafting) would be challenging. Making a one to one correspondence appears reasonable because the typical size of *nano*-domains is close to the diameter of aggregates (Fig. 1.24) and the density of *nano*-domains increases upon increasing of the acid fraction in solution, which makes difficult to resolve them in the AFM images (Fig. 2.7). It makes sense that a large fraction of the acid chains involved in the adsorbed reverse micelles will be first grafted, because these are the closest to the surface. To confirm this scenario, we compare the above adsorption isotherm and the evolution of the surface concentration of grafted acid chains as a function of the undecylenic acid fraction in solution (Fig. 2.10). The colored zones (A and B) recall the concentration range for which domains were observed (*nano*-domains for very dilute solutions corresponding to zone A, and *nano*- and *micro*-domains for the concentration range corresponding to zone B).

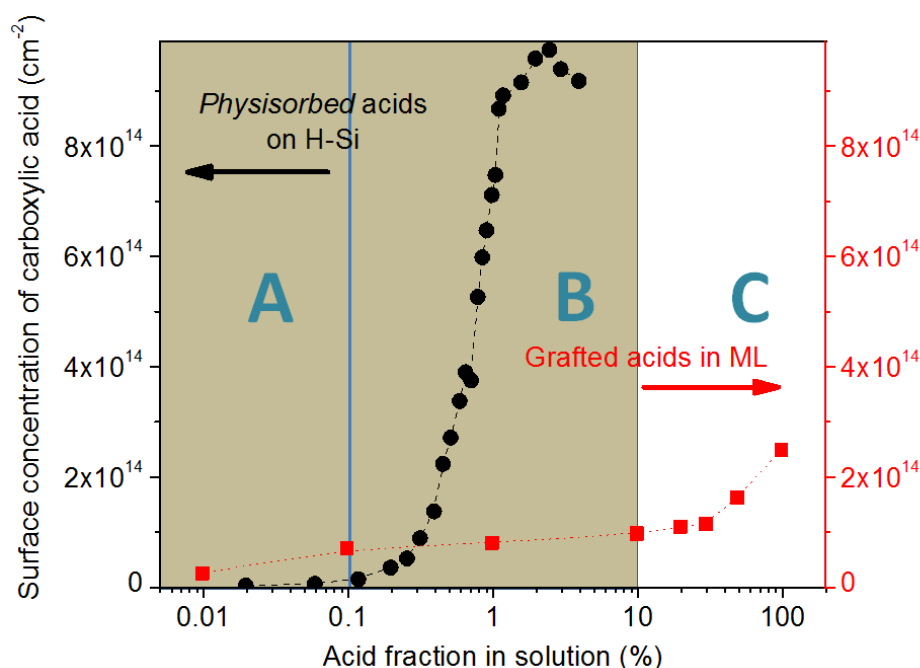


**Figure 2.10.** Concentration of acid chains on Si surfaces as function of the acid content in undecylenic acid/decene mixtures. The black dots (●) correspond to surface concentration of *physisorbed* undecylenic acids on H-Si surfaces, the red squares (■) correspond to acid chains concentration in the MLs prepared by the *one-step* route and after the *complete wiping* procedure.

Figure 2.10 clearly shows that there are enough acid chains next to the surface to generate an acid-rich ML when the acid fraction exceeds 0.03 %. This essentially explains the quasi-constant composition of the MLs in the concentration range corresponding to zone B. Therefore, the formation of a dense layer of nano-aggregates prior to, or at the onset of, the grafting process appears as the main factor governing the composition and the structure of monolayers prepared in undecylenic acid/decene mixtures containing a low acid fraction.

For an acid-chain fraction larger than 10%, (*zone C*) the concentration of acid chains in the MLs increases nearly linearly upon increasing of the acid fraction in solution (Fig. 1.35). In such acid-rich solutions the formation of bilayers instead of the physisorption of nano-aggregates may be anticipated. This would be consistent with the fact that no supra-molecular structure has been evidenced in the case of the MLs prepared in solution with acid content above 10%.

## Conclusions

In this chapter, we tried to better understand the state of surface in solution prior to the grafting procedure. The FTIR measurements of undecylenic acid/decene mixtures containing acid fraction range from 0.02% to 4% have evidenced the adsorption of acid chains on hydrogenated H-Si surfaces. Above 1%, the adsorption of acid chains reaches a saturation level corresponding to an acid concentration of  $\sim 9.5 \times 10^{14} \text{ cm}^{-2}$ . From AFM characterizations, we have evidenced the existence of *nano*-aggregates of acid chains in decene. The properties of the mixture suggest that they are reverse micelles of acid chains. They were preferential adsorbed on the hydrogenated silicon surface and their density increases upon increasing of the acid fraction in solution. This specific adsorption is responsible for the acid enrichment of the surface during the grafting. Our results indicate that the composition and the structure of the MLs prepared in dilute acid solutions are governed by the formation of supra-molecular structures in solution and the spontaneous adsorption of *nano*-aggregates onto the H-Si surfaces, prior to or at the onset of the monolayer grafting.

## References

- (1) Faucheux, A.; Gouget-Laemmel, A. C.; de Villeneuve, C. H.; Boukherroub, R.; Ozanam, F.; Allongue, P.; Chazalviel, J. N. *Langmuir* **2006**, *22*, 153.
- (2) Tanford, C. *Science* **1978**, *200*, 1012.
- (3) Lum, K.; Chandler, D.; Weeks, J. D. *J Phys Chem B* **1999**, *103*, 4570.
- (4) Chandler, D. *Nature* **2002**, *417*, 491.
- (5) Shrestha, L. K. *Self-Organized Surfactants Structures*; Wiley-VCH, 2010.
- (6) Shrestha, L. K.; Shrestha, R. G.; Aramaki, K.; Hill, J. P.; Ariga, K. *Colloids and Surfaces a-Physicochemical and Engineering Aspects* **2012**, *414*, 140.
- (7) Allen, R.; Bandyopadhyay, S.; Klein, M. L. *Langmuir* **2000**, *16*, 10547.
- (8) Voutsas, E. C.; Flores, M. V.; Spiliotis, N.; Bell, G.; Halling, P. J.; Tassios, D. P. *Industrial & Engineering Chemistry Research* **2001**, *40*, 2362.
- (9) Flores, M. V.; Voutsas, E. C.; Spiliotis, N.; Eccleston, G. M.; Bell, G.; Tassios, D. P.; Halling, P. J. *Journal of Colloid and Interface Science* **2001**, *240*, 277.
- (10) Levy, O.; Markovits, G. Y.; Perry, I. *J Phys Chem-US* **1975**, *79*, 239.
- (11) Faucheux, A.; Gouget-Laemmel, A. C.; Allongue, P.; de Villeneuve, C. H.; Ozanam, F.; Chazalviel, J. N. *Langmuir* **2007**, *23*, 1326.
- (12) Ulman, A. *An introduction to Ultrathin organic films from langmuir-Blodgett to self assembly*; Academic Press Limited: Londn, 1991.
- (13) Ulman, A. *Chemical reviews* **1996**, *96*, 1533.

# Chapter 3

## Photoswitching properties of fulgimides in solution

---

### Table of Contents

---

Introduction .....	82
3.1. Experimental illumination set-up and procedures.....	84
3.2. Photoswitching of amino-fulgimide in solution.....	85
3.2.1. UV-Vis absorption spectra of C- and E/Z-forms.....	86
3.2.2. Composition at PSSs .....	88
3.2.3. Kinetics of photoswitching .....	90
3.2.3.1. Dynamic of photo-isomerization during illumination cycles.....	90
3.2.3.2. Time constants over successive UV/Vis illumination cycles .....	92
3.2.3.3. Rate constants as a function of light intensity.....	93
3.3. Discussion .....	93
3.3.1. Photoswitching mechanism .....	93
3.3.2. Kinetics of reactions .....	95
3.3.3. Photo-isomerization cross-section .....	96
3.3.4. Comparison between UV and Vis isomerization cross-sections .....	97
Conclusions .....	99
References .....	100

---

# Introduction

Organic photochromes are bi-stable molecular systems that may exist in two thermodynamically stable states (A and B) and are capable of interconversion ( $A \rightleftharpoons B$ ) under the action of light. More specifically, under illumination these compounds undergo chemical transformations (bond cleavage/formation or cis/trans isomerization) that generally is accompanied by changes of their physico-chemical properties (optical absorption, refractive index, dipolar moment..).<sup>1</sup>

Among different classes of organic photochromes (spiropyrans and spirooxazines, azobenzenes, diarylethenes, ...) indolyfulgides and their derivative indolyfulgimides exhibit interesting properties that make them good candidates for use as optical molecular switches for various field of applications (opto(nano)electronics, chem/biosensors, microfluidics...)<sup>2-6</sup>

Indolyfulgimides exhibit three thermally stable isomers: two colored open E- and Z-forms corresponding to trans and cis isomers and one colorless closed C-form. UV/Vis illumination induces ring-closure/ring-opening reactions leading to the coloration/bleaching process, according to isomerization scheme in Fig. 3.1. Under UV illumination, the ring-closure  $E \rightarrow C$  reaction is not the solely possible reaction since cis-trans  $E \rightleftharpoons Z$  isomerization may also take place.

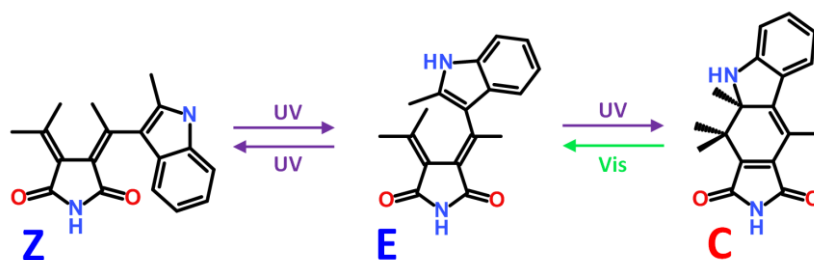


**Figure 3.1. Photochromism of indolyfulgimide under Vis/UV irradiation.**

The photoswitching properties of indolyfulgimides have been investigated in solution for more than one decade.<sup>7-13</sup> These compounds exhibit pronounced photochromism related to the electrocyclic ring-opening ( $C \rightarrow E$ ) and ring-closure ( $E \rightarrow C$ ) reactions which induce strong changes in the UV and Vis absorption spectra. The three E, Z and C isomers all absorb in the UV. The C-isomers exhibit an additional broad absorption band in the Vis spectral range (Fig. 3.2). The existence of well separated absorption bands in the UV and Vis range allows for an individual addressing of either type of isomers. The isomers are thermally stable and exhibit

high photo-chemical stability during repeated UV/Vis illumination cycles. High conversion efficiency due both to well separated absorption bands and high reaction quantum yield, is also reported as well as ultrafast reaction dynamics.<sup>14-22</sup>

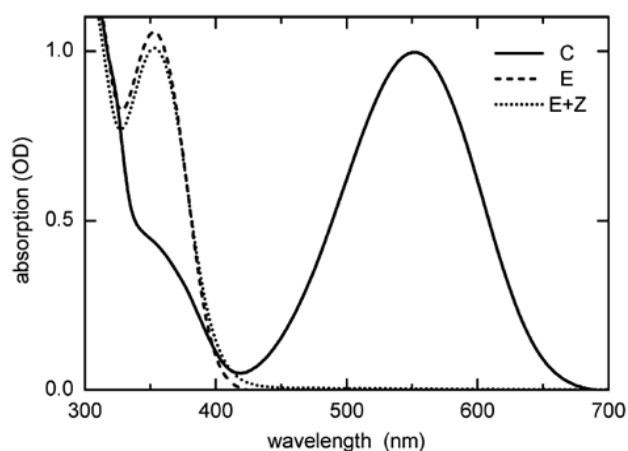


**Figure 3.2.** Absorption spectra of the pure C-form (black line), of the pure E-form (black dashed) and of a mixture between the E- and the Z-form (black dotted). Figure is taken from ref<sup>23</sup>.

The purpose of this chapter is to investigate the photo-isomerization of indolylfulgimide compounds substituted with an amino ethyl linker. These compounds have been specifically synthesized in order to allow for the covalent coupling of indolylfulgimide groups on functionalized Si surfaces through aminolysis reaction. The anchorage of fulgimide ML onto functionalized Si surfaces and their photo-induced isomerization will be discussed in the next chapters.

The photoswitching properties of the amino ethyl indolylfulgimide precursors in solution have been investigated by UV-Vis spectroscopy.

### 3.1. Experimental illumination set-up and procedures

The photo-isomerization of fulgimide compounds have been investigated in solution prior to their immobilization on the Si surfaces. An illumination set-up was specifically designed in order to illuminate *in situ* the quartz cell containing the fulgimide solution (1ml), inside the UV-Vis spectrophotometer (Fig. 3.3). UV ( $\lambda=365$  nm) or Vis ( $\lambda= 525$  nm) LEDs were used as light sources. The light flux can be tuned by inserting neutral filter (36% transmission) on the beam path.

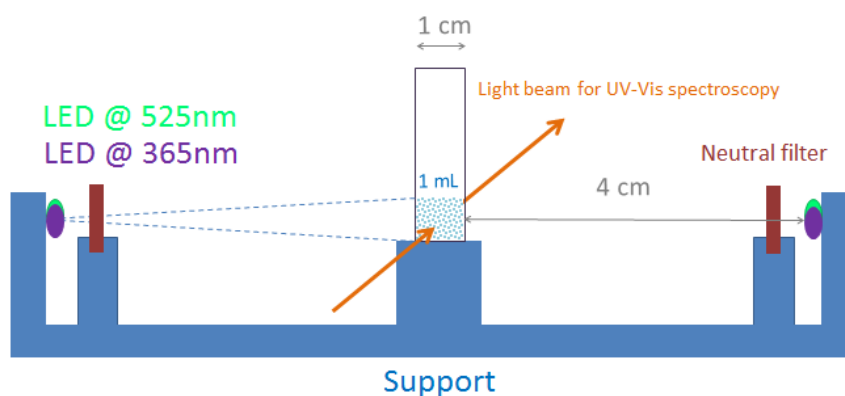


**Figure 3.3.** Experimental set-up for *in situ* Vis or UV illumination in the UV-Vis spectrophotometer. Vis ( $\lambda = 525$  nm, viewing half angle of  $\pm 8^\circ$ ) and UV ( $\lambda=365$ nm, viewing half angle of  $\pm 10^\circ$ ) LEDs were used as light source.

The flux of light beam was measured by a photodiode S2387-R33 purchased from Hamamatsu operating in reverse bias at 24 V. This photodiode has a photosensitive area of  $2.4\text{mm} \times 2.4\text{mm}$  and a photosensitivity of 0.3 and  $0.17 \text{ A W}^{-1}$  at 525 nm and 365 nm, respectively. The current measured is then converted to the light power and photon flux. Note that the solution received light from both sides so that the light power and flux need to be multiplied by two. The results are summarized in Table 3.

	Photon energy (J)	Quartz Cuvette Transmission	Current measured in reverse bias $\mu\text{A}$	Light power $\text{mW cm}^{-2}$	Photon flux $\text{cm}^{-2} \text{s}^{-1}$
Vis Light	$3.89 \times 10^{-19}$	0.87	680	39	$7.3 \times 10^{16}$
UV Light	$5.45 \times 10^{-19}$	0.86	73	7.5	$0.86 \times 10^{16}$

**Table 3.1. Characteristics of the experimental illumination set-up used for the study of fulgimide in solution.**

To investigate the photo-isomerization properties of fulgimides, solutions containing solely E/Z and C forms were prepared ( $13\mu\text{M}$  in acetonitrile) and have been illuminated with UV (365 nm) or Vis (525 nm) LEDs. In practice, UV-Vis spectra were recorded after successive short illuminations. The light was turned off during the recording of spectra between two illumination sequences. Short-time illuminations were repeated until a photostationary state (PSS) was reached.

In the following, solution containing only E/Z-forms or C-forms in acetonitrile is named **Fulgi-E/Z** or **Fulgi-C** solution, respectively.  $\text{PSS}_{\text{UV}}$  or  $\text{PSS}_{\text{Vis}}$  will refer to the PSS reached after UV or Vis illumination sequence. One illumination cycle is defined from the “prior to illumination” state to the PSS. For example, an as-prepared Fulgi-C solution is illuminated under Vis light for C→E reaction until it reaches the  $\text{PSS}_{\text{Vis}}$  of the first cycle illumination or the **first**  $\text{PSS}_{\text{Vis}}$ . Subsequently, the solution is illuminated under UV light for the second cycle illumination and it reaches the **second**  $\text{PSS}_{\text{UV}}$  at the end of the second cycle.

## 3.2. Photoswitching of amino-fulgimide in solution

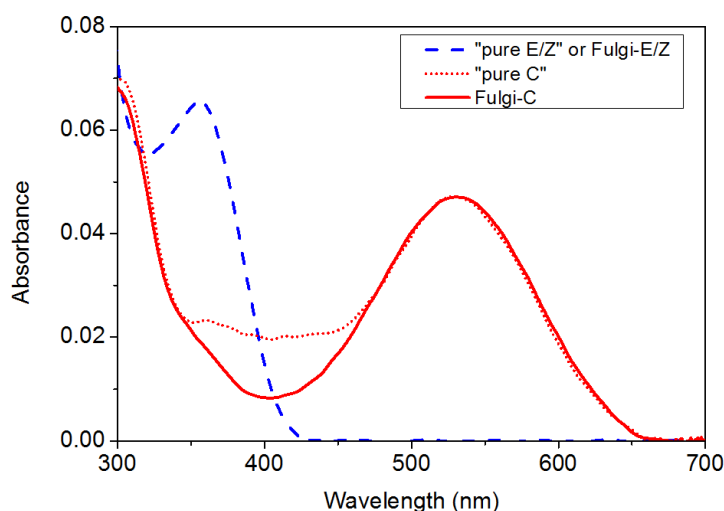
The solution compositions of *pure* solutions were firstly determined via NMR measurements (see Appendix IV). Their analysis show that “pure C” contains only C-forms with no trace of E/Z-forms and “pure E/Z” contains  $\sim 75/25/0$  of E/Z/C-forms (Table 3.2). These results will be used for the further determination of isomeric ratio at PSSs.

	C-forms	E-forms	Z-forms
“pure E/Z”	0 %	75 %	25 %
“pure C”	100 %	0 %	0 %

**Table 3.2.** C/E/Z isomeric ratios in solution “pure E/Z” and “pure C” as determined from NMR analysis.

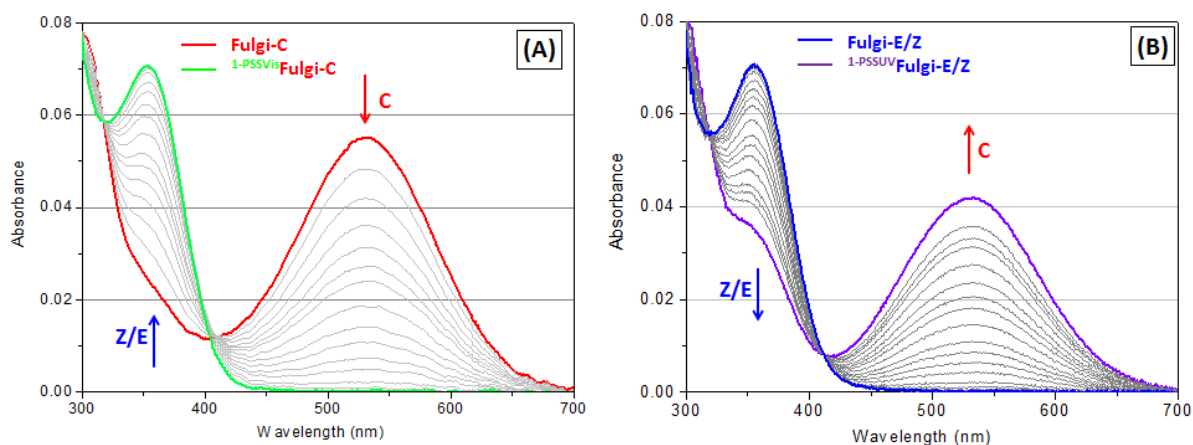
### 3.2.1. UV-Vis absorption spectra of C- and E/Z-forms

Figure 3.4 shows the UV-Vis absorption spectra “pure C” (red dotted line) and “pure E/Z” (blue dashed line) solutions. The spectrum of as-prepared “pure C” solution exhibits a broad absorption in the range  $400 \pm 50$  nm. This broad absorption disappears after the first UV irradiation cycle of the solution. Subsequently, the solution spectrum evolves between two reproducible stationary states  $PSS_{UV}$  and  $PSS_{Vis}$ . The 400 nm band is then thought to be associated with some specific contributions of the initial pure C solution (specific conformation or impurity) which is destroyed upon UV irradiation. On the basis of this assumption, the line shape of the 400 nm band can be obtained by subtracting the spectrum of the first  $PSS_{Vis}$  (recorded before the first UV irradiation) from the spectrum of the third  $PSS_{Vis}$  (recorded after the first UV irradiation). The spectrum of the Fulgi-C solution (Fig. 3.4, red line) was then drawn from the spectrum of the as-prepared “pure C” solution by subtracting to the spectrum of the band at 400 nm. The obtained spectrum turns out to be very close to that given in the literature<sup>23</sup> (Fig. 3.2). This similarity appears as a reasonable check of the previous assumption. On the opposite, no irreversible change is detected during the first illumination cycle of a “pure E/Z” solution. The initial spectrum is identical to that reported in the literature<sup>23</sup>. Therefore, the spectrum of Fulgi-EZ solution will be identified to be the spectrum of the as-prepared “pure E/Z” solution.



**Figure 3.4.** Absorption spectra in the UV/Vis spectral range of the “pure E/Z” solution or Fulgi-E/Z solution (blue dashed line), of the “pure C” solution (red dotted line) and of the Fulgi-C solution (red line).

In order to study the evolution of the UV/Vis absorption spectrum of a “pure C” solution, it is important to take into account the presence of the unwanted broad absorption at ~400 nm before the first UV irradiation. This contribution needs to be subtracted from the spectra recorded before the first UV irradiation (like for obtaining the Fulgi-C spectrum from the pure-C spectrum). When such a correction is performed, the evolution of the spectra during the first Vis irradiation exhibits a nearly perfect isosbestic point at ~400 nm (Fig. 3.5A), a further check of the relevance of the applied correction. As expected, the evolution of the spectrum of a “pure-EZ” solution during the first UV irradiation similarly exhibits a perfect isosbestic point in the absence of any data treatment (Fig. 3.5B).



**Figure 3.5.** Evolution of UV/Vis absorption spectra of “pure C” (A) and “pure E/Z” (B) solutions during the first Vis or UV illumination cycle. Up-down and down-up arrows point out, respectively, a diminution or a raise of the bands intensity. Red and green spectra (A) correspond respectively to the spectra of the “pure C” solution prior to illumination and at PSS<sub>Vis</sub>. Blue and purple spectra on (B) correspond to the spectra of the “pure E/Z” solution prior to illumination and at PSS<sub>UV</sub>, respectively.

### 3.2.2. Composition at PSSs

The spectrum of the PSS<sub>Vis</sub> solution obtained upon visible irradiation of the Fulgi-C solution after correction for the 400 nm band shown in Fig. 3.5A is identical to that of the Fulgi-E/Z solution shown in Fig. 3.4. Therefore, in agreement with previous reports from the literature, only E- and Z-forms appears to be present in the PSS<sub>Vis</sub>. On the contrary, the spectrum of the solution at PSS<sub>UV</sub> contain superficial contributions at ~365 and ~525 nm, suggests that E/Z- and C- forms are present in the solution. As a matter of fact, the spectrum of the PSS<sub>UV</sub> solution is nicely reproduced as the linear superposition of the C-form spectrum (Fig. 3.4, red line) (76%) and the E/Z-form spectrum (Fig. 3.4, blue dashed line) (24%). Since according to Beer-Lambert’s law, absorbance is proportional to the concentration in absorbers, the PSS<sub>UV</sub> solution is found to be a mixture of 76% of C-forms and 24% of E/Z-forms.

The composition of the first PSS of both solutions quantified by UV-Vis absorbance is shown in Table 3.3. The results obtained from HPLC analysis are also indicated for comparisons (HPLC measurements were carried out in K. Rück-Braun’s group at the TU in Berlin). Except that E- and Z-forms cannot be distinguished from UV-Vis absorbance results, the ratio of C and E/Z-forms are found to be nearly the same according to the two

characterizations. The results show that the photoswitching is rather efficient with conversion rates of 77% under UV ( $E \rightarrow C$ ) and 100% under Vis illumination ( $C \rightarrow E$ ).

	UV-Vis spectroscopy		HPLC		
	C-forms	E/Z-forms	C-forms	E-forms	Z-forms
1 <sup>st</sup> PSS <sub>UV</sub> of “pure E/Z”	76 %	24 %	77 %	21 %	2 %
1 <sup>st</sup> PSS <sub>Vis</sub> of “pure C”	0	100 %	0 %	96 %	4 %

**Table 3.3.** C/E/Z isomeric fractions in solution at PSS<sub>UV</sub> and PSS<sub>Vis</sub> as determined from different techniques: UV-Vis spectroscopy or HPLC.

Fulgi-C and Fulgi-E/Z solutions have similarly been characterized by UV-Vis absorbance after successive UV and Vis illumination cycles. Figure 3.6A and B show the fraction of E/Z- and C-forms at PSSs after successive UV/Vis illumination cycles. The starting solutions were *pure* C- (Fig. 3.6A) or E/Z-forms solutions (Fig. 3.6B). The photoswitching shows no fatigue for either case. Reversible photoswitching and reproducible composition of the PSSs were observed which indicate the absence of sizeable photofatigue. As after the first cycle, at PSS<sub>Vis</sub>, complete transformation  $C \rightarrow E$  is observed while, at PSS<sub>UV</sub>, only 76-78 % of C-forms are present.

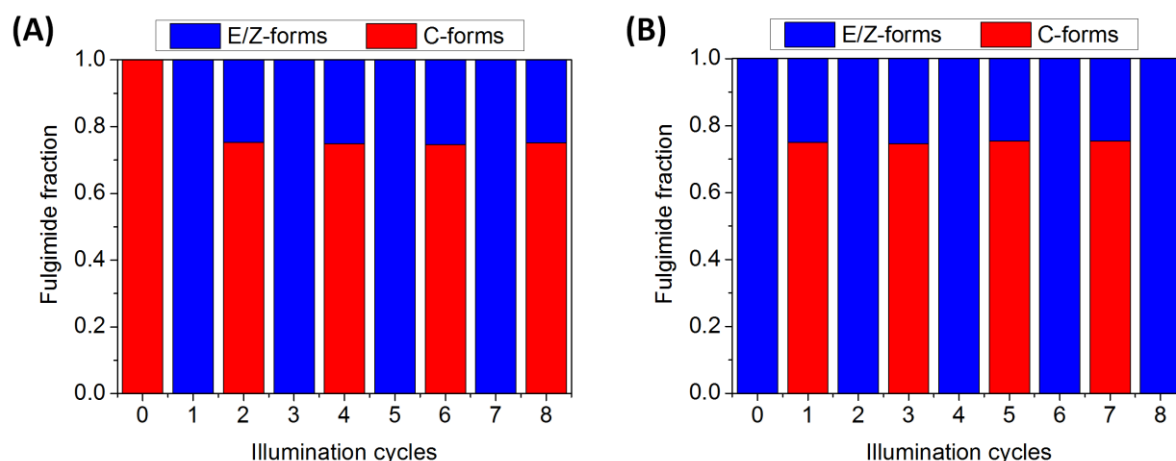


**Figure 3.6.** Fraction of C- (red) and E/Z-forms (blue) at PSS after successive UV/Vis illumination cycles starting from *pure* Fulgi-C (A) or *pure* Fulgi-E/Z (B) solutions.

### 3.2.3. Kinetics of photoswitching

#### 3.2.3.1. Dynamic of photo-isomerization during illumination cycles

The *in situ* illumination set-up in the UV-Vis spectrometer and the capacity of determining the solution compositions have been used for studying the kinetics of fulgimide photo-isomerization in solution. The study was carried out by measuring the concentration of C- and E/Z-forms during successive short times of an illumination cycle.

Figure 3.7A shows the evolution of the concentration of C- ( $\blacktriangle$ ) and E/Z-forms ( $\bullet$ ) during the first two illumination cycles of a Fulgi-C solution (14.4  $\mu\text{M}$ ). During the first Vis illumination cycle, the concentration of C-forms decreases continuously and that of E/Z-forms increases simultaneously. It reveals the process of C $\rightarrow$ E isomerization (ring-opening reaction). After  $\sim 7$  min of illumination the  $\text{PSS}_{\text{Vis}}$  is reached, the solution is totally depleted in C-form. During the subsequent UV illumination cycle, a reverse process is observed, i.e., the disappearance of E/Z-forms in solution and the reappearance of C-forms. The E $\rightarrow$ C isomerization is not complete and at  $\text{PSS}_{\text{UV}}$  (after  $\sim 15$  min), the solution is composed of a mixture of 11.3  $\mu\text{M}$  C-forms and 4.0  $\mu\text{M}$  E/Z-forms (C:E/Z = 0.74:0.26).

Similar measurements have been done for an as-prepared Fulgi-E/Z solution (Fig. 3.7B). The behavior during the first UV illumination cycle looks quite similar to that observed during the second UV illumination cycle found in Fig. 3.7A.  $\text{PSS}_{\text{UV}}$  is reached after  $\sim 15$  min and the solution is composed of a mixture of 10.4  $\mu\text{M}$  C-forms and 4.1  $\mu\text{M}$  E/Z-forms (C:E/Z = 0.72:0.28). After subsequent Vis illumination cycle, the concentration of C-form falls to zero.  $\text{PSS}_{\text{Vis}}$  is reached in 5 min and a *pure* solution composed of only E/Z forms is obtained.

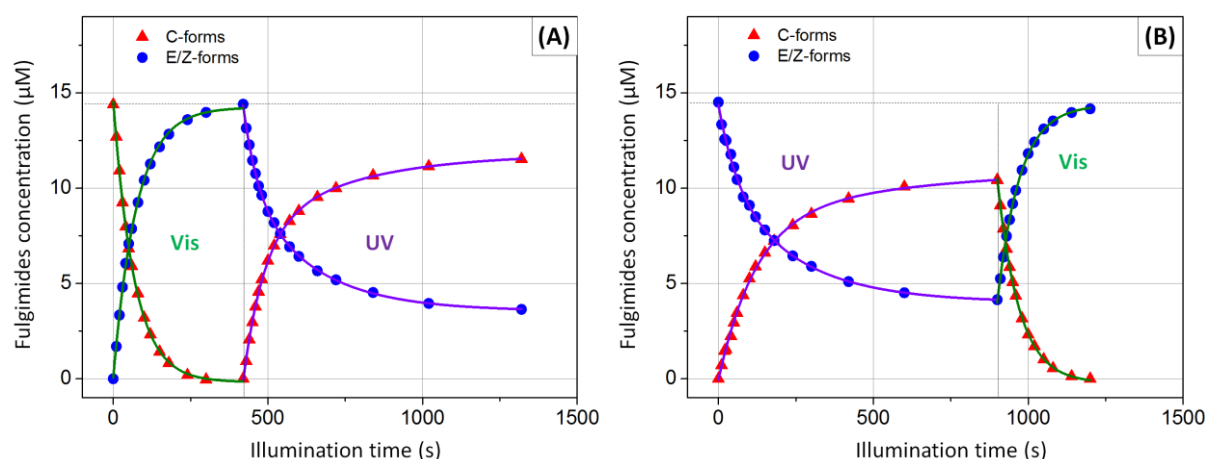


**Figure 3.7.** Evolution of the concentration of C- (▲) and E/Z-forms (●) in acetonitrile during the first two illumination cycles. (A) As-prepared Fulgi-C solution was illuminated with Vis then UV. (B) As-prepared Fulgi-E/Z solution was exposed to UV then Vis light. Dots and triangles are experimental data. The purple and green plots are the fitting curves for UV and Vis illumination cycle, respectively.

The time evolution of the fulgimide concentration for each kind of isomers (C or E/Z) under visible illumination can satisfactorily be fitted to an exponential function. On the opposite, the use of bi-exponential function has been forced to be necessary in order to obtain a good fit for the transient of concentration obtained during UV illumination cycle. The resulting fitting curves are displayed as purple lines (transient under UV) and green lines (transient under Vis) in Fig. 3.7. For examples, the fitting parameters of the transient obtained during the first and second illumination cycles for an as-prepared Fulgi-C solution are summarized in Table 3.4 and Table 3.5, respectively. The fitting parameters obtained from C- or E/Z-forms are close to each other highlighting the complementary evolution of the respective species.

Fulgimides	Vis illumination (1 <sup>st</sup> cycle)		
	$F(t) = Y_0 + A \exp(-t/\tau)$		
	$Y_0$	A	$\tau^{\text{Vis}}$ (s)
C-forms	-0.2	14.7	68
E/Z-forms	14.2	-14.2	75

**Table 3.4.** Fitting parameters of the transients obtained during the first Vis illumination for an as-prepared FulgiC solution. The transients were fitted to an exponential function.

Fulgimides	UV illumination (2 <sup>nd</sup> cycle) $F(t) = Y_0 + A_1 \exp(-t/\tau_1) + A_2 \exp(-t/\tau_2)$				
	$Y_0$	$A_1$	$\tau_1^{UV}$ (s)	$A_2$	$\tau_2^{UV}$ (s)
C-forms	11.3	-5.3	62	-5.5	253
E/Z-forms	4.0	4.7	48	6.1	214

**Table 3.5.** Fitting parameters of the transients obtained during the second UV illumination for an as-prepared FulgiC solution. The transients were fitted to a bi-exponential function.

### 3.2.3.2. Time constants over successive UV/Vis illumination cycles

The fitting procedure was applied on all the data recorded during repeated sequence of illumination. The obtained characteristic time constants  $\tau$  are plotted as a function of the illumination cycles in Fig. 3.8 for both as-prepared Fulgi-C and Fulgi-E/Z solutions.  $\tau^{Vis}$  is the single time constant determined from the fits of the data recorded during Vis illumination cycles using a simple exponential profile. Two  $\tau_1^{UV}$  and  $\tau_2^{UV}$  values are determined from the data recorded during UV illumination cycles, fitted with a bi-exponential profile. Once again, the values determined for the various UV cycles are nearly close to each other ( $\tau_1^{UV} \sim 50$ s and  $\tau_2^{UV} \sim 250$ s). During repeated illumination sequences, the different time constants remain quasi constant indicating a very good reversibility of the isomerization process and also a great photo-stability of the isomers in solution.

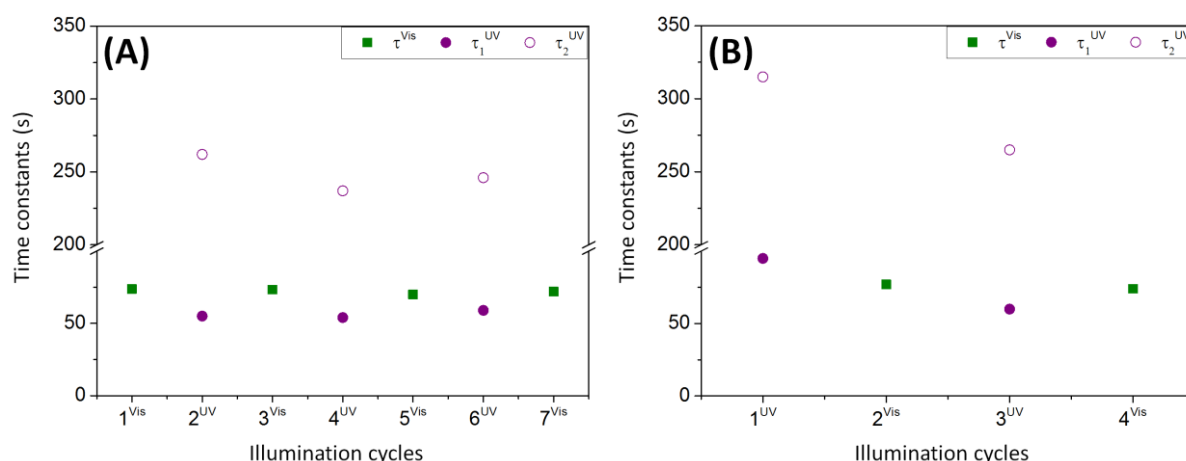


**Figure 3.8.** Time constants  $\tau^{Vis}$  (■),  $\tau_1^{UV}$  (●) and  $\tau_2^{UV}$  (○) of different illumination cycles starting from Fulgi-C (A) and Fulgi-E/Z (B) solutions. A break on Y-axis from 100 to 200 s.

### 3.2.3.3. Rate constants as a function of light intensity

As observed from the previous paragraph, the time constants of solutions  $PSS_{UV}$  and  $PSS_{Vis}$  are nearly unchanged after successive UV/Vis illumination cycles. The influence of photon flux on the kinetics of fulgimides in solution has also been studied. For that purpose, an as-prepared Fulgi-E/Z solution has been illuminated with three different photon flux. The photon flux has been modified by changing (or removing) the neutral filter of the illumination set-up (the neutral filters are removed for the highest photon flux). The studies were done with three different photon fluxes including the one used for the previous studies. Figure 3.9 displays plots of the rate constant determined from UV and Vis transient. In either case, they are found to be proportional to the photon flux.

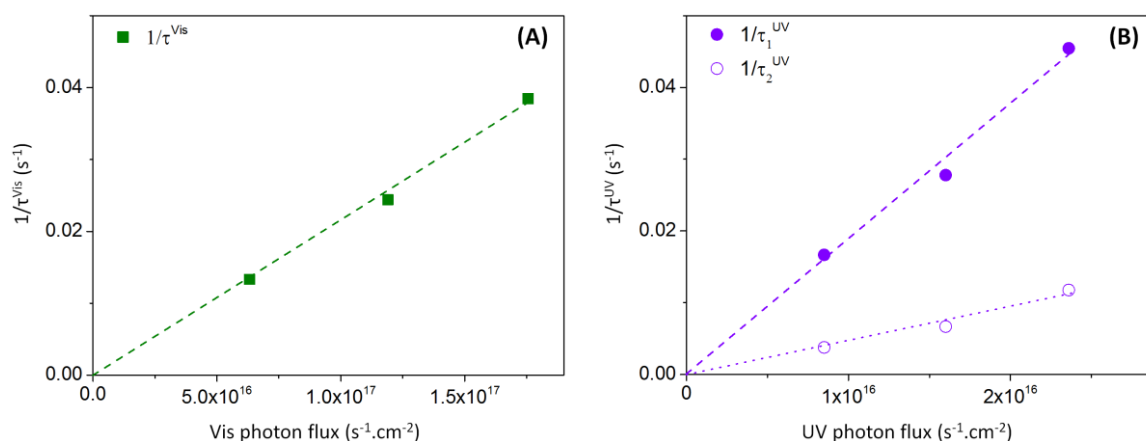


**Figure 3.9.** Rate constants as a function of the photon flux determined from the Vis- (A) or UV-transients (B).

## 3.3. Discussion

### 3.3.1. Photoswitching mechanism

The photochromism scheme in Fig. 3.1 is proposed in general for fulgimide family. However, in the present case, this scheme hardly appears to be able to account for the existence of mixtures of C and E/Z-forms at  $PSS_{UV}$ . Clearly, the lack of possible C→E transformation under UV in the scheme of Fig. 3.1 should yield to a UV photostationary state exclusively made of C-forms. It has been seen that the solutions of indolyfulgimides consist of 100% of E/Z-forms at  $PSS_{Vis}$  but only of ~75% of C-forms at  $PSS_{UV}$ . It suggests that the

reaction scheme must be modified by adding a C→E transformation under UV, according to the scheme depicted in Fig. 3.10.

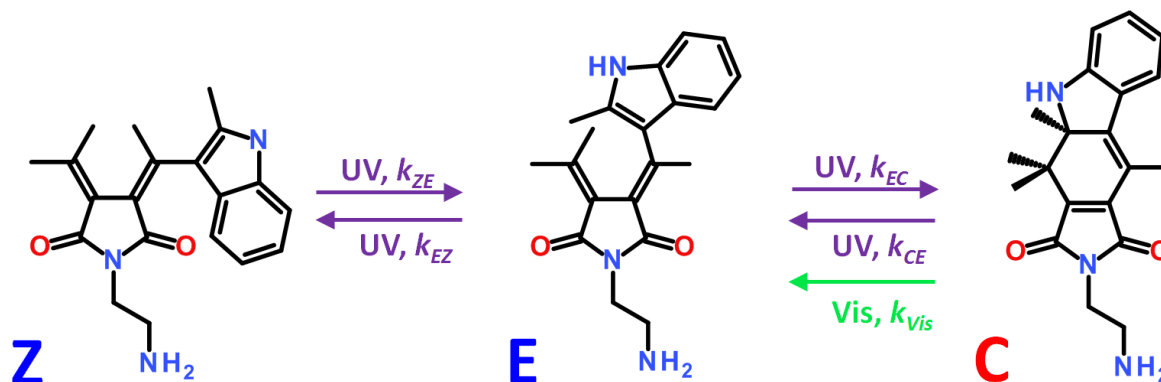


**Figure 3.10.** Photochromism of 2-aminoethylindolylfulgimide under Vis ( $\rightarrow$ ) or UV ( $\rightarrow$ ) illumination. The various  $k_i$ 's stand for rate constants associated with different reaction paths.

The existence of C→E reaction under UV has been evidenced experimentally. Figure 3.11 displays the absorbance spectra of an as-prepared FulgiC solution (containing solely C-isomers) prior to any illumination and after 10 min under UV illumination. A diminution of Vis-band at 525 nm is observed as well as a rising of UV-band at 365 nm. The isomeric composition determined from the spectrum is similar to that at PSS<sub>UV</sub> obtained previously after Vis then UV illumination cycles of a similar solution (Fig. 3.5B).

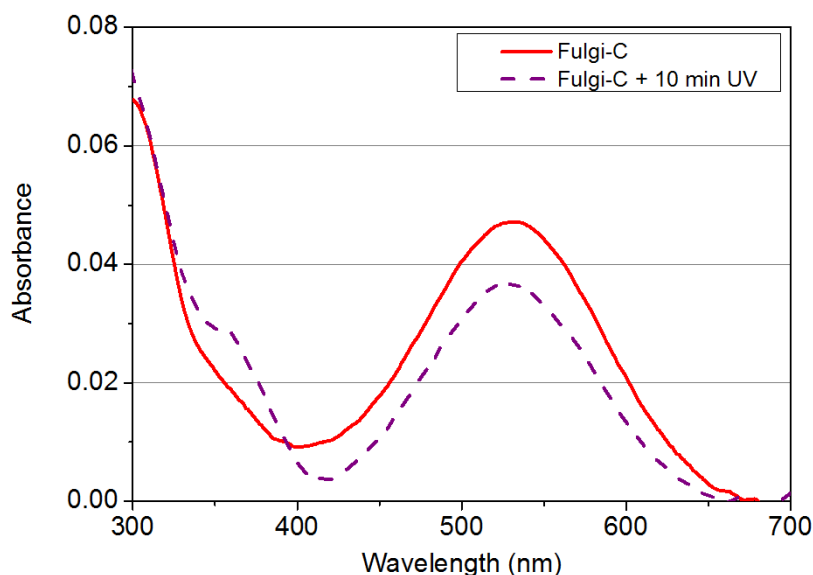


**Figure 3.11.** Absorption spectra in the UV/Vis spectral range of an as-prepared Fulgi-C solution prior to any illumination (red line) and after 10 min under UV illumination (purple dashed line).

Such a scheme can clearly account for the experimentally observed photostationary states. Under Vis reaction, the steady state will correspond to a complete depletion of C-forms. Under UV illumination, a mixture of C- and E/Z-forms is expected with proportion depending upon the respective values of the rate constants of the reactions. We are going to examine what the scheme of Fig. 3.10 is consistent with the experimental profiles of the absorbance evolution under UV and Vis illumination.

### 3.3.2. Kinetics of reactions

Under visible illumination, the reaction scheme as shown in Fig. 3.10 reduces to a single reaction corresponding to a  $C \rightarrow E$  isomerization (Fig. 3.10, Vis path). The kinetics of such a reaction should obey

$$\frac{d[C]}{dt} = k_{vis}[C] \quad \text{Equation 3.8}$$

where  $[C]$  stand for the concentration of C-forms in the solution. Eq. 3.8 can be straightforwardly integrated and the evolution of the C-form concentration  $[C](t)$  is

$$[C](t) = A \exp\left(-\frac{t}{\tau^{vis}}\right) \text{ with } \tau^{vis} = \frac{1}{k_{vis}} \quad \text{Equation 3.9}$$

As experimentally observed, the evolution of the C-form concentration in solution follows an exponential profile.

Under UV illumination, four reactions corresponding to the  $C \leftrightarrow E$  and  $E \leftrightarrow Z$  transformations come into play, according to the purple paths in Fig. 3.10. The kinetics of the systems is therefore more complex. Notifying  $[E]$ ,  $[Z]$  and  $[C]$  the respective concentration of E, Z and C-forms, a system of three rate equations can be written

$$\frac{d[E]}{dt} = k_{ZE}[Z] - k_{EZ}[E] - k_{EC}[E] + k_{CE}[C] \quad \text{Equation 3.10}$$

$$\frac{d[Z]}{dt} = -k_{ZE}[Z] + k_{EZ}[E] \quad \text{Equation 3.11}$$

$$\frac{d[C]}{dt} = k_{EC}[E] + k_{CE}[C] \quad \text{Equation 3.12}$$

This system can be analytically solved (see Appendix III) and yields to solutions

$$[E](t) = U_1 + V_1 e^{-\frac{t}{\tau_1}} + W_1 e^{-\frac{t}{\tau_2}} \quad \text{Equation 3.13}$$

$$[Z](t) = U_2 + V_2 e^{-\frac{t}{\tau_1}} + W_2 e^{-\frac{t}{\tau_2}} \quad \text{Equation 3.14}$$

$$[C](t) = U_3 + V_3 e^{-\frac{t}{\tau_1}} + W_3 e^{-\frac{t}{\tau_2}} \quad \text{Equation 3.15}$$

Noticeably, the solutions are found to be obeyed of a bi-exponential profile.

### 3.3.3. Photo-isomerization cross-section

As seen in the previous part, the rate constants associated to photo-isomerization processes are linearly dependent on the photon flux. This fact underlines that time constants are not quantities intrinsic to the system but dependent on experimental conditions. It therefore appears more appropriate to discuss the results in terms of cross sections, allowing for a proper normalization by the photon flux. Classically, one considers the ratio of (the number of absorbed photon) to (the number of incident photon per unit surface area) during a given (elementary) time. This quantity can therefore be viewed as an area totally absorbing matter present in the probed system. The absorption cross-section is defined by the ratio of this quantity to the concentration of absorbing molecules in the system. By analogy, a photo-isomerization cross-section can be defined according to Eq. 3.16.

$$\sigma = -\frac{1}{\phi \cdot n_{\text{isomerized}}} \frac{\delta n_{\text{isomerized}}}{\delta t} \quad \text{Equation 3.16}$$

where  $\phi$  is the photon flux and  $n_{\text{isomerized}}$  is the number of fulgimides isomerized during illumination cycle.

Let us assume that, under irradiation, the absorbance of the photo-isomerizable fulgimides obeys an exponential law of time constant  $\tau$ . Therefore,

$$n_{\text{isomerizable}} = A_0 \exp\left(-\frac{t}{\tau}\right) \quad \text{Equation 3.17}$$

The number of photo-isomerized molecules during a time  $\delta t$  is

$$\delta n_{\text{isomerized}} = \frac{dn_{\text{isomerizable}}}{dt} \delta t = -n_{\text{isomerizable}} \frac{\delta t}{\tau} \quad \text{Equation 3.18}$$

Therefore, the photo-isomerization cross-section simply writes as :

$$\sigma = \frac{1}{\tau \cdot \phi} \quad \text{Equation 3.19}$$

Such a simple approach holds for the photo-isomerization under Vis illumination, for which the evolution has been found to obey an exponential law. In this case, the Vis isomerization cross-section is denoted as  $\sigma^{\text{Vis}}$ .

Under UV illumination, the concentration of photo-isomerizable molecules has been found to obey a bi-exponential law such as

$$n_{\text{isomerizable}} = A_1 \exp\left(-\frac{t}{\tau_1}\right) + A_2 \exp\left(-\frac{t}{\tau_2}\right) \quad \text{Equation 3.20}$$

In this case, at  $t=0$ , the number of photo-isomerized molecules during a time  $\delta t$  is

$$n_{\text{isomerized}} = -\left(\frac{A_1}{\tau_1} + \frac{A_2}{\tau_2}\right) \delta t \quad \text{Equation 3.21}$$

and the number of photo-isomerizable molecules is simply

$$n_{\text{isomerizable}} = A_1 + A_2 \quad \text{Equation 3.22}$$

Therefore, at  $t = 0$ , the *reduced* photo-isomerization cross-section simply writes as

$$\sigma_0^{\text{UV}} = \frac{A_1}{A_1 + A_2} \sigma_1^{\text{UV}} + \frac{A_2}{A_1 + A_2} \sigma_2^{\text{UV}} \quad \text{Equation 3.23}$$

where, by analogy with the simple exponential case,  $\sigma_1^{\text{UV}}$  and  $\sigma_2^{\text{UV}}$  have been taken as  $1/(\tau_1\phi)$  and  $1/(\tau_2\phi)$ , respectively, which can be considered as photo-isomerization cross-sections for the fast and slow conversion processes. It should be stressed out that the above *reduced* photo-isomerization cross-section is that of the process assessed at time  $t = 0$ . Contrary to the simple exponential case, the sigma value will depend on the time  $t$  at which this assessment is performed (typically, the same result will hold by substituting  $A_1 \exp\left(-\frac{t}{\tau_1^{\text{UV}}}\right)$  to  $A_1$  and  $A_2 \exp\left(-\frac{t}{\tau_2^{\text{UV}}}\right)$  to  $A_2$ ). In the following, we will limit ourselves to this  $\sigma_0$  value assessed at  $t = 0$ .

### 3.3.4. Comparison between UV and Vis isomerization cross-sections

The Vis and UV isomerization cross-sections,  $\sigma^{\text{Vis}}$ ,  $\sigma_1^{\text{UV}}$ ,  $\sigma_2^{\text{UV}}$  and  $\sigma_0^{\text{UV}}$  over successive cycles of as-prepared Fulgi-C and Fulgi-EZ solutions are plotted in Fig. 3.12. At short times, the larger value of  $\sigma_0^{\text{UV}}$  underlines a faster initial  $E \rightarrow C$  evolution under UV, as correspond to the  $C \rightarrow E$  isomerization under Vis illumination. However, at long times, the UV isomerization cross-section reduces to  $\sigma_2^{\text{UV}}$  and the efficiency of the  $E \rightarrow C$  isomerization

is comparable to that of the  $C \rightarrow E$  isomerization under Vis illumination. In view of the kinetic equations derived in the previous section, this slowing down could be ascribed to the existence of the side  $Z \rightleftharpoons E$  isomerization which slows down the production rate of the C-forms.

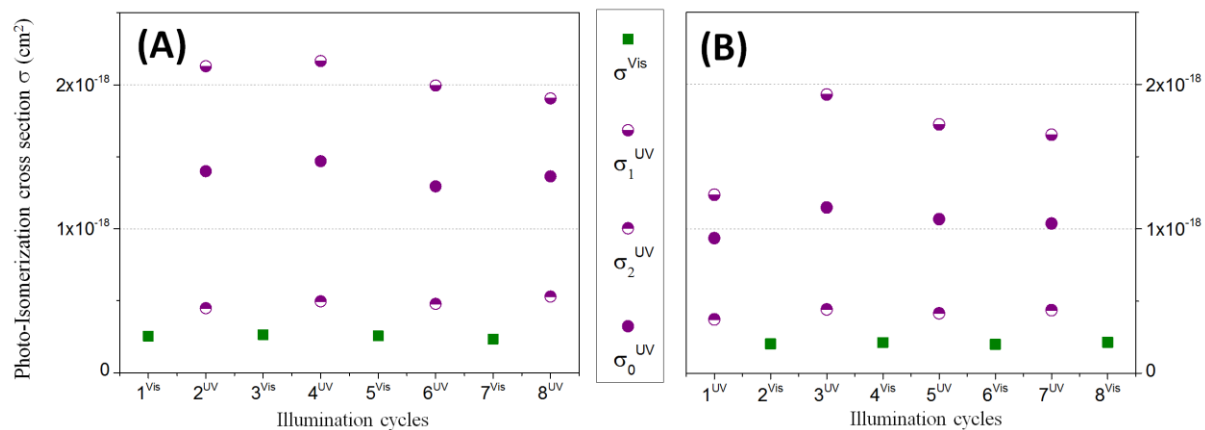


**Figure 3.12.** Photo-isomerization cross section  $\sigma^{\text{Vis}}$  (green square) and  $\sigma_1^{\text{UV}}$ ,  $\sigma_2^{\text{UV}}$  and  $\sigma_0^{\text{UV}}$  (purple circle) over successive cycles of as-prepared Fulgi-C (A) and Fulgi-EZ (B) solutions.

## Conclusions

The photo-isomerization of amino substituted indolylfulgimide was investigated in solution by UV-Vis spectroscopy. Under UV/Vis illumination, reversible and efficient  $C \rightleftharpoons E$  isomerization was demonstrated. The isomeric composition of the solutions at the photostationary states –  $PSS_{Vis}$  and  $PSS_{UV}$  – has been determined through calibration of the UV and Vis absorption bands of the open E/Z- and closed C-forms. It has been shown that after Vis illumination the solution is totally depleted in C-form indicating a complete  $C \rightarrow E$  isomerization (ring-opening reaction). Under UV illumination, the solution is enriched in C-forms and the isomeric composition obtained at PSS corresponds to a mixture of open and closed forms with an isomeric ratio (E/Z):C  $\approx$  25:75. After repeated UV/Vis illumination cycles, the isomeric compositions of the solution at  $PSS_{Vis}$  and  $PSS_{UV}$  remained constant, i.e., no photo-fatigue effect was observed.

Different kinetics laws were evidenced for Vis and UV illumination cycle. Under Vis illumination, the time evolution of the isomer concentrations follows a simple exponential law, which is consistent with the existence of a single possible reaction path, i.e., the  $C \rightarrow E$  ring-opening reaction. Under UV illumination, the reaction scheme is more complex so that their kinetic are bi-exponential dependence as a consequence of the existence of several reaction paths. It is well-known that the  $E \rightarrow C$  ring-closure reaction and the reversible cis-trans  $E \rightleftharpoons Z$  isomerizations occur under UV. Our results showed that the  $C \rightarrow E$  ring-opening reaction can be also activated by UV light. The existence of this reaction under UV illumination accounts for the only partial E/Z  $\rightarrow$  C conversion leading to steady-state isomeric concentration consisting of mixture of open E/Z- and closed C-forms at  $PSS_{UV}$ .

The photo-isomerization cross-sections under Vis and UV illumination have been determined. For short reaction times, the production of C-isomers under UV is found to be more efficient compared to their back conversion into E-isomers under Vis. For longer time, the production of C-isomers becomes less efficient which is related to the existence of side reactions (the  $E \rightleftharpoons Z$  cis-trans isomerization and  $C \rightarrow E$  ring-opening reaction).

Similar reaction rates were observed after repeated illuminations sequences that further sustains the great photo-stability of our fulgimide compounds in solution.

## References

- (1) Bouas-Laurent, H.; Durr, H. *Pure and Applied Chemistry* **2001**, *73*, 639.
- (2) Berns, M. W.; Krasieva, T.; Sun, C. H.; Dvornikov, A.; Rentzepis, P. M. *Journal of Photochemistry and Photobiology B-Biology* **2004**, *75*, 51.
- (3) Port, H.; Hartschuh, A.; Hennrich, M.; Wolf, H. C.; Endtner, J. M.; Effenberger, E. *Molecular Crystals and Liquid Crystals* **2000**, *344*, 145.
- (4) Willner, I. *Accounts of Chemical Research* **1997**, *30*, 347.
- (5) Liang, Y. C.; Dvornikov, A. S.; Rentzepis, P. M. *Proceedings of the National Academy of Sciences of the United States of America* **2003**, *100*, 8109.
- (6) Barachevsky, V. A.; Krayushkin, M. M. *Russian Chemical Bulletin* **2008**, *57*, 867.
- (7) Yokoyama, Y. *Chemical Reviews* **2000**, *100*, 1717.
- (8) Otto, B.; Ruck-Braun, K. *European Journal of Organic Chemistry* **2003**, 2409.
- (9) Liang, Y. C.; Dvornikov, A. S.; Rentzepis, P. M. *Macromolecules* **2002**, *35*, 9377.
- (10) Wolak, M. A.; Gillespie, N. B.; Thomas, C. J.; Birge, R. R.; Lees, W. J. *Journal of Photochemistry and Photobiology a-Chemistry* **2001**, *144*, 83.
- (11) Malkmus, S.; Koller, F. O.; Heinz, B.; Schreier, W. J.; Schrader, T. E.; Zinth, W.; Schulz, C.; Dietrich, S.; Ruck-Braun, K.; Braun, M. *Chemical Physics Letters* **2006**, *417*, 266.
- (12) Chen, X.; Islamova, N. I.; Robles, R. V.; Lees, W. J. *Photochemical & Photobiological Sciences* **2011**, *10*, 1023.
- (13) Chen, X.; Islamova, N. I.; Garcia, S. P.; DiGirolamo, J. A.; Lees, W. J. *Journal of Organic Chemistry* **2009**, *74*, 6777.
- (14) Braun, M.; Malkmus, S.; Koller, F. O.; Heinz, B.; Zinth, W.; Schuiz, C.; Dietrich, S.; Ruck-Braun, K. *Ultrafast Phenomena XV* **2007**, *88*, 291.
- (15) Ramsteiner, I. B.; Hartschuh, A.; Port, H. *Chemical Physics Letters* **2001**, *343*, 83.
- (16) Matsushima, R.; Sakaguchi, H. *Journal of Photochemistry and Photobiology a-Chemistry* **1997**, *108*, 239.
- (17) Wolak, M. A.; Thomas, C. J.; Gillespie, N. B.; Birge, R. R.; Lees, W. J. *Journal of Organic Chemistry* **2003**, *68*, 319.
- (18) Draxler, S.; Brust, T.; Malkmus, S.; Koller, F. O.; Heinz, B.; Laimgruber, S.; Schulz, C.; Dietrich, S.; Ruck-Braun, K.; Zinth, W.; Braun, M. *Journal of Molecular Liquids* **2008**, *141*, 130.
- (19) Islamova, N. I.; Chen, X.; DiGirolamo, J. A.; Silva, Y.; Lees, W. J. *Journal of Photochemistry and Photobiology a-Chemistry* **2008**, *199*, 85.
- (20) Brust, T.; Malkmus, S.; Draxler, S.; Ahmed, S. A.; Ruck-Braun, K.; Zinth, W.; Braun, M. *Journal of Photochemistry and Photobiology a-Chemistry* **2009**, *207*, 209.
- (21) Brust, T.; Draxler, S.; Popp, A.; Chen, X.; Lees, W. J.; Zinth, W.; Braun, M. *Chemical Physics Letters* **2009**, *477*, 298.
- (22) Brust, T.; Draxler, S.; Eicher, J.; Lees, W. J.; Ruck-Braun, K.; Zinth, W.; Braun, M. *Chemical Physics Letters* **2010**, *489*, 175.
- (23) Koller, F. O.; Schreier, W. J.; Schrader, T. E.; Sieg, A.; Malkmus, S.; Schulz, C.; Dietrich, S.; Ruck-Braun, K.; Zinth, W.; Braun, M. *Journal of Physical Chemistry A* **2006**, *110*, 12769.

# Chapter 4

## Fulgimide monolayer on Si surface

---

### Table of Contents

---

Introduction .....	102
4.1. Surface preparation .....	103
4.2. Surface characterization.....	104
4.2.1. Qualitative FTIR analysis .....	104
4.2.2. Quantitative analysis.....	109
4.3. Discussion.....	111
Conclusions .....	115
References .....	116

---

# Introduction

This chapter presents the experimental procedures implemented for the immobilization of the fulgimide groups onto silicon surfaces and the characterization of the as-prepared fulgimides-terminated surfaces. The two forms of 2-aminoethylindolylfulgimides (closed C-form or open E/Z-form) were covalently anchored onto acid tail groups of monolayers grafted on silicon surfaces a two-step protocol. The amino Fulgimides were anchored on MLs with various concentration of COOH anchoring sites using the two- (Fig. 4.1).<sup>1</sup>

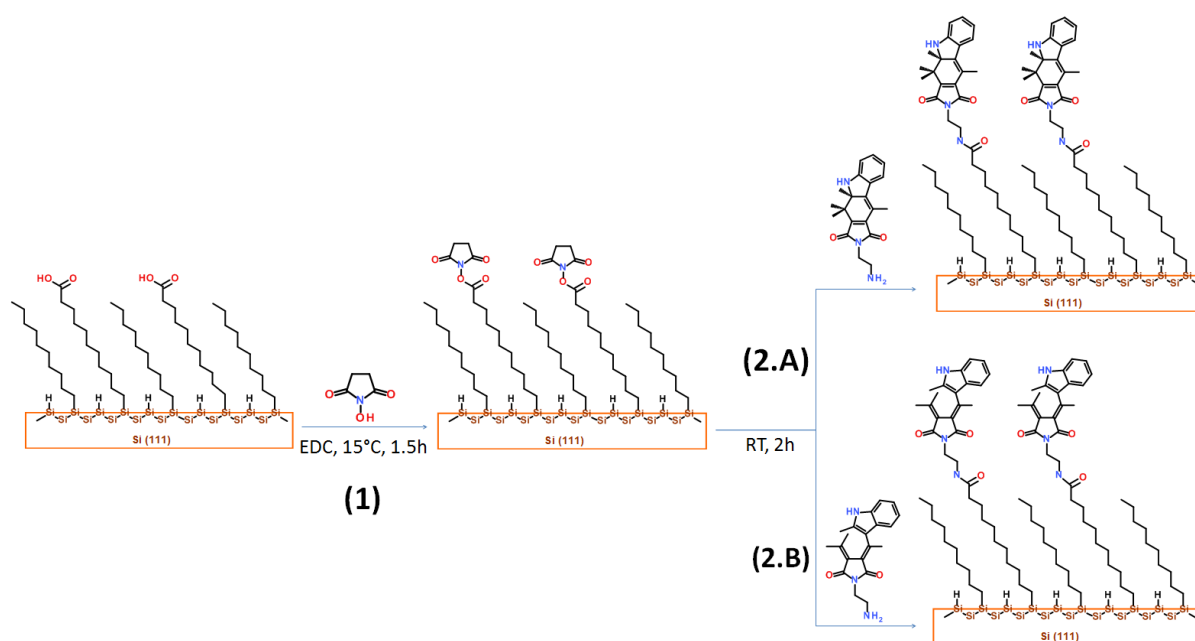


**Figure 4.1.** Multi-step protocol for the covalent coupling of amino indolylfulgimides onto acid terminated monolayer. (1) Conversion of the carboxylic acid tail groups into semi-stable succinimidyl esters (*surface activation*). (2) Covalent coupling of C-isomers (path A) or E-isomers (path B) through aminolysis.

At each step, topological and chemical characterization of the surface has been performed by non-contact atomic-force microscopy (NC-AFM) and FTIR spectroscopy in ATR geometry (ATR-FTIR).

## 4.1. Surface preparation

*Pure* Si-FulgiC or Si-FulgiEZ surfaces, i.e., with solely one type of isomer - closed form (C) or open form (EZ). In order to vary the density of fulgimides on the surface, monolayers with different densities of COOH anchoring sites were prepared. *Pure* acid-terminated monolayers were prepared either by the *one-step* (direct grafting of undecylenic acid) or the *two-step* (grafting of ester precursors and subsequent hydrolysis) routes as previously described in Chapter 1. Mixed monolayers with lower density of anchoring sites were prepared by the grafting of ester/decene mixtures (the *two-step* route), since much more homogeneous distribution of the acid tail groups is expected in that case.

### First step: Surface activation

The transformation of the acid groups into semi-stable succinimidyl esters (COOH → COOSuc) was carried out by immersion of the acid-terminated surfaces into a freshly prepared solution containing 0.1M N-hydroxysuccinimide (NHS) and 0.1M N-(3-Dimethylaminopropyl)-N'-ethylcarbodiimide (EDC) in 0.1 M MES buffer solution at pH 6. The reaction was let to proceed for 1h at 15°C. The activated Si-COOSuc surfaces were then twice rinsed in phosphate buffer solution (pH = 5, 45°C) for 10 min then copiously rinsed with ultra-pure water (UPW, 18 MΩ cm).

### Second step: Aminolysis

Covalent linkage of the fulgimide groups was achieved by immersing the freshly activated Si-COOSuc surfaces into oxygen-free acetonitrile solution containing 5mM of E/Z- or C-form amino fulgimides. The reaction was let to proceed in the dark during 2h at room temperature. The samples were then rinsed 3 times in acetonitrile, blown dry and stored in the dark under nitrogen until their characterization or the photoswitching experiments.

Four kinds of as-prepared fulgimide-terminated surfaces were prepared that differ by the type of isomer - closed form (C) or open form (E/Z) - and/or the fulgimide density. **Dense Si-fulgiC** or **Si-fulgiE/Z** surfaces were prepared from *pure* acid-terminated surfaces. *Dilute* fulgimide MLs were prepared by coupling on *mixed* surfaces obtained by the *two-step* route. These surfaces will be named **Si-fulgiC<sup>30</sup>** and **Si-fulgiC<sup>10</sup>** (respectively **Si-fulgiEZ<sup>30</sup>** and **Si-fulgiEZ<sup>10</sup>**) in the following. The number in index refers to the ester fraction in the grafting solution.

## 4.2. Surface characterization

### 4.2.1. Qualitative FTIR analysis

Figure 4.2 displays FTIR spectra of a *pure* Si-acid<sup>ester</sup> surface prior to (a) and after activation (b) and after the coupling of amino substituted fulgimide (E/Z-form) (c). Figure 4.3 compares the spectra of Si-fulgiC and Si-fulgiEZ monolayers in the range of 1250-1950 cm<sup>-1</sup>. For all the spectra, the reference is the hydrogen-terminated surface H-Si prior to the monolayer grafting. The negative sharp band at ~2080 cm<sup>-1</sup> indicates to the loss of Si-H bonds after ML grafting. The positive bands are assigned to the chemical groups present on the surface after either surface modification. The positions and assignments of the main characteristic bands observed at each step are summarized in Table 4..

The spectrum of the surface prior to activation (Fig. 4.2a), exhibits only the bands characteristic of the carboxyl chains, i.e. one  $\nu\text{C=O}$  band at 1715 cm<sup>-1</sup> corresponding to the carboxylic acid groups and two  $\nu\text{CH}_2$  bands at 2852 and 2923 cm<sup>-1</sup>. After activation (Fig. 4.2b), the  $\nu\text{C=O}$  band at 1715 cm<sup>-1</sup> almost disappeared and is replaced by 3 new bands characteristic of the succinimidyl ester groups, i.e., the  $\nu\text{COOSuc}$  triplet at 1745, 1787 and 1817 cm<sup>-1</sup>. A small shoulder on the low-energy side of the 1745 cm<sup>-1</sup> band indicates the presence of residual acid groups.

At the next step, the successful immobilization of the fulgimide groups is clearly evidenced by the disappearance of the  $\nu\text{COOSuc}$  triplet and the observation of new bands in the carbonyl region and at lower wavenumbers, assigned the fulgimide groups. The covalent linkage of the fulgimide groups is confirmed by the observation of a broad band at 1650 cm<sup>-1</sup> characteristic of amide linkage ( $\nu\text{HNC=O}$ , amide I). Other bands may be also assigned to amide linkage at ~1545 cm<sup>-1</sup> ( $\delta\text{H-N}$ , amide II) and ~1465 cm<sup>-1</sup> ( $\nu\text{C-N}$ , amide III). However these bands overlap with some fulgimide bands which make their assignments less clear.

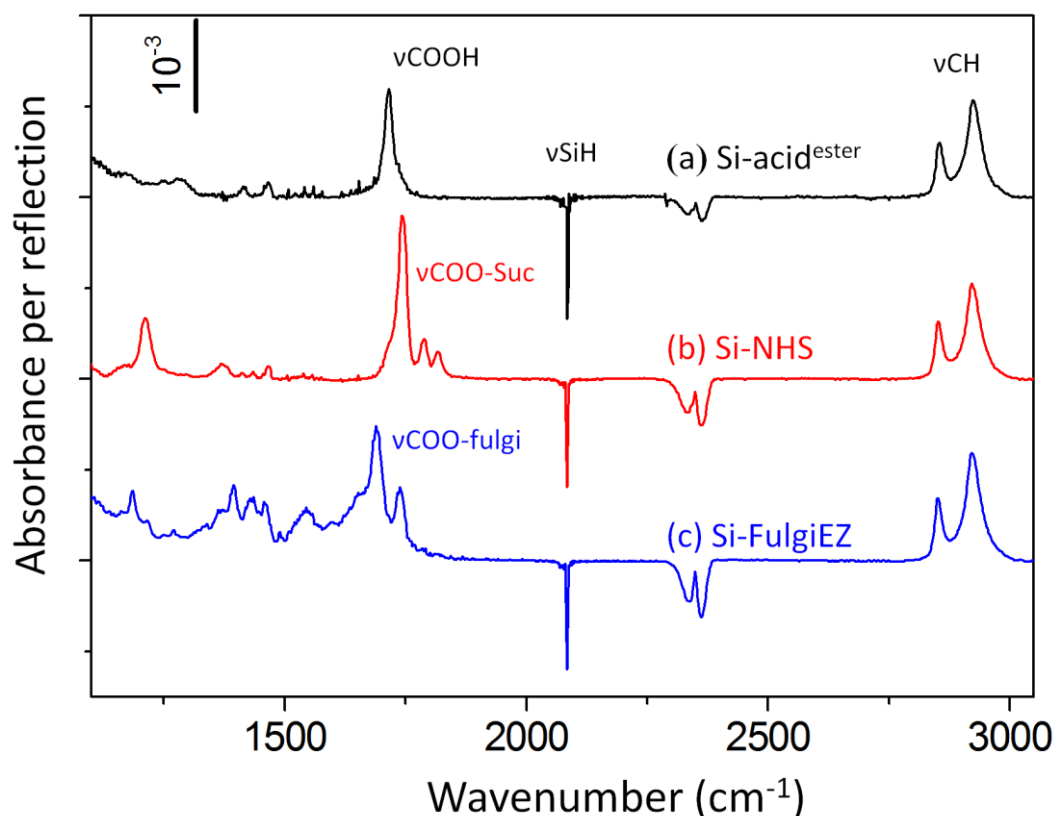


**Figure 4.2.** FTIR spectra at the different steps of the surface preparation of a *dense* Si-fulgiEZ surface. (a) *pure* acid surface prepared by the two-step route, (b) the same surface after activation, (c) the same surface after the coupling of amino substituted fulgimide (E/Z-form). For all the spectra, the reference is the H-Si surface prior to grafting.

Depending on the type of isomer (C- or E/Z-form), slightly different spectra are obtained. Even though, at first glance, the spectra in Fig. 4.3 globally exhibit similar shapes, different band positions and/or intensities are observed for the MLs made of two C- or E/Z-form. The most significant difference is observed in the carbonyl region where different positions are observed for the  $\nu\text{C}=\text{O}$  bands related to the stretching mode of maleimide moieties. The bands stand at 1739 and 1690  $\text{cm}^{-1}$  for the Si-fulgiEZ surface and at 1758 and 1698  $\text{cm}^{-1}$  in the case of Si-fulgiC surface. The positions of these bands are very similar to those reported for the two kinds of isomers in solution.<sup>2</sup> The specific position of the  $\nu\text{C}=\text{O}$  bands allows therefore for a straightforward identification of either C- or E/Z-form.

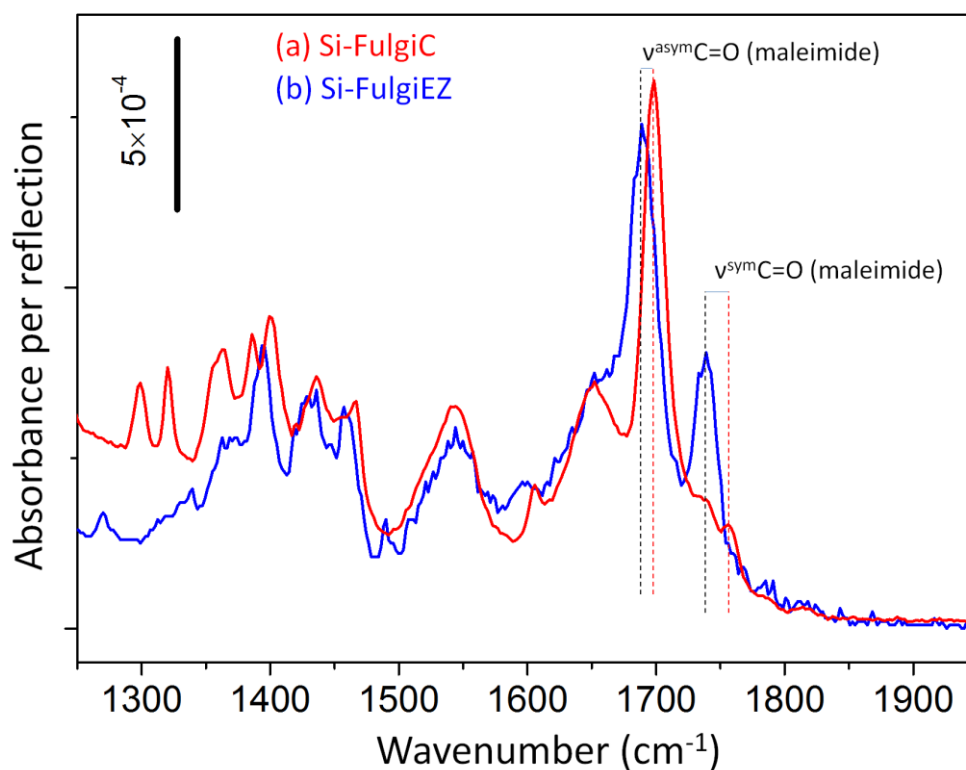


Figure 4.3. Narrow FTIR spectra of *dense* Si-fulgiC (a) and Si-fulgiEZ (b) surfaces.

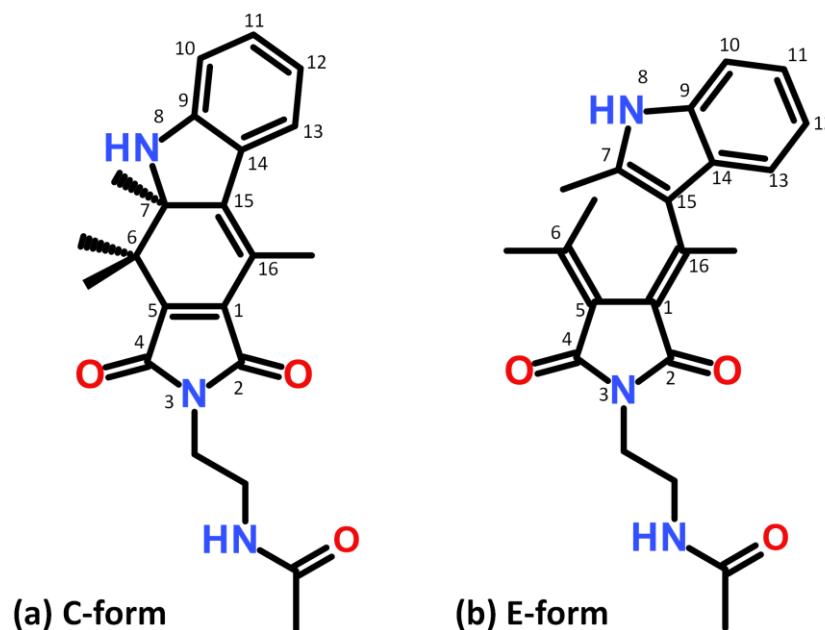
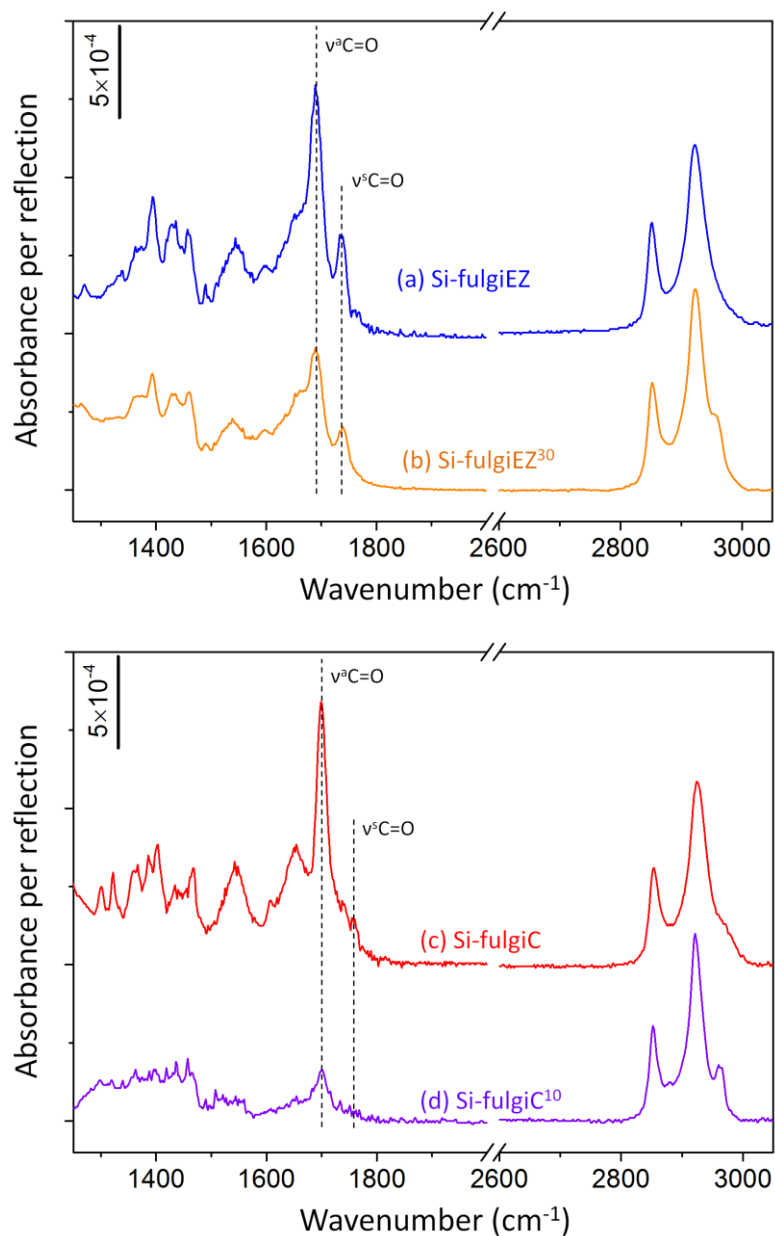


Figure 4.4. Chemical structures of C- and E-form indolyfulgimides coupled through amide bonds to monolayers. Atoms in the fulgimide core were numbered for FTIR identification.

<b>Surface / Band position (cm<sup>-1</sup>)</b>		<b>Band assignment</b>
<b><u>Si-COOH</u></b>		
1715		νC=O carboxylic acid
1467		νCH <sub>2</sub> scissors aliphatic chains
1410		νC-OH in plane carboxylic acid
<b><u>Si-COOSuc</u></b>		
1817		νC=O succinidyl ester stretching
1787		ν <sub>s</sub> C=O succinidyl imide
1745		ν <sub>a</sub> C=O succinidyl imide
<b><u>Si-fulgiEZ</u></b>	<b><u>Si-fulgiC</u></b>	
<u>1739</u>	<u>1758</u>	ν <sub>s</sub> C <sup>4,2</sup> =O maleimide group*
<u>1690</u>	<u>1698</u>	ν <sub>a</sub> C <sup>4,2</sup> =O maleimide group*
1650	1650	νC=O Amide I
1620		νC <sup>1</sup> =C <sup>16</sup> Indolyl ring mode*
1595	1604	νC <sup>10,12,13</sup> -H phenyl group*
1543	1547	νN-H amide II, Indolyl ring mode*
1461	1466	aliphatic νCH <sub>2</sub> scissors
	1320	νC <sup>1</sup> -C <sup>16</sup> , Indolyl ring mode*
	1298	νC <sup>5</sup> -C <sup>6</sup> , Indolyl ring mode*

**Table 4.1. Peak positions and assignments at the different steps of the surface modification. (\*) Fulgimide bands were assigned in agreement with the experimental and predicted data from Koller *et al.*<sup>2</sup>. Numbered atoms refer to the labels shown in Fig. 4.4.**

Spectra of *dense* and *dilute* fulgimide monolayers are compared in Fig. 4.5. Qualitatively, the spectra look very similar. Only variations of the intensity of the fulgimide related bands are observed as well as the appearance of band-related to the methyl end-groups of the decyl chains (νCH<sub>3</sub> at 2963 cm<sup>-1</sup>). The position and shape of the ν<sub>s</sub>C=O and ν<sub>a</sub>C=O bands assigned to maleimide groups remain almost unchanged.



**Figure 4.5.** FTIR spectra of different fulgimide-terminated monolayers. (a) *dense* Si-fulgiEZ, (b) *diluted* Si-fulgiEZ<sup>30</sup>, (c) *dense* Si-fulgiC and (d) *diluted* Si-fulgiC<sup>10</sup> surfaces. For all spectra the reference is the H-Si surface prior to grafting.

### 4.2.2. Quantitative analysis

The surface concentration of the anchoring COOH sites, the *activated* COOSuc ester and the fulgimides groups were determined from quantitative FTIR analysis using previously methods developed in the group.<sup>3,4</sup> The approach relies on absorbance measurements for p- and s-polarized IR beam. It is then necessary to make a calibration of the IR cross-section of the corresponding modes through measurements of their absorbance in solution using the same ATR geometry. Because the calibration of absorbance intensity in solution requires a sufficient amount of the considered chemical groups to get accurate values, it has not been possible to carry out the calibration of the fulgimide-related IR carbonyl peak to truly determine their concentration on the surfaces. Alternatively, we have determined the concentration of fulgimide in the monolayers by considering the loss of COOSuc ester after the coupling reaction. It is noteworthy that the loss of COOSuc groups due to side reactions (as hydrolysis for example) is unlikely since the coupling is carried out in acetonitrile solution containing only the aminoindolylfulgimide as reactant. Therefore the aminolysis of the COOSuc ester by the amino fulgimide to form amide linkage is thought to be the only sizeable reaction yielding to the succinimidyl ester disappearance. Since the  $\nu_{C=O}$  characteristic triplet of succinimide species is actually associated to species bound to the surface via an ester linkage, the fulgimide concentration reported in the following refers to *covalently linked* fulgimide. It does not account, in particular, for the possible presence of physisorbed fulgimides remaining on the surface. A significant under estimation of the fulgimide concentration can be discarded since the AFM imaging reveals homogeneous surfaces free from *significant* amounts of extra physisorbed matters after the coupling reaction (Fig. 4.6).

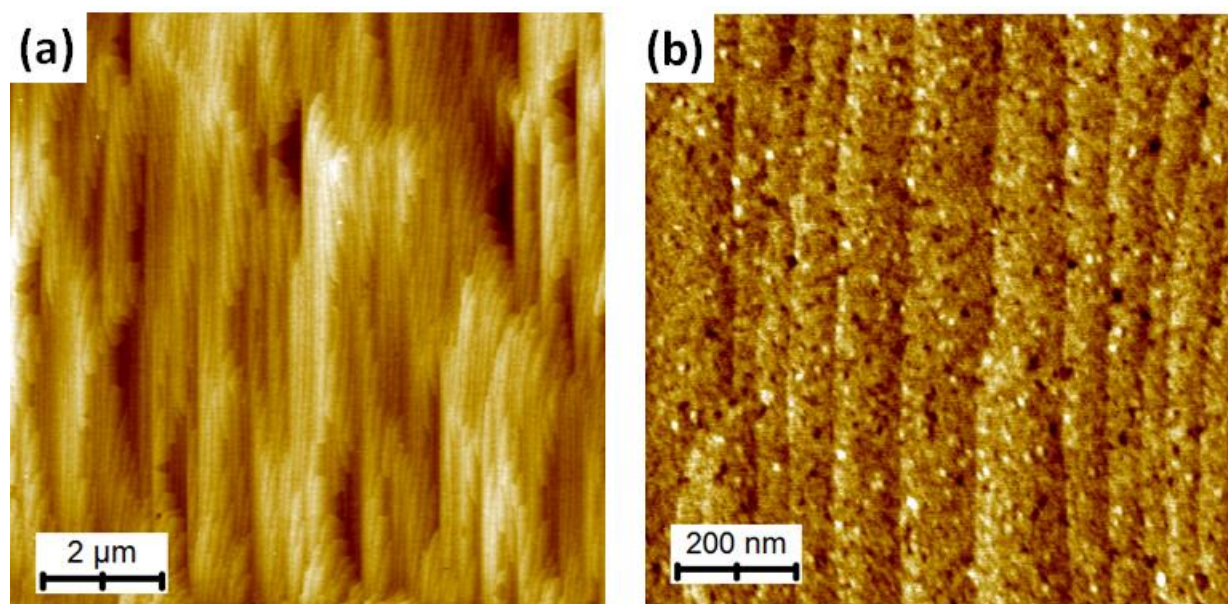


**Figure 4.6.** AFM topography images at different magnification of as-prepared Si-FulgiEZ monolayer.

The surface concentrations of carboxyl, succinimidyl and indolylfulgimide groups as well as the reaction yield are summarized in Table 4.2 for the two *dense* and two *diluted* fulgimide surfaces.

Nominal surface	-COOH groups before activation ( $\times 10^{14} \text{ cm}^{-2}$ )	-COOSuc groups after activation ( $\times 10^{14} \text{ cm}^{-2}$ )	Activation yield (%)	Fulgimide groups ( $\times 10^{14} \text{ cm}^{-2}$ )	Fulgimide Coupling yield (%)
Si-fulgiC	3.0	2.74	91	1.60	58
Si-fulgiEZ	2.8	2.61	89	1.71	66
Si-fulgiEZ <sup>30</sup>	0.94	0.71	76	0.68	96
Si-fulgiC <sup>10</sup>	0.27	0.20	74	0.19	95

**Table 4.2.** Surface concentrations of carboxyl (-COOH), hydroxysuccinimide (-NHS) and indolylfulgimide groups and the activation and coupling yield for four different surfaces.

### 4.3. Discussion

The results displayed in Table 4.2 show different coupling yield of fulgimides depending on the density of anchoring sites on the surface. On surfaces with high density of carboxylic chains (*pure* acid MLs), the coupling yield is ~60% whereas the reaction is almost quantitative (96%) on the *mixed* monolayers exhibiting a lower density of anchoring sites. Since the COOH → COOSuc conversion yield is in all cases  $\geq 75\%$ , it turns out that the activation step is not the limiting step. Steric effects may therefore be anticipated as the factor limiting the density of fulgimides on the surface

Figure 4.7 shows a possible 2D organization of fulgimides on a Si(111) surface corresponding to a fulgimide concentration ( $D_{\text{fulgi}} = 1.3 \times 10^{14} \text{ cm}^{-2}$ ) close to the maximal density observed experimentally. The structure of the fulgimide groups have been optimized using Alchemy software®. The fulgimides are positioned according to an ideal (2×3) structure (blue circles) on top of acid chains arranged according a (2×1) structure (black circles) which corresponds to the maximum surface coverage reachable for long chains acid on a Si(111) surface. The (1×1) structure of the Si(111) surface is plotted as grey circles on Fig. 4.7a.

It should be stressed that this model gives an ideal picture of the molecular 2D organization of the fulgimide MLs which is likely far from the reality. Nevertheless it clearly shows that the maximum fulgimide density that can be accommodated on the surfaces is close to that observed experimentally on the *pure* acid surfaces. In that case, our results indicate therefore the formation of dense MLs independently of the type of isomers (C or E/Z).

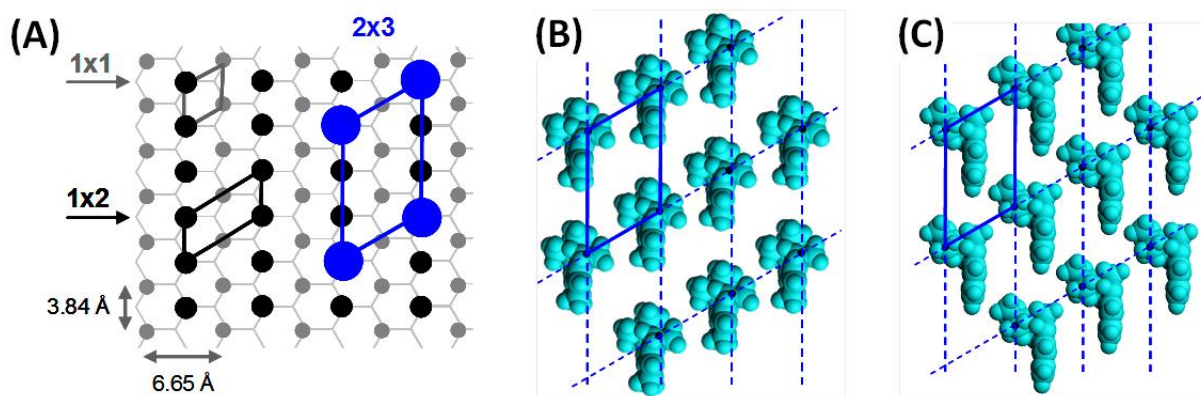


**Figure 4.7. In-plane model of densely packed fulgimide ML on top of densely packed alkyl ML grafted on Si(111) surface. (a) The (1×1) structure of the Si(111) surface is plotted as grey circles, the black circles represent the ideal (2×1) structure corresponding to maximal packing of the carboxyl chains, the blue circles represent fulgimide arranged according to a (2×3) structure corresponding to a surface fulgimide density of  $1.3 \times 10^{14} \text{ cm}^{-2}$  close to the maximal density determined experimentally. (b, c) C- and E-forms arranged according to a (2×3) structure. Notice that this structure allows for accommodating the fulgimide groups without lateral steric hindrance but corresponds to close-packing of fulgimide groups close to the maximum.**

The composition of *dense* and *diluted* fulgimide-terminated surfaces at final stage – in terms of nature and fraction of the terminal end-groups – is summarized in Fig. 4.8. In all the cases, the surfaces exhibit a complex chemical composition with more or less residual acid or succinimidyl groups. It turns out that the fraction of residual groups (mainly acid since the coupling reaction is almost quantitative in that case) is much more limited in the case of *diluted* fulgimide surfaces, leading to a better control of the chemical environment of the fulgimide groups on top of surface. Optimization of the activation conditions on *diluted* fulgimide surfaces should allow for further improvement of the chemical homogeneity of the surfaces.

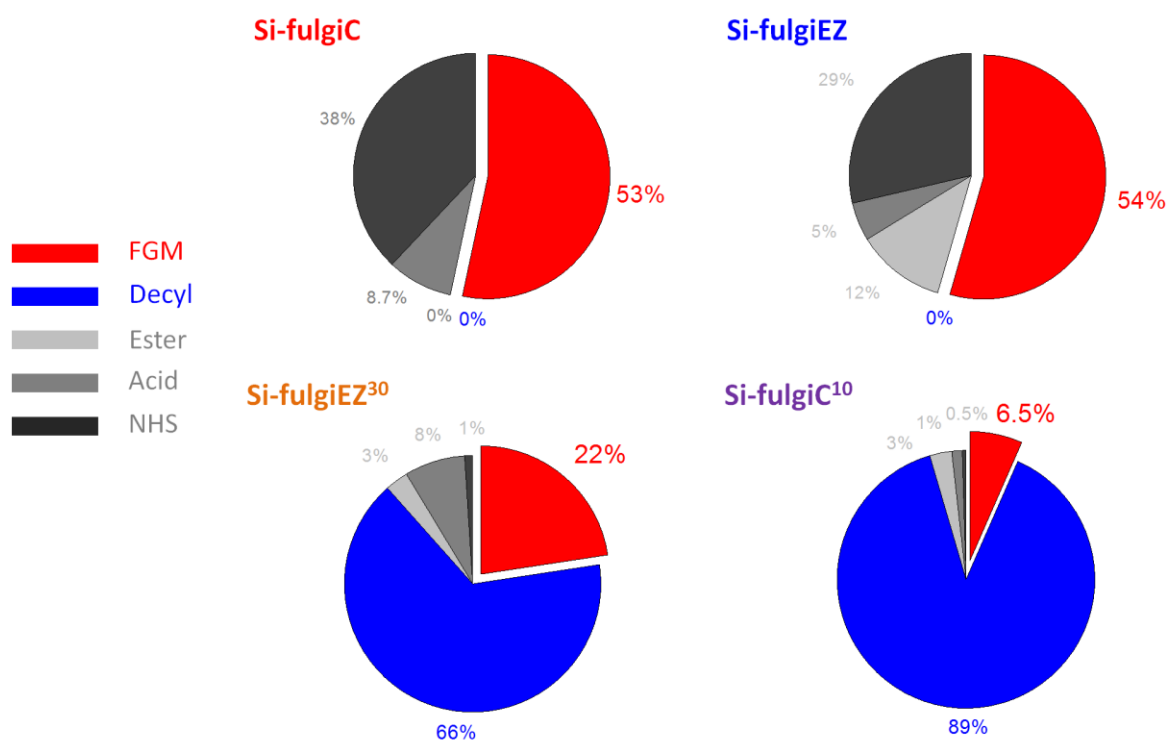


**Figure 4.8.** Nature and fraction of end-groups present on *dense* and *diluted* fulgimide-terminated surfaces.

Fig. 4.9 shows the conformation of C, E and Z-isomers attached to an acid ML through an aminoethyl linker, as calculated by Alchemy® software. C and E isomers stand vertically and have very close conformation that let anticipate that the structural changes leading to the  $C \rightleftharpoons E$  isomerization should not be too much influenced by the presence of residual functional groups on top of the underneath alkyl ML. For the the Z isomers the situation is different. Part of the fulgimide is closer to the underneath molecular carpet which let anticipate that interactions with the chemical tail-group of the ML could influence the rate of the  $E \rightleftharpoons Z$  isomerization. The control of the chemical composition of the molecular carpet surrounding the photochromic compounds then appears as an important issue with respect to the photoswitching properties of fulgimide MLs.

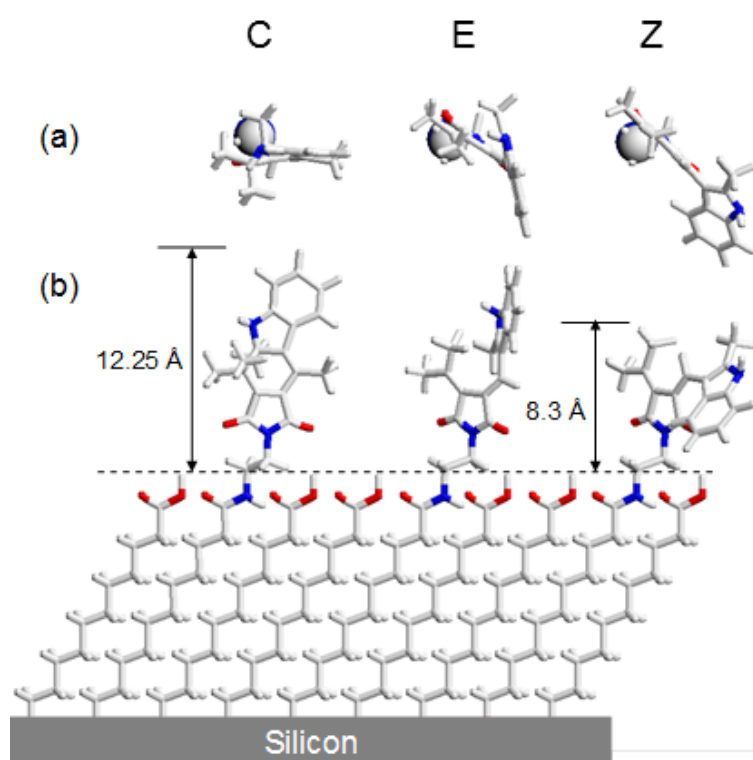


**Figure 4.9.** Top (a) and side (b) views of the structure of C, E and Z isomers linked on top of carboxyl chains grafted on Si surface, through aminoethyl linker.

## Conclusions

In this chapter, we have successfully prepared fulgimide-terminated surfaces with controlled density of photochromic molecules. The surfaces have been prepared by covalent linkage of amino-substituted fulgimides on surfaces exhibiting different surface concentration of COOH anchoring sites. At each step, the composition of the MLs was determined by quantitative FTIR analysis. It has been shown that, on *pure* acid MLs, the coupling reaction is not quantitative because of the bulky structure of indolylfulgimide groups. A maximum concentration of  $\sim 1.7 \times 10^{14}$  fulgimides  $\text{cm}^{-2}$  ( $\sim 60\%$  coverage with respect to the e COOH concentration) was obtained. Such concentration is close to the maximum packing density of indolylfulgimide groups which indicates the formation of densely packed fulgimide MLs. By diminishing the concentration of acid chains within the MLs, less dense fulgimide MLs were obtained allowing for limiting – *a priori* – the steric constraints that could influence the photo-isomerization rates on the surface.

## References

- (1) Touahir, L.; Chazalviel, J. N.; Sam, S.; Moraillon, A.; de Villeneuve, C. H.; Allongue, P.; Ozanam, F.; Gouget-Laemmel, A. C. *Journal of Physical Chemistry C* **2011**, *115*, 6782.
- (2) Koller, F. O.; Schreier, W. J.; Schrader, T. E.; Sieg, A.; Malkmus, S.; Schulz, C.; Dietrich, S.; Ruck-Braun, K.; Zinth, W.; Braun, M. *Journal of Physical Chemistry A* **2006**, *110*, 12769.
- (3) Faucheux, A.; Gouget-Laemmel, A. C.; de Villeneuve, C. H.; Boukherroub, R.; Ozanam, F.; Allongue, P.; Chazalviel, J. N. *Langmuir* **2006**, *22*, 153.
- (4) Moraillon, A.; Gouget-Laemmel, A. C.; Ozanam, F.; Chazalviel, J. N. *Journal of Physical Chemistry C* **2008**, *112*, 7158.

# Chapter 5

## Photoswitching properties of fulgimides at Si surface

---

### Table of Contents

---

Introduction .....	118
5.1. Experimental illumination set-up and procedures.....	120
5.2. FTIR measurements .....	124
5.2.1. Qualitative analysis.....	124
5.2.2. Quantitative analysis.....	127
5.2.2.1. Determination of isomeric composition of monolayers at PSS .....	127
5.2.2.2. Isomeric composition of <i>dense</i> fulgimide-terminated monolayers .....	129
5.2.3. Kinetics of fulgimide photoswitching .....	131
5.2.3.1. Evolution of surface concentration of fulgimides during an illumination cycle...	131
5.2.3.2. Quantitative analysis of differential spectra.....	132
5.2.3.3. Determination of the kinetic parameters.....	133
5.2.3.4. Evolution of kinetic parameters over repeated illumination cycles .....	135
5.2.3.5. Kinetic parameters as function of experimental conditions.....	137
5.3. Discussion .....	139
5.3.1. Photoswitching mechanism .....	139
5.3.2. The concentration of photo- <i>isomerizable</i> species on <i>dense</i> and <i>diluted</i> surfaces.....	140
5.3.3. Local electric field at fulgimide surfaces.....	141
5.3.4. Kinetic parameters .....	143
Conclusions .....	146
References .....	147

---

## Introduction

The anchoring of photochromes on solid surfaces is of great interest for numerous applications (microfluidics,<sup>1</sup> cell culturing<sup>2</sup> /or data storage<sup>3-6</sup>...). Their immobilization on surfaces keeping their photoactivity remains however very often a challenge. One of the main concerns is the peculiar environment of the photochromes. Several studies report the inhibition of light-induced isomerization in dense monolayers because of steric hindrance. Together with steric effects, interactions between neighbor photochromes or with the surface, as well as the close vicinity of the substrate are also factors that are often discussed as possibly affecting the isomerization rate.

Many works dealing with the study of the properties of photocommutation of organic photochromes on surfaces were reported in the literature. The photochromes are in general immobilized on metal surfaces through Self-Assembly of thiol derivatives (SAMs on Gold). The read-out of the commutation is achieved either by monitoring modifications of macroscopic properties (wettability, optical or electrical properties...) or locally at molecular level using Scanning Probe Microscopy (STM, AFM ...). Photoswitching of layers of azobenzene derivatives was investigated by contact angle measurements,<sup>7,8</sup> variations of refractive index<sup>7,9</sup> or surface charge measurements. Measurements of changes of optical properties such as reflectance,<sup>10</sup> fluorescence<sup>4</sup> or absorbance<sup>11</sup> in the UV-Vis range are also reported, as well as electrochemical measurements.<sup>9</sup> Locally, the photocommutation of individual molecules have been detected by SPM by measuring variations of tip height or conductance<sup>7,12-15</sup> or surface charge.<sup>16</sup>

Another important issue concerns the conformational freedom required for photoisomerization, in terms of both photoswitching times and quantum yields<sup>17</sup> taking into account that the steric hindrance effect is much more important than the change in molecular properties induced by immobilization on surface, such as the quenching of electronically excited states.

Despite all the measurements used for the study of switchable monolayers, the quantitative analysis of the density of active groups and the fraction of which is commuting has not been well developed. It turns out that FTIR measurements can be used as a readout method of surface switching for a quantitative analysis of photochromic monolayers on silicon.<sup>18</sup> The technique enables to determine *in situ* the change of the surface composition

during the illumination cycle. As a matter of fact, it brings a possibility to study the kinetics of molecular photoswitching on surface.

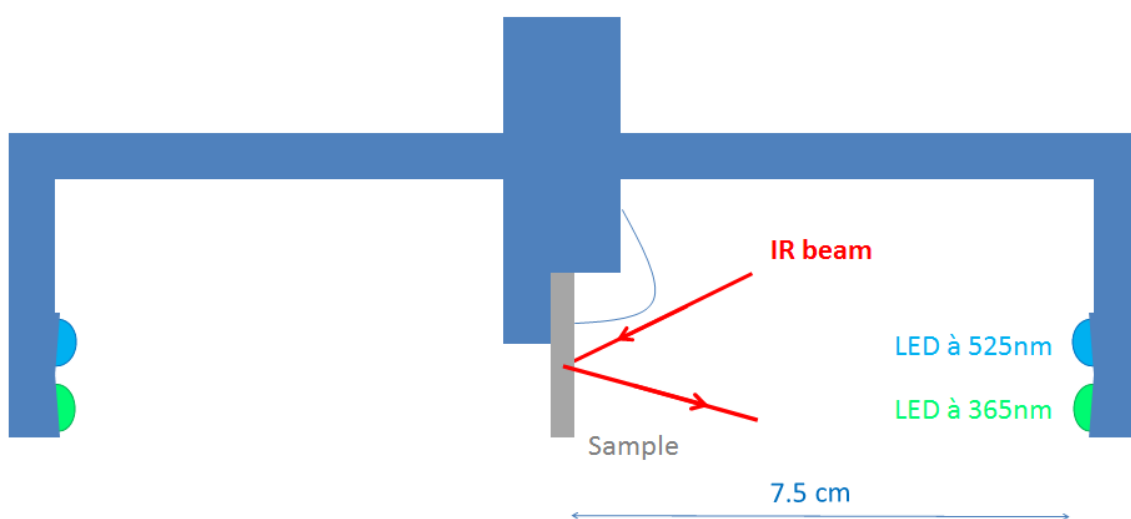
As seen in Chapter 2 and 3, fulgimide molecules with excellent photoswitching reversibility, thermal stability of the different isomers and resistance to fatigue solution were successfully immobilized on  $\omega$ -functionalized surface using the two-step protocol. Finally, the chemical composition was determined using calibrated FTIR measurements.

Within this chapter we have implemented an original approach to investigate the photoswitching properties of fulgimide monolayers on silicon surfaces. The photocommutation was monitored by FTIR measurements that not only allow for a non-destructive read-out of the photo-isomerization but also allow for the quantitative determination of the surface concentration of photochromes and the light-induced variations of isomeric composition on the surface. An illumination set-up was specifically designed for *in situ* illumination of the Si-Fulgimide surfaces during the FTIR measurements. The illumination set up was designed to control the properties of light beam (intensity and polarization) so as to investigate their influence on the photocommutation rate.

## 5.1. Experimental illumination set-up and procedures

### Experimental set-up:

For the study *in situ* UV/Vis of photochromic (PC) species on surface, we used a similar set-up described previously for solution measurement by replacing quartz cuvette with fulgimide-terminated surfaces (Fig. 5.1). Note that the distance between light sources and surfaces (7.5 cm) is longer than that between light sources and cuvette (4 cm). The LEDs can be turned on/off or switched remotely from one to another light from the outside of ATR chamber at its maximum power. The photon flux is measured by a photodiode S2387-R33 purchased from Hamamatsu operated in reverse bias at 24 V. This photodiode has a photosensitive area of 2.4 mm × 2.4 mm and a photosensitivity of 0.3 and 0.17 A W<sup>-1</sup> at 525 nm and 365 nm, respectively. The current measured from the photodiode is then converted to the light power and photon flux. All the characteristics of UV and Vis illumination of this first experimental set-up are listed in Table 5.1.

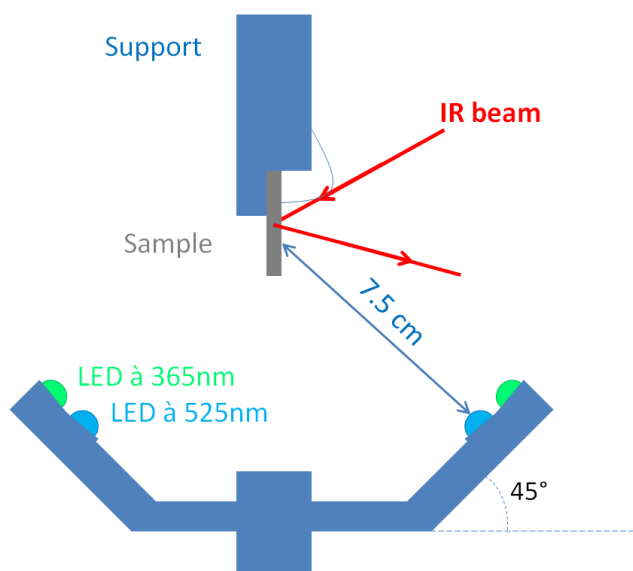


**Figure 5.1.** First experimental set-up used for *in situ* Vis/UV illumination of Si-Fulgi surface inside ATR chamber of the FTIR spectrophotometer.

	Photon energy (J)	Current measured in reverse bias ( $\mu$ A)	Light power (mW cm <sup>-2</sup> )	Photon flux arrived on surface (cm <sup>-2</sup> s <sup>-1</sup> )
Vis Light (525 nm)	$3.89 \times 10^{-19}$	213	12.33	$3.17 \times 10^{16}$
UV Light (365 nm)	$5.45 \times 10^{-19}$	17	1.74	$0.32 \times 10^{16}$

**Table 5.1. Characteristics of the incident beam in the first experimental set-up.**

In the second experimental set-up we have developed, the position of the LEDs was modified in order to have a beam impinging at 45° on the surface. This configuration allows for splitting the electromagnetic field into two components (in-plane and out-of plane) to investigate orientation effects on the isomerization rate - (Fig. 5.2). In this case, the photon flux is calculated by dividing the values in Table 5.1 by  $\sqrt{2}$ .

**Figure 5.2. Second experimental set-up used for *in situ* Vis/UV illuminations in the ATR-chamber of the FTIR spectrophotometer.**

Finally we have designed a third set-up that allows for a better control of the characteristics of the electromagnetic field impinging on the surface (intensity and polarization) (Fig. 5.3).

The whole system is fixed on the basement of the ATR-chamber of the spectrophotometer underneath the sample holder. The system has been designed in such way that it is possible to vary the angle of the beam impinging on the sample surface. Different optical elements were installed on the beam path in order to control the intensity and the polarization of the light (Fig. 5.4):

- Filters (magenta elements) allow for adjusting the photon flux.
- Cylindrical lenses (cyan elements) allows for focalizing the divergent beam and making it parallel and homogeneous.
- Polarizers (green elements) allow for selecting one of the components of the electromagnetic field (s- or p-polarization).

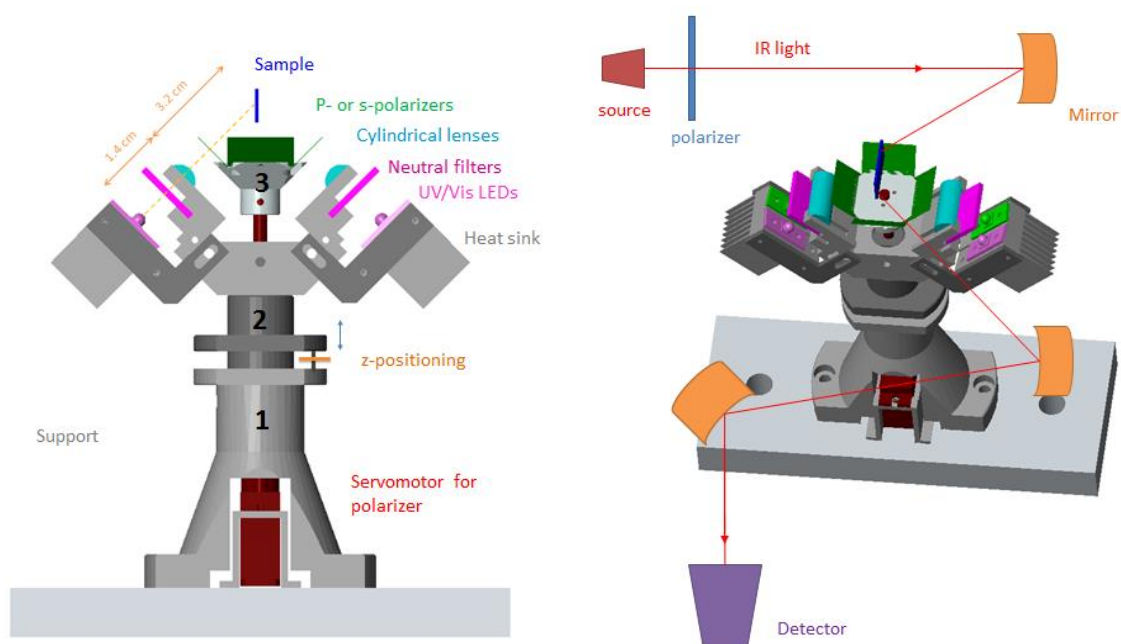


**Figure 5.3.** Third set-up designed for in situ Vis/UV illumination inside the ATR-chamber of the FTIR spectrophotometer.

Figure 5.4 shows all the optical elements in one branch of the alignment. The photon flux is measured using the photodiode described previously, placed at the same place as sample. By moving the window of photodiode to different places inside the light beam, it has been found that the photon flux is homogenous over a surface of  $1 \text{ cm} \times 2 \text{ cm}$  which is required for the study. The Vis and UV photon flux and the transmission coefficient of each optical element are shown in Tables 5.2 and 5.3.

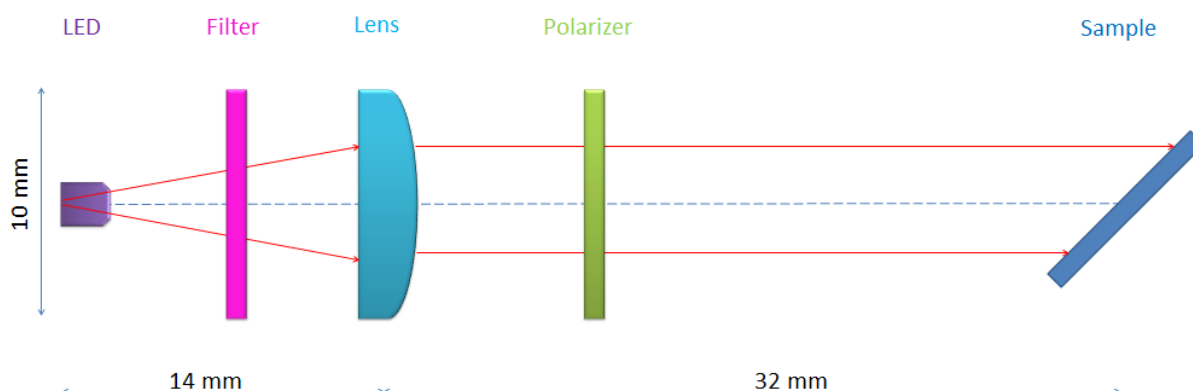


**Figure 5.4.** Scheme of the different optical elements set on the beam path. The filters allow for reducing the photon flux, the cylindrical lens converts the divergent beam into parallel and homogeneous beam, the polarizer allows for selecting one of the component of the electromagnetic field (s- or p-polarization).

Optical elements	Vis Light (525 nm)			
	Current measured in reverse bias ( $\mu\text{A}$ )	Light power ( $\text{mW cm}^{-2}$ )	Photon flux ( $\text{cm}^{-2} \text{s}^{-1}$ )	Transmission coefficient
Lens	1044	42.7	$11 \times 10^{16}$	0.39
Lens + Polarizer	406	16.6	$4.3 \times 10^{16}$	

**Table 5.2. Characteristics of Vis beam light in the third experimental set-up.**

Optical elements	UV Light (365 nm)			
	Current measured in reverse bias ( $\mu\text{A}$ )	Light power ( $\text{mW cm}^{-2}$ )	Photon flux ( $\text{cm}^{-2} \text{s}^{-1}$ )	Transmission coefficient
Lens	99	7.2	$1.3 \times 10^{16}$	0.22
Lens + Polarizer	22	1.6	$0.29 \times 10^{16}$	

**Table 5.3. Characteristics of the UV beam light in the third experimental set-up.**

*Photocommutation experiments:*

For monitoring the isomerization, the Si-Fulgi surfaces were positioned in the middle of the optical device and were illuminated during successive short times. FTIR spectra were recorded after each illumination, while light was turned off. Illumination sequences were repeated until a photo-stationary state (PSS) was obtained ca. until no sizeable change was detected on successive spectra. We define one illumination cycle (UV or Vis) as the cumulated illumination time required to switch a fulgimide ML from its initial state (as-prepared surfaces) to the first  $\text{PSS}_{\text{UV}}$  or  $\text{PSS}_{\text{Vis}}$ , or from one PSS to the next one.

## 5.2. FTIR measurements

Figure 5.5 recalls the photochromism of fulgimides. The fulgimide-terminated surfaces are illuminated under UV (for fulgiEZ-terminated surface) or Vis light (for fulgiC-terminated surface). Once it reaches the photostationary state (PSS), surfaces are labelled as  $\text{PSS}_{\text{UV}}\text{Si-fulgi}$  or  $\text{PSS}_{\text{Vis}}\text{Si-fulgi}$ . Depending on the type of the as-prepared surface; **fulgi** can be replaced by the surface name as labelled in Section 4.1. A number will be put in front of PSS index as the number of illumination cycle. For example, an as-prepared *dense* Si-fulgiC monolayer illuminated under Vis light for C  $\rightarrow$  E reaction until it reaches the  $\text{PSS}_{\text{Vis}}$  of the first illumination cycle is labelled  $^1\text{-PSS}_{\text{Vis}}\text{Si-fulgiC}$ . Subsequently, the surface is illuminated under UV light for the second cycle illumination until it reaches the second  $\text{PSS}_{\text{UV}}$ ; at the end of this second cycle, it is labelled  $^2\text{-PSS}_{\text{UV}}\text{Si-fulgiC}$ .

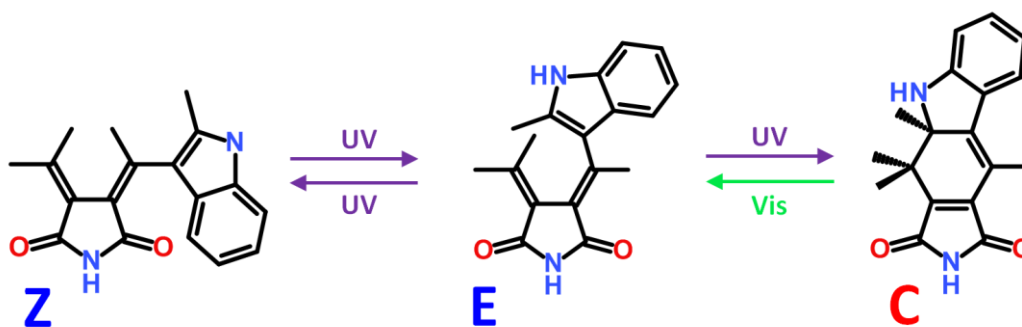
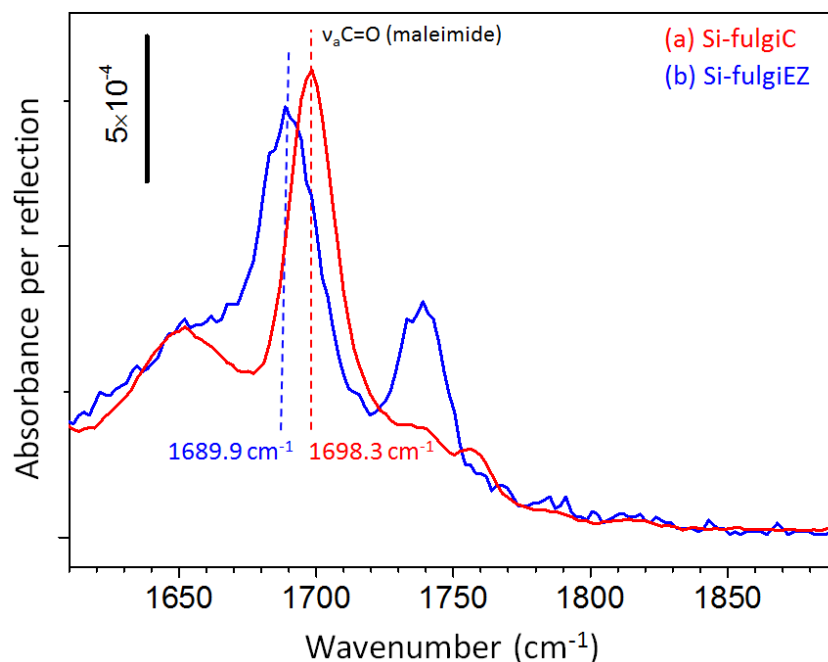


Figure 5.5. Photochromism of indolyfulgimide under Vis/UV irradiation.

### 5.2.1. Qualitative analysis

As shown in Section 4.2.1, E/Z- and C-forms isomers exhibit different IR absorbance bands that provide a mean for identifying them. Figure 5.6 shows the FTIR spectra of two *dense* Si-fulgiEZ and Si-fulgiC surfaces. We recall that the two *open* structures (E- and Z-isomers) exhibit similar IR properties that make it impossible to differentiate them. In the following, we have used the specific IR signature of E/Z- and C-forms to investigate the light induced isomerization on the surface. The read-out of the photoswitching has been first done by monitoring the position the main carbonyl  $\nu_{\text{C=O}}$  peak of maleimide groups. This peak has been chosen because it is intense and stands at well separated position depending on the isomer structure:  $\sim 1698\text{ cm}^{-1}$  for C-isomers and  $\sim 1690\text{ cm}^{-1}$  for E/Z-isomers. It's noteworthy

that the band at  $\sim 1740\text{ cm}^{-1}$  cannot be used because it's an overlap between NHS-related bands and the carbonyl  $\nu_s\text{C}=\text{O}$  peak of maleimide groups.



**Figure 5.6.** FTIR absorbance spectra of *dense* Si-fulgiEZ and *dense* Si-fulgiC showing the main carbonyl  $\nu_a\text{C}=\text{O}$  bands stand respectively at  $1689.9$  and  $1698.3\text{ cm}^{-1}$ .

The occurrence of isomerization under illumination was assessed by looking at the evolution of the absorbance of the main  $\nu_a\text{C}=\text{O}$  bands that stand at specific positions for E/Z ( $1690\text{ cm}^{-1}$ ) and C-forms ( $1700\text{ cm}^{-1}$ ). Figure 5.7 shows two series of IR spectra of a *dense* Si-fulgiEZ surface (fulgimide concentration of  $1.6 \times 10^{14}\text{ cm}^{-2}$ ) captured during UV and subsequent Vis illumination cycles. During UV illumination (Fig. 5.7A) a shift of the main carbonyl band takes place toward greater wavenumber. The band moves backward to its initial position at  $1690\text{ cm}^{-1}$  under Vis illumination (Fig. 5.7B). In parallel, anti-correlated variations of the intensity of the band at  $1739$  and  $1758\text{ cm}^{-1}$  are also observed, indicating the disappearance of EZ-forms and the appearance of C-forms under UV light and reverse process under Vis light. However, comparison of the spectra obtained at the end of the first UV illumination sequence (Fig. 5.7) with the spectra of an as-prepared Si-fulgiC surface (Fig. 5.6) suggests that the photo-isomerization is not total. The spectra modification clearly states light-induced surface modifications that can be assigned to a partial  $\text{E} \rightarrow \text{C}$  then  $\text{C} \rightarrow \text{E}$  isomerization (Fig. 5.5). Moreover, no variation is observed on both  $\nu\text{C}=\text{O}$  bands at  $1788$  and  $1819\text{ cm}^{-1}$  related to the residual succinimide groups indicating that the illumination does not affect the NHS groups under fulgimide layer.

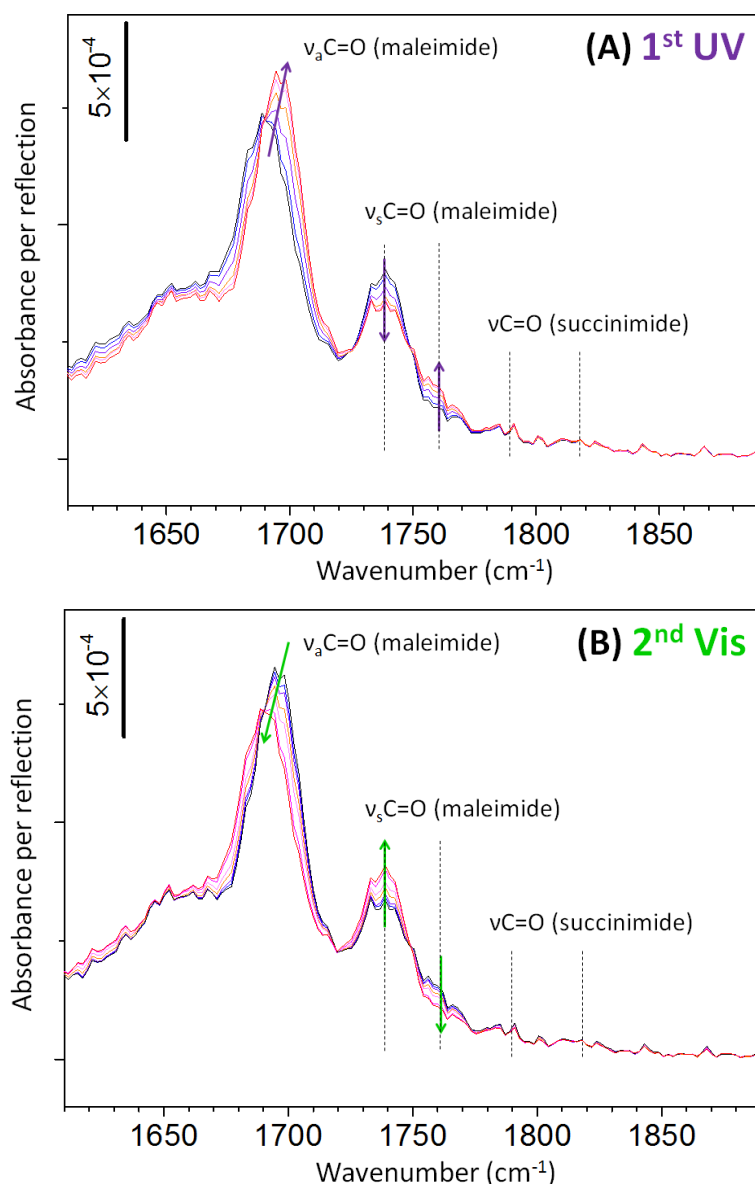


**Figure 5.7.** Evolution of FTIR absorbance spectra of a *dense* Si-fulgiEZ surface ( $1.7 \times 10^{14}$  E/Z-forms  $\text{cm}^{-2}$ ) under UV (A) and then Vis (B) illuminations.

In order to obtain a more detailed analysis, the position of the  $\nu_a\text{C=O}$  peak related to the stretching of the carbonyl mode in maleimide group (see Table 4.) at  $\text{PSS}_{\text{UV}}$  and  $\text{PSS}_{\text{Vis}}$  after successive UV-Vis illumination cycles of as-prepared *dense* Si-fulgiEZ and *dense* Si-fulgiC surfaces are plotted respectively (Fig. 5.8A and B). The position was taken from the fit of the half top part of the peak with a Gaussian profile. In both cases, a reversible shift of the peak between two positions is observed indicating reversible switching between two surface states. It is noteworthy that the position of the peak at PSSs does not fit the position corresponding to *dense* Si-fulgiC or Si-fulgiEZ monolayers. This confirms that at PSS the monolayer is composed of a mixture of E/Z- and C-isomers at PSSs.

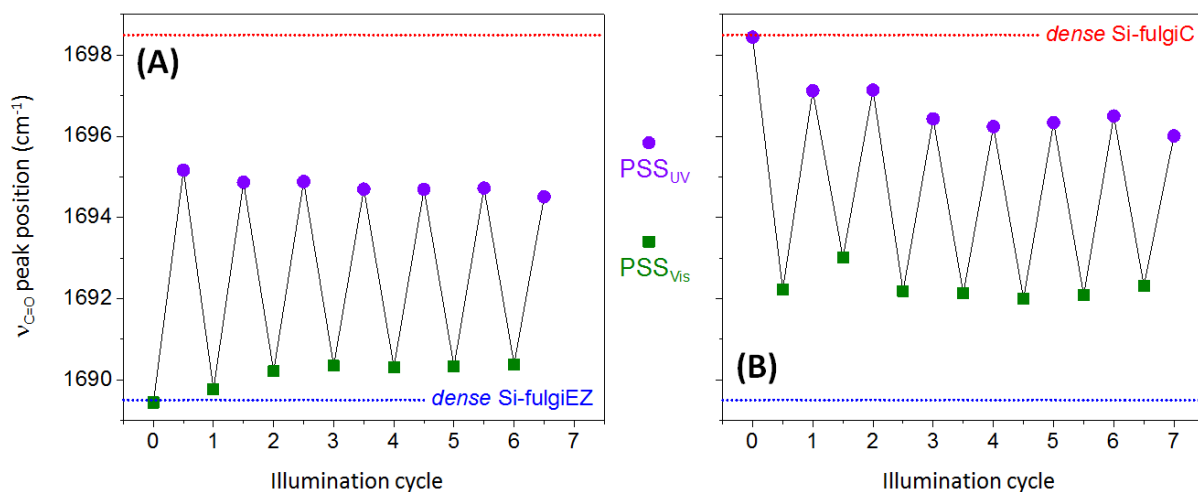


**Figure 5.8.** Position of the main  $\nu_{C=O}$  peak at  $\text{PSS}_{UV}$  and  $\text{PSS}_{Vis}$  after successive UV/Vis illumination cycles of as-prepared *dense Si-fulgiEZ* (A) and *dense Si-fulgiC* (B) surfaces. The red and blue dotted lines correspond to its position found in the initial spectra of two surfaces prior to any illumination.

The formation of C-isomers and their backward conversion to E-isomers is even better evidenced on differential spectra, taking the as-prepared initial surface prior to any light exposure as the reference (see later in Fig. 5.12). On these spectra, only absorbance variations resulting from illumination are observed, the disappearance and appearance of absorbing species giving rise to negative and positive bands, respectively.

## 5.2.2. Quantitative analysis

### 5.2.2.1. Determination of isomeric composition of monolayers at PSS

As shown in Fig. 5.7, the photo-isomerization between open (EZ-) and closed (C-) form can be observed with the evolution of the FTIR spectra of fulgimide surfaces. The analysis of the  $\nu_{C=O}$  peak position indicates that both UV and Vis transformations are not complete. Therefore, a quantitative method is adopted to determine the isomeric composition of the monolayers. For that, two spectra of *pure* EZ- and C-isomer on surface need to be obtained from the spectra of as-prepared *dense Si-fulgiEZ* and *dense Si-fulgiC* surfaces. These two spectra are taken from the following procedure: First, the spectra of as-prepared *dense Si-fulgiEZ* and *dense Si-fulgiC* are plotted referred to the spectra of the same surface prior to fulgimide coupling. The obtained spectra contain only the appearance of the coupled fulgimides and the disappearance of the removed NHS groups. Finally, the spectra of *pure*

EZ- and C-isomer were obtained by adding the previous spectra to the *pure* NHS spectra with an integrated absorbance found in Section 4.2.1 for each surface. In order to fit with these two spectra of *pure* EZ- and C-isomer to obtain the fulgimide composition in monolayer at PSS, each corresponding FTIR spectrum is pre-analyzed with the same previous procedure to obtain the spectrum containing only fulgimide absorbance bands.

The fitting of each analyzed spectrum at PSS is performed by using software named FITUNIV developed by professor Chazalviel. It consists of fitting with two spectra of *pure* EZ- and C-isomer with the well-known surface concentration determined in Section 4.2.2 ( $1.6 \times 10^{14}$  C-isomers  $\text{cm}^{-2}$  and  $1.71 \times 10^{14}$  EZ-isomers  $\text{cm}^{-2}$ ), e.g., the fitting of spectrum of the first PSS<sub>UV</sub> of an as-prepared *dense* Si-fulgiEZ surface is plotted in Fig. 5.9. The surface composition of  $^1\text{-PSS}_{\text{UV}}$  Si-fulgiEZ surface can be then determined as a mixture of  $8.8 \times 10^{13}$  C-isomer  $\text{cm}^{-2}$  and  $8.2 \times 10^{13}$  EZ-isomer  $\text{cm}^{-2}$  which correspond to a ratio 52:48 of C:EZ isomers. The concentration of C-forms will be called as that of photo-isomerizable fulgimides of the *dense* Si-fulgiEZ surface.

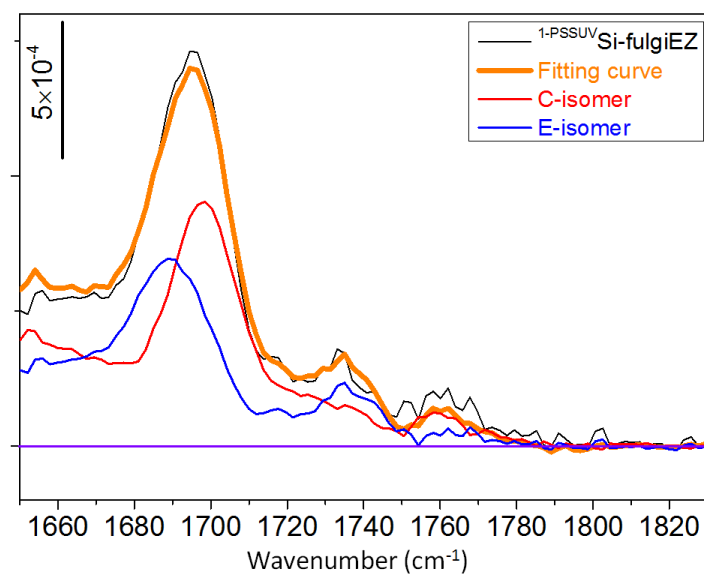


**Figure 5.9.** Experimental spectrum of of an as-prepared *dense* Si-fulgiEZ surface after UV illumination (black plot) and its spectral deconvolution using a linear combination of the spectrum of a *pure* FulgiC- (red plot) and a *pure* FulgiE/Z (blue plot) surface. The resulting fitting curve is plotted in orange.

### 5.2.2.2. Isomeric composition of *dense* fulgimide-terminated monolayers

Figure 5.10 and 5.11 compare the isomeric composition at PSSs during repeated illumination cycles for as-prepared *dense* Si-fulgiC (Fig. 5.10) and *dense* Si-fulgiEZ (Fig. 5.11) surfaces. The surface concentration of closed C- (■) and open E/Z-forms (●) at PSSs and the total fulgimide concentration (▲) are presented as a function of the number of illumination cycles. On the X-axis, odd and even cycle numbers correspond to PSS reached after Vis or UV illumination sequence, respectively. ‘0’ corresponds to the as-prepared surface prior to any illumination.

#### Isomeric composition at PSSs of as-prepared dense Si-FulgiC

Figure 5.10A displays the evolution of the isomeric composition for the *dense* Si-FulgiC surface with a nominal concentration of  $1.6 \times 10^{14}$  FulgiC.cm<sup>-2</sup>).

After the first Vis illumination cycle (cycle 1), ~80% of the C-forms initially present on the surface have been transformed to E-forms (C → E is the sole possible reaction path under Vis illumination). At the first PSS<sub>Vis</sub>, the monolayer is thus composed of a majority of E forms (80%) and of 20% of C isomers that didn’t undergo isomerization. The fraction of *non-photoactive* C-isomers is represented in red dashed bars in Fig. 5.10B. After the subsequent UV illumination (cycle 2) one observes that only a fraction of the E-isomers formed during the previous Vis illumination, is converted in C forms. At the PSS<sub>UV</sub> (cycle 2) the ML is again enriched in C forms (~70%) with however a residual fraction of open forms (~30% EZ isomers). Because E ↔ Z isomerization can also take place under UV, one cannot discard the existence of a mixture of E and Z forms at this stage. Unfortunately, the two open forms give similar IR signatures making impossible their individual identification.

During the next successive illumination cycles, a reversible commutation is observed between two surface states: one corresponding to a ML enriched in C forms (PSS<sub>UV</sub>, even cycles) and the second corresponding to a ML with a majority of open E/Z forms (PSS<sub>Vis</sub>, odd cycles). Over the repeated illuminations, the fraction of *non-photoactive* FulgiC (dashed red bars) remains almost constant even though a slight rising is observed that could indicate the existence of some photofatigue.

If one consider only the fraction of *photoactive* fulgimides (red and blue bars), the (E+Z / C) ratio is (100 / 0) at PSS<sub>Vis</sub> and evolves from (40 / 60) to (50 / 50) at PSS<sub>UV</sub>. The

isomeric composition at  $PSS_{UV}$  is different from that obtained in solution (25 / 75). By comparison less efficient (E,Z)  $\rightarrow$  C conversion is observed under UV.

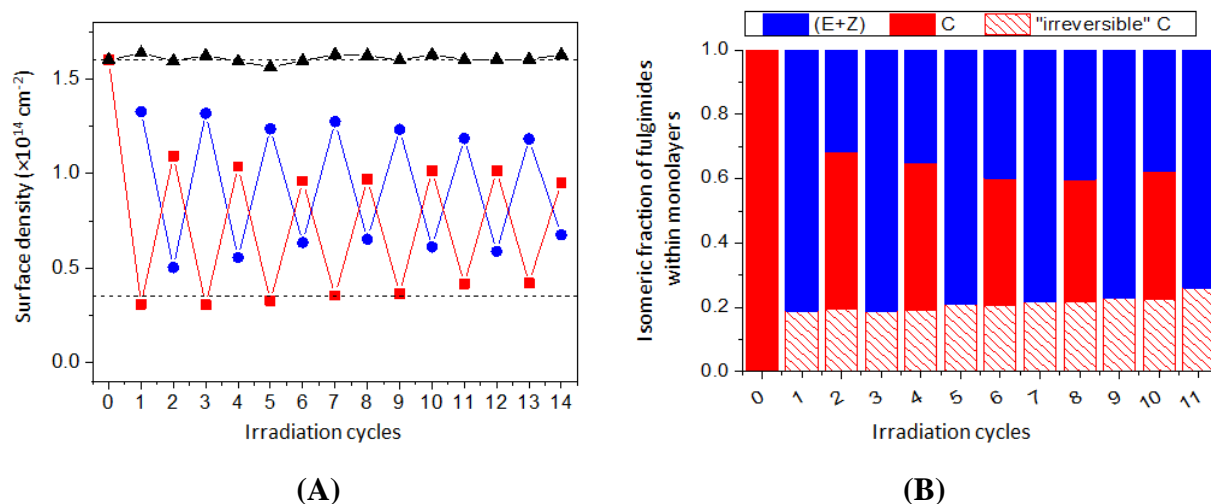


**Figure 5.10.** Isomeric composition of an as-prepared *dense* Si-fulgiC surface at the PSSs after successive Vis/UV illumination. (A) Surface concentration of open forms E/Z (●) and closed forms C- (■). The black triangles (▲) are the sum of C and EZ concentration. (B) Isomeric fraction as a function of the illumination cycles. Red bars correspond to the fraction of C isomers and blue bars to that of EZ isomers. Dashed red bars indicate the fraction of *non photoactive* C-isomers (see text) Odd numbers on X-axis refer to PSSs reached after Vis illuminations and even number to PSSs reached after UV illuminations. “0” gives the ML composition prior to any illumination. The surface was illuminated with the first experimental set-up ( $\phi_{UV} = 0.32 \times 10^{16}$  cm $^{-2}$  s $^{-1}$  and  $\phi_{Vis} = 3.17 \times 10^{16}$  cm $^{-2}$  s $^{-1}$ ).

#### Isomeric composition at PSSs of as-prepared dense Si-fulgiEZ

Similar successive illumination experiments have been carried out starting from a *dense* Si-fulgiEZ surface (initial surface concentration is  $1.7 \times 10^{14}$  EZ-isomer cm $^{-2}$ ). The surface concentration and isomeric fraction of fulgimides in ML at PSSs are plotted in Fig. 5.11A and B, respectively. The surface concentration of closed C- (■) and E/Z-forms (●) at PSSs and the total fulgimide concentration (▲) are presented as a function of the number of illumination cycles (Fig. 5.11A). Surface was illuminated by the first experimental photosystem with UV and Vis photon flux  $\phi_{UV} = 3.2 \times 10^{15}$  cm $^{-2}$  s $^{-1}$  and  $\phi_{Vis} = 3.2 \times 10^{16}$  cm $^{-2}$  s $^{-1}$ .

In this case, odd and even cycle numbers refer to PSSs obtained after UV and Vis illumination, respectively. After the first UV illumination (first cycle), 50% of the E/Z-forms composing the monolayer have been transformed in C-isomers (Fig. 5.11B). After the

subsequent Vis illumination (second cycle) most of the closed C-forms have undergone back  $C \rightarrow E$  conversion (96%). However it is noteworthy that some of the C-forms remain present and that their amount tends to slightly rise over the successive illumination sequences. The monolayer at  $PSS_{Vis}$  remains majority composed of open (Z+E)-forms with at least  $\sim 90\%$ . At  $PSS_{UV}$ , the isomeric ratio (E+Z)/C is 50/50 and remains more or less constant, with however  $\sim 10\%$  of C-forms inactive.

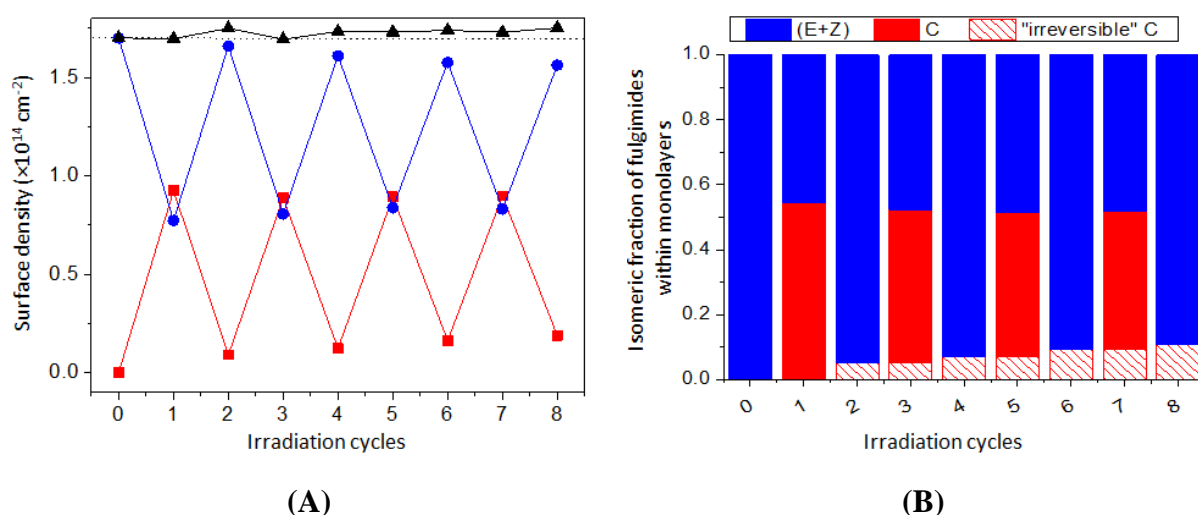


**Figure 5.11.** Isomeric composition of an as-prepared *dense* Si-fulgiEZ monolayer at the PSSs after successive UV/Vis illumination cycles. (A) Surface concentration of E/Z- (●) and C- (■) forms. The black triangles (▲) represent the sum of C and E/Z forms. (B) Isomeric fraction as a function of the number of illumination cycles. The red bars refer to the ratio of C forms and the blue bars to that of EZ forms. Dashed red bars represent the fraction of C forms that become non-photoactive during illuminations. On the X axis odd numbers refer to PSS reached under UV illumination and even numbers to those reached under Vis illumination. “0” gives the composition of the ML prior to any illumination.

### 5.2.3. Kinetics of fulgimide photoswitching

#### 5.2.3.1. Evolution of surface concentration of fulgimides during an illumination cycle

Figure 5.12 shows the change in the infrared spectrum under UV (Fig. 5.12A) then Vis (Fig. 5.12B) illumination using the spectrum at the initial time as a reference. This differential form highlights the evolution in the IR spectrum solely due to illumination. In Fig. 5.12A, the disappearance of E-forms and the formation of C-forms under UV illumination is clearly

evidenced through the simultaneous and progressive growing amplitude of two negative bands at  $\sim 1690$  and  $1739\text{ cm}^{-1}$  (red arrows) and two positive bands at  $\sim 1700$  and  $1758\text{ cm}^{-1}$  (blue arrows). Under subsequent Vis illumination a reverse evolution is observed, the positive and negative bands progressively vanishing, indicating a return to a surface composition close to that prior to UV illumination (Fig. 5.12B). Purple and green arrow indicates the time evolution under UV and Vis light, respectively. At the second PSS<sup>Vis</sup>, the IR bands do not disappear completely, showing that a part of the fulgimides isomerized under UV illumination cannot transform back to their initial form.

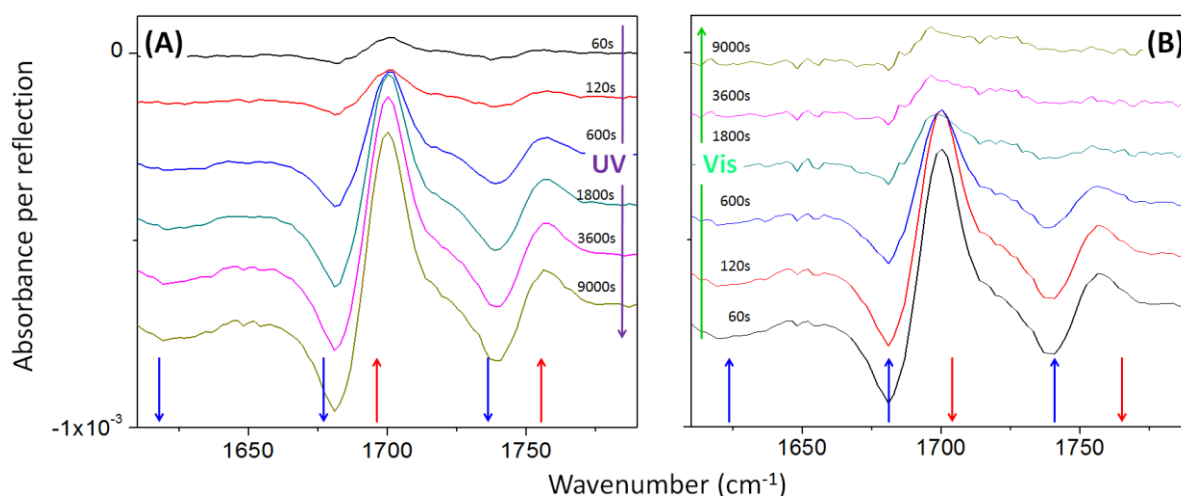


**Figure 5.12.** Differential FTIR spectra highlighting changes in C- and E/Z-isomers during first UV (A) and subsequent second Vis illumination (B). Arrows indicate the evolution of E/Z- (blue) and C-form (red) concentrations. The reference is that of the initially *dense Si-fulgiEZ* surface. The green and purple arrow corresponds to the time axe of illumination.

### 5.2.3.2. Quantitative analysis of differential spectra

The *in situ* illumination set-up in the ATR chamber and the capacity of determining the fulgimide concentrations in monolayer have been used for studying the kinetics of photo-isomerization of fulgimide at surface. The study was carried out by measuring the concentration of C- and E/Z-forms during successive short times of an illumination cycle using the differential spectra such as that shown in Fig. 5.12. For that purpose, the differential spectrum at each illumination time is fitted as a fraction of that at PSS of the same cycle, i.e., a degree of advancement of the photo-isomerization process toward the PSS is determined. For instance, a differential spectrum of the dense Si-fulgiEZ surface after 180s of illumination during the first UV cycle is fitted as a fraction of 0.21 of the differential spectrum of the first

PSS<sub>UV</sub> (Fig. 5.13A). The photo-*isomerized* fulgimide fraction measured from the fit is plotted in Fig. 5.13B as a function of the illumination time during the first UV cycle for an as-prepared *dense* Si-fulgiEZ surface. Similar curves were drawn for different cycles. The good fit observed using this method indicates that the sole apparent change under illumination is related to photo-isomerization.

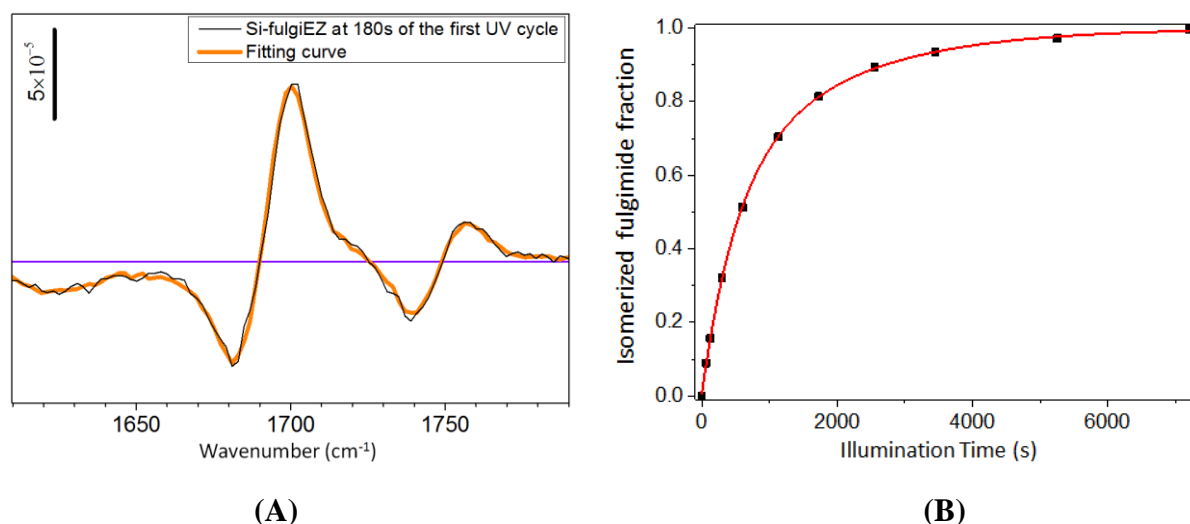


**Figure 5.13.** (A) Differential spectrum (black) of the *dense* Si-fulgiEZ surface at 180s of its first UV cycle and the fitting curve (orange) corresponding to 0.21 of the differential spectrum of its first PSS<sub>UV</sub>. (B) Evolution of *isomerized* coefficient of the first UV cycle on an as-prepared *dense* Si-fulgiEZ surface and its fitting curve (red line).

Using the quantitative determination of the surface composition at PSS, the photo-*isomerized* fulgimide fraction determined from the fit can be converted into a concentration of photo-*isomerized* fulgimides. For example, after 180s during the first cycle, a fraction of 0.21 is found. The concentration of photo-*isomerizable* fulgimides is  $8.8 \times 10^{13} \text{ cm}^{-2}$  for <sup>1-PSS<sub>UV</sub></sup>Si-fulgiEZ surface, as determined in section II.2.1. Therefore, the concentration of photo-*isomerized* fulgimides at 180s of the first cycle is simply  $1.85 \times 10^{13} \text{ cm}^{-2}$ .

### 5.2.3.3. Determination of the kinetic parameters

Figure 5.14 shows an evolution of the surface concentration of fulgimide isomerized during the first UV illumination cycle for an as-prepared *dense* Si-fulgiEZ surface ( $1.7 \times 10^{14} \text{ cm}^{-2}$ ). In a first approach, the evolution was fitted to a mono- or bi-exponential function. The lack of data (only ~12 data points in each illumination cycle) makes the parameters determination not reliable (e.g., very sensitive to the omission of one or two data points). For

that reason, we used another simpler approach consisting in assessing the initial photo-isomerization rate from the linear regression fit over the first three data points at  $t = 0$ ; 60 and 120 s. A simple exponential function yields clearly unsatisfactory fits; though connect fits could be obtained using bi-exponential profile (the slope  $B$  in Fig. 5.14). This value is independent on the number of reaction order and can be used to compare the global kinetic of photo-isomerization. The total surface concentration of fulgimides isomerized at the end of the illumination cycle, i.e., the photo-isomerizable fulgimides of the first UV illumination cycle can be determined from the evolution curve as well (parameter  $A$  in Fig. 5.14). The obtained  $A$  and  $B$  values allows for defining a characteristic evolution time  $\tau_c^{UV}$  and equivalent photo-isomerization cross-section  $\sigma^{UV}$  as

$$\tau_c = \frac{A}{B} \quad \text{Equation 5.24}$$

$$\sigma = \frac{B}{A\phi} \quad \text{Equation 5.25}$$

where  $\phi$  is the photon flux incident on surface. In the limit case of an exponential evolution profile,  $\tau_c$  reduces to the exponential time constant and  $\sigma$  to the photo-isomerization cross-section. The kinetic parameters corresponding to the evolution of surface concentration of fulgimide shown in Fig. 5.14 are summarized in Table 5.4.

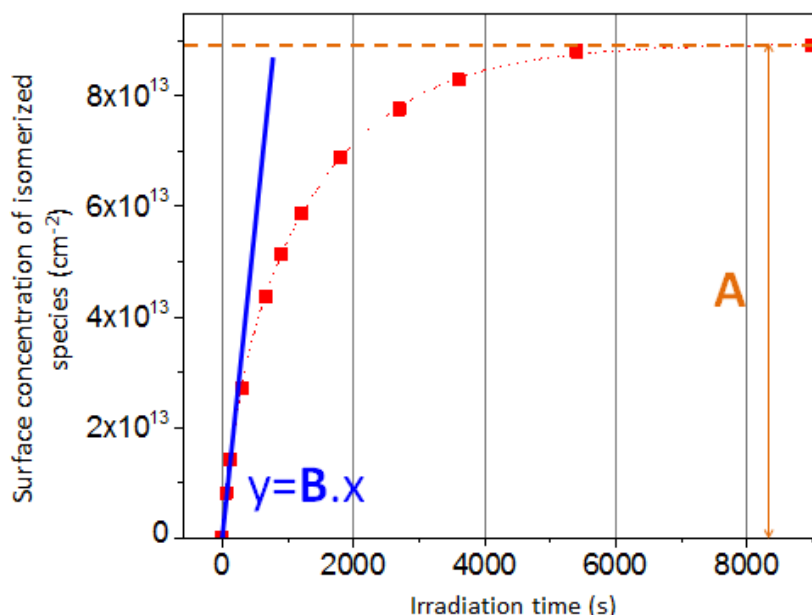


**Figure 5.14.** Time dependence of the surface concentration of *isomerized* fulgimide during the first UV illumination cycle of the *dense* Si-fulgiEZ surface. The slope  $B$  gives the *initial* isomerization rate and  $A$  the concentration of *photo-active* fulgimides.

Surface	<b>A</b> molecule cm <sup>-2</sup>	<b>B</b> molecule s <sup>-1</sup> cm <sup>-2</sup>	$\tau_c^{UV}$ s	$\sigma^{UV}$ cm <sup>2</sup>
dense EZ	$8.8 \times 10^{13}$	$1.22 \times 10^{11}$	724	$4.32 \times 10^{-19}$

**Table 5.4. Kinetic parameters of the first UV illumination cycle of as-prepared dense Si-fulgiEZ surface.  $\phi_{UV} = 3.2 \times 10^{15} \text{ s}^{-1} \text{ cm}^{-2}$ .**

#### 5.2.3.4. Evolution of kinetic parameters over repeated illumination cycles

The kinetic parameters (characteristic times  $\tau_c$  and photo-isomerization cross-section  $\sigma$ ) of UV and Vis isomerization processes over successive illumination cycles are summarized in Tables 5.5 - 5.8, for two *dense* MLs (*pure* Si-fulgiEZ and Si-fulgiC surfaces). The surfaces were illuminated alternatively using UV light ( $\phi_{UV} = 0.32 \times 10^{16} \text{ photons.s}^{-1} \text{ cm}^{-2}$ ) and Vis light ( $\phi_{Vis} = 3.17 \times 10^{16} \text{ photons.s}^{-1} \text{ cm}^{-2}$ ) under normal incidence.

In the case of the *dense* Si-fulgiEZ surface (Tables 5.5 and 5.6) the characteristic times  $\tau_c$  and the cross section  $\sigma$  are lower for the first UV and Vis cycles. For the subsequent illumination cycles no significant evolution of  $\tau_c$  nor  $\sigma$  is observed. . As already pointed out in section II.2, the number of *photo-active* fulgimides **A** decreases slightly during successive cycles and the initial isomerization rate **B** follows the same trend.

In the case of the *dense* Si-fulgiC surface (Tables 5.7 and 5.8), the time evolution measurements were performed only during some illumination cycles (for the others only the IR spectrum at the PSS were measured), so that less data are available. One can observe that for the Vis isomerization process the characteristic time  $\tau_c^{Vis}$  and the equivalent isomerization cross-section  $\sigma^{Vis}$  are found to be similar to that of the *dense* Si-fulgiEZ surface. However,  $\tau_c^{UV}$  and  $\sigma^{UV}$  have respectively, slightly higher and lower values. No evolution of the two kinetic parameters is observed over the successive illuminations. As for the previous surface, the concentration of *photo-active* fulgimides (**A**) and the initial isomerization rate (**B**) decrease over the successive cycles.

In summary, the results obtained from both *dense* surfaces indicate that the kinetics of photo-isomerization on surface remain nearly unchanged over repeated illumination cycles even though an initial slightly faster process is observed during the first cycles.

Cycle number	<b>A</b> molecule cm <sup>-2</sup>	<b>B</b> molecule s <sup>-1</sup> cm <sup>-2</sup>	$\tau_c^{UV}$ s	$\sigma^{UV}$ cm <sup>2</sup>
1	8.8×10 <sup>13</sup>	12×10 <sup>10</sup>	750	4.3×10 <sup>-19</sup>
3	8.0×10 <sup>13</sup>	7.3×10 <sup>10</sup>	1090	2.9×10 <sup>-19</sup>
5	7.7×10 <sup>13</sup>	7.3×10 <sup>10</sup>	1050	3.0×10 <sup>-19</sup>
7	7.4×10 <sup>13</sup>	7.2×10 <sup>10</sup>	1020	3.0×10 <sup>-19</sup>

**Table 5.5.** Kinetic of fulgimide photo-isomerization for an as-prepared *dense* Si-fulgiEZ monolayer during UV illumination cycle.  $\phi_{UV} = 3.2 \times 10^{15} \text{ s}^{-1} \text{ cm}^{-2}$ .

Cycle number	<b>A</b> molecule cm <sup>-2</sup>	<b>B</b> molecule s <sup>-1</sup> cm <sup>-2</sup>	$\tau_c^{Vis}$ s	$\sigma^{Vis}$
2	8.0×10 <sup>13</sup>	1.2×10 <sup>10</sup>	680	4.7×10 <sup>-20</sup>
4	7.7×10 <sup>13</sup>	8.8×10 <sup>10</sup>	870	3.6×10 <sup>-20</sup>
6	7.3×10 <sup>13</sup>	8.4×10 <sup>10</sup>	870	3.6×10 <sup>-20</sup>
8	7.1×10 <sup>13</sup>	8.3×10 <sup>10</sup>	860	3.7×10 <sup>-20</sup>

**Table 5.6.** Kinetic of fulgimide photo-isomerization for an as-prepared *dense* Si-fulgiEZ monolayer during Vis illumination cycle.  $\phi_{Vis} = 3.2 \times 10^{16} \text{ s}^{-1} \text{ cm}^{-2}$ .

Cycle number	<b>A</b> molecule cm <sup>-2</sup>	<b>B</b> molecule s <sup>-1</sup> cm <sup>-2</sup>	$\tau_c^{Vis}$ s	$\sigma^{Vis}$
1	13×10 <sup>13</sup>	15×10 <sup>10</sup>	850	3.7×10 <sup>-20</sup>
3	8.1×10 <sup>13</sup>	9.8×10 <sup>10</sup>	830	3.8×10 <sup>-20</sup>
11	6.1×10 <sup>13</sup>	7.8×10 <sup>10</sup>	780	4.0×10 <sup>-20</sup>
13	6.0×10 <sup>13</sup>	8.0×10 <sup>10</sup>	740	4.3×10 <sup>-20</sup>

**Table 5.7.** Kinetic of fulgimide photo-isomerization for an as-prepared *dense* Si-fulgiC monolayer during Vis illumination cycle.  $\phi_{Vis} = 3.2 \times 10^{16} \text{ s}^{-1} \text{ cm}^{-2}$ .

Cycle number	<b>A</b> molecule cm <sup>-2</sup>	<b>B</b> molecule s <sup>-1</sup> cm <sup>-2</sup>	$\tau_c^{UV}$ s	$\sigma^{UV}$
2	8.2×10 <sup>13</sup>	6.8×10 <sup>10</sup>	1220	2.6×10 <sup>-19</sup>
4	7.6×10 <sup>13</sup>	5.3×10 <sup>10</sup>	1450	2.2×10 <sup>-19</sup>
10	6.2×10 <sup>13</sup>	4.6×10 <sup>10</sup>	1350	2.3×10 <sup>-19</sup>

**Table 5.8.** Kinetic of fulgimide photo-isomerization for an as-prepared *dense* Si-fulgiC monolayer during UV illumination cycle.  $\phi_{UV} = 3.2 \times 10^{15} \text{ s}^{-1} \text{ cm}^{-2}$ .

### 5.2.3.5. Kinetic parameters as function of experimental conditions

After stabilization of their kinetic parameters during two or three illumination cycles, *dense* fulgimide surfaces were submitted to different illumination conditions using the first and second experimental set-ups described in section I. The comparison of kinetic parameters with respect to the incidence angle and the photon flux were investigated. The third experimental set-up was used on *dense* and *diluted* surfaces to study the influence of the beam polarization and the surface concentration of fulgimides on the kinetics of the isomerization process.

Tables 5.9 and 5.10 summarize all the kinetic parameters obtained for different experimental conditions. The experiments are numbered with an index corresponding to the UV or Vis illumination cycle. In the second column S1, S2 and S3 refer the type of illumination set-up used, S1 for the first, S2 for the second and S3 for the third. The index p or s on the right-hand side of S3 indicates the type of beam polarization used for the experiments.

Experiment number	Set-up	$\phi$ s <sup>-1</sup> cm <sup>-2</sup>	<i>A</i> molecule cm <sup>-2</sup>	<i>B</i> molecule s <sup>-1</sup> cm <sup>-2</sup>	$\tau_c^{Vis}$ s	$\sigma^{Vis}$
1 <sup>Vis</sup>	S1	3.2×10 <sup>16</sup>	7.1×10 <sup>13</sup>	8.3×10 <sup>10</sup>	860	4×10 <sup>-20</sup>
2 <sup>Vis</sup>	S2	2.3×10 <sup>16</sup>	7.5×10 <sup>13</sup>	20×10 <sup>10</sup>	380	12×10 <sup>-20</sup>
3 <sup>Vis</sup>	S2	1.1×10 <sup>16</sup>	7.0×10 <sup>13</sup>	9.3×10 <sup>10</sup>	760	12×10 <sup>-20</sup>
4 <sup>Vis</sup>	S3 <sup>p</sup>	4.3×10 <sup>16</sup>	6.4×10 <sup>13</sup>	20×10 <sup>10</sup>	320	7×10 <sup>-20</sup>
5 <sup>Vis</sup>	S3 <sup>p</sup>	4.3×10 <sup>16</sup>	1.4×10 <sup>13</sup>	7.1×10 <sup>10</sup>	200	12×10 <sup>-20</sup>
6 <sup>Vis</sup>	S3 <sup>s</sup>	4.3×10 <sup>16</sup>	1.3×10 <sup>13</sup>	3.4×10 <sup>10</sup>	390	6×10 <sup>-20</sup>

**Table 5.9. Kinetic of fulgimide photo-isomerization during Vis illumination cycles for different experiments.**

Experiment number	Set-up	$\phi$ s <sup>-1</sup> cm <sup>-2</sup>	<b>A</b> molecule cm <sup>-2</sup>	<b>B</b> molecule s <sup>-1</sup> cm <sup>-2</sup>	$\tau_c^{UV}$ s	$\sigma^{UV}$
1 <sup>UV</sup>	S1	3.2×10 <sup>15</sup>	7.4×10 <sup>13</sup>	7.2×10 <sup>10</sup>	1020	3.1×10 <sup>-19</sup>
2 <sup>UV</sup>	S2	2.3×10 <sup>15</sup>	8.3×10 <sup>13</sup>	13×10 <sup>10</sup>	620	7×10 <sup>-19</sup>
3 <sup>UV</sup>	S2	1.1×10 <sup>15</sup>	7.2×10 <sup>13</sup>	4.7×10 <sup>10</sup>	1550	6×10 <sup>-19</sup>
4 <sup>UV</sup>	S3 <sup>p</sup>	2.9×10 <sup>15</sup>	7.3×10 <sup>13</sup>	6.8×10 <sup>10</sup>	1070	3.2×10 <sup>-19</sup>
5 <sup>UV</sup>	S3 <sup>p</sup>	2.9×10 <sup>15</sup>	1.3×10 <sup>13</sup>	1.4×10 <sup>10</sup>	880	4×10 <sup>-19</sup>
6 <sup>UV</sup>	S3 <sup>s</sup>	2.9×10 <sup>15</sup>	1.3×10 <sup>13</sup>	0.6×10 <sup>10</sup>	2020	1.7×10 <sup>-19</sup>

**Table 5.10. Kinetic of fulgimide photo-isomerization during UV illumination cycles for different experiments.**

The experiments 1<sup>Vis</sup> and 1<sup>UV</sup> are taken from the cycles number 7 and 8 in Tables 5.5 and 5.6. They are corresponding to the kinetic parameters of a dense surface illuminated with the first experimental set-up. They are first used to compare with the experiments in second and third row (2<sup>Vis/UV</sup> and 3<sup>Vis/UV</sup>). These values are taken from experiments with the set-up S2 in which the incident beam angle was modified from 90° (for set-up S1) to 45° with respect to surface plan. It's noteworthy that the experiments 1<sup>UV/Vis</sup> and 2<sup>UV/Vis</sup> were performed with the same light sources. The difference in photon flux is due to the incidence angle: the photon flux is divided to square root of two ( $\sqrt{2}$ ) in the case of experiments using set-up S2, i.e., with an oblique 45° incident light. In this case, the equivalent photo-isomerization cross-sections are higher than that obtained from the experiments using set-up S1, i.e., with a normal incident light. The equivalent photo-isomerization cross-section is three times larger at 45° incidence under Vis illumination ( $2^{Vis} / 1^{Vis}$ ) and two times under UV illumination ( $2^{UV} / 1^{UV}$ ).

Another comparison is between experiment 2<sup>UV/Vis</sup> and 3<sup>UV/Vis</sup>. Herein, same surfaces are illuminated using the same illumination set-up (S2) and the only change is the intensity of light by changing the current applied on LEDs. The photon flux is determined from the calibration curve of light power against applied current for each UV or Vis LED. Under Vis light, the photo-isomerization rate **B** increases ~2 times and the characteristic evolution time  $\tau_c^{Vis}$  decreases ~2 times when light intensity increases ~2 times. Therefore, the equivalent photo-isomerization cross-section remains almost unchanged. Similar observation is made in the case of a surface illuminated by UV light except that the proportion of **B** and  $\tau_c^{UV}$  values is

$\sim 2.5$  instead of  $\sim 2$  found in previous case. As a consequence, the  $\sigma^{\text{UV}}$  value in the experiment  $2^{\text{UV}}$  is  $\sim 1.2$  times larger than that in the experiment  $3^{\text{UV}}$ .

Experiments  $4^{\text{UV/Vis}}$ ,  $5^{\text{UV/Vis}}$  and  $6^{\text{UV/Vis}}$  are performed with the third illumination set-up. We recall that this set-up allows for creating a parallel band of light with a possibility of remotely changing between p- or s-polarization. First, experiments  $4^{\text{UV/Vis}}$  and  $5^{\text{UV/Vis}}$  compare the kinetic parameters between an as-prepared *dense* surface (initial concentration  $1.7 \times 10^{14} \text{ cm}^{-2}$ ) and an as-prepared *diluted* surface (initial concentration  $2 \times 10^{13} \text{ cm}^{-2}$ ). The concentration of photo-isomerizable fulgimides **A** on a *dense* surface is found larger by a factor  $\sim 4.5$  to  $\sim 6$  times as compared to a *diluted* surface for Vis or UV illumination, respectively. Therefore, the initial photo-isomerization rate **B** is also larger by a factor 2.8 to 4.8. The characteristic evolution time  $\tau_c^{\text{Vis/UV}}$  obtained in the case of a *dense* surface is slightly larger than that found for a *diluted* surface; as a consequence, the  $\sigma^{\text{UV/Vis}}$  values obtained in the case of a *dense* surface are slightly smaller than that in the case of *diluted* surface. However, the difference is not large enough like previous comparison to conclude that the fulgimides in a *dense* layer exhibit slower switching kinetics than those in a *diluted* layer.

The last comparison is between experiments  $5^{\text{UV/Vis}}$  and  $6^{\text{UV/Vis}}$ . It was performed on the same *diluted* surface which was illuminated under p- or s- polarized UV and Vis light. Herein, the initial photo-isomerization rate **B** under p-polarized light is  $\sim 2.1$  times larger than that under s-polarized light. Similarly, the characteristic time and the equivalent photo-isomerization cross-section differ by factors of  $\sim 0.5$  and  $\sim 2$  between the two experiments. It indicates that the kinetic of fulgimides illuminated by p-polarized light is  $\sim 2$  times faster than that illuminated s-polarized lights.

## 5.3. Discussion

### 5.3.1. Photoswitching mechanism

Figure 5.15 recalls the reaction scheme of fulgimide photo-isomerization in solution proposed in Chapter 4. As shown in the case of the photo-isomerization in solution, the  $C \rightarrow E$  occurred under Vis light is the sole reaction so that their kinetics are exponential time dependence while the evolution under UV obeys a bi-exponential law because of the possibility of several reaction paths. When fulgimides are incorporated on surface, we found

that both UV and Vis photo-isomerization data need are not reliably accounted for by a bi-exponential function.

This observation suggests that the characteristic times associated with the molecular transformation sketched in Fig. 5.15 are distributed, including in the case of the simple  $C \rightarrow E$  photo-isomerization. These different rates are likely to be related to the specific environment of the fulgimide groups in the monolayers. By comparison with what occurs in solution, the steric hindrance may be anticipated as a factor able to influence the isomerization rates.

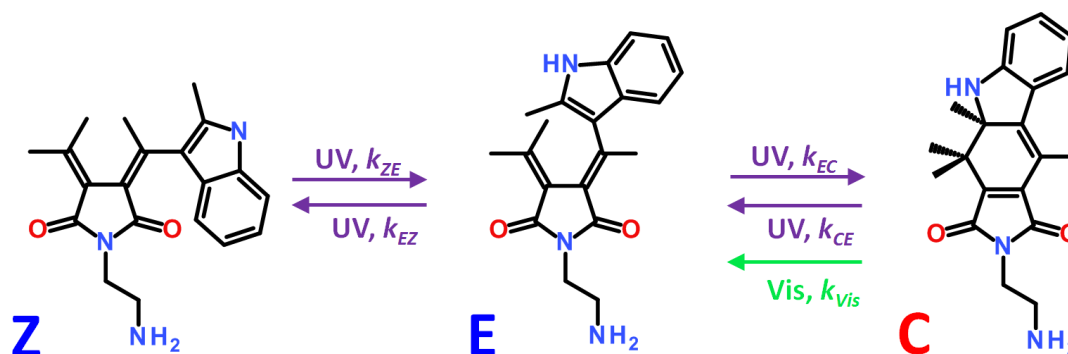


Figure 5.15. Photochromism of 2-aminoethylindolylfulgimide under Vis ( $\rightarrow$ ) or UV ( $\rightarrow$ ) irradiation. The various  $k_i$ 's stand for rate constants associated with the specific reactions.

### 5.3.2. The concentration of photo-isomerizable species on *dense* and *diluted* surfaces

As depicted in the discussion section of Chapter 4 (section 4.3), the density of fulgimides groups immobilized on the Si surface is constrained by the surface Si atom spacing. The ideally close-packed ( $2 \times 3$ ) structure corresponds to a surface density of  $D^* = 1.3 \times 10^{14} \text{ cm}^{-2}$ . However, both as-prepared *dense* Si-fulgiEZ and Si-fulgiC surfaces exhibit a larger surface concentration of  $1.6\text{-}1.7 \times 10^{14} \text{ fulgimides.cm}^{-2}$ . Therefore, even many molecules keep the capability of photoswitching under UV or Vis illumination, crowding effects could account for the observation that only  $\sim 60\text{-}80\%$  of total fulgimides are *photo-active on dense* surfaces. In order to verify this hypothesis, a *dilute* Si-FulgiC surface was prepared and its behavior under UV/Vis illumination investigated. For this experiment the third illumination set-up was used.

Figure 5.16 displays the isomeric fraction at the PSSs after successive illumination cycles of this surface. The fraction of fulgimide that have commuted ( $C \rightarrow E$ ) during the first

Vis illumination reaches  $\sim 95\%$ . Less than 5% of residual C isomers (*non-photoactive* fulgimides) are detected at the PSS which is close to the limit of detection and, much lower than on *denser* MLs. After the subsequent UV illumination, the 75% of the fulgimides have commuted (EZ  $\rightarrow$  C). Compared to the *denser* MLs discussed previously, in the case of this *dilute* ML almost all the fulgimides are photoactive and the isomeric composition at the PSSs is very similar to that observed in solution. At the PSS<sub>Vis</sub> the ML is at nearly purely composed of EZ forms ( $\sim 95\%$ ) and at the PSS<sub>UV</sub> the ML is composed of a majority of C forms (70%) with a fraction of residual EZ forms (30%). Steric hindrance turns out therefore very likely at the origin of the larger fraction of non-photoactive fulgimides and different isomeric compositions observed in the case of *denser* MLs.

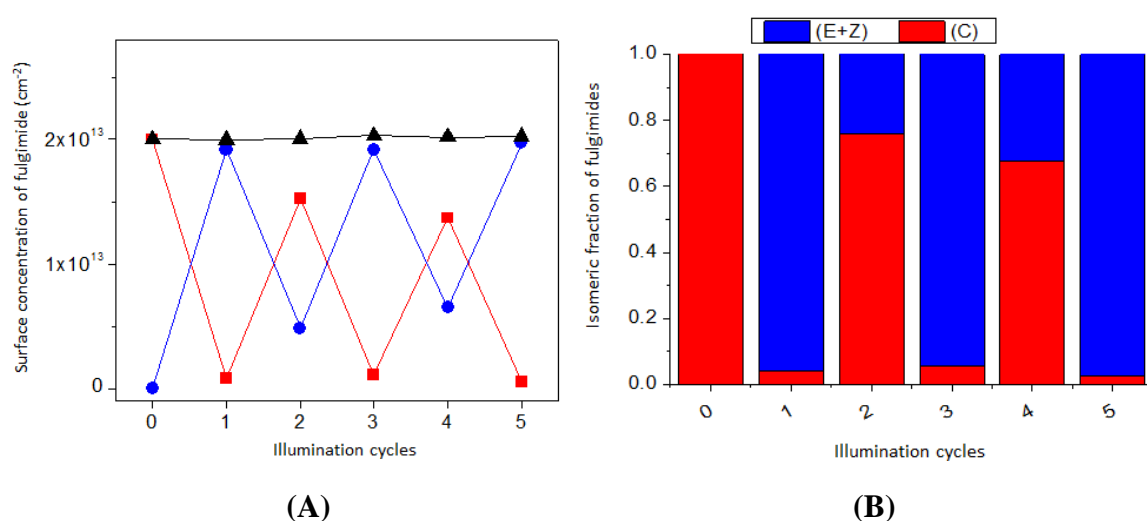


**Figure 5.16.** Isomeric composition of an as-prepared *diluted* Si-fulgiC surface at the PSSs after successive illumination cycles. (A) Surface concentration of E/Z- (●) and C- (■) forms. The black triangles (▲) represent the sum of E,Z and C forms. (B) Isomeric fraction of fulgimides (E/Z- (blue) and C- (red) forms) in the monolayer as a function of the illumination cycles. Odd numbers refer to the PSSs reached after Vis illumination and even to PSSs reached after UV. “0” gives the composition of surface prior to any illumination.

### 5.3.3. Local electric field at fulgimide surfaces

As shown experimentally, the kinetic parameters of the photo-isomerization processes are affected by the illumination intensity and the illumination polarization. When fulgimides are in solution, they can isomerize by adsorbing a photon propagating through a homogeneous medium. Once fulgimides are immobilized on surface, their absorption is determined by the local field, i.e. the exciting electric field, evaluated at the position of the absorbing dipole

corresponding to the electronic transition which depends on the light polarization state. Therefore, the electric field on the surface needs to be calculated from classical electromagnetism.

The local electric field amplitude results from the superposition of the incident and reflected light, which mostly depends on the silicon dielectric constant. The dielectric constant is usually a complex number,  $\tilde{\epsilon} = \epsilon' + i\epsilon''$ , where  $\epsilon'$  and  $\epsilon''$  are the real and imaginary part. In the present case, the dielectric coefficient of silicon at 525 and 365 nm can be found in Table 5.11.

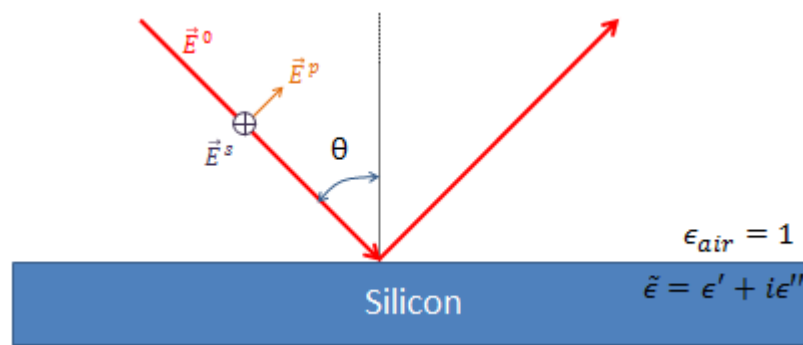


**Figure 5.17.** Scheme of an incidence light beam at an angle  $\theta$  with respect to normal surface, reflected onto an absorbing surface.

Wavelength (nm)	$\epsilon'$	$\epsilon''$	$ \tilde{\epsilon} $
365	35.22	35.28	49.85
525	17.44	0.443	17.45

**Table 5.11.** Dielectric coefficients of silicon surface at 525 and 365 nm (data obtained from the ref<sup>19</sup>).

In air, the electric field corresponding to the incident wave can be simply written as

$$E(r, t) = E^0 \exp(ik \cdot r - i\omega t). \quad \text{Equation 5.26}$$

Let us consider a plane wave externally incident at an angle  $\theta$  as sketched in Fig. 5.17. Following Chabal,<sup>20</sup> the energy field at the interface can be calculated by solving Maxwell's equation with the following boundary conditions:

$D_{\text{normal}}$  continuous (no surface free charge),

$E_{\text{tangential}}$  continuous,

$B=H$  continuous (non-magnetic media).

In this case, E-field can be calculated for s-polarization (E-field parallel to the surface,  $E^s$ ):

$$E^s(z = 0) = \left[ 1 - \frac{(\tilde{\epsilon} - \sin^2 \theta)^{1/2} - \cos \theta}{(\tilde{\epsilon} - \sin^2 \theta)^{1/2} + \cos \theta} \right] E^0 \quad \text{Equation 5.27}$$

and for p-polarization (E-field in plane of incidence,  $E^p$ ), E-field can be then decomposed into two components: one out of the surface plane ( $E^p_{\text{out}}$ ) and other in the surface plane ( $E^p_{\text{in}}$ )

$$E^p_{\text{out}}(z = 0) = \left[ 1 + \frac{\tilde{\epsilon} \cos \theta - (\tilde{\epsilon} - \sin^2 \theta)^{1/2}}{\tilde{\epsilon} \cos \theta + (\tilde{\epsilon} - \sin^2 \theta)^{1/2}} \right] (\sin \theta E^0) \quad \text{Equation 5.28}$$

$$E^p_{\text{in}}(z = 0) = \left[ 1 - \frac{\tilde{\epsilon} \cos \theta - (\tilde{\epsilon} - \sin^2 \theta)^{1/2}}{\tilde{\epsilon} \cos \theta + (\tilde{\epsilon} - \sin^2 \theta)^{1/2}} \right] (\cos \theta E^0) \quad \text{Equation 5.29}$$

The intensity of the various components of the electric field is proportional to the intensity of electric field generated from the source, according to:

$$|E_i(z = 0)|^2 = E_i(z = 0) \cdot E_i^*(z = 0) = c_i \cdot |E_0|^2 \quad \text{Equation 5.30}$$

The surface intensity coefficients  $c_i$  are listed in Table 5.12. It can be noted that the intensity of the *in-plane* E-field ( $E^s$  and  $E^p_{\text{in}}$ ) is much smaller (~10 times) than that of the *out-of-plane* E-field.

Wavelength (nm)	45°			Normal		
	$c^s$	$c^p_{\text{out}}$	$c^p_{\text{in}}$	$c^s$	$c^p_{\text{out}}$	$c^p_{\text{in}}$
365	0.043	1.492	0.043	0.063	0	0.063
525	0.101	1.201	0.101	0.149	0	0.149

**Table 5.12.** Surface intensity coefficient for illumination at 525 and 365 nm.

### 5.3.4. Kinetic parameters

Since photoswitching process is triggered by a photon absorption by the molecule, and that the later process is itself proportional to the electromagnetic field intensity, it appears natural to define an intensity normalized cross-section by scaling the equivalent photo-

isomerization cross-section (Eq. 5.25) to the relevant sum of the intensity coefficients (Eq. 5.30)

$$\sigma_{normalized} = \frac{B}{A\phi^0 \sum c_i} \quad \text{Equation 5.31}$$

where  $\sum c_i$  is the sum of the intensity coefficients depending on the polarization state of the illumination and incidence angle and  $\phi^0$  is photon flux in air ( $\phi^0$  does not depend on the angle of incident light). The *intensity normalized* photo-isomerization cross-section  $\sigma_{normalized}$  for different experiments mentioned in section 5.2.3.5 under Vis and UV illumination are summarized in Tables 5.13 and 5.14.

Experiment number	Set-up	$\sum c_i$	$\phi^0$ $s^{-1} cm^{-2}$	$\sigma_{normalized}^{Vis}$ $cm^2$
1 <sup>Vis</sup>	S1	0.15	$3.2 \times 10^{16}$	<b><math>25 \times 10^{-20}</math></b>
2 <sup>Vis</sup>	S2	0.70	$3.2 \times 10^{16}$	<b><math>12 \times 10^{-20}</math></b>
3 <sup>Vis</sup>	S2	0.70	$1.5 \times 10^{16}$	<b><math>13 \times 10^{-20}</math></b>
4 <sup>Vis</sup>	S3 <sup>P</sup>	1.30	$6.1 \times 10^{16}$	<b><math>4 \times 10^{-20}</math></b>
5 <sup>Vis</sup>	S3 <sup>P</sup>	1.30	$6.1 \times 10^{16}$	<b><math>6 \times 10^{-20}</math></b>
6 <sup>Vis</sup>	S3 <sup>S</sup>	0.10	$6.1 \times 10^{16}$	<b><math>42 \times 10^{-20}</math></b>

**Table 5.13. Kinetic parameters of Vis illumination cycle for different experiments.**

Experiment number	Set-up	$\sum c_i$	$\phi^0$ $s^{-1} cm^{-2}$	$\sigma_{normalized}^{UV}$ s
1 <sup>UV</sup>	S1	0.06	$3.2 \times 10^{15}$	<b><math>49 \times 10^{-19}</math></b>
2 <sup>UV</sup>	S2	0.79	$3.2 \times 10^{15}$	<b><math>6 \times 10^{-19}</math></b>
3 <sup>UV</sup>	S2	0.79	$1.6 \times 10^{15}$	<b><math>5 \times 10^{-19}</math></b>
4 <sup>UV</sup>	S3 <sup>P</sup>	1.54	$4.1 \times 10^{15}$	<b><math>1.5 \times 10^{-19}</math></b>
5 <sup>UV</sup>	S3 <sup>P</sup>	1.54	$4.1 \times 10^{15}$	<b><math>1.8 \times 10^{-19}</math></b>
6 <sup>UV</sup>	S3 <sup>S</sup>	0.04	$4.1 \times 10^{15}$	<b><math>28 \times 10^{-19}</math></b>

**Table 5.14. Kinetic parameters of UV illumination cycle for different experiments.**

Let us now discuss the  $\sum c_i$  value of each experimental set-up. The first set-up S1 allows for surface illumination with a normal incident light which however suppress the out-of-plan component of E-field on surface. Therefore, the coefficient  $\sum c_i$  is quite small for Vis and UV illumination. The similar small values are observed for  $\sum c_i$  of the set-up S3<sup>S</sup>, in which only s-polarized light irradiated surface sample. When surface was illuminated using

set-up S2 or S3<sup>p</sup>,  $\sum c_i$  values increase by a factor of  $\sim 5$  to  $\sim 10$  for Vis light and  $\sim 10$  to  $\sim 20$  for UV light. The difference between the last two cases is that the light used in set-up S2 is non-polarized while the light in set-up S3<sup>p</sup> is p-polarized. As the intensity ratio of p / s has been found to be  $\sim 50/50$ , the  $\sum c_i$  of set-up S2 is therefore nearly a half of that of set-up S3<sup>p</sup>.

Considering the *intensity normalized* photo-isomerization cross-section resulting from the  $\sum c_i$  evaluation confirms that for a given illumination set-up, the same figure is obtained on dense layers (compare 2<sup>UV/Vis</sup> and 3<sup>UV/Vis</sup>). No significant dependency on the fulgimide surface concentration appears as well when comparing experiments 4<sup>UV/Vis</sup> and 5<sup>UV/Vis</sup>. The *intensity normalized* photo-isomerization cross-section is somewhat larger on the *diluted* surface, but steric effects appear to affect more sensitively the amount of the *photo-isomerizable* molecules rather than their photo-isomerization kinetics.

For the experiments in which incident light contain only *in-plane* component of E-field, i.e., experiments 1<sup>UV/Vis</sup> and 6<sup>UV/Vis</sup>, the  $\sigma_{normalized}$  value is much higher than that of other experiments in which a non-zero *out-of-plane* component of E-field is present. It might suggest that the orientation of fulgimide molecules at the surface makes their UV-Vis absorption more efficient when the electric field of the UV or Vis radiation is parallel to the surface. Unfortunately, the present results appear too preliminary for supporting this hypothesis unambiguously.

Similarly, it appears difficult to clearly compare the data obtained with the various illumination set-ups. In principle, the calibration of the illumination performed for each set-up could allow for such a comparison. Various uncertainties actually affect the absolute values obtained for the first two set-up such as the control of the polarization state of the illumination or the finite aperture of the incident beam. It then appears that quantitatively comparison of polarization or intensity effects would require performing all the experiments using an illumination set-up providing such a control, such as the last one designed at the end of the present work. Being able to give a consistent quantitative analysis of the photo-isomerization the derived values (e.g, of the *intensity normalized* photo-isomerization cross-sections) to similar figures for the molecules in solution.

## Conclusions

We have studied fulgimide terminated monolayer on a silicon surface by *in situ* FTIR measurements combining with home-made set-ups with light-emitting diodes. The FTIR qualitative and quantitative analysis demonstrates that fulgimide in the top layer of surface can be switched between its open- and closed- forms when surface was irradiated by UV or Vis lights. The isomeric composition of fulgimides on *dense* and *diluted* surfaces was determined for the photostationary states,  $PSS^{UV}$  and  $PSS^{Vis}$ . On *dense* surfaces, showing a fatigue effect has been evidenced, lowering the amount of photo-*isomerizable* molecules with increasing of the number of illumination cycles. The results proved the existence of fulgimides which cannot isomerize in *dense* surface while they are not observed in *diluted* surface indicating the steric effect on the fraction of photo-*isomerizable* fulgimides in layer.

The photoswitching kinetics were first studied on *dense* surface. It has been found kinetics could remain constant after many cycles. For further investigations, a series of experiments was performed for comparison of photoswitching kinetics of these layers in different illumination conditions. The results showed that the photo-isomerization rate scales with the intensity of illumination and that *intensity normalized* photo-isomerization cross-section are similar for fulgimides at *dense* and *diluted* surfaces.

The presence of an *out-of-plane* component of the E-field increases significantly the intensity of local field. However, the photo-isomerization rate does not increase proportionally, suggesting that the absorption efficiency of fulgimides for the *in-plane* component of the E-field.

## References

- (1) Ichimura, K.; Oh, S. K.; Nakagawa, M. *Science* **2000**, 288, 1624.
- (2) Auernheimer, J.; Dahmen, C.; Hersel, U.; Bausch, A.; Kessler, H. *J. Am. Chem. Soc.* **2005**, 127, 16107.
- (3) Yokoyama, Y. *Chemical Reviews* **2000**, 100, 1717.
- (4) Rath, S.; Hellig, M.; Port, H.; Wrachtrup, J. *Nano Letters* **2007**, 7, 3845.
- (5) Song, H.; Reed, M. A.; Lee, T. *Advanced Materials* **2011**, 23, 1583.
- (6) Willner, I.; Pardo-Yissar, V.; Katz, E.; Ranjit, K. T. *J Electroanal Chem* **2001**, 497, 172.
- (7) Wen, Y. Q.; Yi, W. H.; Meng, L. J.; Feng, M.; Jiang, G. Y.; Yuan, W. F.; Zhang, Y. Q.; Gao, H. J.; Jiang, L.; Song, Y. L. *J Phys Chem B* **2005**, 109, 14465.
- (8) Dietrich, P.; Michalik, F.; Schmidt, R.; Gahl, C.; Mao, G.; Breusing, M.; Raschke, M. B.; Priewisch, B.; Elsasser, T.; Mendelsohn, R.; Weinelt, M.; Ruck-Braun, K. *Applied Physics a-Materials Science & Processing* **2008**, 93, 285.
- (9) Jung, U.; Filinova, O.; Kuhn, S.; Zargarani, D.; Bornholdt, C.; Herges, R.; Magnussen, O. *Langmuir* **2010**, 26, 13913.
- (10) Chen, Y.; Xiao, J. P.; Yao, B. L.; Fan, M. G. *Optical Materials* **2006**, 28, 1068.
- (11) Kohno, Y.; Tamura, Y.; Matsushima, R. *Journal of Photochemistry and Photobiology a-Chemistry* **2009**, 201, 98.
- (12) Yasuda, S.; Nakamura, T.; Matsumoto, M.; Shigekawa, H. *J. Am. Chem. Soc.* **2003**, 125, 16430.
- (13) Kumar, A. S.; Ye, T.; Takami, T.; Yu, B. C.; Flatt, A. K.; Tour, J. M.; Weiss, P. S. *Nano Letters* **2008**, 8, 1644.
- (14) Snegir, S. V.; Marchenko, A. A.; Yu, P.; Maurel, F.; Kapitanchuk, O. L.; Mazerat, S.; Lepeltier, M.; Leautic, A.; Lacaze, E. *Journal of Physical Chemistry Letters* **2011**, 2, 2433.
- (15) Uchida, K.; Yamanoi, Y.; Yonezawa, T.; Nishihara, H. *J. Am. Chem. Soc.* **2011**, 133, 9239.
- (16) Bunker, B. C.; Kim, B. I.; Houston, J. E.; Rosario, R.; Garcia, A. A.; Hayes, M.; Gust, D.; Picraux, S. T. *Nano Letters* **2003**, 3, 1723.
- (17) Klajn, R. *Pure and Applied Chemistry* **2010**, 82, 2247.
- (18) de Villeneuve, C. H.; Michalik, F.; Chazalviel, J. N.; Ruck-Braun, K.; Allongue, P. *Advanced Materials* **2013**, 25, 416.
- (19) Palik, E. D. *Handbook of Optical Constants of Solids*; Elsevier Inc., 1997.
- (20) Chabal, Y. J. *Surface Science Reports* **1988**, 8, 211.

## General Conclusion

This thesis aims at characterizing the organization within mixed molecular layers, identifying the factors governing this organization and the impact of the organization on the monolayer properties. The latter aspect has been addressed by studying the photoswitching of photochromic compound in an organic monolayer. For that purpose, it was of prime interest to control the preparation of surfaces with a density and distribution of controlled anchoring sites. This is an important factor because it defines the distribution of the photochromic compounds grafted on the adlayer.

*Mixed* carboxydecyl/decyl surfaces were prepared by the *one-step* or *two-step* routes. Chemical characterization of mixed layers was obtained through quantitative FTIR analysis and the surface was observed by high-resolution NC-AFM imaging. In the case of surface prepared by the *two-step* route, monolayers exhibit a homogeneous distribution of acid end-groups which is proportional to the concentration of ester precursors in the grafting solution. In the case of surface prepared by the *one-step* route, we have demonstrated phase segregations at surface whose origin was related to the formation of supramolecular assemblies in solution (segregation of amphiphilic acid chains in hydrophobic decene). The composition and density of the monolayer on the obtained acid surface shows that it is possible to vary the density of acid sites in monolayer by changing the acid content in the grafting solution. However, this density remained much higher than expected when acid content in the grafting solution was lower than 10%.

For grafting solutions with a low acid content, undecylenic acid adsorption takes place on the hydrogenated silicon surface. The presence of adsorbed acid is the origin of the preferential grafting of acid chains on surface. This fact gives us a clue for better understanding the mechanism of our hydrosilylation methods.

The second part of the thesis dealt with the photochromic behavior of C-form and E/Z-form of amino substituted indolylfulgimide in acetonitrile and at silicon surface. The photochromism of fulgimide is based on the electrocyclic C→EZ ring-opening under Vis illumination and the reverse EZ→C ring-closure under UV illumination, i.e., the photoisomerization of fulgimides. The unwanted photochemical E↔Z isomerization also takes place:



The investigation focused on the isomeric composition (closed C- and open EZ-forms) during illumination cycles and the kinetics of photoswitching during each cycle.

The photoswitching behaviors of fulgimides were first studied in solution using an *in situ* UV/Vis spectrophotometry under irradiation. Under Vis illumination, only ring-opening reaction occurs and the evolution of photo-*isomerized* fulgimides obeys simple exponential kinetics. At the photostationary state (PSS), the isomerization induced by the Vis illumination is complete. In contrast, UV illumination triggers both ring-opening and -closure reactions. In this case, the evolution of photo-*isomerized* fulgimide obeys bi-exponential kinetics. The fact that both photo-isomerization occur at the same time explains the coexistence of open and closed forms at PSS<sub>UV</sub>. For both UV and Vis illumination, fulgimide molecules in solution show no fatigue after many cycles and their kinetics remain unchanged.

In a second step, amino substituted fulgimides were immobilized onto acid terminated monolayers forming *dense* or *diluted* photochromic monolayers. The immobilization of fulgimides on acid-terminated surfaces was performed by a simple chemical route (NHS/EDC – activated amidation). Quantitative FTIR analysis shows that a maximal packing of fulgimide  $\sim 1.6 \times 10^{14} \text{ cm}^{-2}$  limits the coupling yield of fulgimide on *dense* surfaces. A model of atomic structure suggests that the ideal density should be  $\sim 1.3 \times 10^{14} \text{ cm}^{-2}$ . Moreover, this prediction was confirmed by the high coupling yield of fulgimide on *diluted* surfaces.

The photoswitching of fulgimide at silicon surfaces has also been studied by *in situ* FTIR measurements under illumination, using a home-made set-up with LEDs. The photo-isomerization of fulgimides at surface was evidenced. On *dense* surfaces, a fraction ( $\sim 70\%$ ) of fulgimide molecules presents at the surface is photo-*isomerizable*, a consequence of steric hindrance effects. This fraction decreases when the number of illumination cycles increases, showing a fatigue effect of the system. Those effects were not observed in the case of *diluted* fulgimide surfaces. The kinetics of photo-isomerization are similar at *dense* and *diluted* surface and remain constant after many cycles. Preliminary results suggest that the absorption of fulgimides is more efficient for the *in-plane* component of the illuminations electric field than for the *out-of-plan* one.

The studies on photoswitching kinetics of fulgimide immobilized on surface can only be considered as preliminary. There is an obvious need for measuring all the kinetic

parameters using a single illumination system ensuring a good control of the geometry, intensity and polarization state of the illuminations. It should also be ensured that the measured values are not depending on the state (or the isomeric composition) of surface prior to illumination. For that reason, it would be interesting for such quantitative investigations to measure the kinetics on fresh samples systematically, or to perform the studies on diluted surfaces for which fatigue effects appear essentially absent.

Another interesting piece of information would be to know the isomerization rate of individual molecules at the surface. In solution, pump-probe experiments have demonstrated that the photoswitching is quite fast.<sup>1</sup> It would be interesting to know whether such fast photoswitching capability remains preserved when the molecule is attached at a surface.

## References

- (1) Koller, F. O.; Schreier, W. J.; Schrader, T. E.; Malkmus, S.; Schulz, C.; Dietrich, S.; Ruck-Braun, K.; Braun, M. *Journal of Physical Chemistry A* **2008**, *112*, 210.

## Appendix I

# Amplitude Modulation – Atomic Force Microscopy

---

### I.1. The principle of AM-AFM

The atomic force microscopy (AFM) is one of scanning probe microscopy (SPM) techniques which is tools for imaging, measuring and manipulating matter at nanoscale. It was first introduced by Binnig et al in 1986<sup>1</sup> and rapidly was commercialized in 1989. AFM has several advantages : (i) providing a three-dimensional surface profile, (ii) very high resolution (obtain atomic resolution in ultra-high vacuum), (iii) samples viewed by AFM do not require any special treatments that would irreversibly change or damage the sample, (iv) working perfectly well in ambient air or even in a liquid environment. Therefore, AFM can be applied to various environments and types of materials such as metal, semiconductor, organic thin film, biological samples, conductive and non-conductive materials. AFM can also be used for size measurements or manipulations of nano-objects.

The AFM consist of a cantilever with a sharp tip attached to the free end of a cantilever and can be brought very near to the surface for analyzing (Fig. I.1). The force acting (attractive or repulsive forces) between the tip and the surface leads to a deflection of the cantilever. AFM measures the deflection using a laser beam which is reflected from the back side of the cantilever into an array of photodiodes. The change of signal detected from photodiode can be used in a feedback loop to alter the z-direction of a piezoelectric scanner to maintain a constant force between the tip and the surface. At the same time, piezoelectric scanner can move in x, y directions for scanning. In some other AFM devices, sample can be mounted on another piezoelectric element which can move in x, y directions for scanning.

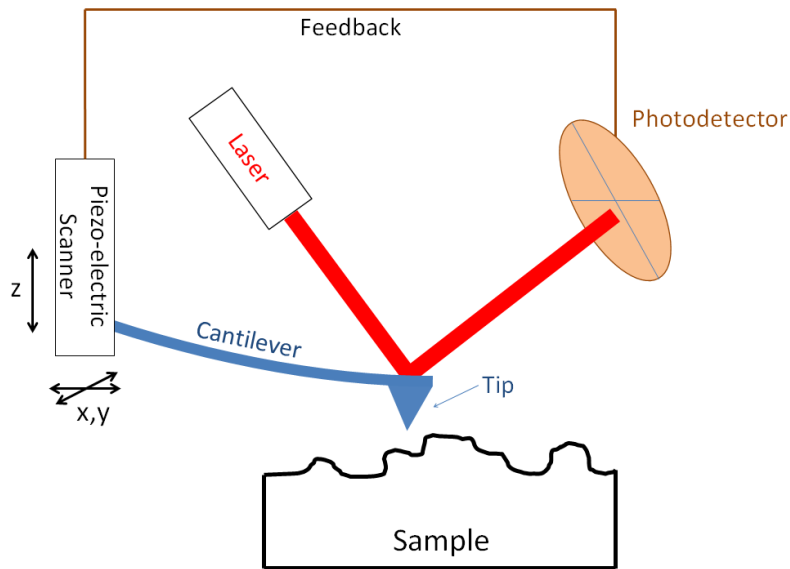


**Figure I.1. Schematic description of the operation principle of AFM. The feedback loop monitors the cantilever deflection and keeps it constant by adjusting the vertical position of the cantilever.**

There are two primary modes of operations for an AFM: static mode and dynamic mode. In static mode, the force between the tip and the surface is kept constant during the scanning. It's also called *contact mode* because the tip is very close to the surface. The z feedback signal from the static tip reflects the topography image of surface. In dynamic mode, the cantilever is externally oscillated at or close to its resonance frequency. The oscillation amplitude is used as a feedback parameter to image the sample topography. Depending on the distance between a tip and surface, it can be divided into two other modes: *tapping mode* and *non-contact mode*.

When tip approaches the surface, it interacts with the force field associated with the surface. The tip-surface interaction force  $F_{ts}$  depends on the distance between tip and surface. It can be long-range interaction of van der Waals ( $F_{vdw}$ ) or short-range repulsive force ( $F_{Morse}$ ). These different contact modes are illustrated on the force diagram as a function of the distance between the probe and surface (Fig. I.2).

While static AFM is very simple, efficient and fast scanning, the great advantage of dynamic AFM is that it offers a powerful tool for simultaneous mapping of topography and chemical composition. First is called topographic imaging and second is called phase-contrast imaging. The phase imaging is also a potential method to detect variations in material properties such as adhesion, elasticity and viscoelasticity.

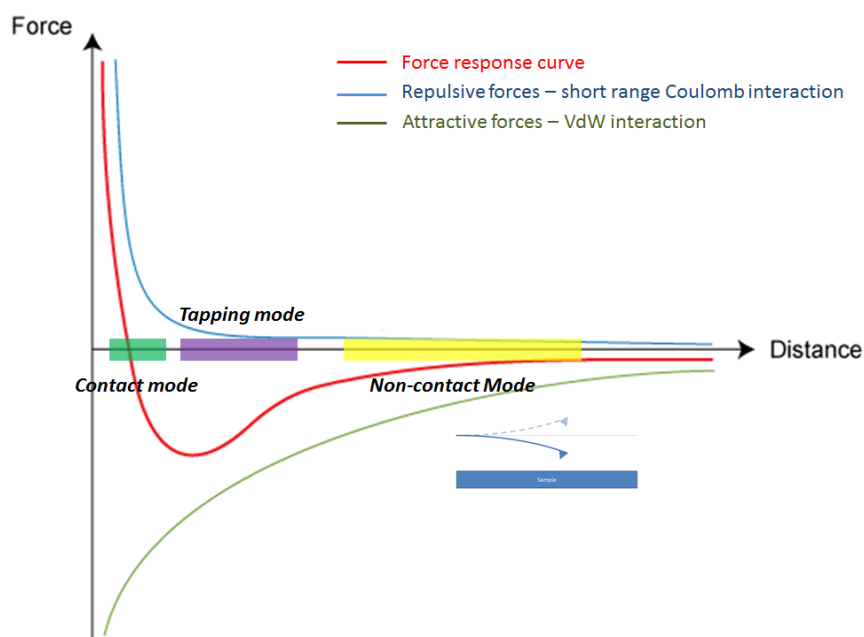


Figure I.2. Interaction forces as a function of tip-sample distance.

## I.2. Dynamic mode AFM (AC-AFM)

Dynamic AFM was first introduced by Martin *et al.* in 1987 by operating a force microscope in an oscillating mode.<sup>2</sup> In their experiments, the vibration amplitude was very small (below 1 nm) and the changes in the amplitude were dominated by long-range attractive forces of van der Waals type. A few years later Zhong *et al.* reintroduced tapping mode AFM (or intermittent contact AFM).<sup>3</sup> Their cantilever was excited with larger oscillation amplitudes up to 100 nm and its spring constants were about  $40 \text{ N m}^{-1}$ . It was thought that those values were needed to avoid the trapping of the tip by surface forces. It was also believed that short-range repulsive forces were responsible for the amplitude reduction.

AC-AFM offers several advantages comparing the contact mode. First, this dynamic mode allows obtaining very high lateral resolutions because the lateral forces are eliminated. Second, the weak applied force on surface makes it become an ideal scanning microscopy for soft layers (membrane, polymer, organic monolayer, biomolecule). Last, the tip can reserve its form during scanning as it doesn't have any contact or close to surface.

The basic set-up of AC-AFM is shown in Fig. I.3. A piezoelectric actuator is attached below the substrate containing the cantilever-tip ensemble. The application of an oscillating voltage to the actuator produces its vibration and this in turn produces the oscillation of the microcantilever. In AC-AFM, a stiff cantilever is excited at or near its free resonance

frequency. The oscillation amplitude is used as a feedback parameter to measure the topography of the sample surface. The phase shift between the driving force and the tip oscillation is recording simultaneously which shows the material properties variations on surface.

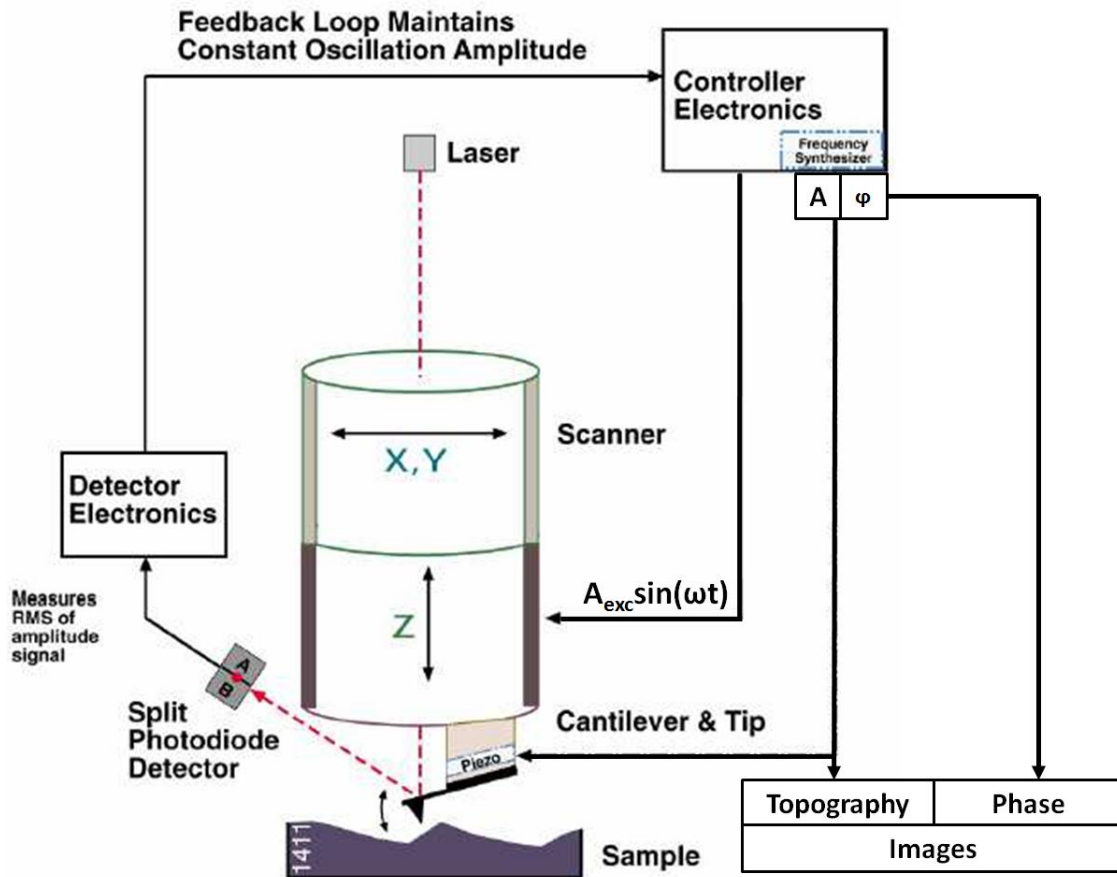


Figure I.3. Dynamic Atomic Force Microscopy.

### I.3. Experimental conditions

In our work, AFM images are obtained with the Multimode 5100 AFM/SPM microscopy (Agilent Technologies, Santa Clara, CA). The instrument was operated in AC mode with silicon nitride probes (PPP-NCL, 21-98 N.m-1) purchased from Nanosensors. Images were taken at the fundamental resonant frequency of the silicon cantilever of 146-180 kHz. The sample was attached to a metal stub using double-sided sticky tape and mounted onto a strong magnet located on the sample stage. Samples were scanned in a chamber purged with dry nitrogen gas. The imaging set point was kept around 100mV for all the experiments to make surface scope traces tracked and obtain the clearest images. Scan speed was selected at 1 line per second for large sizes (500 nm × 500 nm, 1.0 μm × 1.0 μm, 10 μm × 10 μm) and

at 2 lines per second for small sizes (100 nm × 100 nm, 200 nm × 200 nm). The digital resolution of all images is 512×512 pixels. The measurements have not been corrected for the convolution with tip shape (Nominal Tip Radius of Curvature : 10nm) which can significantly affect the absolute values for the lengths, heights and widths measured, but not affecting the trends in the relative values for these measurements.

### References

- (1) Binnig, G.; Quate, C. F.; Gerber, C. *Physical Review Letters* **1986**, *56*, 930.
- (2) Martin, Y.; Williams, C. C.; Wickramasinghe, H. K. *J Appl Phys* **1987**, *61*, 4723.
- (3) Zhong, Q.; Inniss, D.; Kjoller, K.; Elings, V. B. *Surf Sci* **1993**, *290*, L688.

## Appendix II

### FTIR Spectroscopy in ATR geomtry

---

#### II.1. The basic set-up of ATR-IR Spectroscopy

ATR is an FTIR sampling technique that provides excellent quality data in conjunction with high reproducibility and fast sampling. Most importantly, the improved spectral acquisition due to multiple reflections leads to better quality database building for more precise material verification and identification. This technique enables *in situ* studies by providing chemical information on any change detected on surface. ATR also provides an extremely robust and reliable technique for quantitative studies involving liquid and surface measurements.

The measurements are carried out using a geometry referred to as attenuated total internal reflection (ATR-FTIR) which provides multiple reflections in order to increase the signal-to-noise ratio. An attenuated total reflection accessory operates by measuring the changes that occur in a totally internally reflected infrared beam when the beam comes into contact with a sample (Fig. II.1). An infrared beam is directed onto an optically dense crystal with a high refractive index at a certain angle. The total reflection of electromagnetic wave occur at the interface when the angle of incidence is larger than the critical angle;  $\theta_c$ , which is defined as

$$\theta_c = \sin^{-1} \left( \frac{n_2}{n_1} \right) \quad \text{Equation II.1}$$

where  $n_1$  and  $n_2$  are the refraction index of the crystal and the sample positioned at the interface, respectively, with  $n_1 > n_2$ . ATR crystal is often made from zinc selenide, silicon, germanium or diamond.

The internal reflectance creates an evanescent wave that extends beyond the surface of the crystal into the sample held in contact with the crystal. This evanescent wave protrudes only a few microns ( $0.5 \mu - 5 \mu$ ) beyond the crystal surface and into the sample. The intensity of the evanescent wave decays exponentially with increased distance from the interface. The decay length or penetration depth,  $d_p$ , of the evanescent wave is given by

$$d_p = \frac{\lambda}{2\pi\sqrt{n_1^2 \sin^2 \theta - n_2^2}} \quad \text{Equation II.2}$$

where  $\lambda$  and  $\theta$  are the wavelength of light and the angle of incident, respectively. The  $d_p$  is greater at smaller  $\theta$  as long as  $\theta < \theta_c$ . In regions of the infrared spectrum where the sample absorbs energy, the evanescent wave will be attenuated or altered. The attenuated energy from each evanescent wave is passed back to the IR beam, which then exits the opposite end of the crystal and is passed to the detector in the IR spectrometer. The system then generates an infrared spectrum.

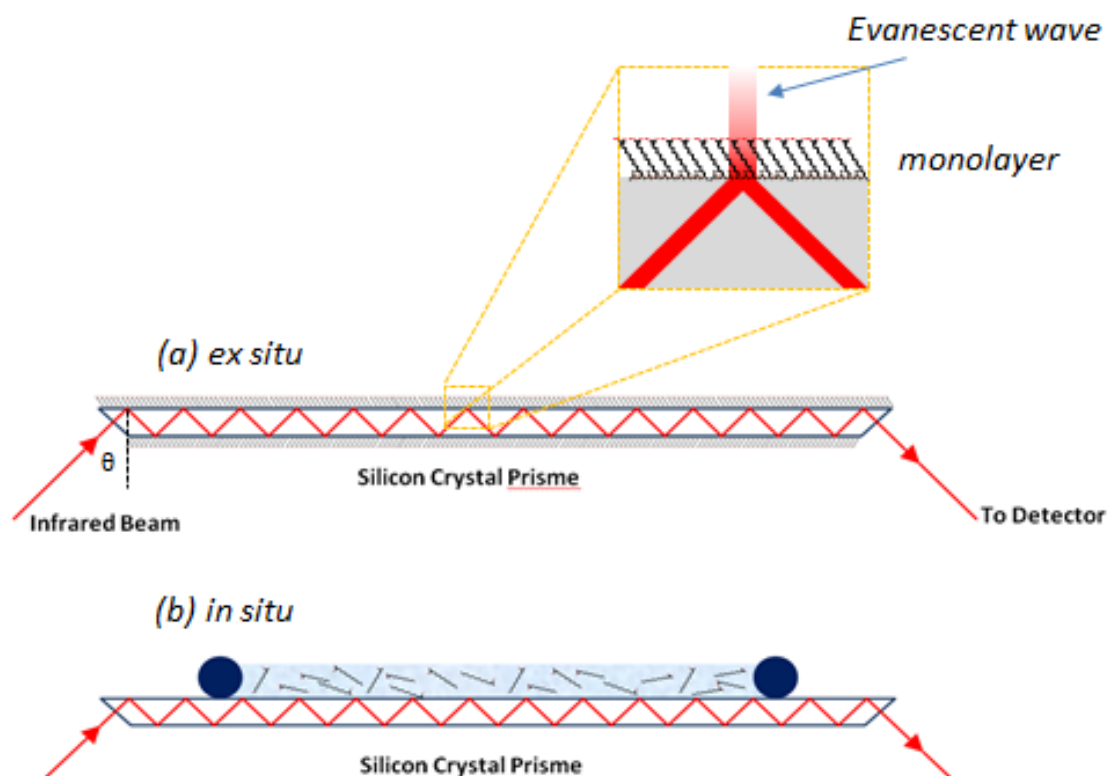


**Figure II.1.** ATR-IR system for *ex situ* (a) and *in situ* (b) measurements and the schematic of the evanescent field at the surface.

All measurements were made with a Bruker EQUINOX 55 spectrometer with a liquid nitrogen cooled mercury cadmium telluride (MCT) detector. Double-polished n-Si(111) wafers are cut into pieces of  $1 \times 1 \text{ cm}^2$  and polished to obtain ATR-crystals with  $45^\circ$  bevels ( $\pm 25$  internal reflections). The infrared light is incident on one of the  $45^\circ$  edges of the silicon prism, provides  $d_p$  in range of 147-338 nm for the group frequency region. Spectra (150 scans) were recorded with p-polarized and s-polarized light at a resolution of  $4 \text{ cm}^{-1}$ . The

spectrometer and sample chamber were continuously purged with water and carbon dioxide depleted nitrogen gas.

## II.2. Quantitative analysis method

### II.2.1. Principle

ATR-IR can be used as a tool to quantitatively analyze monolayer composition. This method was developed in the laboratory.<sup>1</sup> The IR absorbance values of a sample are related to its concentration, analogous to the way concentration is related to absorbance in transmission spectroscopy through the Beer-Lambert law. As we know the penetration depth of evanescent wave, the measurement in a liquid-phase experiment provides a convenient way to calibrate the corresponding integral to the number of molecule detected. An adsorbate layer may then be regarded as a slice of thickness  $\delta$  and effective dielectric function  $\varepsilon = \varepsilon' + i\varepsilon''$  at the interface between a solid of refractive index  $n_1$  and a non-absorbing medium of refractive index  $n_2$ .<sup>2</sup>

In this method, we consider the surface concentration of vibrators  $N$  corresponding to the projection of the dynamic dipole of the vibrational mode in the interface plane,  $N_{//}$ , and that corresponding to the projection of the dynamic dipole along the z direction,  $N_{\perp}$ .

$$N = N_{//} + N_{\perp} \quad \text{Equation II.3}$$

$$N_{//} = \frac{a_s I'_y C}{a'_s I_y 3} d \quad \text{Equation II.4}$$

$$N_{\perp} = n_1^4 \frac{I_y a_p - I_x a_s I'_y C d_p}{I_z a'_s I_y 3 2} \quad \text{Equation II.5}$$

where  $a_s$  and  $a_p$  are the integral of the absorbance infrared s- and p-polarized signals of the monolayer.  $n_1$ ,  $d_p$  are the infraction index of molecule and the penetration depth of the evanescent wave.  $I_x$ ,  $I_y$ ,  $I_z$  and  $I'_y$  are numerical coefficients depending on the infraction index of solution and adsorbent layer and the angle of incidence.  $a'_s$  is the integral of the absorbance s-polarized signal of the solution containing  $C$  concentration of molecule that have the vibrators corresponding. If we consider  $a'_s$  and  $C$  can be experimentally determined through a calibration of absorbance  $a'_s$  of the characteristic bands versus concentration  $C$  of the molecule in solution.

By using this method, we can determine the density of molecules grafted on surface from their characteristic bands. For each bands, it firstly needs to be calibrated using solution contained the desired group via *in situ* FTIR following a fitting process adapted to the

absorbance band on the spectra measured from both solution and surfaces. The details of 4 different bands used for quantification in this thesis will be presented in the next part including acid, ester, methylene, nitro and succinimide groups.

### II.2.2. Quantification method for acid groups

#### Fitting process

In the first approach, the  $\nu\text{C}=\text{O}$  band of acid solution were used to find the best fit. It was then fit with only one peak and one linear baseline and seems to be good (Fig. II.2a). The process was applied on *pure* and *mixed* acid surfaces prepared via one step preparation. In many cases for *mixed* surface, it turned out that the fitting curve could not superpose the data. An example of one-peak fitting curve on a *mixed* Si-acid<sup>20</sup> surface is shown in Fig. II.1a. A shoulder on the left side of center peak is obviously needed and added for two-peak fitting process (Fig. II.1b). Such a contribution was found to also improve the fit of the  $\nu\text{C}=\text{O}$  bands of the spectra of acid solution (Fig. II.2b). All the  $\nu\text{C}=\text{O}$  bands of undecanoic acid solutions and acid-terminated surfaces prepared via one step route were then fit to a model consisting of two contributions, as shown in Fig. II.1b. The first contribution was taken as a Gaussian peak at  $\sim 1690\text{ cm}^{-1}$ , the second one as a Lorentzian peak at  $\sim 1715\text{ cm}^{-1}$ . A linear baseline was added to the model. The fitting parameters are detailed in Table II.1 and Table II.2.

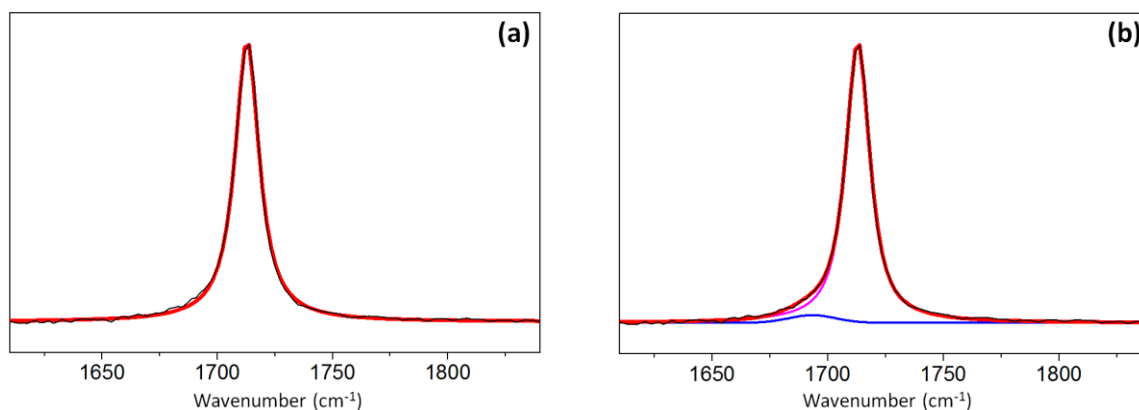


**Figure II.2.** Examples of the one-peak and two-peak fitting process of the  $\nu\text{C}=\text{O}$  band of 60 mM undecanoic acid in decane.

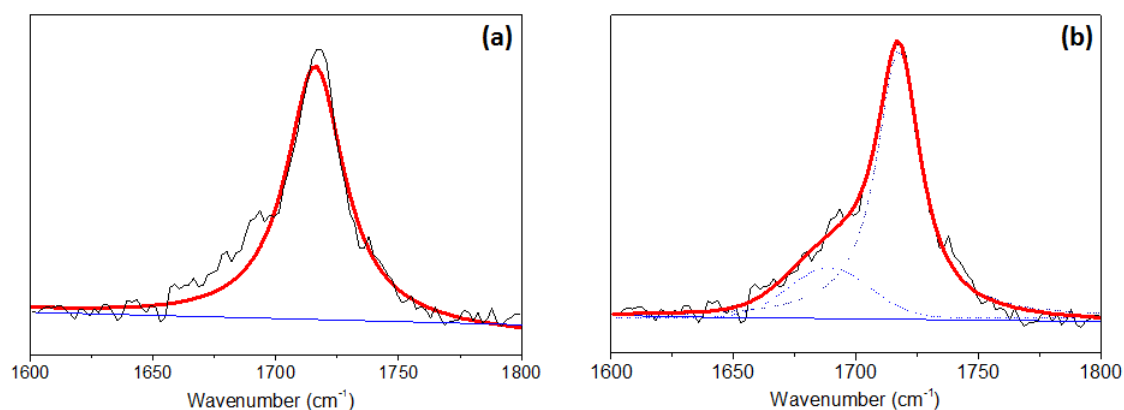


**Figure II.3.** Examples of the one-peak and two-peak fitting process of the  $\nu\text{C}=\text{O}$  band of a *mixed Si-acid*<sup>20</sup> surface.

The process applied to acid-terminated surfaces prepared by the *two-step* route after hydrolysis uses two-peak fitting. Herein, a shoulder was observed on the right-hand side of the acid peak. Therefore, the  $\nu\text{C}=\text{O}$  bands were fit with two peaks at  $\sim 1715$  and  $\sim 1740$   $\text{cm}^{-1}$  and one linear baseline (Fig. II.4). The  $1740$   $\text{cm}^{-1}$  peak is straightforwardly assigned to ester groups and allows for assessing the hydrolysis yield. The fitting parameters are detailed in Table II.3.

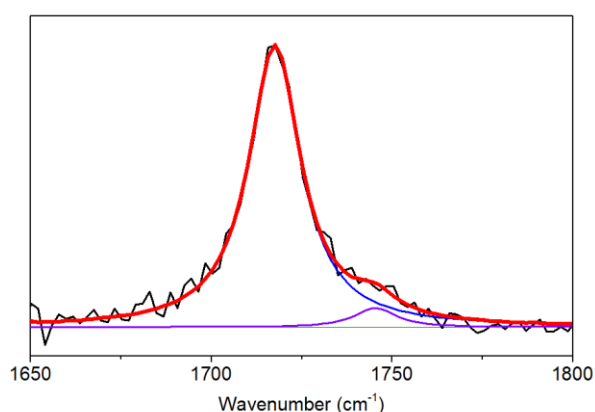


**Figure II.4.** Examples of the two-peak fitting process of the  $\nu\text{C}=\text{O}$  band of a *mixed Si-acid*<sup>ester-30</sup> surface.

Peak assignment	Peak position ( $\text{cm}^{-1}$ )	Abs.	Width ( $\text{cm}^{-1}$ )	Int. Abs. (Nreflex)	Shape
	1693.3	0.0005	24	0.004	Gauss
$\nu\text{C}=\text{O}$	1713.0	0.0181	12	0.099	87:13 Lorentz:Gauss

**Table II.1.** Example of fitting parameters used for the spectral deconvolution of the  $\nu\text{C}=\text{O}$  bands in the spectra of 60mM undecanoic acid in decane in Fig. II.2b.

Peak assignment	Peak position (cm <sup>-1</sup> )	Abs.	Width (cm <sup>-1</sup> )	Int. Abs. (Nreflex)	Shape
	1689.8	0.001	24	0.002	Gauss
vC=O	1716.7	0.004	22	0.012	Lorentz

**Table II.2.** Example of fitting parameters used for the spectral deconvolution of vC=O bands in the spectra of a *mixed Si-acid*<sup>20</sup> monolayer in Fig. II.3b.

Peak assignment	Peak position (cm <sup>-1</sup> )	Abs.	Width (cm <sup>-1</sup> )	Int. Abs. (Nreflex)	Shape
vC=O acid	1716.2	0.0042	21	0.011	Lorentz
vC=O ester	1744.2	0.0003	18	0.001	Lorentz

**Table II.3.** Example of fitting parameters used for the spectral deconvolution of vC=O bands in the spectra of a *mixed Si-acid*<sup>ester-30</sup> monolayer in Fig. II.4.

#### Acid calibration

The vC=O peak at 1715 cm<sup>-1</sup> is intense and strait that can be used to quantify the number of acid molecular in the monolayer grafted. The calibration of this peak was taken with the measurements of undecanoic acid in decane solution to ensure the validity of the conditions relating to the refraction index.

The measurements were realized in a small cell volume (Damien, joint Kalrez d=10mm) as you can see in Fig. II.5. A prism was mounted on the open side of the cell. The surface was passivated by grafting a decyl monolayer to prevent physisorption of organic molecular. The infrared beam gets through the silicon surface in ATR geometry, which allows for measuring the infrared absorption of the liquid adjacent to the surface.

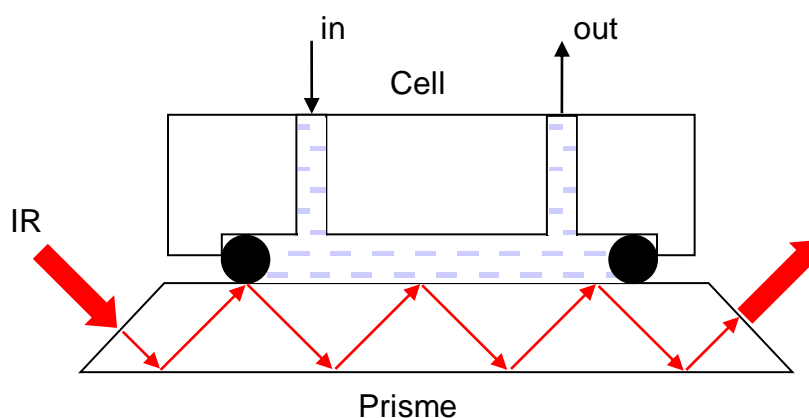


**Figure II.5.** The Assembly of Calibration System

The reference spectrum was taken with pure decane. The following spectra were taken with increasing then decreasing of acid concentration in solution. For each measurement, the previous solution was removed by suction with a syringe and injected the new solution. The volume necessary to fill the cell was approximately 0.8ml. Before each measurement the cell was rinsed by passing 2-3 mL of acid solution of the same concentration. The spectra were recorded with the cell full and in closed position. Figure II.6 presents the integrated intensity of  $\nu\text{C=O}$  peak at  $1715\text{ cm}^{-1}$  in s-polarization as a function of the acid fraction in decane solution.

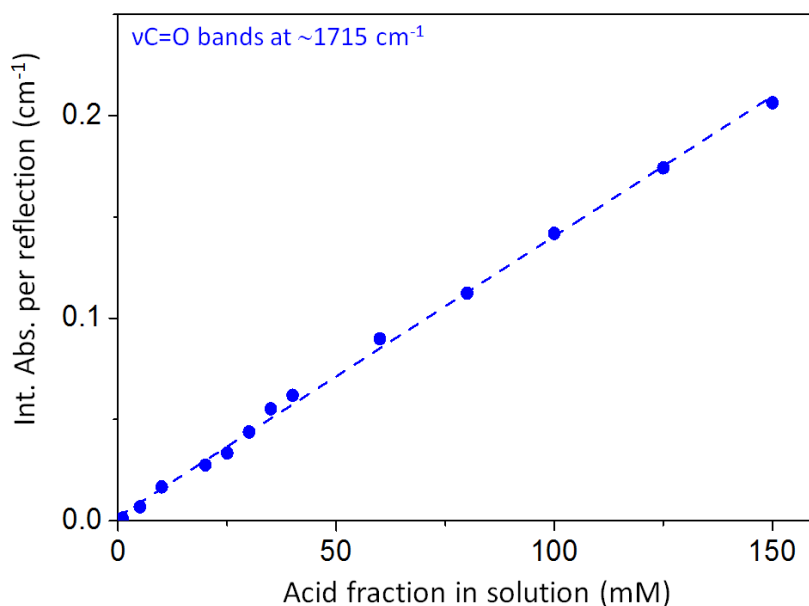


**Figure II.6.** The integrated absorbance in s-polarization as a function of the undecanoic acid concentrations in decane solution. Points correspond to the experimental values and lines correspond to the linear regression fits.

By fitting all the points to a simple regression line, a linear equation was obtained:

$$Abs_{\text{calib}}^s = (0.00148 \pm 0.00002) \cdot [\text{acid}] + (0.00208 \pm 0.00116) \quad \text{Equation II.6}$$

#### Acid quantification

By taking the slope of the linear function of  $Abs_{\text{calib}}^s$  (0.00138) corresponding to an absorbance of 1 mM acid and an incident angle  $\theta$  of  $46^\circ$ , we can deduce from Eq. II.3, II.4 and II.5 for the acid concentration within monolayer:

$$N_{\parallel}(\text{acid}) = 0.6197 \times 10^{16} \times Abs_{1715}^s \text{ (cm}^{-2}\text{)} \quad \text{Equation II.7}$$

$$N_{\perp}(\text{acid}) = 1.1626 \times 10^{16} \times Abs_{1715}^p - 1.0545 \times 10^{16} \times Abs_{1715}^s \text{ (cm}^{-2}\text{)} \quad \text{Equation II.8}$$

where  $N_{\parallel}$  and  $N_{\perp}$  are respectively the number of vibrators corresponding to the projection of the dynamic dipole of the vibration mode in the interface plane and that corresponding to the projection of the dynamic dipole along the  $z$  direction.  $Abs_{1715}^s$  and  $Abs_{1715}^p$  stand for the integrated absorbance per reflection of the  $\nu\text{C}=\text{O}$  peak at  $\sim 1715\text{ cm}^{-1}$  measured in s and p polarization. The surface acid concentration is then directly deduced as the sum of  $N_{\parallel}(\text{acid})$  and  $N_{\perp}(\text{acid})$  from Eq. II.7 and II.8.

### II.2.3. Quantification method for ester groups

#### Fitting process

The  $\nu\text{C}=\text{O}$  bands has been fit with one Voigt peak at  $\sim 1740\text{ cm}^{-1}$  and one linear baseline. This approaches turns out to be satisfactory for *pure* and *mixed* ester surfaces. The fitting parameters are summarized in Table II.4.

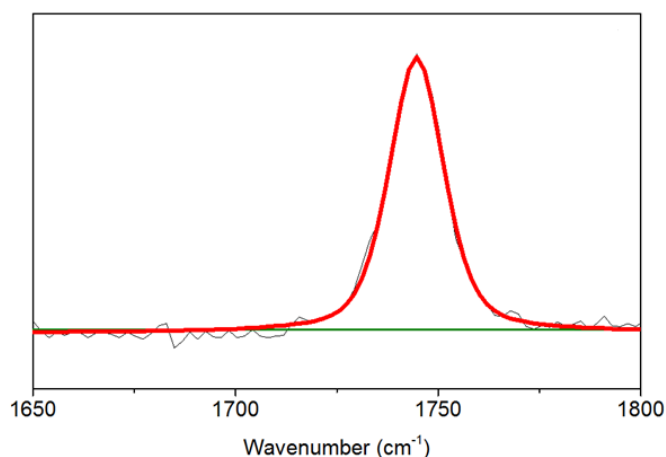


Figure II.7. Examples of the one peak fitting process of the  $\nu\text{C}=\text{O}$  band of a *mixed* Si-ester<sup>30</sup> surface.

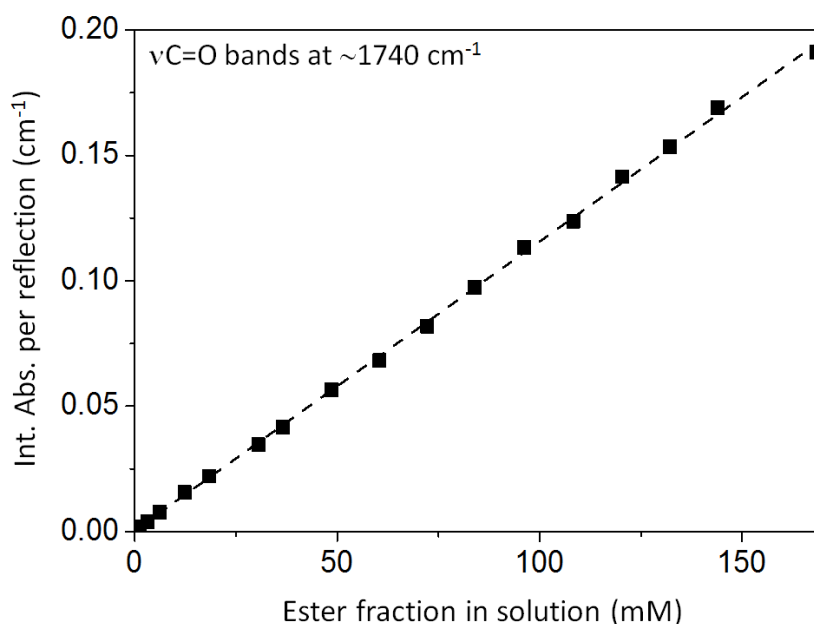
Peak assignment	Peak position ( $\text{cm}^{-1}$ )	Abs.	Width ( $\text{cm}^{-1}$ )	Int. Abs. (Nreflex)	Shape
$\nu\text{C}=\text{O}$ ester	1744.2	0.003	18	0.009	Lorentz

Table II.4 : Example of fitting parameters used for the spectral deconvolution of  $\nu\text{C}=\text{O}$  bands in the spectra of a *mixed* Si-ester<sup>30</sup> monolayer.

#### Ester calibration

The calibration of ester was made using the same technique described above for acid calibration. In this case, undecylenic acid is replaced by ethyl undecanoate. The reference spectrum was taken with pure decane. The following spectra were taken with increasing then

decreasing of ester concentration in solution. Fig. II.8 presents the integrated intensity of  $\nu\text{C}=\text{O}$  peak at  $1740\text{ cm}^{-1}$  in s polarization as a function of the ester fraction in decane solution.



**Figure II.8.** The integrated absorbance of the  $\nu\text{C}=\text{O}$  bands in s polarization as a function of the ethyl undecanoate concentrations in decane solution. Points correspond to the experimental values and lines correspond to the linear regression fits.

By fitting linear regression, an equation was obtained:

$$Abs_{\text{calib}}^s = (0.00115 \pm 0.00001) \cdot [\text{ester}] + (0.00036 \pm 0.00066) \quad \text{Equation II.9}$$

### Ester quantification

By taking the slope of the linear function of  $Abs_{\text{calib}}^s$  (0.00115) corresponding to an absorbance of 1 mM ester and an incident angle  $\theta$  of  $46^\circ$ , we can deduce from Eq. II.3, II.4 and II.5 for ester concentration within monolayers:

$$N_{\parallel}(\text{ester}) = 0.8534 \times 10^{16} \times Abs_{1740}^s \text{ (cm}^{-2}\text{)} \quad \text{Equation II.10}$$

$$N_{\perp}(\text{ester}) = 1.6011 \times 10^{16} \times Abs_{1740}^p - 1.4523 \times 10^{16} \times Abs_{1740}^s \text{ (cm}^{-2}\text{)} \quad \text{Equation II.11}$$

where  $N_{\parallel}$  and  $N_{\perp}$  are respectively the number of vibrators corresponding to the projection of the dynamic dipole of the vibration mode in the interface plane and that corresponding to the projection of the dynamic dipole along the z direction.  $Abs_{1740}^s$  and  $Abs_{1740}^p$  stand for the integrated absorbance per reflection of the  $\nu\text{C}=\text{O}$  peak at  $\sim 1740\text{ cm}^{-1}$  measured in s and p polarization. The surface concentration of ester is directly deduced as the sum of  $N_{\parallel}(\text{ester}) + N_{\perp}(\text{ester})$ .

## II.2.4. Quantification method for Methylene groups

### Fitting process

The  $\nu$ CH bands have been fitted using seven Voigt functions and a linear baseline. Fig. II.9 displays the experimental spectrum and the spectral deconvolution of a *mixed* Si-acid<sup>20</sup> surface. The corresponding fitting parameters and band assignment are reported in Table II.5.

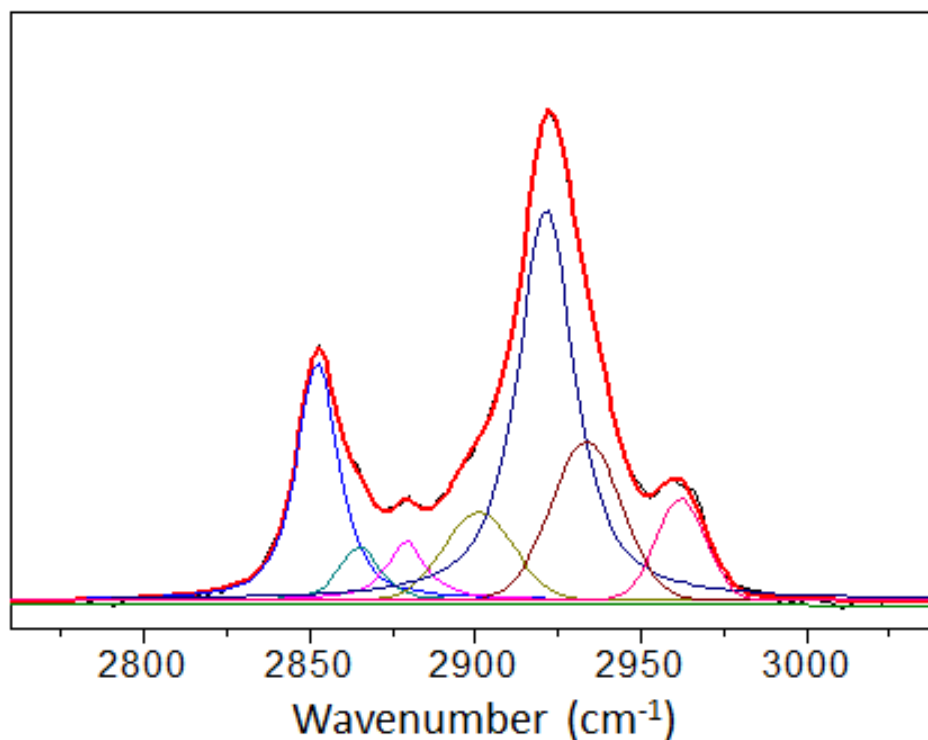


Figure II.9. Experimental spectra of a *mixed* Si-acid<sup>20</sup> monolayer (black) and spectral deconvolution of  $\nu$ CH bands (the resulting envelop and the different components are plotted respectively in red and different colors).

Peak assignment	Peak position (cm <sup>-1</sup> )	Abs.	Width (cm <sup>-1</sup> )	Int. Abs. (Nreflex)	Shape
$\nu_s\text{CH}_2$	2852	0.0054	16	0.113	59% Lorentz+Gauss
$\nu_s\text{CH}_2$ (chain end)	2865	0.0014	15	0.031	93% Lorentz+Gauss
$\nu_s\text{CH}_3$	2881	0.0015	14	0.033	Lorentz
$\nu_{\text{Fermi}}\text{CH}_2$	2903	0.0018	25	0.055	30% Lorentz+Gauss
$\nu_a\text{CH}_2$	2922	0.0083	19	0.231	80% Lorentz+Gauss
	2933	0.0044	26	0.148	43% Lorentz+Gauss
$\nu_a\text{CH}_3$	2963	0.0030	16	0.055	18% Lorentz+Gauss

**Table II.5 : Example of fitting parameters used for the spectral deconvolution of the spectra of a mixed Si-acid<sup>20</sup> monolayer in  $\nu\text{CH}$  region.**

The concentration of the alkyl chains in the monolayers was determined from the sum of integrated absorbance of two  $\nu_s\text{CH}_2$  peaks (2852 and 2865 cm<sup>-1</sup>). These peaks have been chosen because they few overlap with the others with reduced incertitude with respect to the determination of the integrated absorbance.

#### **Methylene calibration**

The calibration of methylene groups was made using the similar method described above for acid calibration. In this case, decane is prepared in (THF) solution and the reference spectrum was taken with pure THF solution. Figure II.10 displays the sum of integrated absorbance of two  $\nu_s\text{CH}_2$  peak (at 2752 and 2765 cm<sup>-1</sup>) in s-polarization as a function of the decane fraction in THF solution.

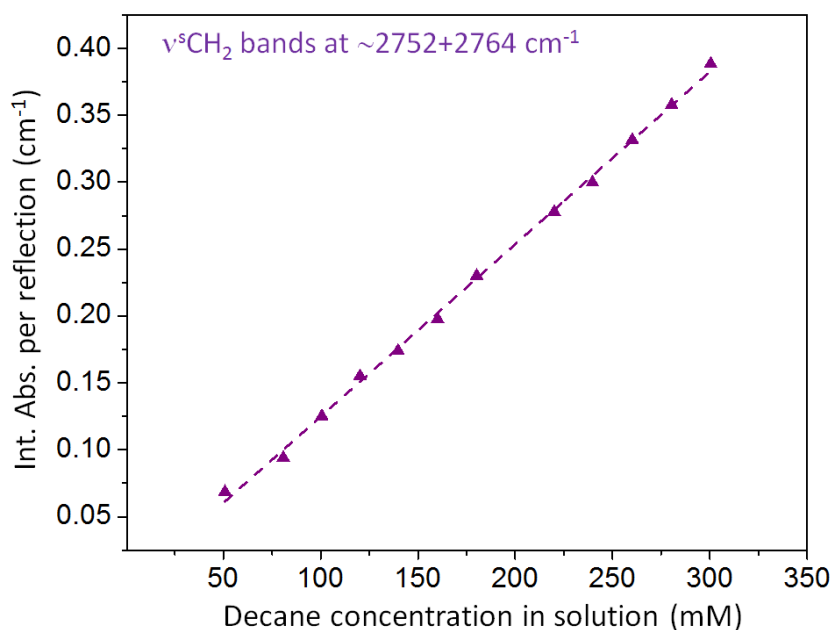


**Figure II.10.** The integrated absorbance in s polarization of  $\nu_s\text{CH}_2$  bands as a function of the decane concentrations in THF solution. Points correspond to the experimental values and lines correspond to the linear regression fits.

By fitting linear regression, an equation was obtained:

$$Abs_{\text{calib}}^s = (0.01290 \pm 0.00001) \cdot [\text{decane}] + (0.00414 \pm 0.00312) \quad \text{Equation II.12}$$

#### Methylene quantification

Knowing that decane contains 8  $\text{CH}_2$  groups per chain and taking the slope of the linear function of  $Abs_{\text{calib}}^s$  (0.06445) corresponding to an absorbance of 1 mM decane and an incident angle  $\theta$  of  $46^\circ$ , we can then deduce from Eq. II.3, II.4 and II.5 the equation for ester concentration within monolayers

$$N_{\parallel}(\text{CH}_2) = 1.8168 \times 10^{17} \times Abs_{\nu_s\text{CH}_2}^s \text{ (cm}^{-2}\text{)} \quad \text{Equation II.13}$$

$$N_{\perp}(\text{CH}_2) = 3.4085 \times 10^{17} \times Abs_{\nu_s\text{CH}_2}^p - 3.0918 \times 10^{17} \times Abs_{\nu_s\text{CH}_2}^s \text{ (cm}^{-2}\text{)} \quad \text{Equation II.14}$$

where  $N_{\parallel}$  and  $N_{\perp}$  are respectively the number of vibrators corresponding to the projection of the dynamic dipole of the vibration mode in the interface plane and that corresponding to the projection of the dynamic dipole along the z direction.  $Abs_{\nu_s\text{CH}_2}^s$  and  $Abs_{\nu_s\text{CH}_2}^p$  stand for the sum of integrated absorbance per reflection of two  $\nu_s\text{CH}_2$  peaks measured in s and p polarization for a monolayer. The methylene concentration is then deduced from the integrated absorbance of  $\nu_s\text{CH}_2$  bands in s and p polarization. The chain concentration in the layer is then determined as the sum of  $N_{\parallel}(\text{CH}_2)$  and  $N_{\perp}(\text{CH}_2)$  divided by the number of

methylene groups in each molecular chain knowing that decyl, carboxydecyl and ethylcarboxydecyl chains contain 9, 10 and 11 methylene groups, respectively.

## II.2.5. Quantification method for Nitro groups

### Fitting process

The  $\nu_s\text{NO}_2$  and  $\nu_a\text{NO}_2$  bands have been fit separately and satisfactory with one Voigt peak and one linear baseline (Fig. II.11). The fitting parameters are detailed in the Table II.6.

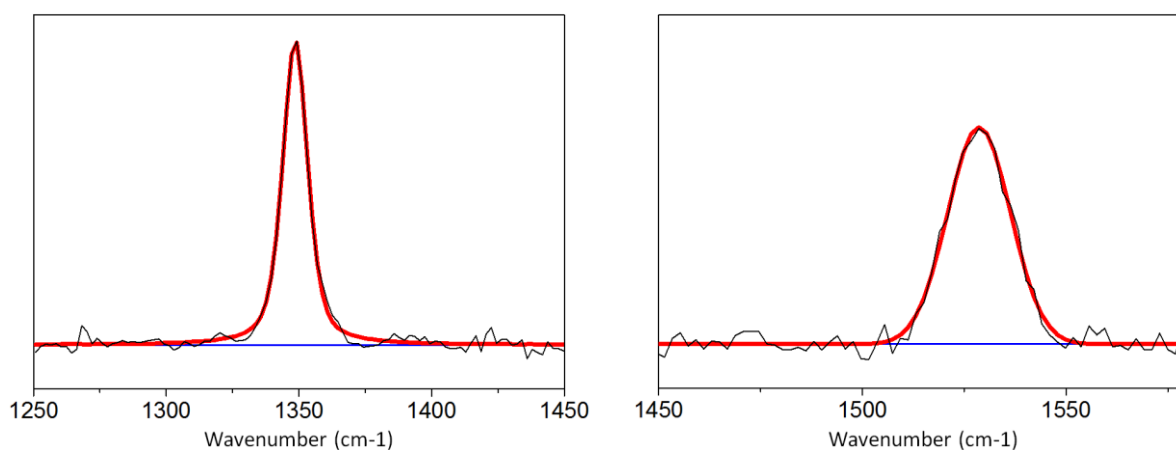


**Figure II.11.** Examples of the one peak fitting process of two  $\nu_s\text{NO}_2$  and  $\nu_a\text{NO}_2$  bands of a *mixed* Si-acid<sup>10</sup> surface after esterification (Si-nitro<sup>acid-10</sup>).

Peak assignment	Peak position (cm <sup>-1</sup> )	Abs.	Width (cm <sup>-1</sup> )	Int. Abs. (Nreflex)	Shape
$\nu_s\text{NO}_2$	1348.6	0.007	11	0.010	Lorentz
$\nu_a\text{NO}_2$	1528.7	0.005	18	0.009	Lorentz

**Table II.6.** Example of fitting parameters used for the spectral deconvolution of  $\nu_s\text{NO}_2$  and  $\nu_a\text{NO}_2$  bands in the spectra of a *mixed* Si-nitro<sup>acid-10</sup> monolayer.

### Nitro calibration

The calibration of nitro groups is made using the similar method described above for acid calibration. In this case, nitrophenethyl alcohol (NPEA) is prepared in dichloromethane (DCM) solution and the reference spectrum was taken with pure DCM. Figure II.12 displays the integrated intensity of  $\nu_s\text{NO}_2$  and  $\nu_a\text{NO}_2$  peak at 1348 and 1521 cm<sup>-1</sup>, respectively, in s polarization as a function of the nitrophenethyl alcohol fraction in DCM solution.

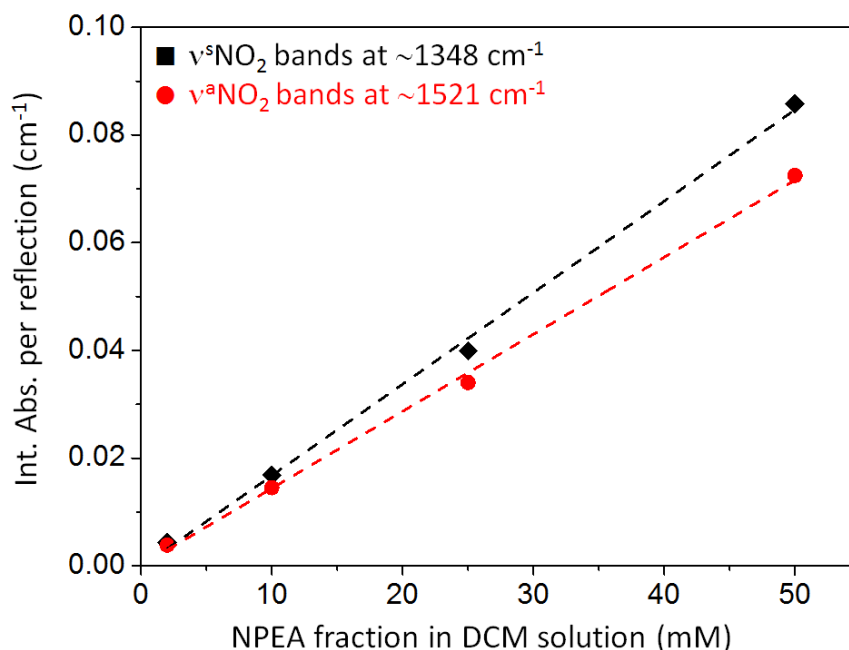


**Figure II.12.** The integrated absorbance in s-polarization of  $\nu^s\text{NO}_2$  and  $\nu^a\text{NO}_2$  bands as a function of the nitrophenethyl alcohol concentration in DCM solution. Points correspond to the experimental values and lines correspond to the linear regression fits.

By fitting linear regression, two equations were obtained for both peaks at 1348 and 1521  $\text{cm}^{-1}$ :

$$Abs_{\text{calib}}^s(1348) = (0.00170 \pm 0.00005) \cdot [\text{NPEA}] + (0.00023 \pm 0.00154) \quad \text{Equation II.15}$$

$$Abs_{\text{calib}}^s(1521) = (0.00143 \pm 0.00004) \cdot [\text{NPEA}] + (0.00008 \pm 0.00121) \quad \text{Equation II.16}$$

### Nitro quantification

By taking the slope of the linear function of  $Abs_{\text{calib}}^s$  (0.00131 and 0.0011) corresponding to an absorbance of 1 mM NPEA and an incident angle  $\theta$  of  $46^\circ$ , we can deduce from Eq. II.3, II.4 and II.5 separately two pairs of equation which can be used for the determination of nitro group concentration within monolayers:

$$N_{\parallel}(\text{nitro})^{1348} = 0.7511 \times 10^{16} \times Abs_{1348}^s (\text{cm}^{-2}) \quad \text{Equation II.17}$$

$$N_{\perp}(\text{nitro})^{1348} = 1.4091 \times 10^{16} \times Abs_{1348}^p - 1.2782 \times 10^{16} \times Abs_{1348}^s (\text{cm}^{-2}) \quad \text{Equation II.18}$$

and

$$N_{\parallel}(\text{nitro})^{1521} = 0.7911 \times 10^{16} \times Abs_{1521}^s (\text{cm}^{-2}) \quad \text{Equation II.19}$$

$$N_{\perp}(\text{nitro})^{1521} = 1.4842 \times 10^{16} \times Abs_{1521}^p - 1.3463 \times 10^{16} \times Abs_{1521}^s (\text{cm}^{-2}) \quad \text{Equation II.20}$$

where  $N_{\parallel}$  and  $N_{\perp}$  are respectively the number of vibrators corresponding to the projection of the dynamic dipole of the vibration mode in the interface plane and that corresponding to the projection of the dynamic dipole along the z direction.  $Abs_{1348}^s$ ,  $Abs_{1348}^p$ ,  $Abs_{1521}^s$  and  $Abs_{1521}^p$  stand respectively for the integrated absorbance per reflection in s and p polarization of the  $\nu C=O$  peak at 1348 and 1521  $cm^{-1}$  measured. The surface concentration of nitro groups can be deduced separately as the sum of  $N_{\parallel}(\text{nitro})^{1348}$  and  $N_{\perp}(\text{nitro})^{1348}$  or as the sum of  $N_{\parallel}(\text{nitro})^{1521}$  and  $N_{\perp}(\text{nitro})^{1521}$ . The average of two results is used as the final surface concentration of nitro groups.

## References

- (1) Faucheux, A.; Yang, F.; Allongue, P.; De Villeneuve, C. H.; Ozanam, F.; Chazalviel, J. N. *Appl Phys Lett* **2006**, 88.
- (2) Chabal, Y. J. *Surface Science Reports* **1988**, 8, 211.

## Appendix III

### Kinetics of photo-isomerization reaction

The photochromism scheme of indolylyfulgimide is shown in Fig. III.1. Under visible reaction, the steady state will correspond to a complete depletion of C-forms from the solution. Under UV irradiation, a mixture of C- and E/Z-forms is expected with proportion depending upon the respective values of the rate constants of the reactions operating under UV.

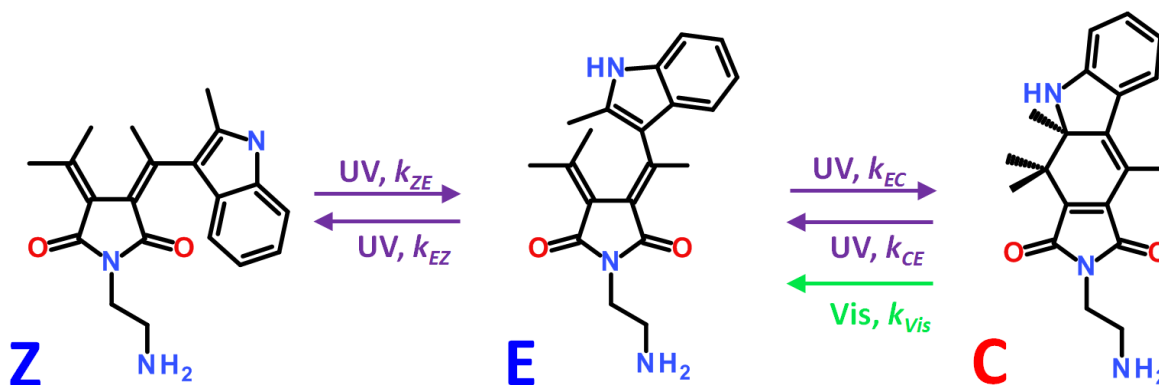


**Figure III.1.** Photochromism of fulgimide precursors under Vis ( $\rightarrow$ ) or UV ( $\leftarrow$ ) illumination. The various  $k_i$ 's stand for rate constants associated with the specific reactions.

Following Beer-Lambert, we can write the equation of absorbance

$$Abs = c\sigma_{Abs}L \quad \text{Equation III.1}$$

where  $c$ ,  $\sigma_{abs}$  and  $L$  are the concentration of absorbing species, the absorption cross section and the distance the light travels through the solution, respectively.

Let us assume that the absorption of flux photon is low, so that a small number of photons  $\delta N_i$  is absorbed and gives rise to photo-isomerization. We then can define the photo-isomerization cross-section analytically by

$$\delta N_i = -c\sigma_i l N \quad \text{Equation III.2}$$

with  $N = \phi S \delta t$ . From this condition, we consider that the variation of  $\delta N_i$  causes a variation homogenous of molecular concentration  $\delta C_i = \frac{\delta N_i}{l.S}$ , therefore

$$\delta N_i = -c\sigma_i l \phi S \delta t = l S \frac{\delta Abs}{\sigma_{Abs} L} \quad \text{Equation III.3}$$

$$\delta Abs = -\sigma_i \phi Abs \delta t \quad \text{Equation III.4}$$

Under visible illumination, the reaction scheme as shown in Fig. III.1 reduces to a single reaction corresponding to a C→E transformation (Fig. III.1, **Vis** path). The kinetics of such a reaction should obey

$$\frac{-dC}{dt} = k_{vis} C \quad \text{Equation III.5}$$

where C stand for the C-form concentration. Eq. III.5 can be straightforwardly integrated and the evolution of the C-form concentration C(t) is

$$C(t) = A \exp\left(-\frac{t}{\tau^{vis}}\right) \text{ with } \tau^{vis} = \frac{1}{k_{vis}} \quad \text{Equation III.6}$$

As experimentally observed, the evolution of the C-form concentration is solution follows an exponential profile.

Under UV illumination, four reactions corresponding to the C↔E and E↔Z transformations come into play, according to the **purple** paths in Fig. III.1. The kinetics of the systems are therefore more complexes. Notify E, Z and C the respective concentration of the solution in E, Z and C-forms, a system of three rate equations can be written

$$\frac{dE}{dt} = k_{ZE}Z - k_{EZ}E - k_{EC}E + k_{CE}C \quad \text{Equation III.7}$$

$$\frac{dZ}{dt} = -k_{ZE}Z + k_{EZ}E \quad \text{Equation III.8}$$

$$\frac{dC}{dt} = k_{EC}E - k_{CE}C \quad \text{Equation III.9}$$

Firstly, the system can be transformed to a homogeneous system of matrix 3×3. The detailed solution of this system can be found in Appendix III. The characteristic equation of system can be then written as

$$\left(\frac{1}{\tau}\right)^2 - (k_{EZ} + k_{ZE} + k_{EC} + k_{CE})\left(\frac{1}{\tau}\right) + k_{EC}k_{ZE} + k_{CE}k_{EC} + k_{CE}k_{EZ} = 0 \quad \text{Equation III.10}$$

and its discriminant is

$$D = (k_{EC} + k_{CE} - k_{EZ} - k_{ZE})^2 + 4k_{EC}k_{EZ} \quad \text{Equation III.11}$$

where  $D > 0$  for all kinetic constants. The system has then two distinct real roots,  $\frac{1}{\tau_1}$  and  $\frac{1}{\tau_2}$ . If we consider that  $k_{EC}k_{EZ} \ll (k_{EC} + k_{CE} - k_{EZ} - k_{ZE})^2$ , then

$$\frac{1}{\tau_1} \approx k_{EC} + k_{CE} \quad \text{Equation III.12}$$

$$\frac{1}{\tau_2} \approx k_{ZE} + k_{EZ} \quad \text{Equation III.13}$$

The general solution of the system can be expressed as

$$E(t) = U_1 + V_1 e^{-\frac{t}{\tau_1}} + W_1 e^{-\frac{t}{\tau_2}} \quad \text{Equation III.14}$$

$$Z(t) = U_2 + V_2 e^{-\frac{t}{\tau_1}} + W_2 e^{-\frac{t}{\tau_2}} \quad \text{Equation III.15}$$

$$C(t) = U_3 + V_3 e^{-\frac{t}{\tau_1}} + W_3 e^{-\frac{t}{\tau_2}} \quad \text{Equation III.16}$$

The relation between all constants  $U_i$ ,  $V_i$  and  $W_i$  can be found by replacing the system of Eq. III.14, III.15 and III.16 to the system of Eq. III.7, III.8 and III.9

$$U_2 = \frac{k_{EZ}}{k_{ZE}} U_1, V_2 = \frac{k_{EZ}\tau_1}{k_{ZE}\tau_1 - 1} V_1, W_2 = \frac{k_{EZ}\tau_2}{k_{ZE}\tau_2 - 1} W_1 \quad \text{Equation III.17}$$

$$U_3 = \frac{k_{EC}}{k_{CE}} U_1, V_3 = \frac{k_{EC}\tau_1}{k_{CE}\tau_1 - 1} V_1, W_3 = \frac{k_{EC}\tau_2}{k_{CE}\tau_2 - 1} W_1 \quad \text{Equation III.18}$$

These constants also depend on the value of C, E and Z at a time constant. Eq. III.16 shows clearly that the cyclization kinetic under UV is bi-exponential time dependence.

## Appendix IV

### NMR analysis of fulgimides in solution

---

The liquid-state NMR spectra were recorded on a Bruker AvanceII 300 spectrometer (300 MHz for  $^1\text{H}$ ).  $^1\text{H}$  spectra were internally referenced from peaks of residual protons in deuterated solvents. The number of protons was determined by integration of the signals. Multiplicities of the signals were abbreviated as follows: s = singlet, d = doublet, t = triplet, q = quartet, m = multiplet, br. = broad. Reagents were dissolved in chloroform ( $\text{CDCl}_3$ ).

**E/Z-isomer** ( $\text{CDCl}_3$ ,  $25^\circ\text{C}$ , d) : the ratio of mixture of isomers can be define from the peaks in the 7.0-7.5 ppm range. Herein, E-isomer can be identified as 7.43 (d, 1H) and 7.27 (d, 1H). Similarly, Z-isomer can be identified as 7.48 (d, 1H) and 7.33 (d, 1H). The ratio E:Z was found to be  $1:0.35 \approx 0.75:0.25$ .

**C-isomer** ( $\text{CDCl}_3$ ,  $25^\circ\text{C}$ , d) : 7.57 (dd, 1H), 7.15 (t, 1H), 6.77 (m, 2H), 3.67 (m, 4H), 2.40 (d, 2H), 2.03 (s, 1H), 1.52 (s, 3H), 1.29 (s, 3H), 1.15 (s, 3H). NMR results of C-isomer show only those characteristic peaks of C-isomer. No peak of E- or Z- isomers is observed. The peak at 1.26 was not belonging to any isomer.

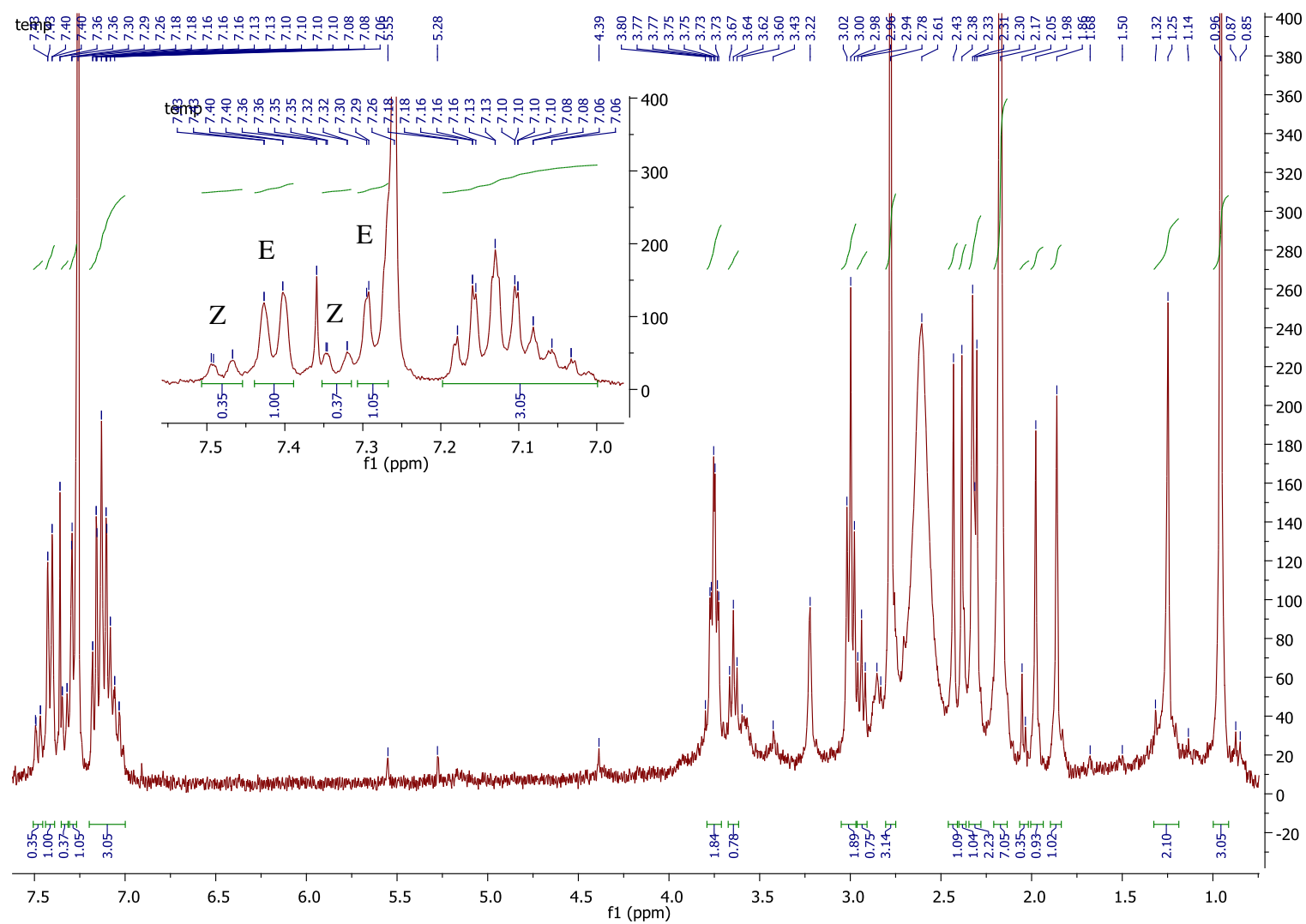


Figure IV.1. NMR spectrum of EZ-isomer showing a ratio E:Z = 0.75:0.25.

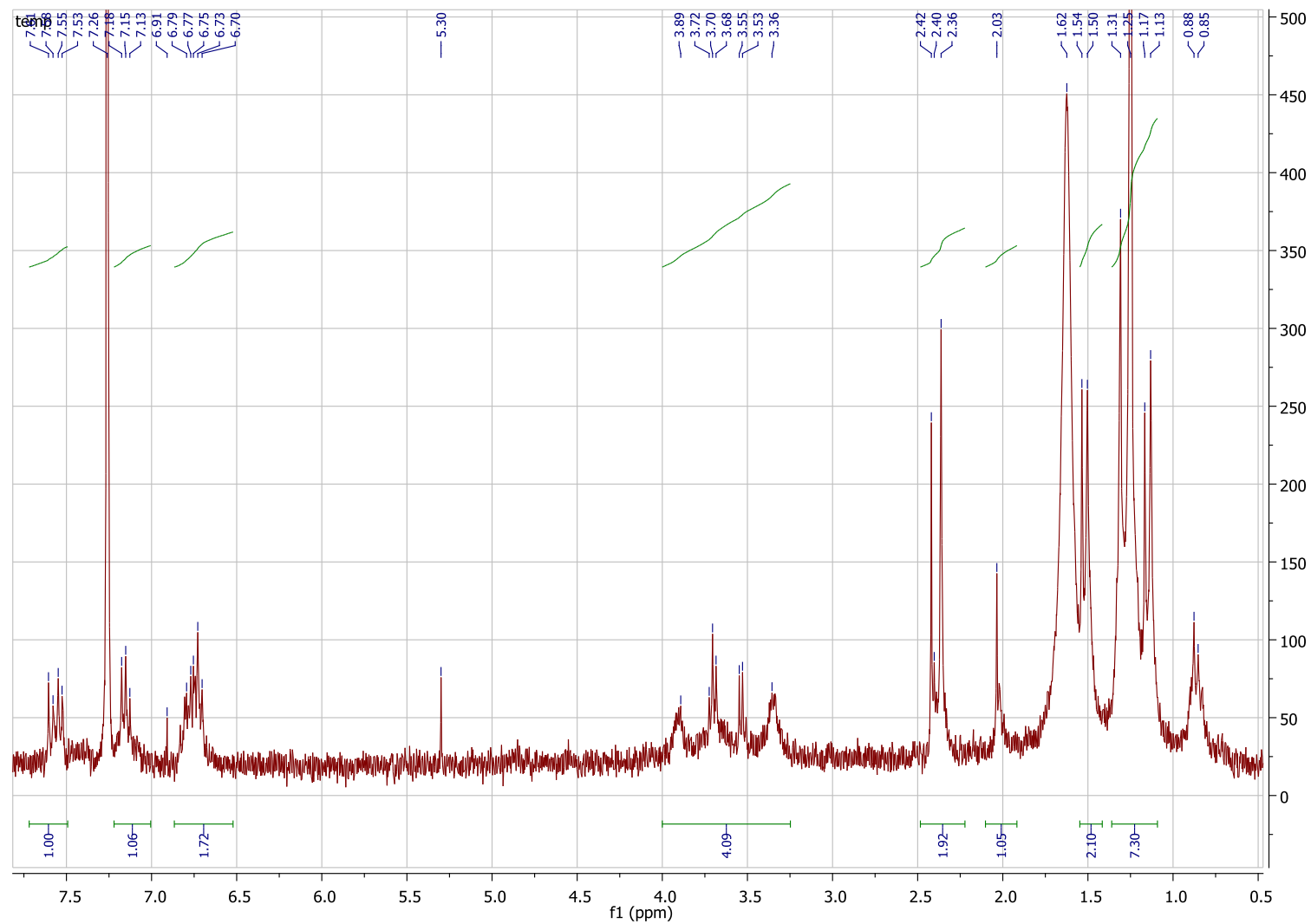


Figure IV.2. NMR spectrum of C-isomer.